

**The Pennsylvania State University
The Graduate School**

**DEVELOPMENT OF AN ION TIME-OF-FLIGHT SPECTROMETER
FOR NEUTRON DEPTH PROFILING**

A Thesis in
Nuclear Engineering
by
Mustafa Sacit Çetiner

© 2008 Mustafa Sacit Çetiner

Submitted in Partial Fulfillment
of the Requirements
for the Degree of

Doctor of Philosophy

May 2008

The thesis of Mustafa Sacit Çetiner was reviewed and approved* by the following:

Kenan Ünlü, Ph.D.
Senior Scientist, Radiation Science and Engineering Center
Professor of Mechanical and Nuclear Engineering Department
Thesis Advisor, Chair of Committee

Jack S. Brenizer, Ph.D.
J. 'Lee' Everett Professor of Mechanical and Nuclear Engineering Department
Nuclear Engineering Program Chair

Arthur T. Motta, Ph.D.
Professor of Mechanical and Nuclear Engineering Department

Vijaykrishnan Narayanan, Ph.D.
Professor of Computer Science and Engineering Department

R.Gregory Downing, Ph.D.
National Institute of Standards and Technology (NIST)
Special Member

Tim Z. Hossain, Ph.D.
Advanced Micro Devices (AMD)
Special Member

Michael S. Gordon, Ph.D.
IBM T. J. Watson Research Center
Special Member

*Signatures are on file in the Graduate School.

ABSTRACT

Ion time-of-flight spectrometry techniques are investigated for applicability to neutron depth profiling. Time-of-flight techniques are used extensively in a wide range of scientific and technological applications including energy and mass spectroscopy.

Neutron depth profiling is a near-surface analysis technique that gives concentration distribution versus depth for certain technologically important light elements. The technique uses thermal or sub-thermal neutrons to initiate (n, p) or (n, α) reactions. Concentration versus depth distribution is obtained by the transformation of the energy spectrum into depth distribution by using stopping force tables of the projectiles in the substrate, and by converting the number of counts into concentration using a standard sample of known dose value.

Conventionally, neutron depth profiling measurements are based on charged particle spectrometry, which employs semiconductor detectors such as a surface barrier detector (SBD) and the associated electronics. Measurements with semiconductor detectors are affected by a number of broadening mechanisms, which result from the interactions between the projectile ion and the detector material as well as fluctuations in the signal generation process. These are inherent features of the detection mechanism that involve the semiconductor detectors and cannot be avoided.

Ion time-of-flight spectrometry offers highly precise measurement capabilities, particularly for slow particles. For high-energy low-mass particles, measurement resolution tends to degrade with all other parameters fixed. The threshold for more precise ion energy measurements with respect to conventional techniques, such as direct energy measurement by a surface barrier detector, is directly related to the design and operating parameters of the device.

Time-of-flight spectrometry involves correlated detection of two signals by a coincidence unit. In ion time-of-flight spectroscopy, the ion generates the primary input signal. Without loss of generality, the secondary signal is obtained by the passage of the ion through a thin carbon foil, which produces ion-induced secondary electron emission (IISSE). The time-of-flight spectrometer physically acts as an ion/electron separator. The electrons that enter the active volume of the spectrometer are transported onto the microchannel plate detector to generate the secondary signal. The electron optics can be designed in variety of ways depending on the nature of the measurement and physical requirements.

Two ion time-of-flight spectrometer designs are introduced: the parallel electric and magnetic (PEM) field spectrometer and the cross electric and magnetic (CEM) field spectrometer. The CEM field spectrometers have been extensively used in a wide range of applications where precise mass differentiation is required. The PEM field spectrometers have lately found interest in mass spectroscopy applications. The application of the PEM field spectrometer for energy measurements is a novel approach.

The PEM field spectrometer used in the measurements employs axial electric and magnetic fields along the nominal direction of the incident ion. The secondary electrons are created by a thin carbon foil on the entrance disk and transported on the microchannel plate that faces the carbon foil. The initial angular distribution of the secondary electrons has virtually no effect on the transport time of the secondary electrons from the surface of the carbon foil to the electron microchannel plate detector. Therefore, the PEM field spectrometer can offer high-resolution energy measurement for relatively lower electric fields. The measurements with the PEM field spectrometer were made with the Tandem linear particle accelerator at the IBM T. J. Watson Research Center at Yorktown Heights, NY.

The CEM field spectrometer developed for the thesis employs axial electric field along the nominal direction of the ion, and has perpendicular magnetic field. As the electric field accelerates and then decelerates the emitted secondary electron beam, the magnetic field steers the beam away from the source and focuses it onto the electron microchannel plate detector. The initial momentum distribution of the electron beam is observed to have profound effect on the electron transport time. Hence, the CEM field spectrometer measurements suffer more from spectral broadening at similar operating parameters. The CEM field spectrometer measurements were obtained with a ^{210}Po alpha source at the Penn State Radiation Science and Engineering Center, University Park, PA.

Although the PEM field spectrometer suffers less from electron transport time dispersion, the CEM field spectrometer is more suited for application to neutron depth profiling. The multiple small-diameter apertures used in the PEM field configuration considerably reduces the geometric efficiency of the spectrometer. Most of the neutron depth profiling measurements, where isotropic emission of charged particles is observed, have relatively low count rates; hence, high detection efficiency is essential.

TABLE OF CONTENTS

List of Figures	ix
List of Tables	xiii
List of Symbols	xiv
Acknowledgments	xv
Chapter 1	
Introduction	1
1.1 Motivation	2
1.2 Statement of Objectives	5
Chapter 2	
Theory and Background	6
2.1 Transport of Ions in Solids	7
2.1.1 Definitions	8
Stopping Force	8
Mean Energy Loss	8
Path Length	9
Mean Projected Range	9
Energy Loss Fluctuation or Energy Loss Straggling	9
Range Straggling	10
Higher Moments of Range Profiles	10

2.1.2	Stopping of Energetic Ions in Matter	11
	Stopping and Range of Ions in Matter (SRIM)	11
2.2	Neutron Depth Profiling	12
2.2.1	The (n, p) and (n, α) Reactions	14
2.2.2	Depth Calculations	15
2.2.3	Concentration Calculations	15
2.3	Uncertainties	18
2.3.1	Uncertainties that Result from Sample Substrate	20
	Amorphous Material	20
	Crystalline Material	22
2.3.2	Uncertainties that Result from Geometry	24
2.3.3	Uncertainties that Result from Detector	32
	Semiconductor Detectors	32
	Microchannel Plates	34
2.3.4	Uncertainties that Result from Measurement Electronics	35
2.3.5	A Comparison of Uncertainties between Conventional Charged-Particle Spectrometry and Ion Time-of-Flight Spectrometry	36
2.4	Time-of-Flight Spectrometry	39
2.4.1	Principles of Time-of-Flight Spectrometry	39
2.4.2	Applications of Time-of-Flight Spectrometry	41
2.4.3	Correlation between the Time and Energy Spectra	43
2.5	Particle-Induced Electron Emission	45
2.5.1	Background and Theory	47
	Early Theories	48
	The Semiempirical Theory	49
	The Theory of Sternglass (1957)	49
	The Theory of Parilis and Kishinevskii (1960)	50
	The Theory of Schou (1980)	50
2.5.2	Kinetic Electron Emission from Ion Penetration through Thin Films	51

Chapter 3

	Ion Time-of-Flight Spectrometry	57
3.1	Parallel Electric and Magnetic (PEM) Field Ion Time-of-Flight Spectrometer	57
3.1.1	Design of the Device	58
	Design of the Acceleration Stages	58
	Design of the Magnet	58
	Simulations of Electron Transport	60
	Focal Length	61
3.2	Cross Electric and Magnetic (CEM) Field Ion Time-of-Flight Spectrometer	64
3.2.1	Design of the Device	64
	Design of the Magnet	64

Design of the Acceleration Stages	66
Chapter 4	
Experimental	70
4.1 Description of the Experimental Facilities	70
4.1.1 Penn State Radiation Science and Engineering Center, Breazeale Nuclear Reactor	71
4.1.2 IBM T. J. Watson Research Center, Tandem Linear Accelerator	75
4.2 Neutron Depth Profiling by Energy Spectrometry	76
4.2.1 Description of the Experimental Setup	76
4.2.2 Measurement Electronics	77
4.3 Ion Time-of-Flight Spectrometry	79
4.3.1 Description of the Experimental Setup	79
4.3.2 Measurement Electronics	80
Effect of Input Signal Width	83
Time Drift	84
Effect of Delay	86
Chapter 5	
Results and Discussion	88
5.1 Neutron Depth Profiling based on Energy Measurements	88
5.1.1 Intel SEA2 Borophosphosilicate Glass Sample	89
5.1.2 AMD 120-keV Boron Implanted Silicon Wafer	93
5.2 Experiments with the PEM Field Time-of-Flight Spectrometer	97
5.2.1 Experimental Measurements	98
Response of the Spectrometer to Beam Energy	99
Response of the Spectrometer to Electron Acceleration Potential	102
Effect of Carbon Foil Thickness	105
5.2.2 Discussions on Experimental Results	106
Calculation of the Ion Flight Path Length	106
Calculation of the Electron Flight Path Length	107
Offset and Delay Correction of the Ion Time-of-Flight Spectrum	108
Energy Calibration of the Time-of-Flight Spectrum	111
Resolution of the PEM Field Spectrometer	113
Detection Efficiency of the PEM Field Spectrometer	115
5.3 Experiments with the CEM Field Time-of-Flight Spectrometer	116
5.3.1 Experimental Measurements	118
Response of the Spectrometer to Electron Acceleration Potential	118
Response of the Spectrometer to Magnetic Field Variation	119
5.3.2 Discussion on Experimental Results	122
Offset and Delay Correction of the Ion Time-of-Flight Spectrum	122
Energy Calibration of the Time-of-Flight Spectrum	124
Resolution of the CEM Field Spectrometer	126

Detection Efficiency of the CEM Field Spectrometer	128
Chapter 6	
Summary and Conclusions	129
6.1 Summary of the Research	129
6.2 Conclusions	133
6.3 Recommendations and Future Work	136
6.3.1 Future Designs	139
Bibliography	140
Appendix A	
Equations of Motion for Electrons in Free Space	149
A.1 Parallel Electric and Magnetic (PEM) Fields	149
A.2 Cross Electric and Magnetic (CEM) Fields	151
Appendix B	
Library of Computational Tools	153
B.1 Definitions of Physical Constants	153
B.2 Depth Profiling Calculations	155
B.3 Automated TRIM Simulations	160
B.4 Monte Carlo Simulator for Solid Angle Estimation	162
Appendix C	
Bibliography on Neutron Depth Profiling	165

LIST OF FIGURES

1.1	Block diagram representation of interaction mechanisms in a measurement system.	2
2.1	Correlation between the residual energy and the depth of reaction site for (top) alpha particles coming from $^{10}\text{B}(n, \alpha)^7\text{Li}$ reaction, (bottom) ^{14}C recoil coming from $^{14}\text{N}(n, p)^{14}\text{C}$ reaction; both in silicon substrate. . . .	13
2.2	Distribution of alpha particle energies after penetrating a 100-nm silicon layer.	21
2.3	Geometry of an isotropic on-axis point source and a detector.	26
2.4	Expected time-of-flight dispersion of an on-axis isotropic point source due to geometric convolution.	27
2.5	Monte Carlo simulation of the time of flight spectrum for a monoenergetic isotropic point source of alpha with energy $E_0 = 1472 \text{ keV}$; detector diameter 25 mm , source-detector separation 50 mm	28
2.6	(top) Geometry of an isotropic off-axis point source and a detector; (bottom) Explicit depiction of geometric convolution for an off-axis point source.	29
2.7	Expected time-of-flight dispersion from an off-axis isotropic point source.	30
2.8	Evaluated time-of-flight dispersion from an isotropic planar source of 10-mm diameter at energy $E_0 = 1472 \text{ keV}$ with a 25-mm diameter detector; source-detector separation 50 mm	31
2.9	Monte Carlo simulation of the time of flight spectrum for a monoenergetic isotropic planar source of alpha with energy $E_0 = 1472 \text{ keV}$; source diameter 10 mm , detector diameter 25 mm , source-detector separation 50 mm	31
2.10	Sensitivity of energy with respect to the location of the peak on the time spectrum.	44

2.11	A simplified depiction of ion-induced secondary electron emission from a thin carbon foil upon impact of an energetic ion.	46
2.12	Forward, backward and total electron yields, γ_F , γ_B and γ_T , respectively, versus incident proton energy E_i from thin carbon foil	54
2.13	Electron yield versus incident H^+ energy for the range 20 keV-1 MeV .	55
2.14	Electron yield from thin carbon foil versus incident lithium ion energy at various charge states	56
3.1	Variation of on-axis magnetic field inside the solenoid along the acceleration stages.	59
3.2	Parallel electric and magnetic (PEM) field ion time-of-flight spectrometer.	61
3.3	Electron ray tracing in parallel electric and magnetic fields.	62
3.4	Projection of the electron traces in Figure 3.3 on the (y, z) plane.	63
3.5	Three-dimensional drawing of the Helmholtz coil pair.	66
3.6	On-axis distribution of the magnetic field created by the Helmholtz coil.	67
3.7	The simulated electron trajectories for the CEM field spectrometer in x , y and z directions.	68
3.8	Ion time-of-flight spectrometer that employs cross electric and magnetic (CEM) fields.	69
4.1	Differential neutron flux spectrum at the beam port location #4.	72
4.2	The vacuum chamber, beam port BP4 and the measurement electronics in the neutron beam laboratory area.	73
4.3	Layout of the reactor core, D_2O tank, graphite reflector, concrete wall, target chamber and the beam catcher.	74
4.4	Alpha energy spectra obtained with a surface barrier detector measured at IBM T. J. Watson Research Center.	76
4.5	Block diagram of the measurement electronics used in neutron depth profiling by energy spectroscopy.	77
4.6	Electronics used in the ion time-of-flight spectrometry measurements. .	81
4.7	Microchannel plate time pick-off circuit.	82
4.8	The response of the Ortec 9327 1-GHz Preamplifier and Timing Discriminator to 2-ns width input pulses (AMP-INP) generated by a precision oscillator.	83
4.9	Measured uncertainties at various input signal widths.	84
4.10	Uncertainty variation with respect to input signal width.	85
4.11	The effect of the length of the device operation on 50-ns delay for the same input signal.	86
4.12	Measured time offset at various delay values.	87
5.1	Ion energy spectrum of Intel SEA2 borophosphosilicate glass sample obtained with a silicon PIN photodiode.	90

5.2	Detail from Figure 5.1 showing the two alpha peaks from the $^{10}\text{B}(n, \alpha)^7\text{Li}$ reaction.	91
5.3	Boron concentration profile versus depth in borophosphosilicate glass calculated from the 1471.9-keV alpha spectrum in Figure 5.2.	92
5.4	Ion energy spectrum from the measurement of AMD 120-keV boron implanted silicon wafer.	94
5.5	Detail from Figure 5.4 showing the alpha peaks from the $^{10}\text{B}(n, \alpha)^7\text{Li}$ reaction.	95
5.6	Boron concentration versus depth profile in silicon substrate calculated from the 1472-keV peak in Figure 5.5.	96
5.7	Energy spectrum of the alpha beam from the Tandem accelerator measured with a surface barrier detector.	97
5.8	A simplified sketch of the PEM field spectrometer.	98
5.9	Computed energy spectra of alpha particles after penetrating carbon foils of 50 nm and 200 nm.	99
5.10	Time-of-flight spectra of the alpha beam at various energies.	100
5.11	Variation of temporal resolution of the spectrometer with respect to beam energy.	101
5.12	Spectral response to variation in electron accelerating electric field. . . .	102
5.13	Spectral shift and spread variation with respect to electron accelerating potential.	103
5.14	Variation of standard deviation with respect to accelerating electric field. .	104
5.15	Time-of-flight spectra for 1.5-MeV alpha beam obtained with different carbon foil thicknesses. The spectra were normalized with respect to maximum count rate.	105
5.16	Offset and delay corrected ion time-of-flight spectra of the data shown in Figure 5.10.	109
5.17	Offset and delay corrected spectra for 5-kV/m and 50-kV/m electric fields from the measurements presented in Figure 5.13.	110
5.18	Energy spectra obtained from the alpha time-of-flight spectra shown in Figure 5.16.	111
5.19	Variation of the energy resolution of the spectrometer with respect to beam energy.	112
5.20	Energy spectra obtained from the alpha time-of-flight spectra shown in Figure 5.17.	113
5.21	Variation of the energy resolution of the PEM spectrometer with respect to accelerating electric field.	114
5.22	Efficiency variation of the PEM field spectrometer with respect to alpha beam energy.	115
5.23	Simplified drawing of the CEM field spectrometer showing the ion and secondary electron trajectories and associated detectors.	116

5.24	Exptected alpha energy spectrum of the ^{210}Po alpha source obtained with the TRIM simulation.	117
5.25	Time-of-flight spectra of the ^{210}Po source at different electric and magnetic field values obtained with the CEM field spectrometer.	119
5.26	Variation of the count rate on the electron microchannel plate with respect to the electrical current through the magnet coils at 4 kV/m electric field.	120
5.27	Variation of the count rate on the electron microchannel plate with respect to the electrical current through the magnet coils at 16 kV/m electric field.	121
5.28	Offset and delay corrected ion time-of-flight spectra of the ^{210}Po alpha source obtained with the CEM field spectrometer at different electric and magnetic field values.	123
5.29	Energy spectrum of alpha particles from the ^{210}Po alpha source after calibration.	125
5.30	Simulate electron flight time dispersion at 150-V acceleration potential due to initial momentum spread.	127
5.31	Variation of electron flight time dispersion with respect to E/B ratio calculated by the Monte Carlo simulation.	128
6.1	Conceptual parallel electric/magnetic (PEM) field spectrometer for improved measurement resolution.	137
6.2	Ion time-of-flight spectrometer using a nonuniform electric field in a triangular domain.	138

LIST OF TABLES

2.1	Relative Atomic Mass of the Isotopes used in the Calculation of Initial Kinetic Energies of Reaction Products from $^{10}\text{B}(n, \alpha)^7\text{Li}$ and $^{14}\text{N}(n, p)^{14}\text{C}$	12
2.2	List of isotopes that undergo (n, p) or (n, α) reactions with thermal neutrons with cross sections larger than 0.01 b	14
2.3	A comparison of uncertainties in a charged particle spectrometer and a time-of-flight spectrometer introduced by different components in a measurement system	38
4.1	Performance specifications of the Hamamatsu S3590-09 PIN photodiode as given by the manufacturer	78
4.2	Performance specifications of the ORTEC 142A preamplifier as given by the manufacturer	78
4.3	Performance specifications of the ORTEC 572 spectroscopy amplifier as given by the manufacturer	79
4.4	Performance specifications of the Canberra 8713 ADC analog-to-digital converter as given by the manufacturer	79
4.5	Performance specifications of the ORTEC 9327 1-GHz Preamplifier and Timing Discriminator as given by the manufacturer	81
4.6	Performance specifications of the ORTEC 9308 picosecond Time Analyzer as given by the manufacturer	82

LIST OF SYMBOLS

c	Speed of light; $c = 299\,792\,458\text{ m/s}$
h	Planck constant; $h = 6.626\,068\,96(33) \times 10^{-34}\text{ J s}$
\hbar	$\hbar = h/2\pi \approx 1.054\,571\,628(53) \times 10^{-34}\text{ J s}$
e_0	Atomic unit charge; $e_0 = 1.602\,176\,487(40) \times 10^{-19}\text{ C}$
m_e	Electron rest mass; $m_e = 9.109\,382\,15(45) \times 10^{-31}\text{ kg}$
μ_0	Permeability of free space; $\mu_0 = 4\pi \times 10^{-7}\text{ N/A}^2 \approx 12.566\,370\,614... \times 10^{-7}\text{ N/A}^2$
ϵ_0	Permittivity of free space; $\epsilon_0 = 1/(\mu_0 c^2) \approx 8.854\,187\,817... \times 10^{-12}\text{ F/m}$
Z_1	Projectile atomic number
Z_2	Target material atomic number
M_1	Projectile atomic mass
v	Projectile speed (m/s)
v_0	The Bohr velocity; $v_0 = e_0^2/\hbar \approx c/137\text{ m/s}$
β	Relative speed of projectile; $\beta = v/c$
γ	Electron yield, i.e. number of electrons emitted per incident particle
E	Projectile energy (J)
n	Target atomic density (atoms/cm^3)

* Fundamental physical constants were obtained from NIST database, <http://physics.nist.gov/cuu/Constants/index.html>

ACKNOWLEDGMENTS

V.I.X.X.D.E.
Visita Interiora Terræ
Rectificando
Invenies Occultum Lapidem

I am indebted to Prof. Kenan Ünlü for his continued support and patience for this research over the last five years. Kenan Abi, you were always there to listen to any problem that we encountered in our lives. Your kindness and willingness to help will always be remembered and appreciated.

My sincere appreciation goes to Prof. Jack S. Brenizer for his guidance and support. Our discussions on many problems I faced during the research helped me jump to the next step.

I owe special debt of gratitude to Dr. R. Gregory Downing and Dr. Raymond (Lei) Cao from the National Institute of Standards and Technology (NIST). Greg, you are a true mentor and an excellent friend. Many times, it was your moral support that kept me going in this arduous endeavor. I cannot think of a time that I did not learn a new thing from you. It was always a pleasure to work with you. And Raymond, I cannot thank enough for your assistance throughout one of the most stressful periods of my life. You worked with me day and night, weekdays and weekends. You always kept my spirits high while performing the experiments, which I desperately needed. It will always be remembered as ‘crystal’ clear as it was yesterday.

Special thanks go out to Dr. Michael S. Gordon from IBM T. J. Watson Research Center. Mike, your visit to Penn State Radiation Science and Engineering Center was a turning point in the progress of my research. Not only did you provide knowledge and guidance, but you also offered your time and the resources of the Tandem linear

accelerator facility. I would also like to thank the members of the Thin Film Metallurgy and Soft Error Rate Research Department, in particular Dr. Kenneth P. Rodbell for his support of this project at IBM. I should mention that IBM T. J. Watson is a wonderful research environment. I really enjoyed being there while doing my experiments. My special thanks go out to Carl E. Bohnenkamp who helped this project turn into a reality.

IBM has another significance in this research. The idea of neutron depth profiling was first proposed by J. F. Ziegler while he worked at IBM T. J. Watson Research Center. He worked in the same laboratory as some of the measurements in this study were performed. To me, it was one of the most rare and extraordinary coincidences in life.

I would like to thank Prof. Arthur Motta of Penn State Mechanical and Nuclear Engineering Department, Prof. Vijaykrishnan Narayanan of Penn State Computer Science and Engineering Department and Dr. Tim Z. Hossain from Advanced Micro Devices (AMD) for being in my committee. Special thanks to Prof. Motta for his thorough critiques on the manuscript.

I would also like to thank the Penn State Breazeale Nuclear Reactor (PSBR) staff, in particular Ronald Eaken II –Machiniste Extraordinaire and Mac Bryan. Ron, this research would not be completed without your contributions. And Mac, thank you very much for all your help whenever I needed it.

B.: Cory L. Trivelpiece deserves a special thank for a final review of the thesis, and his remarkably precise and detailed grammar and syntax corrections. Brother, I will always remember and miss our long political discussions and debates in our office. I would also like to thank my L^AT_EX guru Cihangir Çelik for his assistance in typesetting this manuscript, particularly in preparation of the tables.

My dear friend Prof. Melik Demirel was always supportive during this study. Melik, your passion for science has always been a source of inspiration for me.

My father- and mother-in-laws, Nejat and Tevhide Özgan ran for help in our most needy times without hesitation to take care of our little son. I do now understand that this thesis would not be realized without your help.

I am indebted to my father Abdullah and my mother Gülser. Your altruistic support was nothing short of exceptional nobility and has laid the foundation of this long process. You provided me with all the means in your power at the expense of your own comfort. My sister Ruveyda and my brother Tahir... You will always be special for me.

And my life, my wife, ma belle... Words are not enough to express my gratitude for your everlasting support and to tell my appreciation for the sacrifices we had to make. From now on, life, one day at a time...

DEDICATION

*For my sun, my son Sarp,
and ma belle Esmeralda, ma fleur-de-Nesrin...*

CHAPTER

1

INTRODUCTION

Neutron depth profiling (NDP) is a nondestructive near-surface analysis technique that is used to obtain transverse concentration distributions of certain isotopes in almost any solid material. A thermal or sub-thermal neutron beam is used to induce prompt emission of swift secondary ions. Upon neutron absorption, certain isotopes of light elements undergo isotropic emission of either a proton or an alpha particle, and diametrical emission of a recoil nucleus. The particles are emitted with their characteristic energies determined by the total energy balance of the reaction. Since the incident neutrons have negligible kinetic energy compared to the final energies of the emitted particles, the emission can be confidently considered monoenergetic.

The use of thermal neutron beam as an isotopic probe was first proposed by Ziegler et al. [1]. Ziegler and colleagues used charged particle and recoil nucleus emission induced by the absorption of low-energy neutrons to determine the implantation range and profile parameters of boron in semiconductor silicon. Biersack and coworkers [2] improved the technique to present capabilities. The nomenclature “neutron depth profiling” was later adopted by Downing et al. [3] as the technique matured in providing unique features as well as demonstrating complementary information with other analytical techniques such as secondary ion mass spectroscopy (SIMS), Rutherford backscattering (RBS), Auger electron spectroscopy (AES).

The analysis of neutron depth profiling spectrometry is as follows: The reaction products emitted by the neutron capture process are monoenergetic. As these particles move towards the surface boundary, they undergo various collisions predominantly with the cloud of electrons of the substrate matrix and rapidly lose energy. The amount of energy loss by charged particles, in a first-order approximation, is a function of the atomic number of the projectile and the substrate, and the depth of the original compound nucleus. However, surface topography, the path traveled by particles, depth distribution of compound nucleus and stochastic nature of the energy loss process cause deviations from the expected value of the final energy of particles. Hence, particles emerging from the surface of the substrate are no longer monoenergetic. The energy spectra of these particles can be measured with standard charged particle spectroscopy techniques [4–8].

1.1 Motivation

The residual energies of particles can be measured with a silicon semiconductor detector, typically a surface barrier detector (SBD), a passivated implanted planar silicon (PIPS) detector, or a silicon PIN photodiode.

The spectrum acquired by the spectrometer is a convolution of the actual energy distribution of the particles and the measurement system as a whole. Each component of the system, i.e. the sample, the detector and the spectroscopy electronics, introduces uncertainties, hence causes spectral broadening to the measured energy of the particle based on their respective convolution mechanisms. Therefore, the measured energy spectrum can be considered as the transformation of the actual energy spectrum by various interaction mechanisms and each system component. The ultimate effect of these uncertainty sources is loss of energy, and consequently depth resolution.

Consider a monolayer of a monoenergetic emitter of energy E_i at a depth δ in a substrate of known composition as shown in the block diagram form in Figure 1.1.

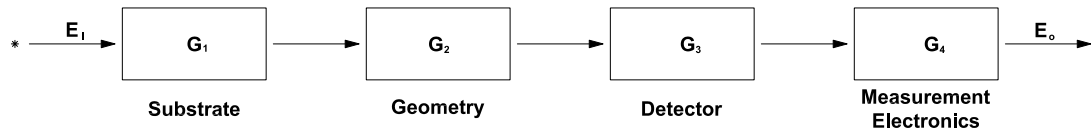


Figure 1.1. Block diagram representation of interaction mechanisms in a measurement system.

The energy registered by the measurement electronics, E_o , can be represented mathematically as

$$E_o = G_4 \otimes (G_3 \otimes (G_2 \otimes (G_1 \otimes E_i))) \quad (1.1)$$

where \otimes is the convolution operator. For certain interactions, the convolution is a linear operator under certain assumptions. However, in the general case, the uncertainty propagation is nonlinear; therefore the order of operands is important.

Since the emission is monoenergetic, E_i is simply an impulse function whose area is equal to the source strength. However, E_o is no longer an impulse function but rather a distribution whose characteristics are determined by individual system components and their cross-interactions. The area of the distribution must equal the area of the impulse function.

Each component of the broadening mechanisms can be divided into subcomponents. For instance, the interactions in the substrate can be itemized as straggling, multiple small-angle scattering, etc. Each broadening mechanism must be treated independently to obtain the actual spectrum of particles.

The uncertainties introduced by various interactions between the projectile and the substrate material are inevitable. However, the uncertainties resulting from other components of the measurement system can be reduced by modifying the spectroscopy system.

Neutron depth profiling offers certain features, some of which are unique, and some complementary to other analytical techniques [9–12]. As an example, neutron depth profiling is virtually a non-destructive measurement technique that allows for multiple testing of the sample. Most analytical techniques employ high-current high-energy ion beams or photon beams that cause significant sputtering of the surface or excessive charging for critical components. Since a neutron does not have a charge and it carries very little momentum at thermal energies, the damage caused by neutrons can be considered insignificant for practical purposes.

One other important feature that neutron depth profiling technique offers is the absolute depth measurement capability, since there is a direct correlation between the depth of the compound nucleus and the residual energy of the detected particle, which is simply the stopping force of the projectile traveling in the target material. Because of this feature, neutron depth profiling was proposed and successfully used as the standard calibration method for other analytical techniques [13].

The rapid progress in technology requires higher precision and sensitivity in various applications. For instance, in semiconductor technology, the feature sizes of microchip components shrink on a regular basis as faster, more power conservative, and higher-

mobility devices are demanded by the end user. As the market gets more competitive, the margin of error in the production of components narrows even further as it demands more strict quality assurance and quality control practices by the manufacturer. These requirements stipulate that improved analytical techniques be used for characterization measurements. Increasingly, the semiconductor industry is making use of low energy ion implants for shallow junction formation. These implants, which are often made at between a few hundred to a few thousand electron volts, require an analysis capability that will allow sub-nanometer depth resolution to be obtained. A significant fraction of the implanted dose is located within the top few nm. Therefore, there is a significant need for a technique that will not cause sputtering of the top layers as done by the techniques using high-energy ion beams.

The motivation behind this research is the fact that the resolution of the neutron depth profiling technique has come to its physical limits using conventional charged particle energy spectrometry. Improvements in the last decade in pulse-processing electronics makes it possible to employ ion time-of-flight spectrometry for neutron depth profiling for lighter nuclei with improved resolution.

The time-of-flight concept has been a powerful measurement technique for mass identification, isotope separation and for accurate determination of the velocity of a particle. The performance of a time-of-flight measurement system depends strongly on the performance characteristics of the instrumentation. As new-generation pulse-processing electronics improve the instrumental time resolution from nanoseconds to only a few picoseconds, resolution based on time-of-flight measurements can also be improved.

Application of time-of-flight spectrometry for neutron depth profiling was first proposed by Schweikert [14]. Schweikert used the time-of-flight technique to measure the flight time spectrum of recoil nuclei. Since recoil nuclei are more massive and less energetic, significant improvement can be achieved in depth resolution. As the secondary signal, Welsh et al. used the ion-induced secondary electrons emitted from the sample [15, 16]. The technique was later improved and successfully used by Welsh [17].

The fact that the ion-induced secondary electron emission from the sample was used as the secondary signal limits the applicability of the time-of-flight technique for neutron depth profiling. In order to transport the secondary electrons from the sample towards the electron detector, the sample surface must have a conductive layer to establish the electric field lines. In this study, a more generalized ion time-of-flight technique was used for application on any sample, where the secondary electrons were generated by the passage of ions through a thin carbon foil.

1.2 Statement of Objectives

In this study, it was demonstrated that time-of-flight spectroscopy can be incorporated into the neutron depth profiling technique. The fundamental claim behind this idea is that the uncertainty components of the detection system, which is the detector and the measurement electronics, can be further reduced than what is available with the charged particle energy spectrometry if the time-of-flight technique is employed.

The premise that the uncertainties can be reduced by employing a time-of-flight spectrometer emanates from the following arguments:

- A time-of-flight measurement does not require an energy proportional output; hence microchannel plate detectors can be used to mark the arrivals of the start –also called time-zero– and stop signals. Microchannel plate detectors can generate sharp signals, making them ideal tool for fast timing applications.
- A time-of-flight measurement employs a coincidence technique, therefore the background noise commonly encountered in conventional energy spectrometers can be significantly suppressed.

In this dissertation, it was intended to achieve the following goals:

- introduce the principles of time-of-flight spectroscopy, present the available literature on the technique, mention briefly the available designs
- develop a comparative analysis of uncertainties for direct energy measurement and time-of-flight spectrometry
- lay out the theoretical foundation of the application of time-of-flight spectrometry to neutron depth profiling
- conduct a critical analysis of the available time-of-flight spectrometer designs
- propose, engineer and evaluate improvements to the available designs

Chapter 2 provides brief background information on neutron depth profiling and gives the theory on physical processes involved in measurements by the conventional charged particle energy spectrometry and time-of-flight spectrometry. Chapter 3 introduces the design principles of two ion time-of-flight spectrometers used in this research. Chapter 4 gives description of the facilities and the experimental setup. Chapter 5 presents the experimental data followed by comprehensive analysis. Chapter 6 gives a summary of the thesis and offers recommendations for future study.

CHAPTER

2

THEORY AND BACKGROUND

The neutron depth profiling technique was first introduced by Ziegler et al. [1] in 1972. The technique depends on the illumination of a sample substrate with a thermal or sub-thermal neutron beam. Certain light elements interact with slow neutrons and undergo either (n, p) or (n, α) reactions. The reaction products are emitted into 4π . Since the incoming neutron carries insignificant energy compared to the Q-value of the reaction, the particle emission can be considered monoenergetic for practical purposes.

As the charged particle travels in the substrate, it loses kinetic energy predominantly through coulombic interactions with electron gas of the matrix atoms. The amount of energy loss is a function of the atomic number and the energy of the ion as well as the material composition of the substrate. Hence, given the initial energy of the ion and the substrate composition, the depth of the reaction site can be determined from the energy loss.

Section 2.1 briefly explains the mechanism of ion transport in solid media. Section 2.2 gives details about the technique and the depth calculations. Section 2.3 presents the uncertainties associated with the ion transport and the detection processes.

2.1 Transport of Ions in Solids

Marie Curie [18] discovered that alpha and beta particles are stopped in matter while gammas are transmitted. Rutherford, Thompson and several others performed pioneering studies on the stopping process, and Bohr devised a theory, which influenced all subsequent development of ion transport calculations [19, 20]. Bohr arrived at predictions of electronic stopping force and straggling as well as mean ranges and fluctuations on the basis of classical mechanics including relativistic corrections, assuming electrons in the stopping medium to be bound harmonically as in classical dispersion theory. A major progress was made when Bethe, Bloch and Møller [21–24] approached the problem from the perspective of quantum mechanics and derived the fundamental equations for the stopping of very fast particles in a quantized medium. This theoretical approach remains the basic method for evaluating the energy loss of light particles with velocities above 1 MeV/u [25]. Bohr’s treatise on *“The penetration of atomic particles through matter”* became the primary source of information for the subsequent generation of researchers [26] .

Historically, the range R of ions was the quantity of primary interest. Stopping force ($-dE/dx$) was later introduced as a theoretical tool defined as

$$R = \int_{E_f}^{E_0} \frac{dE'}{(-dE'/dx)} \quad (2.1)$$

where E_0 is the initial and E_f is the final energy of the particle.

In 1954, Lindhard [27] developed the first comprehensive study of the energy loss of a particle in a free electron gas (FEG). Using the first Bohr approximation, he found a complete solution that included polarization of the medium by the particle’s fields. Later, Lindhard and Winther [28] developed analytic expansions for the energy loss. Bonderup [29] used the Lindhard formalism for the first time in the calculation of stopping powers. There are two fundamental assumptions implied in Lindhard stopping theory: (1) the electron density in target varies slowly with position, (2) available energy levels and transition strengths of the atoms of the solid are identical to those in a free electron gas.

In-depth analysis of ion transport mechanism in solid media is beyond the scope of this thesis. A more detailed review of the process can be found in Ziegler [25] and Sigmund [30, 31].

2.1.1 Definitions

Definitions that are essential for the comprehension of ion transport and central to the presentation of this thesis are introduced below.

Stopping Force

The central quantity in particle stopping is the *stopping force* or *stopping power*. While stopping power is a more broadly accepted nomenclature, stopping force is a more precise description of the phenomenon [32], and will be the preferred terminology throughout this text. It is defined as the average loss of kinetic energy E per path length ℓ , i.e. $(-dE/d\ell)$.

The stopping force is related to the average change in momentum P per path length according to

$$\frac{dE}{d\ell} = v \frac{dP}{d\ell} \quad (2.2)$$

where v is the projectile speed, $P = M_1 \gamma v$ the momentum, M_1 the projectile mass,

$$\gamma = \frac{1}{\sqrt{1 - \beta^2}} \quad (2.3)$$

$$\beta = \frac{v}{c} \quad (2.4)$$

where c is the speed of light.

Mean Energy Loss

The energy loss ΔE at a given path length ℓ is a stochastic variable that obeys a statistical distribution $F(\Delta E, \ell)$, which depends on path length and ion-target combination. The mean energy loss is defined according to

$$\Delta E = \int d(\Delta E) \Delta E F(\Delta E, \ell) = -\frac{dE}{d\ell} \ell \quad (2.5)$$

provided that ℓ is small enough so that the variation of $dE/d\ell$ across the path length segment is negligible.

Path Length

Every segment in the trajectory of a projectile is called the *path length* ℓ . The path length between two points 1 and 2 is related to the stopping force by

$$\ell = \int_1^2 d\ell = \int_{E_1}^{E_2} \frac{dE}{dE/d\ell} = \int_{E_1}^{E_2} \frac{dE}{nS(E)} \quad (2.6)$$

where n is the target atomic number density. This equation holds true under the condition that energy loss fluctuations can be neglected.

Mean Projected Range

Mean range can be calculated by using

$$R = \int_0^{E_0} \frac{dE}{nS(E)} \quad (2.7)$$

which is a valid approximation when straggling is negligible.

For a given range distribution $F(x)$, the mean projected range can be found using

$$R = \frac{1}{N} \int_0^\infty dx \, x \, F(x) \quad (2.8)$$

where $N = \int_0^\infty dx \, F(x)$ is the normalization factor.

For discrete range distribution $F(x_i)$, mean projected range can be calculated from

$$R = \frac{1}{N} \sum_{i=1}^N F(x_i) \quad (2.9)$$

where N is the number of bins in the distribution.

Energy Loss Fluctuation or Energy Loss Straggling

The fluctuation in energy loss (also called *energy loss straggling*) is defined as the second moment of the average energy loss quantity, i.e.

$$\sigma_E^2 = \langle (\Delta E - \langle \Delta E \rangle)^2 \rangle \quad (2.10)$$

σ_E^2 is proportional to the path length ℓ traveled by the particle if individual energy loss events are statistically independent. Further discussion on the approximate analytical calculation of energy loss straggling is presented in Section 2.3.

Range Straggling

It is also possible to define the variance in range σ_R^2 using the formula

$$\sigma_R^2 = \int_0^{E_0} dE \frac{nW(E)}{[nS(E)]^3} \quad (2.11)$$

where $W(E)$ is the straggling parameter defined as

$$W = \frac{1}{n} \frac{d\sigma_R^2}{d\ell} \quad (2.12)$$

It should be noted that Equation (2.11) is valid in the limit of low straggling.

Given a continuous range distribution $F(x)$, range straggling σ_R^2 is defined as the second moment according to

$$\sigma_R^2 = \frac{1}{n} \int_0^\infty dx (x - R)^2 F(x) \quad (2.13)$$

where R is the mean projected range as defined in Equation (2.8).

For a discrete range distribution $F(x_i)$, range straggling takes the form

$$\sigma_R^2 = \langle \Delta F(x_i)^2 \rangle = \frac{1}{N} \sum_{i=1}^N (F(x_i) - R)^2 \quad (2.14)$$

where N is the number of bins in the distribution, and R is the mean projected range defined according to Equation (2.9).

Although defined as the variance above, range straggling is sometimes given as the standard deviation, i.e. the square root of the variance.

Higher Moments of Range Profiles

It is possible to define higher moments. The terms *skewness* and *kurtosis* are commonly encountered in ion implantation. Skewness is defined as the third moment of the range distribution and indicates whether the peak is skewed towards the surface (negative values) or away from the surface (positive values):

$$\gamma = \frac{\langle \Delta x_i^3 \rangle}{\langle \Delta x_i^2 \rangle^{3/2}} \quad (2.15)$$

Kurtosis is the fourth moment of the range distribution and indicates the extent of the distribution tails:

$$\beta = \frac{\langle \Delta x_i^4 \rangle}{\langle \Delta x_i^2 \rangle^2} \quad (2.16)$$

A value of 3.0 is considered a *Gaussian distribution*.

2.1.2 Stopping of Energetic Ions in Matter

Stopping force and range values are central to the neutron depth profiling calculations. There are analytical procedures to calculate the stopping force and range values of an ion in almost any medium. However, under certain circumstances, experimental data and the theoretical calculation may noticeably deviate from each other. Stopping force and range values are updated on a regular basis as more experimental measurements become available.

A history of ion stopping as well as a comprehensive analytical treatment based on the Ziegler-Biersack-Littmark binary collision theory can be found in [33].

Stopping and Range of Ions in Matter (SRIM)

The software package SRIM has almost become the *de facto* standard in ion stopping and range calculations as well as ion transport simulations in almost any media [34]. The SRIM package includes multiple applications: (1) Ion Stopping and Range Tables, (2) Transport of Ions in Matter (TRIM), (3) `SR.Module`. Ion Stopping and Range Tables application gives the calculated values of stopping force and range for almost any projectile in any target material for a given energy range. The TRIM application is a Monte Carlo-based tool that simulates projectile trajectories for a given number of particles and a wide range of initial energies. The TRIM application can be called from the SRIM user interface, or externally using a `trimauto` script. The standalone `SR.Module` application is used for generation of stopping force and range values for given energies, and can be called externally from within other applications.

SRIM uses several different stopping theories to evaluate the accuracy of experimental stopping force. SRIM can calculate the stopping force for all ions in any target material as well as a single heavy ion in a solid medium of multiple species. Calculations are made from fundamental theories such as the Brandt-Kitagawa theory [35] and Lindhard-Scharff-Schiøtt (LSS) theory [36]. If the experimental values are within reasonable agreement with the set of theoretical calculations, the experimental values are

weighed with the theoretical values to obtain a final stopping force value [34].

2.2 Neutron Depth Profiling

Neutron depth profiling technique can be considered a variant of the *nuclear reaction analysis* (NRA) technique, where a primary ion beam of various energies is used to induce reactions with charged particle exit channels. The ions in the beam have to carry enough energy to penetrate the Coulomb barrier of the isotope to be analyzed and induce a reaction. The beam energy can be tuned to the resonance energy of the isotopes present in the substrate for a particular reaction. However, since an energetic beam is involved, the surface of the analyzed sample suffers from sputtering, i.e. removal of top layers, which results in alteration of the sample and loss of information on the top layers.

In neutron depth profiling, neutrons are used to induce the *in situ* reactions with charged particle exit channels. Because the neutron does not carry a charge, it can initiate exoergic reactions $Q > E_b^*$ with essentially zero kinetic energy. One advantage of using a neutron beam for material analysis is that, unlike charged particles, neutrons can penetrate deep into the substrate and initiate said reactions, making it possible to analyze thick as well as multi-layered samples.

Variation of residual energies of ions with respect to the depth of the reaction site is shown in Figure 2.1. The data was obtained for $^{10}\text{B}(n, \alpha)^7\text{Li}$ and $^{14}\text{N}(n, p)^{14}\text{C}$ reactions in silicon. The plot data was generated with the standalone SRIM application SRModule_2007 [37]. The atomic masses used in the calculations of initial energies of reaction products are given in Table 2.1.

Table 2.1. Relative atomic mass of the isotopes used in the calculation of initial kinetic energies of reaction products from $^{10}\text{B}(n, \alpha)^7\text{Li}$ and $^{14}\text{N}(n, p)^{14}\text{C}$ reactions [38]

Isotope	Relative Atomic Mass (u)
^1p	1.007 825 032 07
^1n	1.008 664 915 74
^4He	4.002 603 254 15
^7Li	7.016 004 55
^{14}C	14.003 241 988 70
^{14}N	14.003 074 004 78

In neutron depth profiling calculations, a similar mapping procedure is applied to transform the energy spectrum into depth distribution. For instance, for the $^{10}\text{B}(n, \alpha)^7\text{Li}$ reaction, if the alpha particle is detected with the full energy, it is possible to deduce that the particle originated from the surface and hence lost almost no energy to interactions with substrate atoms. In a similar fashion, each energy bin in the spectrum can be converted to a corresponding discrete layer of depth using the aforementioned procedure. The procedure will be elaborated in Section 2.2.2.

In this section, a brief history of the neutron depth profiling technique is presented followed by the introduction of the principal reactions.

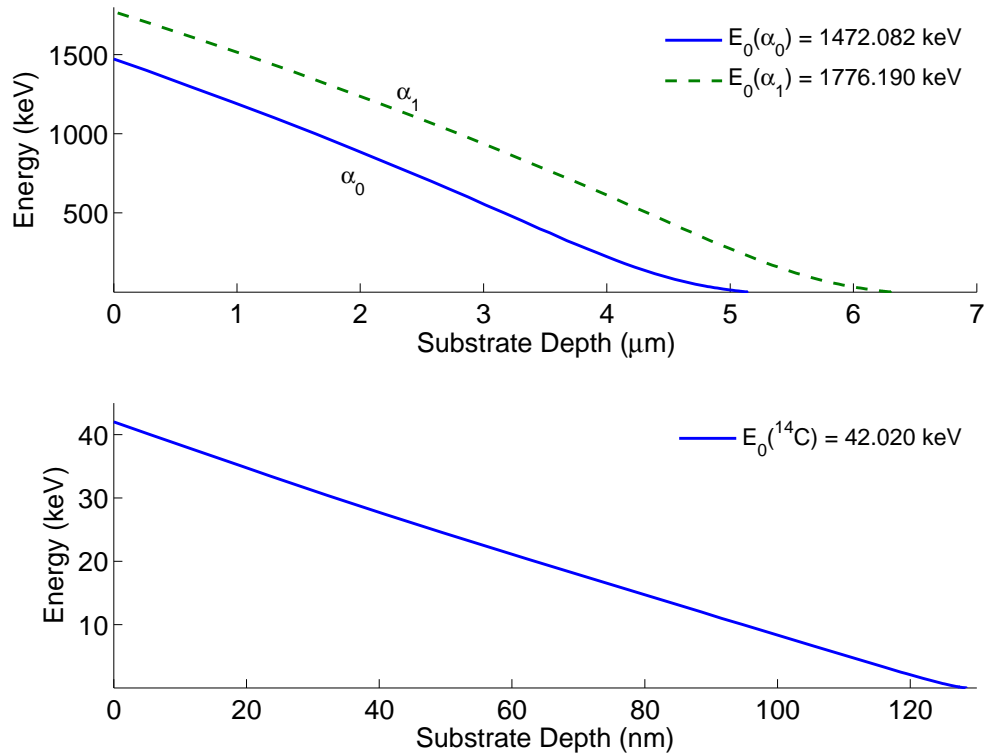


Figure 2.1. Correlation between the residual energy and the depth of reaction site for (top) alpha particles coming from $^{10}\text{B}(n, \alpha)^7\text{Li}$ reaction, (bottom) ^{14}C recoil coming from $^{14}\text{N}(n, p)^{14}\text{C}$ reaction; both in silicon substrate.

2.2.1 The (n, p) and (n, α) Reactions

The most probable reactions induced by neutrons are (n, p) and (n, α) . There are a limited number of isotopes that undergo these reactions, and even more limited number of isotopes with a reaction cross section above $0.01b$. The list of isotopes satisfying the aforementioned condition is presented in Table 2.2.

Table 2.2. List of isotopes that undergo (n, p) or (n, α) reactions with thermal neutrons with cross sections larger than $0.01 b$

Element	Reaction	Abundance* (%)	Parent Halflife	Energy of Emitted Ions ^{§§} (keV)		Cross Section [†] (barns)
				α or p	Recoil	
He	${}^3\text{He}(n, p){}^3\text{H}$	0.000 137(3)	stable	572	191	5328
Li	${}^6\text{Li}(n, \alpha){}^3\text{H}$	7.59(4)	stable	2055	2727	940.3
Be	${}^7\text{Be}(n, p){}^7\text{Li}$	$[2.5 \times 10^{14}]^\dagger$	53.22 d [§]	1438	207	48000
B	${}^{10}\text{B}(n, \alpha){}^7\text{Li}$	19.9(7)	stable	1472	840	3837
				1776	1013	
N	${}^{14}\text{N}(n, p){}^{14}\text{C}$	99.632(7)	stable	584	42	1.769
O	${}^{17}\text{O}(n, \alpha){}^{14}\text{C}$	0.038(1)	stable	1413	404	0.24
Na	${}^{22}\text{Na}(n, p){}^{22}\text{Ne}$	$[4.4 \times 10^{15}]^\dagger$	2.6027 y [✱]	2247	103	31000
S	${}^{33}\text{S}(n, \alpha){}^{30}\text{Si}$	0.76(2)	stable	3081	411	0.1686
Cl	${}^{35}\text{Cl}(n, p){}^{35}\text{S}$	75.78(4)	stable	598	17	0.489
K	${}^{40}\text{K}(n, p){}^{40}\text{Ar}$	0.0117(2)	stable	2231	56	4.400
Ni	${}^{59}\text{Ni}(n, \alpha){}^{56}\text{Fe}$	$[1.3 \times 10^{20}]^\dagger$	76400 y [◇]	4757	340	12.3

* Data obtained from Rosman et al. [39].

† Values in atoms/mCi.

§ Data obtained from Tilley et al. [40].

✱ Data obtained from Firestone [41].

◇ Data obtained from Baglin [42].

‡ Data obtained from JENDL3.2, Nakagawa et al. [43].

§§ Data obtained from Audi et al. [38].

2.2.2 Depth Calculations

The shortest path length ℓ traversed by the particle and the depth of the reaction site d are correlated as

$$\ell = \frac{d}{\cos \vartheta} \quad (2.17)$$

where ϑ is the mean emittance angle at depth d . Given the material composition, the energy loss of the ions ejected from the compound nucleus can be calculated using the stopping force of the projectile in the substrate:

$$\ell = \int_E^{E_0} \frac{dE'}{nS(E')} \quad (2.18)$$

where ℓ is the path length traveled by the particle, E_0 is the initial kinetic energy of the particle, E is the expected residual energy of the particle, n is the atomic number density and $S(E) = dE/dx$ is the stopping force of the substrate for an ion at energy E .

The path length and the range are correlated in the following fashion:

$$\begin{aligned} \ell = \int_E^{E_0} \frac{dE}{nS(E)} &= \int_E^0 \frac{dE}{nS(E)} + \int_0^{E_0} \frac{dE}{nS(E)} \\ \Rightarrow \ell &= \int_0^{E_0} \frac{dE}{nS(E)} - \int_0^E \frac{dE}{nS(E)} \\ \Rightarrow \ell &= R(E_0) - R(E) \end{aligned} \quad (2.19)$$

where $R(E_0)$ and $R(E)$ are the range of the particle with initial kinetic energies E_0 and E , respectively. The depth of the reaction site is then found by

$$d = \ell \cos \vartheta \quad (2.20)$$

Given a spectrum of discrete energies represented by the count distribution $c_i\{E_i\}$, the depth distribution can be calculated using a variant of Equation (2.19)

$$\frac{d_i}{\cos \vartheta} = R(E_0) - R(E_i) \quad (2.21)$$

which gives the count distribution $c_i\{d_i\}$ with respect to depth d_i .

2.2.3 Concentration Calculations

To determine the nuclide concentration, a sample of known implantation dose value can be used as the calibration material in the same geometric configuration. Subsequent

concentration calculations can be performed using the reference material.

Implantation dose is defined as the number of isotopes per unit area of the sample. Throughout this text, implantation dose will be referred to simply as *dose*. It is an integral quantity in the transverse direction. Isotopic concentration is defined as the number of atoms in unit volume. Given a continuous concentration distribution $C(x)$ across a layer of thickness δt . Implantation dose \mathfrak{D} and concentration C are correlated by

$$\mathfrak{D} = \int_0^{\delta t} dx C(x) \quad (2.22)$$

For a discrete concentration distribution, Equation (2.22) becomes

$$\mathfrak{D} = \sum_{i=1}^N C_i \Delta x_i \quad (2.23)$$

Consider a substrate with an isotope of known implantation dose \mathfrak{D} , mass density ρ in units of kg/m^3 , areal density μ in units of kg/m^2 uniformly distributed along a layer of thickness δt . The mass density, the areal density and the layer thickness are correlated by

$$\delta t = \frac{\mu}{\rho} \quad (2.24)$$

The atomic concentration C and implantation dose \mathfrak{D} are correlated by

$$C = \mathfrak{D} \frac{\rho}{\mu} = \frac{\mathfrak{D}}{\delta t} \quad (2.25)$$

Let Δx_i represent the thickness of a series of discrete layers in a known thickness of δt such that

$$\delta t = \sum_{i=1}^N \Delta x_i \quad (2.26)$$

where i is the index of the corresponding layer, and N is the total number of layers. If the stopping force of the target material for the projectile ion can be considered constant, it is possible to write

$$\delta t = N \Delta x \quad (2.27)$$

This approximation is valid if the particle velocity does not drop drastically across the layer.

Let c_i be the number of counts collected from the layer with index number i , and c_T

be the total number of counts, i.e.

$$c_T = \sum_{i=1}^N c_i \quad (2.28)$$

Local nuclide concentrations can be calculated using the following:

$$C_i = \frac{c_i}{c_T} \frac{\mathfrak{D}}{\Delta x_i} \quad (2.29)$$

where C_i is local isotopic concentration in units of m^{-3} for the depth index i and \mathfrak{D} is the sample implantation dose in units of m^{-2} . If the approximation in Equation (2.27) is valid, then Equation (2.29) can be rewritten as

$$C_i = N \frac{c_i}{c_T} \frac{\mathfrak{D}}{\delta t} \quad (2.30)$$

Sample implantation dose \mathfrak{D} can be calculated using the reference material implantation dose according to

$$\mathfrak{D} = \frac{c_T}{(c_T)_{\text{ref}}} \mathfrak{D}_{\text{ref}} \quad (2.31)$$

where c_T and $(c_T)_{\text{ref}}$ are the total counts of the sample and the reference material acquired in the same time period. Using the equality 2.31 in Equation (2.29), one gets

$$C_i = \frac{c_i}{(c_T)_{\text{ref}}} \frac{\mathfrak{D}_{\text{ref}}}{\Delta x_i} \quad (2.32)$$

Alternatively, the count-to-concentration transformation can be done in the following fashion: The local volumetric rate R_i of the (n, p) or (n, α) reactions can be calculated using

$$R_i = C_i \sigma \varphi \quad (2.33)$$

where σ is the microscopic cross section of the isotope for the reaction type being investigated (in units of m^2) and φ is the neutron flux (in units of $m^{-2}s^{-1}$). For a distributed isotopic concentration along the transverse axis x , the total areal reaction rate is

$$R_a = \int_0^{\delta t} dx C(x) \sigma \phi(x) \quad (2.34)$$

If self-shielding is neglected, Equation (2.34) simplifies to

$$R_a = \sigma \varphi \int_0^{\delta t} dx C(x) \quad (2.35)$$

For a discrete concentration distribution, Equation (2.35) can be written as

$$R_a = \sigma \varphi \sum_{i=1}^N C_i \Delta x_i \quad (2.36)$$

Equations (2.33) and (2.36) can be used to relate the discrete and areal count rates R_i and R_a to the discrete and total counts c_i and c_T , respectively.

$$R_i = c_i \frac{1}{\epsilon \Delta t} \quad (2.37)$$

$$R_a = c_T \frac{1}{\epsilon \Delta t} \quad (2.38)$$

where ϵ is the overall detection efficiency and Δt is the spectrum acquisition time. Substituting these definitions into Equations (2.33) and (2.36), and using the Equation (2.23), one obtains

$$C_i = \frac{1}{\sigma \varphi} \frac{c_i}{\epsilon \Delta t} \quad (2.39)$$

$$\mathfrak{D} = \frac{1}{\sigma \varphi} \frac{c_T}{\epsilon \Delta t} \quad (2.40)$$

The accuracy of the depth and concentration calculations depends on the accuracy of the tabulated stopping force or range values, and the mass density used in the calculations. In general, nominal mass densities are used for the substrate matrix. The presence of impurities such as the isotope being measured is usually ignored, since their effect on stopping force is negligible for practical purposes.

2.3 Uncertainties

The resolution of a measurement system is defined as the smallest change that results in registration of a distinct value.

The transport of the ion in solid material is a stochastic process. The ion loses its kinetic energy as it experiences numerous collisions along its trajectory before it leaves the sample surface. The final energy of the ion is also affected by nonhomogeneities in

material properties as well as other nonuniformities such as surface roughness. Once it emerges from the surface, it travels in vacuum until it hits the particle detector. Since the experiments are performed in non-ideal vacuum conditions, sporadic collisions with gas molecules are possible. However, for practical purposes, uncertainty contributions from collisions in vacuum are negligible. When the particle finally hits the detector, it initiates certain dynamics in the medium that cause it to generate a response. The dynamics of interactions and the mean response time are detector specific. Once the output signal is generated by the detector, it is transferred to the measurement electronics. The measurement electronics has its own response characteristics for input signals.

The minimum detectable signal and the precision of the amplitude measurement are limited by fluctuations. The signal formed in a detector fluctuates, even for a fixed energy absorption. Generally, detectors convert absorbed energy into signal quanta. In a silicon semiconductor detector, energy deposited by the charged particle is converted into a number of charge pair, i.e. electrons and holes. The absorbed energy divided by the excitation energy yields the average number of signal quanta [44]

$$N = \frac{E}{E_i} \quad (2.41)$$

The number fluctuates statistically, so the relative resolution

$$\frac{\Delta E}{E} = \frac{\Delta N}{N} = \frac{\sqrt{FN}}{N} = \sqrt{\frac{FE_i}{E}} \quad (2.42)$$

The resolution improves with the square root of energy. F is the *Fano factor*, which comes about because multiple excitation mechanisms can come into play and reduce the overall statistical spread. For instance, in a semiconductor detector, absorbed energy forms electron/hole pairs, but also excites lattice vibrations -quantized as phonons- whose excitation energy is much smaller (meV versus eV). Thus, many more excitations are involved than apparent from the charge signal alone, which reduces the statistical fluctuations of the charge signal.

It is seen that from the instant the particle is created until the particle is finally registered by the last component of the measurement electronics, uncertainties play a significant role in the process. Uncertainties that result from the sample are inherent to any measurement technique that exploits the same principle. Geometric uncertainties, however, are determined by the experimental setup. The detector and the measurement electronics also contribute to measurement uncertainty.

2.3.1 Uncertainties that Result from Sample Substrate

The source of uncertainty from the sample substrate is the collisions between the projectile ion and the target atoms. The scattering process results in an infinite number of trajectories. Variation in trajectories also results in variation in energy loss as the particle exits the substrate.

There are a number of interaction mechanisms inside the substrate that lead to spectral spread. The uncertainties in amorphous and crystalline substrates are presented separately due to variation of interaction mechanisms in the two structures.

Amorphous Material

The major uncertainty sources in amorphous substrates are presented below.

Energy Loss Straggling

Energy loss straggling was introduced in Section 2.1.1. In this section, approximations that define straggling in terms of material properties, and ion atomic number and energy are introduced.

The simplest approach to modeling straggling is the Bohr formalism [19, 20, 26], which is expressed in SI units as

$$\sigma_{\text{BOHR}} = \frac{Z_1 e_0^2}{2\epsilon_0} \sqrt{\frac{Z_2 n \ell}{\pi}} \quad (2.43)$$

where σ_{BOHR} is in units of Joule, $e_0 = 1.6022 \times 10^{-19} \text{ C}$ is the unit electricity charge, $\epsilon_0 \approx 8.854 \times 10^{-12} \text{ C}^2 \text{N}^{-1} \text{m}^{-2}$ is the permittivity of free space, Z_1 and Z_2 are the atomic numbers of the projectile ion and the target material, n is the atomic density of the target material, ℓ is the path length traveled by the particle inside the matrix.

The Bohr straggling model assumes that the projectile ion is stripped of its electrons as it moves through the matrix. This assumption is only valid when the velocity of the particle is much larger than the speed of its electrons in the innermost orbit [19, 20], i.e.

$$v \gg Z_1 v_0 \quad (2.44)$$

where v is the particle velocity and $v_0 = c/137$ is the Bohr velocity.

Figure 2.2 shows the energy distribution of alpha particles with initial kinetic energy 1472 keV, having penetrated a silicon membrane of 100 nm. The distribution obtained by the TRIM simulation performed with 9999 particles, and the normal distribution

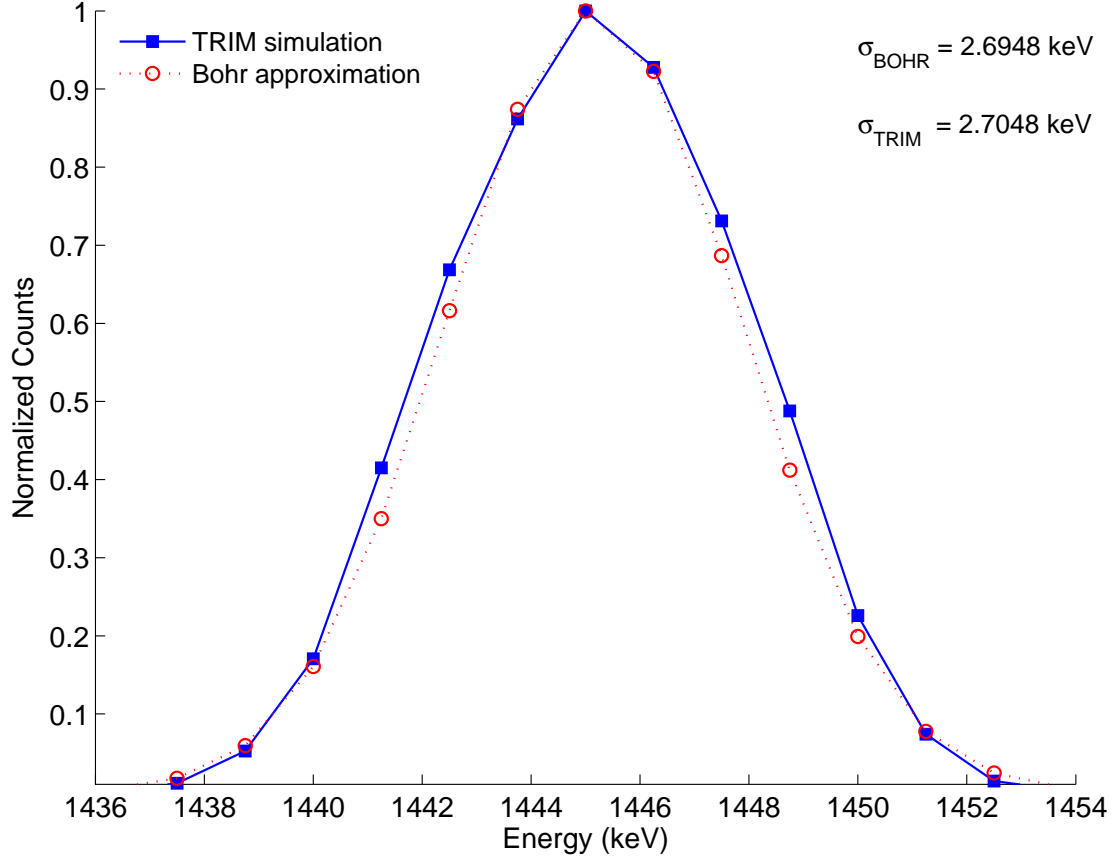


Figure 2.2. Distribution of alpha particle energies after penetrating a 100-nm silicon layer.

generated using the straggling value from the Bohr approximation match within 8% for the normalized counts.

Angular Scattering

Multiple scattering was first studied by Bothe [45], and the theory was later developed by Molière [46], Bethe [47], Meyer [48], and Amsel et al. [49]. Further information can be found in Sigmund [32] and Fink [50].

The energy spread can be approximated by

$$\sigma_{\text{SCAT}} = S(E) \sigma_{\text{X-SCAT}} \quad (2.45)$$

where σ_{SCAT} is the standard deviation of the energy broadening caused by scattering, $S(E)$ is the stopping force, and $\sigma_{\text{X-SCAT}}$ is the spread in particle path lengths due to scattering. The spread in particle path length resulting from the spread of emittance

angles σ_{ϑ} due to scattering is obtained as

$$\sigma_{\text{X-SCAT}} = d \sigma_{\vartheta} \left(\frac{\sin \vartheta}{\cos^2 \vartheta} \right) \quad (2.46)$$

where d is the depth and ϑ is the particle emittance angle relative to the sample normal. As an approximation, the emittance angle can be replaced by its average $\bar{\vartheta}$, and the spread of emittance angle σ_{ϑ} by the deflection angle width σ_{ψ} . Upon substitution, Equation (2.45) becomes

$$\sigma_{\text{SCAT}} = d S(E) \sigma_{\psi} \left(\frac{\sin \bar{\vartheta}}{\cos^2 \bar{\vartheta}} \right) \quad (2.47)$$

The width of the deflection angle can be approximated by

$$\sigma_{\psi} = \frac{4}{2.355} \frac{Z_1 Z_2 e^2}{\bar{E} a} C (\pi a^2 n \ell)^M \quad (2.48)$$

where \bar{E} is the average energy of the particle, C and M are fitting parameters based on experimental data, n is the atomic density of the material, and a is the screening radius as defined by

$$a = \frac{0.855 a_0}{\sqrt{Z_1^{2/3} + Z_2^{2/3}}} \quad (2.49)$$

with Bohr radius $a_0 = 5.29 \times 10^{-11} \text{ m}$. Spahn et al. [51] report fitted values of $C = 0.30$ and $M = 0.85$. Further material on the derivation of uncertainty caused by angular scattering can be found in Sigmund et al. [52] and Belery et al. [53].

Surface Roughness and Sample Porosity

Surface roughness and porosity can drastically affect the measurement resolution since the energy loss of charged particles varies significantly depending on the path length traveled in the substrate. Therefore, the surface structure may be investigated by other techniques, and the results can be taken into account in the depth calculations.

Crystalline Material

Ion scattering may differ significantly in crystalline matter depending on the orientation of the crystal. A brief review of major effects in crystals is given below.

Channeling Effect

As the lattice atoms of a crystal arrange along its low index directions to chains or planes, the crystal exhibits a high transparency in these directions for penetrating

particles. Atomic planes act as potential barriers for particles with small impact angles ϕ . If the impact angle is below some critical angle ϕ_{crit} , the particles are reflected. Having passed the potential valley between two neighboring potential barriers, the particles suffer reflection at a glancing angle with the opposite barrier back towards the first one. Hence, they follow an oscillatory-shaped trajectory. In three dimensions, the trajectory becomes spiral. There are various modes of particle motion:

1. **Hyperchanneling:** This is an extreme case where the particle trajectory is nearly parallel to the crystal planes. The particle is affected only by the distant potentials, which are small. A transition from one channel to a neighboring channel is restricted. Therefore the particle experiences almost no stopping.
2. **Channeling:** For low ion beam divergences below a critical angle ϕ_{crit} , the particle undergoes some oscillatory motion along an axial channel. Occasional transitions to neighboring channels may be observed.
3. **Quasichanneling:** If the impact angle is close to the critical angle, i.e. $\phi \approx \phi_{\text{crit}}$, the particle may escape from the channel after a few oscillations, and enter in a neighboring channel where it continues the oscillatory motion.
4. **Ridging:** For sufficiently high energies with $\phi \gg \phi_{\text{crit}}$, the particle essentially follows a straight trajectory as if in an amorphous medium. The particle trajectory, however, is influenced by lattice periodicity, hence it exhibits small but observable wiggles. The energy loss differs slightly from the loss in an amorphous medium.
5. **Bridging:** The motion along the crystal plane normal, i.e. $\phi = 90^\circ$, is an extreme case of ridging and is referred to as bridging.

The critical impact angle from a calculation proposed by Gemmell [54] is as follows:

$$\phi_{\text{crit},\text{x}} = 2.61 \left(\frac{Z_1 Z_2 a^2}{E d^3} \right)^{1/4} \quad (2.50)$$

for the axial orientation, and

$$\phi_{\text{crit},\text{p}} = 0.172 \left(\frac{n Z_1 Z_2 a}{E} \right)^{1/4} \quad (2.51)$$

for the planar orientation, where Z_1 and Z_2 are the atomic numbers of the projectile and lattice atoms, d is the separation between atoms in a plane, a is the screening radius

defined by Equation (2.49), and E is the energy of the projectile. If E is in MeV , d and a are in nm , and n is in nm^{-2} , the critical impact angle is calculated in degrees.

Stopping force values in a crystal channel or plane are lower than those in random directions. As proposed by Fichtner et al. [55], the maximum range R_{\max} for the best channeled ions can be calculated by

$$R_{\max} = \frac{d}{n} \frac{\sqrt{E}}{A} (1 + Bb_{\max})^5 \quad (2.52)$$

where b_{\max} is the maximum collision distance, d the atomic distance, n the number of atoms projected into the area normal to the channeling direction, E ion energy and A ($eV^{1/2}$) and B (cm^{-1}) are two system-dependent constants (e.g. Ag in Si , $A = 2.90 eV^{1/2}$ and $B = 1.2 \times 10^{10} m^{-1}$). This equation takes into account only electronic stopping, neglects Z_1 oscillations and assumes that the energy loss is proportional to instantaneous ion velocity.

Biersack et al. [56] verified that the depth distribution of well-channeled ions can be described by considering only the electronic stopping process. The channeled depth profiles have the same shape as the random ones, but are shifted towards greater depths.

Blocking Effect

Blocking is an inverse process to channeling that affects ions emerging from a lattice site. If the ion travels at a small angle relative to a crystal plane, it may suffer a large-angle deflection by the nearest neighbor atom. The motion of particles along crystal axes differs from Rutherford scattering process due to the collective action of many lattice atoms.

The particle beam intensity decreases exponentially in deeper depths due to electronic and nuclear *dechanneling*, i.e. the large-angle scattering event caused by an impurity atom, a self-interstitial, displaced atoms, atoms belonging to another lattice structure or a thermally strongly oscillating atom. Hence, deep blocking emission patterns approach the isotropic emission patterns of amorphous media. For further discussion and references on the effects of channeling and blocking in NDP measurements, interested reader may refer to Fink [50].

2.3.2 Uncertainties that Result from Geometry

Geometric uncertainties are those that originate from the way the sample and detector are placed. The geometric layout is generally dictated by the measurement environment, dimensions of the sample and the detector, as well as the count rate. Unlike the

uncertainties that result from the sample substrate, geometric uncertainties can be manipulated to minimize the effects. There are two major geometric uncertainty factors: geometric acceptance angle and transit time spread due to increased distance. Acceptance angle causes spread in both energy spectrometry and time-of-flight spectrometry. Transit time spread, however, only takes place in time-of-flight measurements.

Acceptance Angle

Since the detector subtends a finite acceptance angle Ω , a range of emittance angles exists for a given emission depth d . Variation in path lengths results in spread of measured energies. Energy broadening due to geometrical path length spread σ_{GEOM} can be approximated by

$$\sigma_{\text{GEOM}} = S(E) \sigma_{\text{X-GEOM}} \quad (2.53)$$

where $\sigma_{\text{X-GEOM}}$ is the spread in path length due to possible range of acceptance angles, which can be calculated from

$$\sigma_{\text{X-GEOM}}^2 = \int_0^{\pi/2} d\vartheta \, \wp(\vartheta) \, (\ell - \bar{\ell})^2 \quad (2.54)$$

where $\wp(\vartheta)$ is the normalized probability distribution of all detectable emission angles and $\bar{\ell}$ is the average path length. The normalized detection probability distribution is expressed as

$$\wp(\vartheta) = \frac{W(\vartheta)}{\int_0^{\pi/2} d\vartheta \, W(\vartheta)} \quad (2.55)$$

with $W(\vartheta)$ as the weighting function. The average path length $\bar{\ell}$ can be calculated by

$$\bar{\ell} = \int_0^{\pi/2} d\vartheta \, \wp(\vartheta) \ell(\vartheta) = \int_0^{\pi/2} d\vartheta \, \wp(\vartheta) \frac{d}{\cos \vartheta} = d \langle \cos \vartheta \rangle \quad (2.56)$$

The weighting function $W(\vartheta)$ in Equation (2.55) can be expressed by

$$W(\vartheta) = \int_0^{R_s} dr_s \, \Im(r_s) \Delta\Psi(r_s, \vartheta) \quad (2.57)$$

where R_s is the radius of the sample, $\Im(r_s)$ is the normalized neutron intensity incident on the sample radius r_s , and $\Delta\Psi(r_s, \vartheta)$ is the detection coverage. For a given detector-to-sample distance D , detector radius R_d , emittance position r_s and emittance angle ϑ , the detection coverage can be expressed by

$$\Delta\Psi(r_s, \vartheta) = 2 \cos^{-1} \frac{D^2 \tan^2 \vartheta + r_s^2 - R_d^2}{2 r_s D \tan \vartheta} \quad (2.58)$$

The spread in geometric path length can then be calculated by

$$\sigma_{X\text{-GEOM}}^2 = d^2 \int_0^{\pi/2} d\vartheta \wp(\vartheta) \left(\frac{1}{\cos \vartheta} - \left\langle \frac{1}{\cos \vartheta} \right\rangle \right)^2 \quad (2.59)$$

A more comprehensive analysis can be found in Maki et al. [57].

Time-of-Flight Dispersion

This uncertainty applies only to time-of-flight spectrometry. Time-of-flight dispersion -also called transit time spread- results from variation in particle flight times from the source plane to the detector plane. Even if the particles emerge from the surface of the source at the same speed, the flight path variations due to angular spread causes variations in flight time. Consider a monoenergetic isotropic point source at energy E_0 at a distance L from the center of the detector as shown in Figure 2.3. The particles are expected to reach the detector with a nominal flight time τ_0

$$\tau_0 = \frac{L}{v} \quad (2.60)$$

where $v = \sqrt{2E/m}$ is the speed of the particle. Because of the angular spread, distance traveled by the particles varies depending on the angle of departure from the surface. Since the emission is isotropic, probability of traveling an arbitrary distance $\ell \in [L, L']$ is identical.

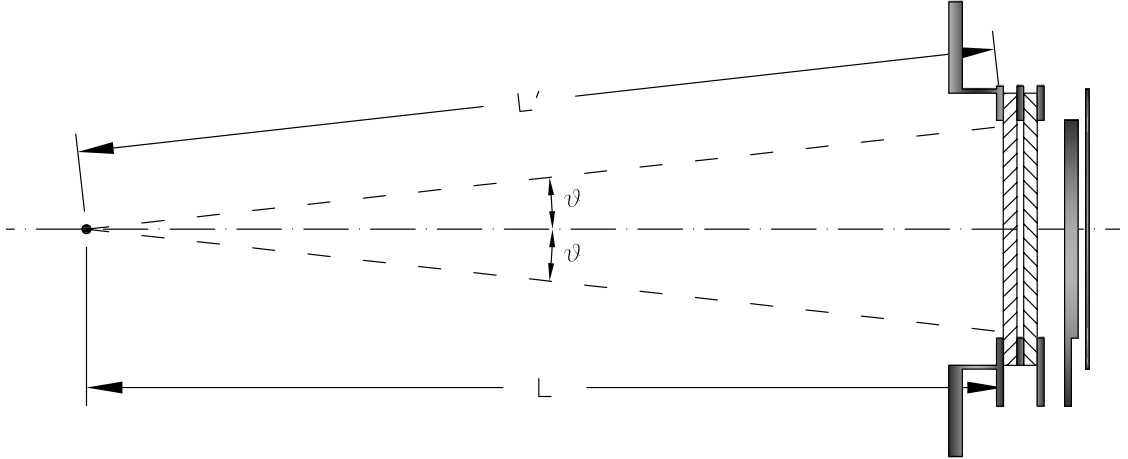


Figure 2.3. Geometry of an isotropic on-axis point source and a detector.

The maximum time-of-flight deviation can be calculated from

$$\tau_{\max} = \frac{L'}{v} = \frac{L \sec \vartheta}{v} = \tau_0 \sec \vartheta \quad (2.61)$$

Time dispersion stretches from the nominal flight time of τ_0 to the geometrically possible maximum flight time τ_{\max} . Only particles that reach the very center of the detector travel within the nominal flight time τ_0 , whereas particles detected elsewhere on the detector surface will experience longer flight times depending on the emission angle. An expected time of flight dispersion is shown in Figure 2.4.

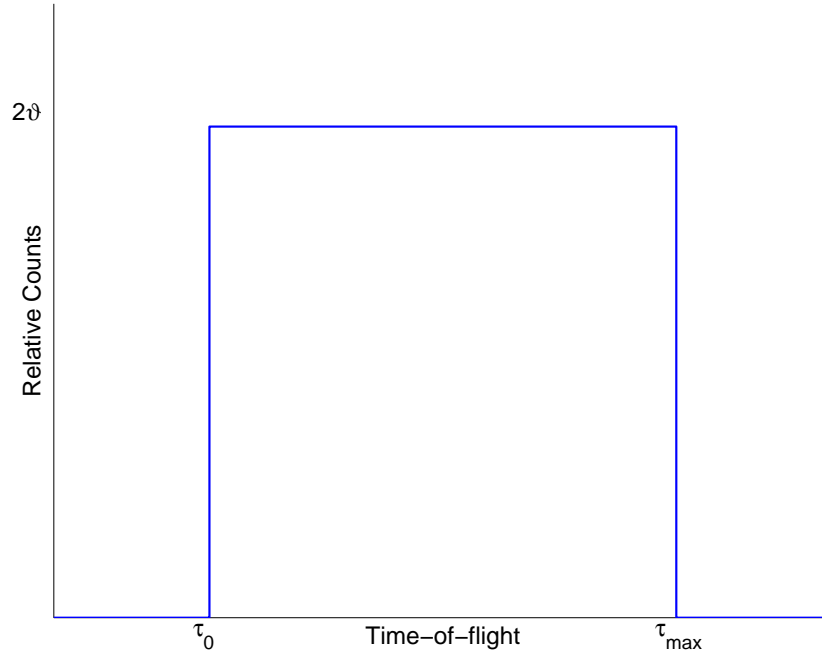


Figure 2.4. Expected time-of-flight dispersion of an on-axis isotropic point source due to geometric convolution.

The simulated time-of-flight spectrum of such a system is shown in Figure 2.5 obtained with the Monte Carlo algorithm presented in Appendix B.4. This simulation assumes an isochronous start trigger and does not take into account other spectrum broadening mechanisms. The emitter is a monoenergetic isotropic point source with initial energy $E_0 = 1472 \text{ keV}$. The detector diameter is 25 mm and is separated by 50 mm from the source. The total number of tallied particles is 10^6 .

Figure 2.6 shows a two-dimensional geometry where a concentric planar source and a detector are separated by a nominal distance L . x is the distance to the center from an arbitrary point on the surface of the source, r is the radius of the detector, L' and L''

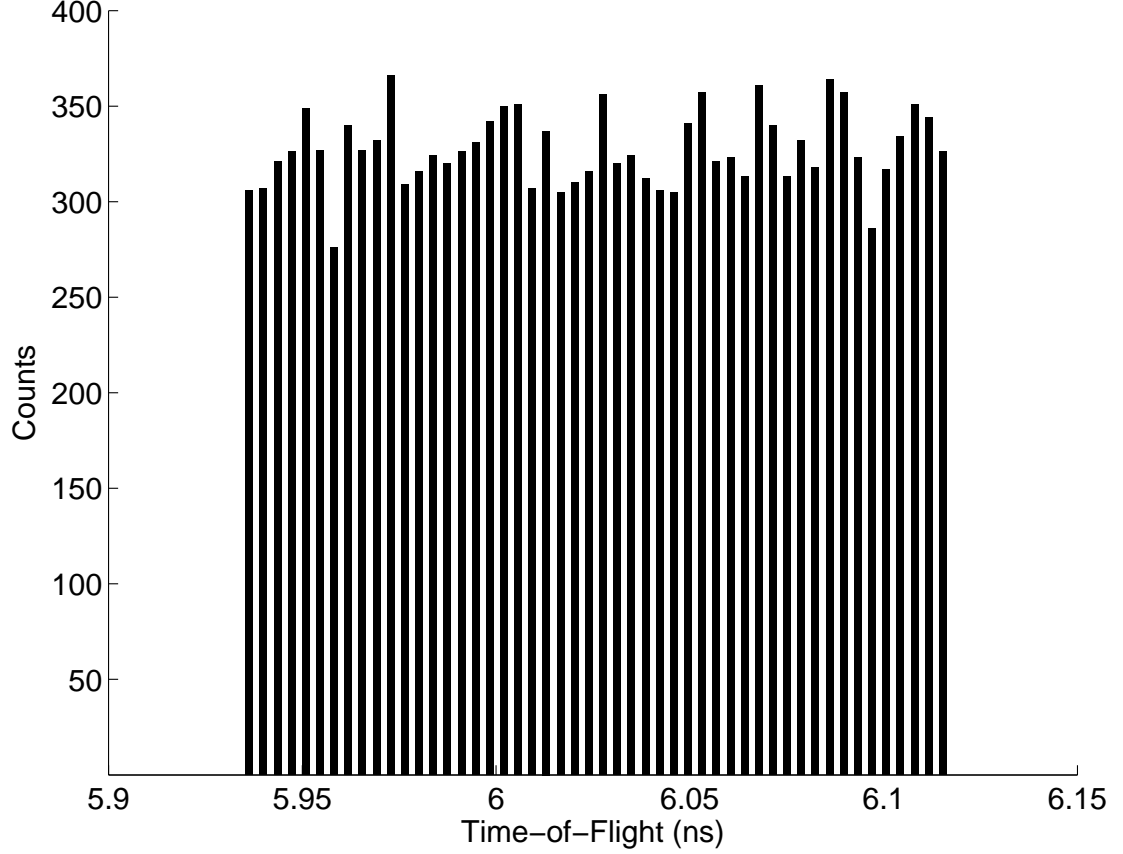


Figure 2.5. Monte Carlo simulation of the time of flight spectrum for a monoenergetic isotropic point source of alpha with energy $E_0 = 1472 \text{ keV}$; detector diameter 25 mm , source-detector separation 50 mm .

are distances to closer and farther edges of the detector.

Particle flight times vary according to

$$\tau_1 = \frac{L'}{v} = \frac{L \sec \vartheta_1}{v} = \tau_0 \sec \vartheta_1 \quad (2.62)$$

$$\tau_2 = \frac{L''}{v} = \frac{L \sec \vartheta_2}{v} = \tau_0 \sec \vartheta_2 \quad (2.63)$$

Regions I and II, as shown in the bottom drawing in Figure 2.6, resemble the special case of an isotropic point source, as explained previously. Region III, however, creates asymmetry in the flight time dispersion. Since the number of particles from an isotropic source emitted into a cone is proportional to its solid angle, regions I and II collect the same number of counts and suffer the same amount of dispersion. The expected time of flight dispersion from an off-axis isotropic point source is shown in Figure 2.7.

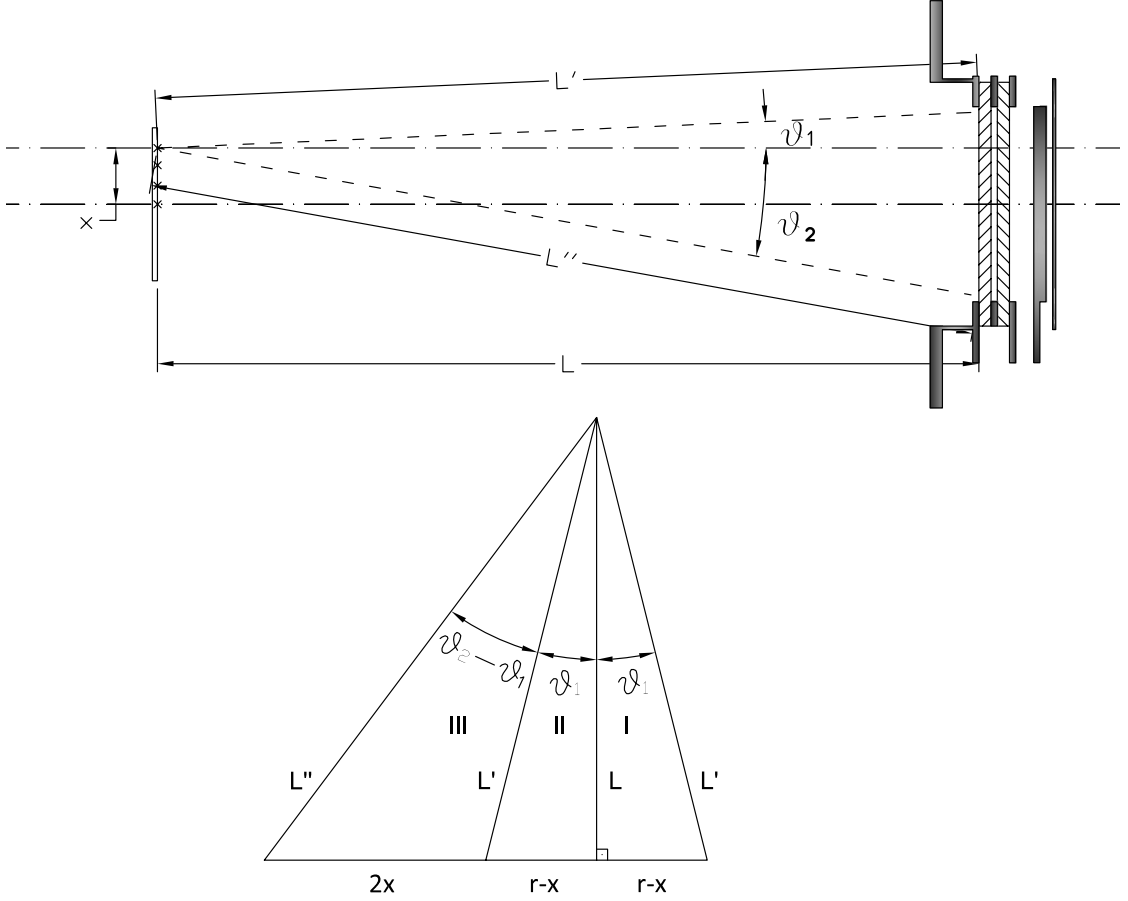


Figure 2.6. (top) Geometry of an isotropic off-axis point source and a detector; (bottom) Explicit depiction of geometric convolution for an off-axis point source.

Let $\mathfrak{h}(\rho, r, L, x)$ be a function that represents the geometry of the system, where ρ is the radius of the source, r is the radius of the detector, L is the distance between the source and the detector, and x is an arbitrary point on the surface of the source. The overall spectrum of the system can then be obtained by integrating the function \mathfrak{h} over the entire surface of the source:

$$\mathfrak{H} = \iint_{\mathcal{A}} dx \mathfrak{h}(\rho, r, L, x) \quad (2.64)$$

Such a treatment is rather tedious analytically since \mathfrak{h} is not an analytical function. However, numerical integration of Equation (2.64) can be carried out easily. Figure 2.8 shows an evaluated time-of-flight spectrum of monoenergetic particles emitted isotropically from a planar source as shown in Figure 2.6. The calculation was carried out for

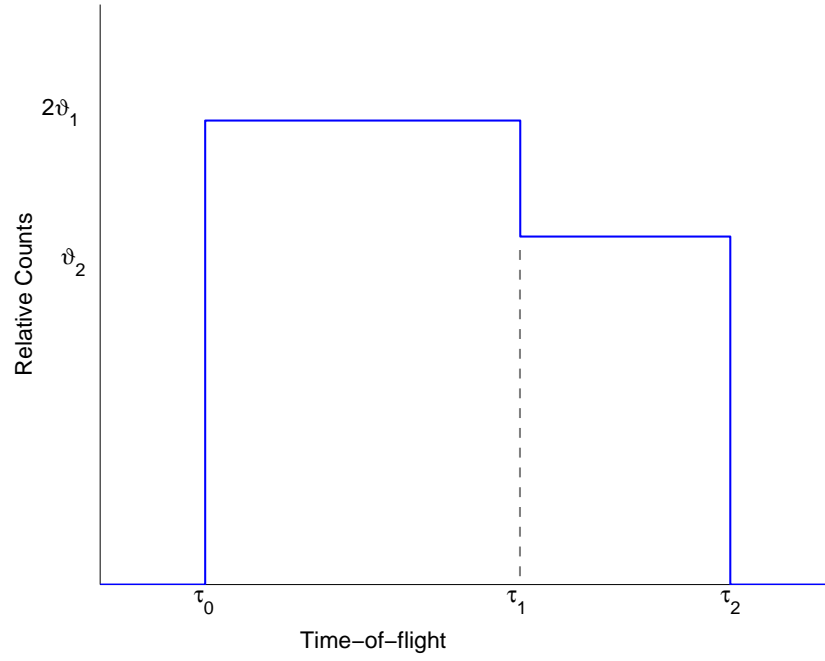


Figure 2.7. Expected time-of-flight dispersion from an off-axis isotropic point source.

1472 *keV* alpha particles emitted from a 10-*mm* diameter source and detected with a 25-*mm* diameter detector separated by 50 *mm* from the source.

This calculation was confirmed with a Monte Carlo simulation for the same geometry as shown in Figure 2.9. The number of particles used in the simulation is 10^7 . The magnitude of the uncertainty demonstrates the importance of flight-time dispersion if the detection resolution is to be improved.

The time-of-flight dispersion can be reduced by reducing the solid angle subtended by the detector. Larger source diameter also escalates the time dispersion. The optimal magnitude of the solid angle can be found by a trade-off between the dispersion and the count rate.

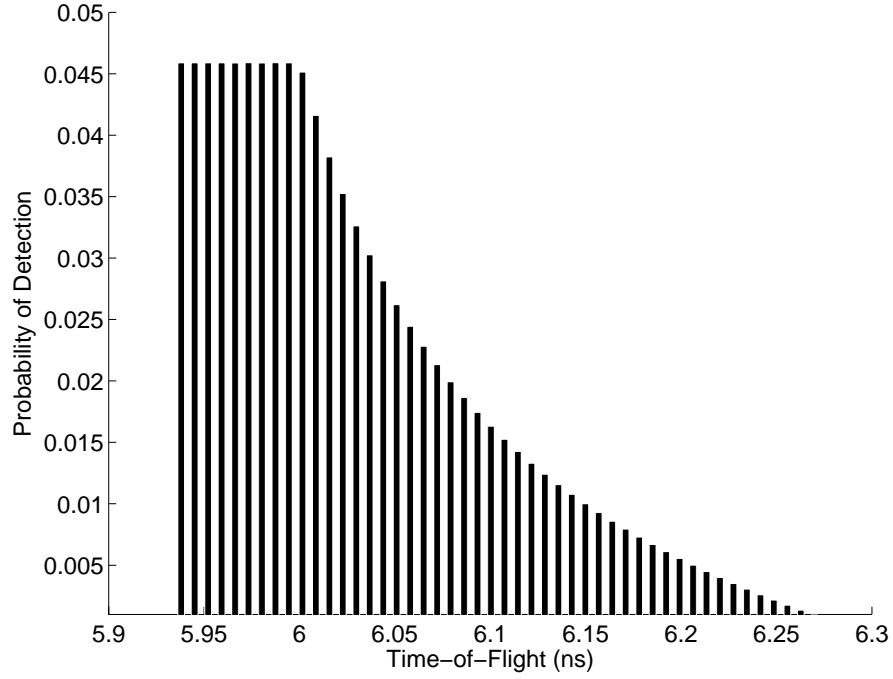


Figure 2.8. Evaluated time-of-flight dispersion from an isotropic planar source of 10-*mm* diameter at energy $E_0 = 1472 \text{ keV}$ with a 25-*mm* diameter detector; source-detector separation 50 *mm*.

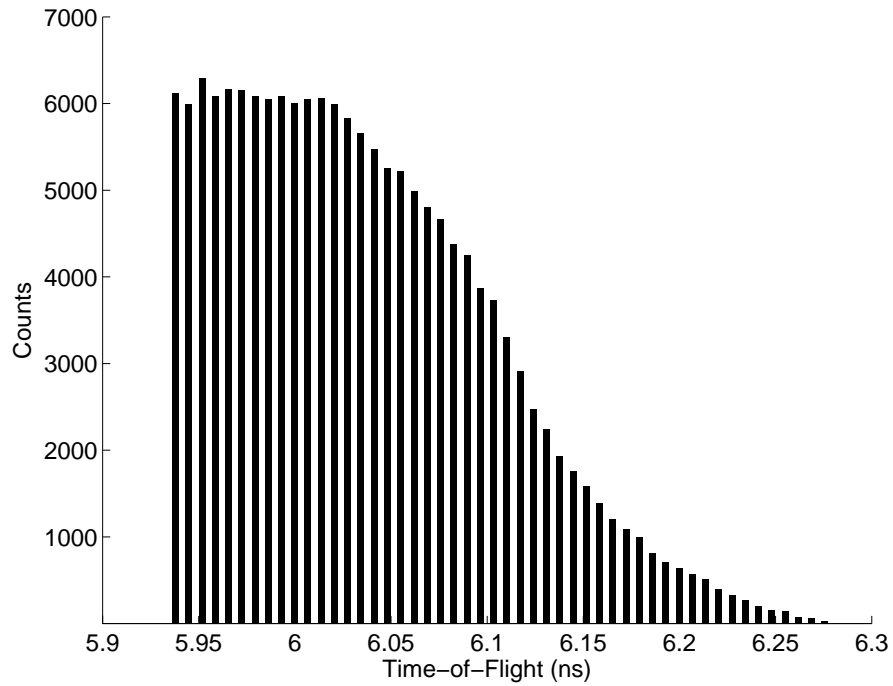


Figure 2.9. Monte Carlo simulation of the time of flight spectrum for a monoenergetic isotropic planar source of alpha with energy $E_0 = 1472 \text{ keV}$; source diameter 10 *mm*, detector diameter 25 *mm*, source-detector separation 50 *mm*.

2.3.3 Uncertainties that Result from Detector

In conventional neutron depth profiling, which is based on energy spectrometry, various detector types can be used including silicon Surface Barrier Detector (SBD), Passivated Implanted Planar Silicon (PIPS) detector or silicon Positive Intrinsic Negative (PIN) photodiodes.

In this section, uncertainty contributions from detectors is summarized. Uncertainties are divided into two categories, i.e. semiconductor detectors and microchannel plates, due to the fact that the response dynamics in two detector types are significantly different. Semiconductor detectors generate energy-proportional output whereas microchannel plate output has no direct correlation with the incident particle energy.

Semiconductor Detectors

Semiconductor detectors are widely used in high-energy physics experiments. The most commonly used material is silicon, but germanium, gallium-arsenide and diamond are also useful in some applications. The density of silicon and its small ionization energy result in adequate signals with active layers only 100-300 μm thick. This also provides fast signal output. Semiconductor detectors depend crucially on low-noise electronics, so the detection sensitivity is determined by signal charge and capacitance [58].

Silicon detectors are p - n junction diodes operated under reverse bias. This forms a sensitive region depleted of mobile charge and sets up an electric field that sweeps radiation-liberated charge to the electrodes. As mentioned earlier, there are various semiconductor detector types such as surface barrier, PIPS or PIN photodiode. Surface barrier detectors employ a metallic coating – usually gold or aluminum evaporated on the surface of the silicon crystal. The thickness of the evaporated layer is on the order of 100 nm in silicon equivalence. PIPS detectors, on the other hand, have a thinner contact layer formed through metal implantation – either aluminum, gold or palladium. Because of their thinner contact layer, PIPS detectors are expected to have better performance than that of surface barrier detectors under ideal circumstances [44]. However, their performance deteriorate in presence of gamma field in a measurement environment due to their increased gamma- and x-ray sensitivity.

In the PIN diode configuration, an intrinsic semiconductor layer is sandwiched between p and n noninjecting contacts at either surface. This type of arrangement helps reduce the leakage current observed in diodes. The p -layer is formed by selective diffusion of boron to a thickness of approximately 1 μm . The spectral and frequency response of the PIN diode can be adjusted by varying the implantation depth as well as the dop-

ing concentration. An experimental study on the comparison of the response of PIN photodiode and silicon surface barrier detector (Au/n-Si) is given by Zhang et al. [59].

Straggling in Entrance Window

As explained in Section 5.1, a silicon surface barrier or PIPS detector consist of an n -type crystal. The evaporated metallic layer provides electrical contact for signal readout. PIN photodiodes, however, do not employ metallic layers because of the way they are designed.

Although the entrance window is a thin metallic layer, a dead layer of an indeterminate thickness extends into silicon from beneath the contact layer. Although the incident particle suffers energy loss as it penetrates the dead layer, it does not contribute to the pulse height since it is an inefficient medium for charge collection. The thickness of the dead layer is a function of the bias voltage. A detailed analysis of ion interaction in the entrance layers is given by Steinbauer et al. [60].

The thickness of the metallic layer is kept small to minimize the energy loss straggling. Typical values are 100 nm of silicon equivalent for surface barrier detectors and 50 nm of silicon equivalent for PIPS detectors. Using special techniques, dead layers of 27 nm for gold, 28 nm for aluminum and 19 nm for palladium -all in terms of silicon equivalence- have been fabricated [61].

Figure 2.2 shows the distribution of alpha particle energies obtained by a TRIM simulation and a Bohr straggling calculation. The spectral broadening was found to be $\sigma_{\text{str}} \approx 2.70 \text{ keV}$ by both techniques.

Charge Carrier Statistics

An important factor that determines the measurement resolution that can be obtained from semiconductor detector is the statistical nature of charge carrier formation. The limiting resolution can be calculated by

$$\sigma_{\text{lim}} = \sqrt{FE\epsilon} \quad (2.65)$$

where F is the Fano factor, ϵ is the ionization potential, which for silicon, $F = 0.11$, $\epsilon = 3.62 \text{ eV}$, and E is the particle energy. Using the energy value of $E = 1472 \text{ keV}$ for alpha particles from $^{10}\text{B}(n, \alpha)^7\text{Li}$ reaction, the theoretical limit is found approximately to be

$$\sigma_{\text{lim}} \approx 765 \text{ eV}$$

A theoretical model of the charge collection process in a silicon surface barrier detector is presented by Kanno [62], and in a silicon PIN photodiode by Simon et al. [63].

Energy Loss Fluctuations

Another uncertainty component results from the fact that a small portion of the alpha particle energy is lost to recoil creation. The low-energy recoils lose energy through quasielastic collisions, therefore do not contribute to charge formation. The uncertainty comes from the statistical fluctuation in the portion of energy transferred to recoil nuclei. Alkhazov et al. [64] estimate that the uncertainty contribution due to these fluctuations is approximately 3.5 keV for 6-MeV alpha particles.

Other Broadening Components

In addition to the spectral broadening mechanisms mentioned above, mechanisms such as incomplete charge collection and pulse-height defect may cause additional broadening. For lower charged particle energies and detectors with higher capacitance values, the effect of the electronic noise may be more dominant. In such case, fluctuations in the detector leakage current becomes a major source of uncertainty, and may result in significant broadening.

Microchannel Plates

The dominant source of uncertainty in signal generated by microchannel plates (MCP) is the *transit time spread*. Transit time is defined as the time it takes from the instant of first secondary electron generation in the MCP until the time electron multiplication along the channel is complete. The transit time spread is defined as the standard deviation of the distribution of transit times.

The main cause of the transit time spread is the initial momentum distribution of the secondary electrons and the repetition of the collisions. The significant portion of the spread is produced in the initial stage of the multiplication process where the number of electrons involved is still small. As the number of electrons increase, the transit time spread does not grow any further [65]. The transient time spread of microchannel plate detectors is reported by Kume et al. to be less than 50 ps [66]. Monte Carlo simulations demonstrate that the transit time spread within a single microchannel plate can be further reduced by using smaller channel diameter [65].

2.3.4 Uncertainties that Result from Measurement Electronics

Electronic noise originates as both velocity or number fluctuations. Velocity fluctuations arise from thermal excitation. The spectral density of the noise power is derived from the long wavelength limit of Planck's theory of black body radiation. Number fluctuations occur when charge carriers are injected into a sample independently of one another. Thermionic emission or leakage current through a semiconductor *pn*-junction are known examples [44].

In electronic circuits, noise can be modeled as voltage or current sources. In general, frequency spectra of the signal and the noise differ. The noise spectra extend over a greater frequency band than the signal. Therefore, the optimal signal-to-noise ratio can be obtained by shaping the frequency response of the system.

The leakage current of a semiconductor detector fluctuates due to electron emission statistics, which can be represented by a current generator in parallel with the detector. Resistors exhibit noise due to thermal velocity fluctuations of the charge carriers. This noise source can be modeled as voltage generator. The noise by the amplifier can be described by a combination of voltage and current sources at its input.

A portion of the noise current flows through the detector capacitance resulting in a frequency-dependent noise voltage, which is added to the noise voltages in the input circuit. Since each individual noise contributions are random and uncorrelated, they are added in quadrature. The total noise at the output of the pulse shaper is obtained by integrating over the full bandwidth of the system.

Energy Spectrometers - Pulse Height Measurements

Since radiation detectors are typically used to measure charge, the noise level of the system can be expressed as an equivalent noise charge Q_n , which is equal to the detector signal that yields a signal-to-noise ratio of one. The noise level can be reduced by having lower detector capacitance and leakage current.

Timing Spectrometers

While pulse height measurements emphasize measurement of signal charge, timing measurements seek to optimize the determination of the time of event. In timing measurements, the slope-to-noise ratio must be optimized rather than the signal-to-noise ratio. Therefore, the rise time t_r is important. The timing variance σ_t , called *jitter*, of a time spectrum is calculated by

$$\sigma_t = \frac{\sigma_n}{(dS/dT)_{S_T}} \approx \frac{t_r}{S/N} \quad (2.66)$$

where σ_n is the root mean square (rms) noise and the derivative of the signal dS/dt is evaluated at the trigger level S_T . The amplifier bandwidth should match the rise time of the detector signal to increase dS/dt without incurring excessive noise. The 10 – 90% rise time of an amplifier with bandwidth f_u is

$$t_r = 2.2\tau = \frac{2.2}{2\pi f_u} = \frac{0.35}{f_u} \quad (2.67)$$

Let's consider a detector pulse with peak amplitude V_0 and rise time t_{rs} passing through an amplifier chain with a rise time t_{ra} . The cumulative rise time at the amplifier output (discriminator output) can be calculated by

$$t_r = \sqrt{t_{rs}^2 + t_{ra}^2} \quad (2.68)$$

The timing jitter can be approximated by

$$\sigma_t \approx \frac{\sqrt{t_{rs}}}{V_0} \sqrt{\frac{t_{rs}}{t_{ra}} + \frac{t_{ra}}{t_{rs}}} \quad (2.69)$$

The optimum timing resolution improves with decreasing signal rise time $\sigma_t \propto \sqrt{t_{rs}}$ and increasing signal amplitude V_0 .

Another important factor that limits the time resolution is *time walk*. Walk is the systematic dependence of the time marker on the amplitude and rise time of the analog input pulse. The higher amplitude pulses cross the discriminator threshold earlier than the smaller pulses with the same rise time. Similarly, for two pulses with equal amplitudes, the input pulse with the faster rise time is detected earlier than the pulse with the slower rise time.

In a detailed theoretical investigation, Cova et al. [67] studied the limitations on timing of microchannel plate detectors combined with fast amplifiers. They showed that using a 1-GHz preamplifier adds approximately 10 ps in timing uncertainty for edge detection due to electronic circuit noise.

2.3.5 A Comparison of Uncertainties between Conventional Charged-Particle Spectrometry and Ion Time-of-Flight Spectrometry

A quantitative justification for potential resolution improvement can be made by listing all major uncertainty mechanisms in a measurement process. The origin of uncertainties is categorized as sample, geometry, detector and instruments. The uncertainties were calculated for 1472-MeV alpha and 840-keV lithium for charged particle spectrometry

and time-of-flight spectrometry.

For the uncertainties caused by the sample, the calculations were done for a 200-*nm* silicon. For straggling, Bohr approximation was used as given by σ_{BOHR} in Equation (2.43). The reported straggling is not an average spread but the maximum spread for the distance traveled in the substrate. For multiple small-angle scattering, the energy spread was calculated by Equation (2.47). Energy spread due to geometric acceptance angle was found by Equation (2.53). In time dispersion calculations, methodology given in Section 2.3.2.

For the detector uncertainty calculations, a commonly encountered 50-*nm* silicon equivalent gold layer thickness was used. An additional 50 *nm* dead layer thickness was assumed to exist in the entrance window. Straggling and multiple small-angle scattering calculations were performed the same way as in the sample. Ionization uncertainty was found using the total spread and the spread caused by straggling. A commonly reported spread value of 7.2 *keV* was used [68]. These calculations apply only for a semiconductor charged particle detector. For transit time spread, which is only applicable to microchannel plate detectors, an average reported spread value of 8.5 *ps* was used [66] in the calculations.

For instrumental uncertainty, the measured data obtained with the experimental equipment was used. For conventional charge particle spectrometer, the standard deviation was calculated from the full-width at half maximum of the pulser peak. For the time-of-flight spectrometer, fast pulses were generated by Stanford Research Systems DG535 Digital Delay/Pulse generator. The signal from the pulse generator was fed into the Ortec 9327 1-GHz Preamplifier and Timing Discriminator. The output of the discriminator was split with a T-connector. One of the split signal was fed into the Ortec 9308 picosecond Time Analyzer start input line. The other split signal was connected to the Ortec 425A nanosecond Delay input and the output of the delay unit was connected to the stop input line. This created a consistent time difference between the start and the stop input pulses. The only difference was expected to occur due to various noise mechanisms in the measurement electronics.

The calculated values for the uncertainty components are presented in Table 2.3. Energy spread due to multiple small-angle straggling and geometric acceptance angle are practically insignificant for a thin sample as used in these calculations. Energy straggling is the predominant mechanism of uncertainty. It can be seen that the uncertainty introduced by the semiconductor charged particle detector is slightly greater than the uncertainty from the sample.

For the time-of-flight calculations, transit time dispersion is the predominant mechanism of spread as can be seen in Table 2.3. If the lithium signal is to be used, the uncertainty due to transit time dispersion becomes almost a half of the spread in α caused by the sample. The uncertainty in the microchannel plate detector is also much smaller than the other uncertainty components in a semiconductor charged particle detector. It is easy to see that the energy resolution of a time-of-flight spectrometer improves further for slower particles.

In these calculations, the secondary signal was assumed to be a very consistent trigger in that it does not introduce additional uncertainty. If the particle-induced secondary electrons are used as the secondary signal, the time dispersion in electron transport from the sample surface to the microchannel plate detector causes significant spectral broadening, especially for faster particles. As will be presented in Chapter 5, the spread in the electron transport time is the predominant source of uncertainty in determining the exact flight time of a particle, especially at low electric field values. Therefore, the actual resolution of a time-of-flight spectrometer can be considerably inferior.

Table 2.3. A comparison of uncertainties in a charged particle spectrometer and a time-of-flight spectrometer introduced by different components in a measurement system

Uncertainty Source	Physical Mechanism	Conventional (α)	Conventional (Li)	Time-of-Flight (α)	Time-of-Flight (Li)
Sample	Straggling	3.81 keV	5.72 keV	3.81 keV	5.71 keV
	Multiple Small-Angle Scattering	0.03 keV	0.05 keV	0.03 keV	0.05 keV
Geometry	Acceptance Angle	0.06 keV	0.06 keV	0.06 keV	0.06 keV
	Time Dispersion	N/A	N/A	3.67 keV	2.10 keV
Detector	Straggling	2.70 keV	4.04 keV	N/A	N/A
	Multiple Small-Angle Scattering	0.02 keV	0.03 keV	N/A	N/A
	Ionization	6.80 keV	6.80 keV	N/A	N/A
	Time Spread	N/A	N/A	1.06 keV	0.34 keV
Instruments	Electronic Noise	9.12 keV	9.12 keV	0.97 keV	0.32 keV

2.4 Time-of-Flight Spectrometry

In this work, time-of-flight spectrometry will be referred to as the correlated detection of an energetic ion and the secondary electrons emitted as it passes through a thin carbon foil. The term *particle telescope* is commonly used for any detection scheme that obtains information at more than one point along the trajectory of the ion.

The technique is widely used for many scientific and technological applications including the characterization of recoil nuclei produced by energetic heavy ion reactions, measurements of energy loss ΔE , total energy E and time-correlated position.

2.4.1 Principles of Time-of-Flight Spectrometry

Time-of-flight spectrometry establishes a correlation between the flight time of the particle and the quantity to be measured. For instance, in time-of-flight mass spectroscopy, the spectrometer is designed in such a way that the flight time of the particle is correlated with its mass-to-charge ratio. Once the charge state of the particle is fixed, the measured flight time becomes dependent only on the particle mass. In time-of-flight energy spectrometry, the spectrometer must be designed so that the particle flight time ultimately becomes correlated to its energy.

Particle flight time is obtained by creating a chronometer that initiates with a start trigger, and ends with a stop trigger. The measured time is a relative quantity, and is the difference between the arrival times of the two triggering events:

$$\tau = \tau_{\text{stop}} - \tau_{\text{start}} \quad (2.70)$$

where τ_{stop} is the arrival time of the stop trigger, and τ_{start} is the arrival time of the start trigger.

In order to create a time space that is merely correlated on particle energy, at least one of the trigger events must generate a consistent value independent of the variation of the other quantity, or must yield a minimally dispersed continuum of values. The consistency of arrival time is called the *isochronous property*. Any dispersion mechanism in any of the trigger events will propagate and ultimately result in broadening of the measured spectrum, thus reducing resolving power.

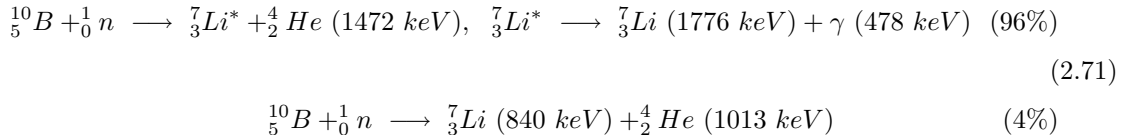
In certain time-of-flight techniques, both start and stop event triggers can be readily obtained from the experimental setup. For instance, in matrix-assisted laser desorption/ionization (MALDI) spectroscopy, a sample volume is vaporized by a laser beam, and the vaporized molecules are accelerated and transported to a time-of-flight mass

spectrometer. The ionizing laser is operated in the discrete mode. The clock signal that controls the laser operation is used as an event trigger, whereby creating a highly consistent source.

On the other hand, in some measurements, only one event trigger is readily available and the second trigger must therefore be created. The generated trigger is called an induced event. The induced event is usually created by the available trigger through some kind of interaction mechanism. This interaction must ideally be a non-intrusive process in the sense that it should not alter the quantity to be measured. In reality, an interaction mechanism that will cause minimal distortion in the quantity must be sought. The original and induced event triggers are time correlated, and this correlation is usually governed by a simple equation. For minimal dispersion in the measured spectrum, the induced event must conform to the requirements that were previously explained.

Depending on the experimental setup and the sample geometry, time-of-flight neutron depth profiling may fall into one of the two categories. For instance, in the case of optically thin samples, i.e. samples thin enough to allow escape of both particles generated in the neutron capture reaction, both event triggers are available since the emission of charged particles, i.e. alpha or proton, and the recoil nucleus is diametric [69, 70]. Parikh et al. measured the lithium concentration depth profile by mapping the ${}^4\text{He}-{}^3\text{H}$ coincidence counts in energy space by using the ${}^6\text{Li}(n, \alpha){}^3\text{H}$ reaction. Because of the increase in solid angle subtended by the detectors, an improvement of two orders of magnitude in counting statistics can be achieved with no loss of depth resolution [71]. This configuration will not work for a thick sample since one of the particles cannot penetrate the sample. In this case, an induced event is needed to create a coincidence.

In the special case of boron, a gamma-ray quantum is ultimately emitted by the lithium recoil at the excited state, ${}^7_3\text{Li}^*$, as shown in Equation (2.71). The gamma signal can be used as one event trigger and the alpha particle as the other trigger. However, using the gamma signal complicates the experimental setup since the gamma is emitted into 4π independent of the emission direction of ${}^7_3\text{Li}^*$.



Another technique to generate the secondary trigger is the ion-induced secondary electron emission. An brief summary on the use of the technique is presented in Section

2.4.2, and further discussion on the emission phenomenon is given in Section 2.5.

Welsh et al. used the secondary electrons emitted from the sample induced by recoil nuclei in their recoil-nucleus time-of-flight neutron depth profiling measurements [15–17, 72].

Timing spectrometry is based on the distribution of temporal detection intervals of a certain event. The absolute detection interval of the event of interest is created by a second event that has an immediate correlation with the original event. Generally, one of the events starts a chronometer in a timing circuit and the other event stops it, which effectively gives the time difference between the detection of two events. Assuming the coincident event has a unique flight time from the source to the detector, then the registered time difference is directly correlated to the flight time of the original event.

2.4.2 Applications of Time-of-Flight Spectrometry

The first applications of time-of-flight spectroscopy involved the characterization of recoil nuclei produced by energetic heavy ion reactions [73]. The technique was also used to measure the stopping force of a number of low-energy heavy ions in thin carbon foils and the charge states of these ions emerging from such foils. Lang et al. [74] proposed two variants of the start detector design, which they called zero-time detector. They also used a thin carbon foil for secondary electron generation. They demonstrated that the spectrometer can be successfully used to measure the energy spectrum of ^{252}Cf fission products. Zebelman et al. [75] introduced a 180° -turn isochronous electron transport system to minimize time dispersions during the transport of electrons. Bowman et al. [76] also employed a 180° -turn electron transport system on a similar start detector design. A similar technique was adopted by Gloeckler et al. [77] for particle identification at energies from 2-400 $keV/\text{nucleon}$. Gloeckler et al. suggested the application of the technique for the detection and identification of low-energy interplanetary and magnetospheric particles. The technique was also used as a position-sensitive detector in a design proposed by Busch et al. [78], where they used an electrostatic mirror to separate the electrons from ions. A comprehensive analysis of the time-of-flight spectrometers introduced until 1984 for identification of nuclear particles is presented by Wilken [79]. Similar designs were proposed for various applications, either to improve the detection precision, detection sensitivity, or both [80–87]. The majority of the designs employed the time-of-flight telescope to create the start signal. Almost all of the designs used microchannel plates to detect the electron, or both the electron and ion.

One of the primary issues with the ion time-of-flight spectrometers is the telescopic

configuration that results in low geometric efficiency due to the fact that the ion has to go through multiple apertures to reach the detector. Therefore, a number of remedies were proposed to improve the geometric efficiency in order to enhance detection sensitivity. Kraus et al. [81] introduced a design that used a large-area detecting surface (active areas of 270 and 1000 mm^2), and reported that detection efficiencies in excess of 75% was measured for alpha particles. Mizota et al. [82] also used a large-area detector (effective area of 1380 mm^2), and was the first to propose to use a time-of-flight telescope to generate both the start and stop signals. They reported an intrinsic time resolution (FWHM) of 60 ps for 85-MeV ^{16}O ions, and a detection efficiency of 91% for 5.5-MeV alpha particles. Andreyev et al. [83] also used the time-of-flight telescope in a similar configuration. They, however, incorporated a double-triggering mechanism signaled by two microchannel plates located on both sides of the emitter foil. By gating the signals from both microchannel plates, they significantly improved the time resolution. They reported registration efficiency close to 100% for heavy ions for a single time-of-flight detector.

Fang et al. [85, 86] used triangular electrostatic filter in a cross electric magnetic field configuration. The advantage of a triangular filter was the preferential acceleration of electrons in adverse relation to their proximity to the microchannel plate, which improved the timing resolution of the spectrometer. They claimed a transit time spread of less than 50 ps , and a detection efficiency of more than 70% for 4.0-MeV alpha particles.

In another application, Kuznetsov et al. [87] used the time-of-flight telescope technique along with the direct energy measurement. The time-of-flight telescopes were used as both the start and stop detectors. The ion energy was determined from the difference of arrival times of the two signals. The ion was ultimately stopped by a charged particle detector and its energy was registered. The technique was called time-of-flight - energy (TOF-E). Kuznetsov et al. reported a detection probability of $\sim 10\%$ for alpha particles and $\sim 99\%$ for fission fragments from a ^{252}Cf source.

Time-of-flight spectrometers are widely used in space plasma applications. Gloeckler et al. [88] reported the solar wind ion composition spectrometer (SWICS) to be deployed on Ulysses to determine the elemental and ionic-charge composition, the temperature and mean speeds of all major solar-wind ions, from H through Fe , at solar wind speeds ranging from 175 km/s (protons) to 1280 km/s Fe^{8+} . The instrument combines an electrostatic analyzer with post-acceleration, followed by a time-of-flight and energy measurement, and is capable of measuring an energy per charge range from 0.16 to 59.6 keV/e in ~ 13 min . They predicted a pre-flight counting efficiency in the range of

30 to 80% for ions heavier than He in the energy range of the SWICS.

Another space application of time-of-flight - energy (TOF-E) technique is introduced by Gubler et al. [89]. Their instrument, the cylindrically symmetric mass spectrometer (CYLMAS), combines linear and isochronous time-of-flight instruments to improve the mass resolution, and to determine charge and mass separately. Further deployment of time-of-flight spectrometers for various space plasma applications is reported [90, 91].

2.4.3 Correlation between the Time and Energy Spectra

For the application of time-of-flight spectrometry in neutron depth profiling, the acquired time spectrum is converted to energy spectrum. The energy of the ion and its arrival time is correlated by

$$E = \frac{1}{2}m_{\text{ion}}v^2 = \frac{1}{2}m_{\text{ion}}\left(\frac{L}{\tau}\right)^2 \quad (2.72)$$

where E denotes the calculated energy of the ion, m_{ion} is the mass of the ion, L is the nominal flight path, and τ is the measured arrival time. The conversion is not a linear transformation.

Another important point on time-to-energy conversion is the sensitivity of the energy on the point of time on the spectrum to the unit variation in time. In other words, every point on the time spectrum has a different worth in energy space for unit temporal displacement.

The sensitivity can be expressed mathematically by differentiating Equation (2.72)

$$|\delta E| = m_{\text{ion}}\frac{L^2}{\tau^3}|\delta t| \quad (2.73)$$

where δt and δE designate perturbations in time and energy. Figure 2.10 shows the plot of the sensitivity given in Equation (2.73) for a temporal perturbation of $\delta t = 1.2 \text{ ns}$, which is the nominal instrumental resolution of the Ortec 9308 time analyzer used in the experimental measurements. As can be seen in the figure, the conversion is more sensitive to time variations at low arrival times of the spectrum.

As an example, consider the sensitivity of conversion from time to energy around $\tau = 675.3 \text{ ps}$ to $\delta t = \mp 1.2 \text{ ps}$ variation is $\mp 1 \text{ MeV}$, a value calculated using Equation (2.73). That means, if a particle arrives the microchannel plate with a flight time of $\tau \sim 675 \text{ ps}$, and is detected with a time measurement error δt of merely $\sim 1.2 \text{ ps}$, the energy of the particle will have an uncertainty δE of $\sim 1 \text{ MeV}$. Considering the measured instrumental resolution, as presented in Section 5.3, of $\sigma = 14.57 \text{ ps}$, the significance of

time resolution can be better understood.

This observation directly results from the quadratic relation between the particle flight time and its energy. In order to circumvent high sensitivity to time perturbations, the flight path of the primary ion must be lengthened thus extending the time of flight of the particle and moving it to less sensitive locations in the time spectrum.

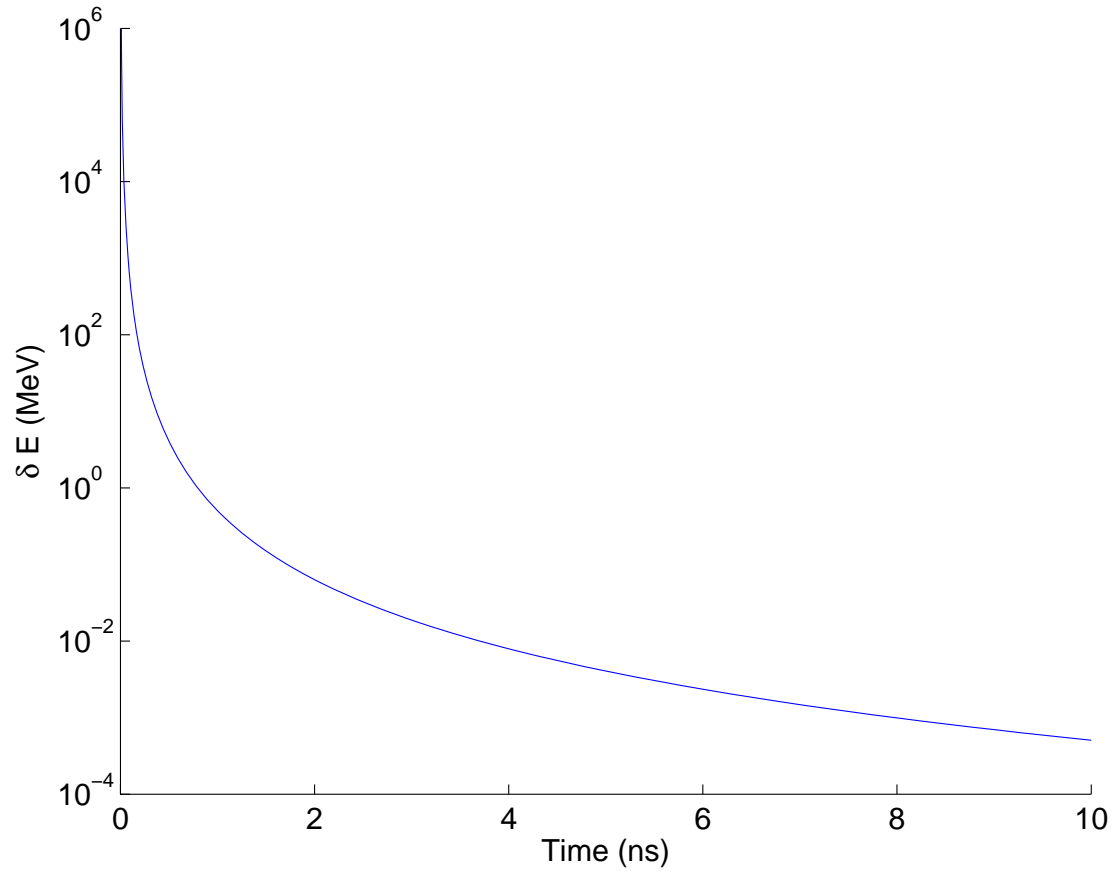


Figure 2.10. Sensitivity of energy with respect to the location of the peak on the time spectrum.

2.5 Particle-Induced Electron Emission

Particle-induced electron emission (PIEE) is a phenomenon where a number of electrons are emitted from the surface of a condensed matter upon impact of an incident ion with sufficient kinetic energy ($v_p/v_0 > 0.1$, v_p particle velocity, v_0 Bohr velocity). If the incident particle –also called projectile– is an ion, the process is called ion-induced electron emission (IIEE). If the surface is bombarded by a primary electron (PE) beam, the process is called secondary electron emission (SEE). Hence, particle-induced electron emission (PIEE) must be considered as the general term that covers both processes, i.e. IIEE and SEE. The emission in both cases is a consequence of various combinations of elastic and inelastic interactions between the incident particles and the solid state electrons and nuclei. The number of electrons ejected per incident particle is called *electron yield* –sometimes secondary electron yield, or *emission yield*, and is usually designated by γ .

The electron yield is commonly classified into three quantities: (1) forward yield γ_F , (2) backward yield γ_B and (3) total yield γ_T . Forward electron emission is considered as the emission in the direction of the ion, and the backward emission in the opposite direction. Total yield is considered as the sum of forward and backward yields, i.e.

$$\gamma_T = \gamma_B + \gamma_F$$

A simple sketch of the forward and backward emission due to impact of an ion on a thin foil is shown in Figure 2.11.

There are two main excitation mechanisms that lead to ion-induced electron emission: (1) kinetic electron emission (KEE), where electrons are excited as a consequence of the motion of the projectile, (2) potential electron emission (PEE), where electron excitation results from the conversion of internal energy brought by the projectile through an Auger process.

Section 2.5.1 presents a brief discussion on the background and theory of secondary electron generation. An extensive analysis of the process is beyond the scope of this thesis. Interested reader is recommended to refer to the cited literature for a more thorough analysis of the phenomenon. Section 2.5.2 focuses on the electron emission that result from thin carbon foils, and presents the latest experimental data available in the literature.

For experimental purposes, the focus is generally limited to the following quantities and relations:

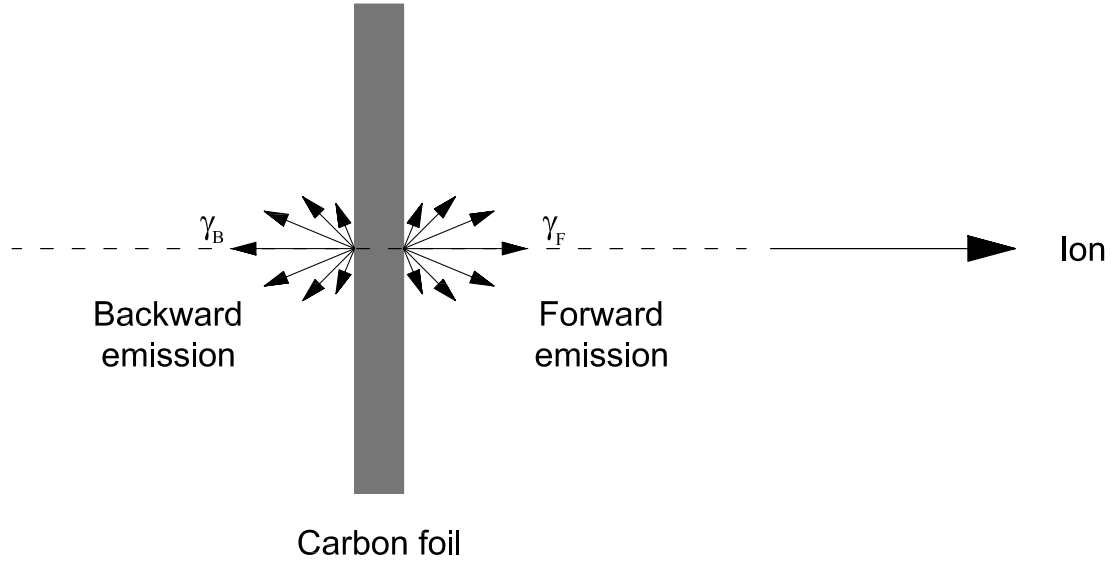


Figure 2.11. A simplified depiction of ion-induced secondary electron emission from a thin carbon foil upon impact of an energetic ion.

- The total electron yield, γ_T , the forward electron yield, γ_F and the backward electron yield, γ_B from thin foils:

This information is needed to estimate the number of electrons that can be expected. In order to improve the detection efficiency, and avoid signal loss, sufficient electron yield must be guaranteed per ion pass. On the other hand, a high electron yield may cause transit time spread since the electrons emerge from the surface of the emitter foil with different energy and directions. Therefore, the induced trigger is designed to give an optimal yield taking into account the electron detection efficiency of the detector and the transport efficiency of the electron optics system.

The attention in this study is limited to detection of electron emission only in the forward hemisphere. However, as a future research topic, the signal from the backward electron emission can be used to improve the counting statistics as presented in Section 6.2.

- The energy and angular distributions of secondary electrons, $d\gamma/dE$ and $d\gamma/d\Omega$, respectively, emitted from the entrance and exit sides of the material:

This information will be used to estimate the transit time spread of the time spectrum due to initial electron velocity distribution. The theoretical energy and angular distributions as well as the experimental data will be used as the probability density functions of the quantity to be sampled in a Monte Carlo simulation.

- Dependence of electron yields, γ_F and γ_B , on the target material type, target thickness, and the incident ion:

This information is needed to select the optimal thickness of the target material. The target must create as little uncertainty as possible, such as energy straggling of the incident particle, yet yield sufficient signal.

- Dependence of electron yields, γ_F and γ_B , on target material surface conditions, i.e. gas adsorption and oxide formation:

This information will provide insight on how much care must be given to the condition of the target material, and how much it can deteriorate in the conditions, under which the experiment will be performed.

2.5.1 Background and Theory

In almost all theoretical treatments of particle-induced electron emission, electron emission due to the impact of the energetic ions is usually described in three stages: In the first stage, internal secondary electrons are generated through excitation as the particle penetrates the target material. In the second stage, these excited electrons are transported in the medium going through numerous collisions including cascade multiplication process. A portion of the internal secondary electrons migrate towards the surface. In the third stage, the electrons that reach the surface of the material with sufficient energy to penetrate the potential barrier escape into the vacuum.

One common assumption in all theoretical treatments is that all the above steps are statistically independent processes, and can be treated separately.

The internal electrons are produced mainly by two processes [92, 93]:

1. direct collision processes between the projectile (incident particle) and target atoms and ions:
 - by excitation of conduction electrons into free states above the Fermi level,
 - by ionization of inner shells of the target atoms,
 - by ionization in outer and inner shells of the projectiles,
 - and electron loss of electrons from the projectile;
2. by secondary processes:
 - cascade multiplication of diffusing secondary electrons,

- excitation of target electrons by energetic recoil atoms (recoil ionization) and by backscattered projectiles,
- one-electron-decay of volume and surface plasmons generated either by energetic primary ions or by secondary electrons,
- by photons produced in projectile-target collisions.

In the following section, a synopsis on the progression of the theory is presented on particle-induced electron emission. Most of the theories mentioned here are semiempirical. Common features of all theoretical treatments reviewed here are that the distinct sources of electron emission such as plasmon decay, electron loss, Auger electrons, etc. are neglected. Furthermore, only a normal incident angle on the target is considered. Other angle of incidences are considered to vary as $\sec \vartheta$. Local secondary electron generation inside the solid material is assumed to be isotropic, and the surface potential barrier is approximated as planar. These simplifying assumptions yield a cosine angular distribution outside the surface.

Early Theories

The first mention of secondary electron emission (SEE) dates back to early 1899 [94]. The phenomenon was discovered by Austin and Starke [95] as they were studying the reflection of cathode rays from metal surfaces. They observed that the metal target emitted a larger number of electrons than it received, leading them to the conclusion that the primary electrons liberated additional ones. The concept was later recognized around 1905 [96–98]. Historically, the electrons emitted from a solid surface as a result of alpha particle bombardment were called *δ -electrons*. The first distinction between electrons ejected due to the impact by *canal rays*, also called anode rays- and the alpha particles was made by Rüchardt [99] and Geiger [100]. Later Bethe [101] used the same nomenclature to denote the ejected electrons with energy larger than the ionization energy.

A theoretical approach to the process first appeared in the literature in 1923 by Kapitza [102]. Kapitza hypothesized that the secondary electrons derive their energy from local heating produced by the passage of ions, which leads to the assumption that thermodynamic equilibrium is established during the rapid and localized energy exchange processes between the ion and the substrate. The resulting theory depends on the thermal constants and thermionic work function of the material, which is not in agreement with the experimental measurements.

The Semiempirical Theory

This theory was based on the theory of electron emission induced by electron bombardment and was first formulated by Salow [103]. Salow derived the total electron yield as

$$\gamma = \frac{PL}{2J} \left(\frac{dE}{dx} \right)_e \quad (2.74)$$

where P is the mean escape probability, L is the mean free path of electrons, J is the mean energy to produce a free electron inside the solid, and $(dE/dx)_e$ is the inelastic (or electronic) stopping force of the projectile in the solid. Since the factor $PL/2J$ is a material parameter, the yield becomes proportional only to the stopping force. Since the stopping force increases with the square of the effective charge Z_{eff} of the projectile, this leads to the following conclusion:

$$\gamma \propto Z_{\text{eff}}^2$$

The weakness of the theory was the dependence on ambiguous parameters such as the mean escape probability P , the mean free path L , and the mean energy J . The stopping force is also a mean quantity that does not take into account different electron excitation mechanisms [104].

The Theory of Sternglass (1957)

Sternglass's treatment [105] is similar to the semiempirical theory. However, the internal electron generation process is treated in more detail. Two main generation processes are proposed: (1) distant (large-impact parameter collisions with small energy transfer), which results in large number of low-energy secondary electrons; (2) close (small-impact parameter collisions with large energy transfer), which produces small number of energetic δ -electrons.

The rate of internal electron production of each process is proportional to the corresponding inelastic stopping powers, $(dE/dx)_d$ and $(dE/dx)_c f(v_p, x)$, respectively, where subscripts d and c designate distant and close collisions. From Bohr-Bethe's equipartition rule of stopping force [21, 26], which considers that the distant- and the close-collision stopping forces are equal to one half of the electronic stopping force, one obtains:

$$\left(\frac{dE}{dx} \right)_d = \left(\frac{dE}{dx} \right)_c = \frac{1}{2} \left(\frac{dE}{dx} \right)_e \quad (2.75)$$

where $(dE/dx)_e$ is the total inelastic stopping force.

The final form of the Sternglass' derivation of the total electron yield is:

$$\gamma = \frac{(P'L}{2J} \left(\frac{dE}{dx} \right)_e (1 + F(v_p)) \quad 0.5 \geq F > 0 \quad (2.76)$$

where P' is the escape probability, L is the mean free path, J is the mean energy to produce free electrons, and the function $F(v_p)$ is related to the mean free paths of slow and δ -electrons.

His work also included the energy distribution of the secondaries; dependence of emission yield on the ion angle of incidence, and on the target material temperature. The effect of gas adsorption and oxide formation on the surface of the target material on secondary electron yield was also included. Finally, the yield equation was modified to include the mass and initial charge state of the ion.

Sternglass' theory was in good agreement with the experimental data of Hill et al. [106] and Aarset et al. [107]. The major weakness of the theory was that the equipartition rule was not always fulfilled. The theory was also not applicable at low impact energies since the slowing down of projectiles with the escape depth is not considered.

The Theory of Parilis and Kishinevskii (1960)

Parilis and Kishinevskii [108] described the process of electron generation by an effective ionization cross section σ^* and the expression for Auger process ω (including the escape probability). The total electron yield γ was then calculated as

$$\gamma = N\sigma^*L\omega \quad (2.77)$$

where L is the mean free path of electrons and N is the number density of the target.

The Theory of Schou (1980)

In a later work, Schou [109, 110] used the Boltzman transport equation whose input quantities are the microscopic cross sections for collisions, the magnitude of the surface barrier, and binding energy of the liberated electrons. His model was based on the similarities between electron emission and sputtering, namely electron cascade theory. Since the cross sections are not accurately known, the yields and the energy distributions are expressed by quantities that depend weakly on the parameters specifying the model cross sections, such as stopping force. His theoretical treatment did not impose any

restrictions as to the type of the incident particle, i.e. it covered both incident electrons and ions. The formulas for the energy and angular distribution of the emitted secondary electrons as well as the yield formulations are derived. Schou also takes into account the effect of recoiling target atoms on secondary emission. Schou's derivations however, did not include the effect of the charge state of the incident ions.

If recoil ionization is neglected the electron yield can be written as

$$\gamma = \Lambda D_e \quad (2.78)$$

where D_e is the amount of inelastic energy deposited at the surface, and Λ is given as

$$\Lambda = \int_0^\infty dE \frac{\Gamma_m E}{4 \left| \frac{dE_i}{dx} \right| (E + W)^2} \quad (2.79)$$

where $E = E_i - W$, Γ_m is a function dependent on the exponent of the used power cross section (tabulated by Schou [109]), and dE_i/dx is the stopping force for low-energy electrons in the solid. The surface potential barrier W in metals is determined by the Fermi energy, $E_F = \hbar^2 k_F^2 / 2m$, and the work function Φ , i.e. $W = E_F + \Phi$.

The expression for the energy spectrum is given as

$$\frac{d\gamma}{dE} = \frac{\Gamma_m D_e E}{4 \frac{dE_i}{dx} (E + W)^2} \quad (2.80)$$

which depends only on the properties of the target material. Neither Z of the incident ion type nor its energy has any effect on the spectrum. This is a very important outcome of Schou's theory.

It should be noted that, although the incident particle energy is mostly used in the equations, it is the particle velocity, hence the energy per atomic mass unit, that governs the interaction processes between the particle and target atoms.

2.5.2 Kinetic Electron Emission from Ion Penetration through Thin Films

In order to generate electron emission to use as a secondary signal that is coincident with the primary signal without causing substantial deviation in the energy of the primary particle, thin foils can be used. This configuration preserves the primary particle so that a primary signal can be generated. The amount of deviation in the information carried by the particle is a function of incident particle energy and atomic number,

and the target material atomic number. The experimental knowledge base of emission characteristics of target materials is still limited. Usually a combination of theoretical calculations and experimental measurements are used to predict the emission response of a target material to the incident ion at the energy of interest.

In determining a proper target foil material, following decision criteria must be met:

1. The energy straggling of the projectile in the target foil must be small. The energy straggling is the dominant factor in projectile uncertainty. Since the energy straggling is approximately proportional to the square of the atomic number of the target material, Z_T^2 from the Bohr approximation, the target material must have as small atomic number as possible. Using a high atomic number target material Z_T defeats the whole purpose of developing and implementing the time-of-flight spectrometer for neutron depth profiling with the ultimate goal to improve profiling resolution.
2. The target material must be conductive to establish the field lines between the foil and the rest of the electron optics system. Failure to do so creates a significant black hole in the detection system and results in loss of a sizeable percentage of electrons. This criterion limits the selection portfolio to metals.
3. The target material must have adequate strength to be self-supporting. The foils can be coated with a thin layer of collodion (cellulose nitrate) to improve the strength. However, introduction of additional mass introduces further energy straggling and other uncertainty mechanisms, ultimately resulting in loss of resolution.
4. The electron yield of the target material must be sufficient to compensate for the losses in the electron focusing system. It is desired that on the average, the number of electrons ejected per incident ion, the electron yield, must be greater than unity. On the other hand, a large electron yield will result in broadening of the time spectrum. The loss mechanisms in the electron focusing system are the detection efficiency of the microchannel plate detectors, and the disruption of the field uniformities due to imperfections in the design of the spectrometer or due to the presence of stray fields extending into the field space where electron transport takes place.

Secondary electron emission yield varies with the energy of the incident ion. At very high energies, the ion is less ionizing hence induces less electron emission from the foil. As the incident ion energy gets lower, the yield, both backward and forward, increases due

to higher number of interactions between the projectile and the target electrons. Figure 2.12 shows the forward, backward and total electron yields due to protons impinging on a thin carbon foil.

The thickness of the foil is reported to be 1000 Å [111]. As seen in the figure, the proton beam above 2 MeV generates less than one electron per particle in both backward and forward emission.

Figure 2.13 shows the variation of the forward, backward and the total electron yields from H^+ ions impinging on a thin carbon foil in a wide energy range, 2 keV-1 MeV [112]. The emission yields increase until the incident ion energy reduces down to 100 keV. Below that energy the yield starts to trend down as the ion gets slower. As explained in the foregoing paragraph, the increase in electron emission yield results from more interactions between the projectile and target electron gas. This trend is analogous to the trend of the stopping force. The interaction probability peaks around the energy where the electronic stopping force equals the nuclear stopping force.

Another interesting observation is the effect of the initial charge state of impinging ions on emission yield. An experimental data is shown in Figure 2.14 [111]. The 1000-Å thick carbon foil is bombarded by lithium ions at the equilibrium charge states of 2+ and 3+ at various kinetic energies. Although it makes almost no difference in the forward emission yield, it causes some discrepancy in the backward emission yield. Since only the electrons emitted into the forward hemisphere is considered in this work, it is possible to conclude that the emission yield is independent of the charge state of the ion.

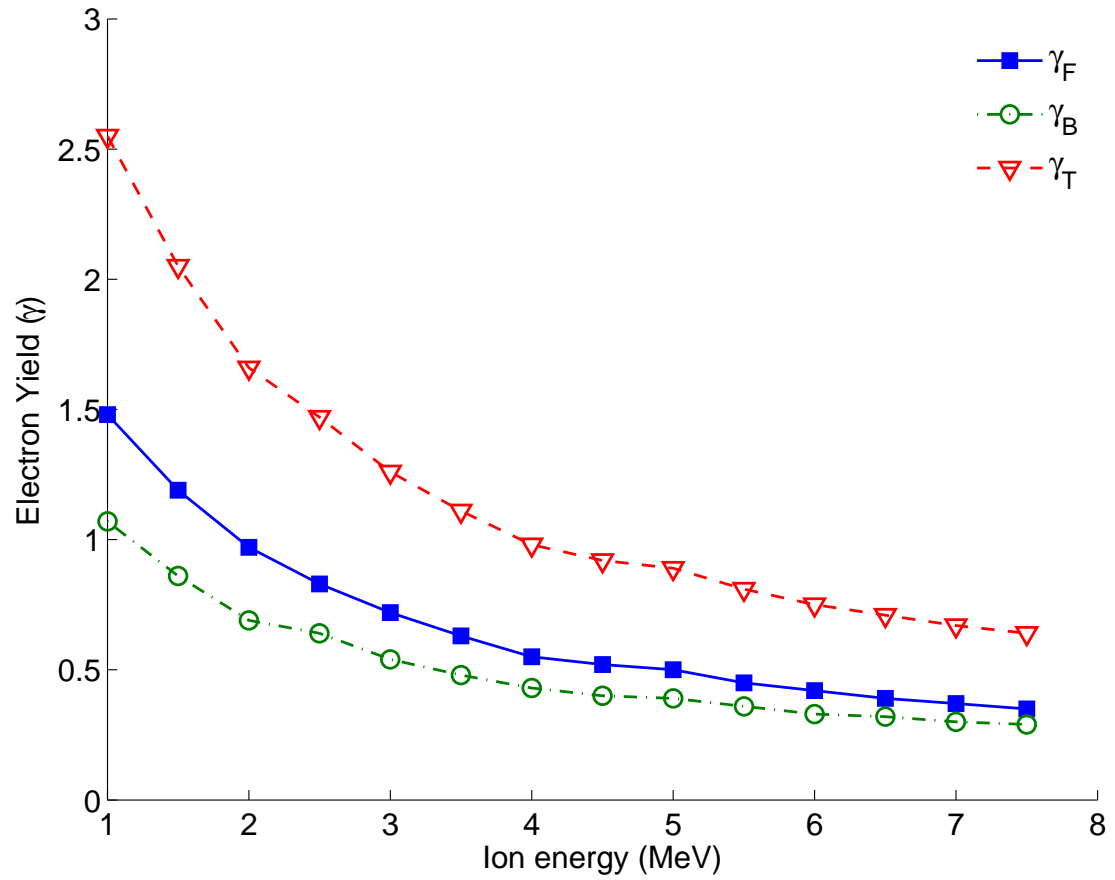


Figure 2.12. Forward, backward and total electron yields, γ_F , γ_B and γ_T , respectively, versus incident proton energy E_i from thin carbon foil –plot courtesy of *Physical Review B* [111].

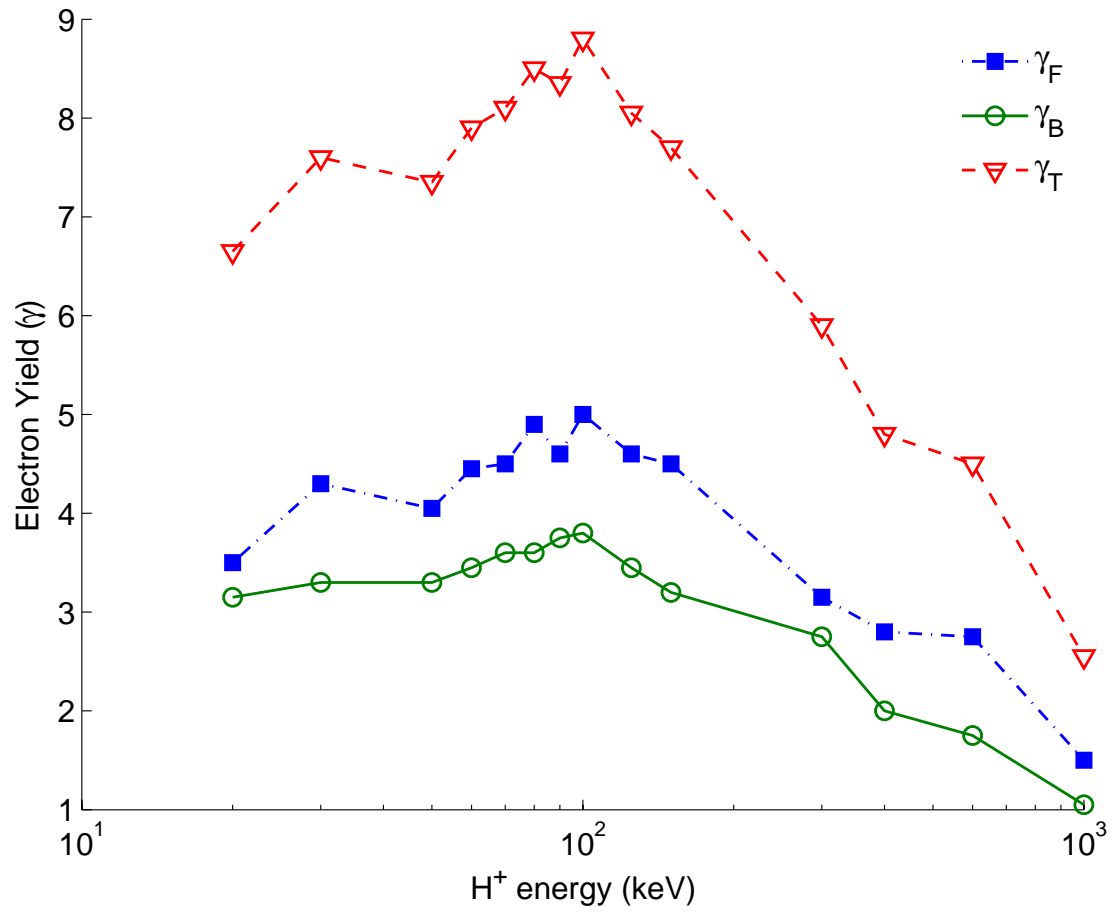


Figure 2.13. Electron yield versus incident H^+ energy for the range 20 keV-1 MeV -plot courtesy of "Elsevier Limited" [112].

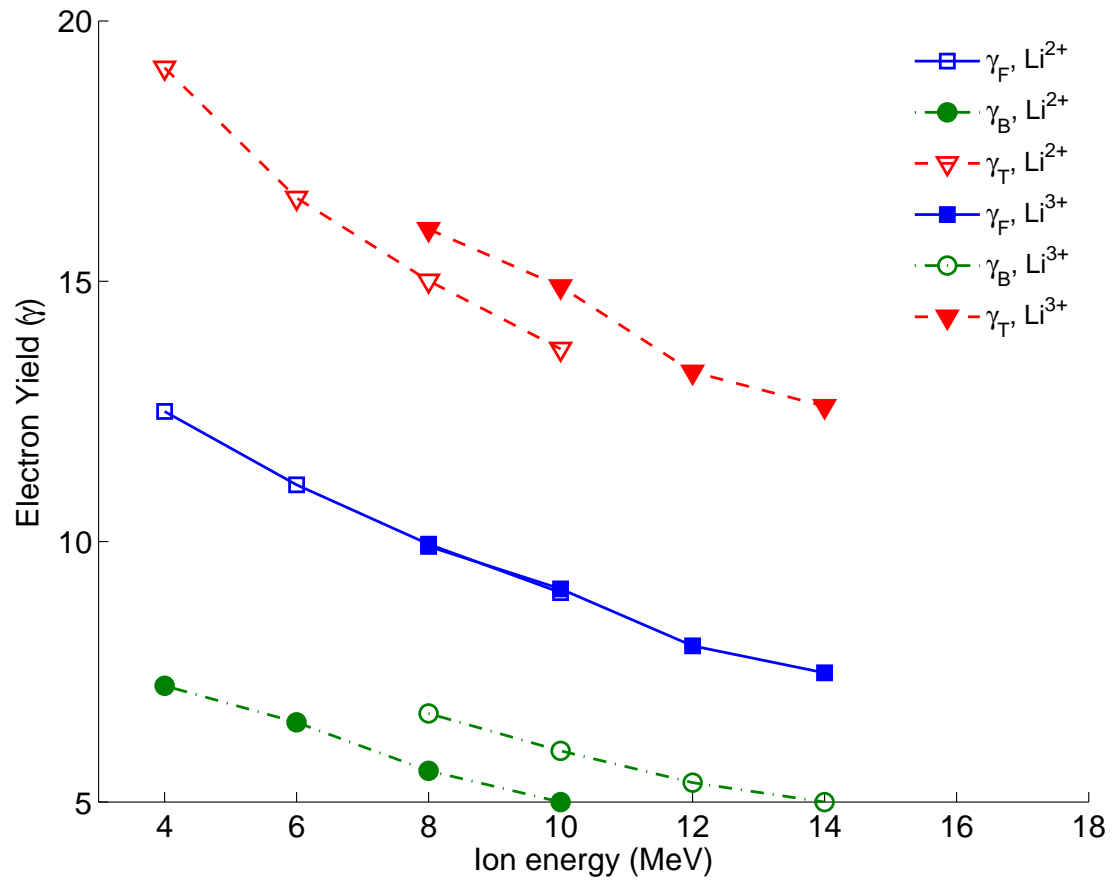


Figure 2.14. Electron yield from thin carbon foil versus incident lithium ion energy at various charge states –plot courtesy of *Physical Review B* [111].

CHAPTER

3

ION TIME-OF-FLIGHT SPECTROMETRY

This chapter introduces the spectrometer systems developed for ion energy measurement. Two different spectrometers were developed, tested and compared. Design and operation parameters are specified for each device. The complete experimental setup for each spectroscopy technique is introduced in Chapter [4](#).

3.1 Parallel Electric and Magnetic (PEM) Field Ion Time-of-Flight Spectrometer

The parallel electric/magnetic (PEM) field spectrometer design was based on the principle of a direct write electron lithography system [[113](#)]. The principle of the device can be summarized as follows: the ion goes through a thin carbon foil and continues on its path with insignificant deviation from its incident direction. The passage of the ion creates secondary electrons in the carbon foil. These electrons are accelerated in a volume with uniform electric and magnetic fields. The premise is that, as will be presented in the following sections, the electric and magnetic fields established along the direction of the central axis of the spectrometer exert a restrictive force on the electron beam ejected

from the carbon foil by the passage of the ion. The focusing capability guarantees that all ejected electrons are collected on the electron detector.

Following sections elaborate on the selection of the design parameters for the device.

3.1.1 Design of the Device

The equations of motion for the electrons in parallel electric and magnetic (PEM) fields are presented in Appendix A.1. In the PEM field spectrometer, the nominal electron velocity is parallel to the direction of both the electric and magnetic fields. The electron accelerates as it approaches the detector because of the net electrostatic force exerted on it. For an electron ejected in the direction of the surface normal of the carbon foil, the magnetomotive force is zero since

$$\mathbf{F} = -\mathbf{v} \times \mathbf{B}$$

However, for electrons ejected at an angle with respect to the surface normal, the net force is non-zero, hence the electron undergoes a helicoidal motion due to the presence of the magnetic field. The radius of the helix is greater for larger emission angles.

Design of the Acceleration Stages

A uniform accelerating field was established by evenly separated disks with equal voltage drops. Equal voltage drops were obtained by a resistor network. The accelerating disks were made of aluminum with an outer diameter of 125 mm, and were separated by plexiglass rings. The interior disks have 16-mm diameter aperture, whereas the entrance disk has 10-mm diameter and the exit disk has 25.4-mm diameter aperture. A carbon foil is stretched across the aperture of the entrance disk as the secondary electron generator. The beam hits the foil at an angle of $\approx 15^\circ$.

The separation between the accelerating stages were chosen to be 25 mm, with four stages making a total flight path of 100 mm for the electrons. A 250-V voltage drop was assigned for each stage as the design basis, creating a static field of

$$E = \frac{250 \text{ V}}{25 \times 10^{-3} \text{ m}} = 10^4 \text{ V/m}$$

Design of the Magnet

In order to establish a uniform magnetic field in the direction of the electron, a solenoid was designed that accommodates the accelerating stages inside. The on-axis magnetic

field profile inside the solenoid can be calculated using the formula given in Equation (3.1).

$$B = \frac{\mu_0 i N}{2l} \left(\frac{x + l/2}{\sqrt{(x + l/2)^2 + r_i^2}} - \frac{x - l/2}{\sqrt{(x - l/2)^2 + r_i^2}} \right) \quad (3.1)$$

where $\mu_0 = 4\pi \times 10^{-7} \text{ H/m}$ is the permeability constant of the free space, i is the wire current in A , N is the total number of turns of wire in the solenoid, l is the solenoid length in m , and r_i is the inner diameter of the solenoid in units of m . This formula gives the magnetic field B in units of T . It is recommended that the length of the solenoid be equal to or greater than its inner diameter for better field uniformity.

For the design of the solenoid, the following parameters were chosen: $l = 200 \text{ mm}$, $r_i = 125 \text{ mm}$, $N = 600$ turns. A regular enamel coated AWG 18 magnet wire was used. The total length of the solenoid could accommodate 200 turns for each layer of the wire; therefore the solenoid was wound as three layers. Figure 3.1 shows the on-axis field profile of the solenoid with the selected parameters. The x axis is normalized with respect to the total length of the solenoid, and only the field profile along the accelerating stages is shown. The field uniformity is within 9% for this section in L_2 norm. The maximum magnetic field value is $B = 7 \text{ mT}$ at 1 A current.

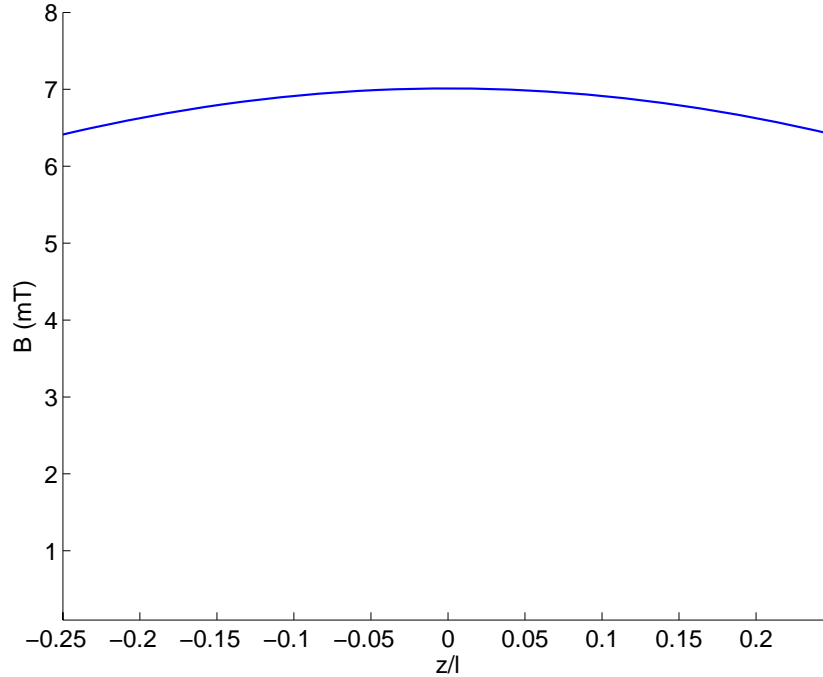


Figure 3.1. Variation of on-axis magnetic field inside the solenoid along the acceleration stages.

With the above parameters, the magnet weighs 3.5 kg , and the resistance is $\sim 5 \Omega$. The power rating of the magnet at 1 A current is $\sim 5 \text{ W}$. Low impedance reduces the power consumption, hence keeping the solenoid from overheating inside the vacuum chamber, where the major heat transfer mechanism is radiation to the chamber walls.

The acceleration stages are fixed between plexiglas rings. A resistor network is installed internally to apply the potentials to the acceleration disks. The resistors were chosen to match within 0.1% so that equipotential drops can be established between successive plates to preserve field uniformity. The plexiglas body was assembled using tape. The solenoid is wound around the body, and fixed by retaining rings on both sides.

A three-dimensional drawing of the spectrometer is shown in Figure 3.2. The ion beam enters through the 5-mm aperture on a tantalum disk at an angle of 15° . The first disk has the carbon foil on a 3-mm aperture. The ion beam continues on its path with insignificant distortion in its direction. However, it loses a portion of its kinetic energy as it passes the foil, which must be taken into account in obtaining the energy spectra. The beam is extracted on the exit side of the stages through the apertures, where it is finally detected by the ion microchannel plate. The secondary electrons generated by the ion emerge from the carbon foil and are attracted by acceleration stages. At each stage, the electron gains equal kinetic energy. The surface potential of the electron microchannel plate was adjusted so that the electric field between the exit plate and the microchannel plate surface equals the electric field between the acceleration stages.

The PEM field spectrometer is a more generalized approach than that proposed by Goulding et al [73], which uses a carbon foil stretched on a thin wire grid in the entrance of the microchannel plate. The secondary electrons emerging from the carbon foil by the passage of the ion are accelerated in the field between the foil and the front surface of the microchannel plate. The PEM field spectrometer incorporates an electron focusing device into this design.

Simulations of Electron Transport

Figure 3.3 shows the simulated electron trajectories for initial kinetic energy $E_0 = 1 \text{ eV}$, acceleration potential $V_a = 1000 \text{ V}$, electron flight path $L = 100 \text{ mm}$, magnetic field $B = 14 \text{ mT}$ with isotropically distributed initial directions. The figure was created by tracing twenty five electron rays.

As the particle moves it accelerates, and as a result, the trajectory becomes a helix with a variable pitch h as demonstrated in Figure 3.4, which is the projection of Figure 3.3 on the $(y-z)$ plane. One of the interesting observations in this figure is that the initial

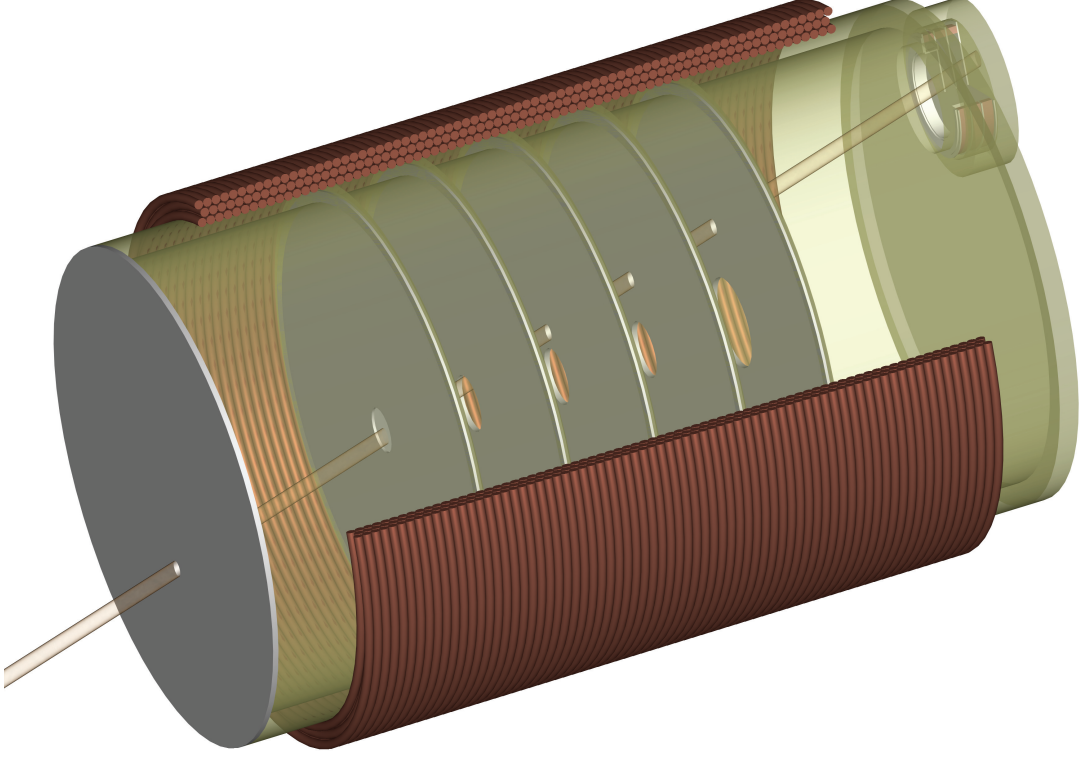


Figure 3.2. Parallel electric and magnetic (PEM) field ion time-of-flight spectrometer.

(x, y) position on the source surface from which the electron was emitted is mapped to the same position on the target 100 mm downstream by the electron optical device.

Focal Length

The trajectory of an electron is a helix [114], the step of which in Gaussian approximation is

$$\Delta z = \pi \sqrt{\frac{8m_e V^*}{B^2}} \quad (3.2)$$

where $\Delta z = z_1 - z_0$ is the distance between the two successive images, m_e is the rest mass of the electron, B is the static magnetic field, and V^* is the relativistically corrected initial potential, which is

$$V^* = V \left(1 + \frac{|e_0 V|}{2m_e c^2} \right)$$

with V designating the initial potential of the electron. If this condition is satisfied, the magnification between the frontal plates becomes unity with rotation π . For electrons

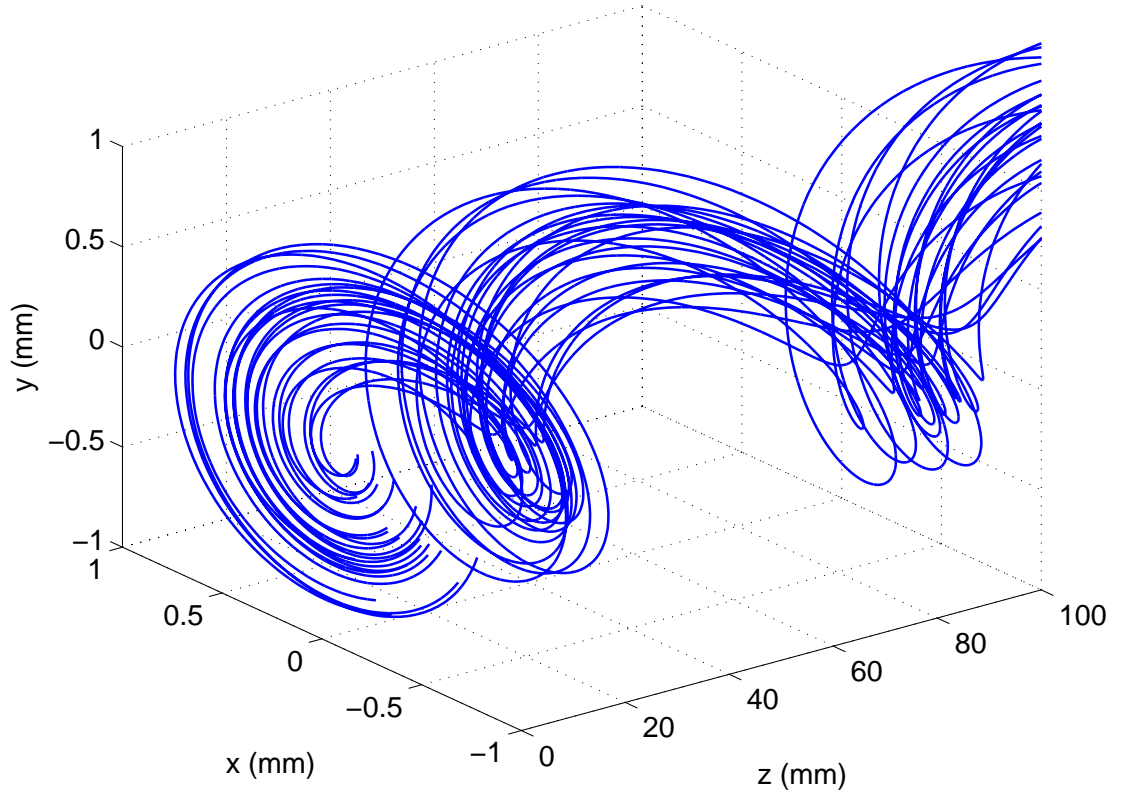


Figure 3.3. Electron ray tracing in parallel electric and magnetic fields.

in an accelerating field, the focal length of the PEM field lens becomes [113]

$$\Delta z = \frac{2\pi}{B} \sqrt{\frac{2m_e V_0}{e_0}} + \frac{2\pi^2 m_e E}{e_0 B^2} \quad (3.3)$$

where E is the accelerating field, $e_0 V_0$ is the kinetic energy at the object plane prior to acceleration, B is the uniform static magnetic field. If $E = V_a/z$ is substituted into the Equation (3.3), where V_a is the accelerating potential along z , then the magnetic field required for unity magnification is obtained.

$$\begin{aligned} z &= 2\pi \sqrt{\frac{2m_e V_0}{e_0}} + \frac{2\pi^2 m_e V_a}{e_0 B^2 z} \\ \Rightarrow B^2 &= \frac{2\pi}{z} \sqrt{\frac{2m_e V_0}{e_0}} B - \frac{2\pi^2 m_e V_a}{e_0 z^2} = 0 \\ \Rightarrow B_{1,2} &= \frac{1}{2} \left(\frac{\pi}{z} \sqrt{\frac{2m_e V_0}{e_0}} \pm \sqrt{\frac{4\pi^2}{z^2} \frac{2m_e V_0}{e_0} + 4 \frac{2\pi^2 m_e V_a}{e_0 z^2}} \right) \end{aligned}$$

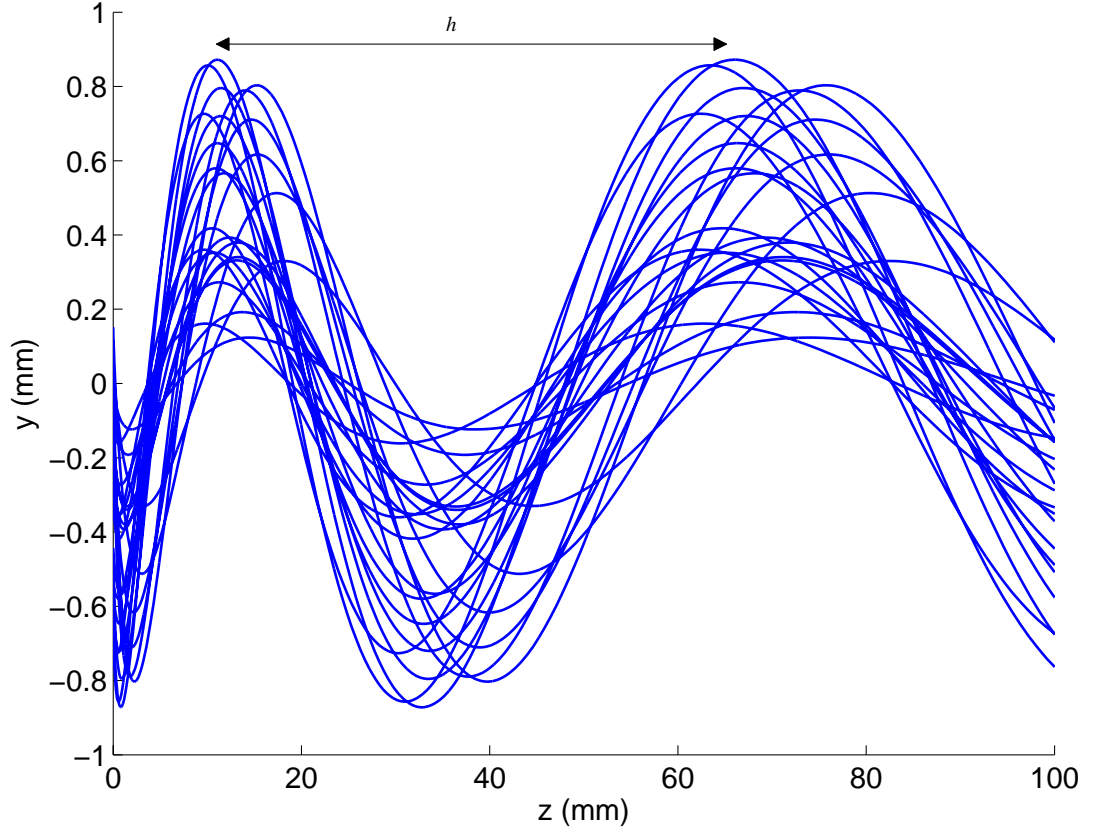


Figure 3.4. Projection of the electron traces in Figure 3.3 on the (y, z) plane.

$$\Rightarrow B_{1,2} = \frac{\pi}{z} \sqrt{\frac{m_e}{2e_0}} \left(\sqrt{V_0} \pm \sqrt{V_0 + V_a} \right) \quad (3.4)$$

The physically meaningful solution is

$$B = \frac{\pi}{z} \sqrt{\frac{m_e}{2e_0}} \left(\sqrt{V_0} + \sqrt{V_0 + V_a} \right) \quad (3.5)$$

This result provides an important tool to attain high detection efficiency with the time-of-flight spectrometer. Since the magnification between the frontal planes is unity, all the electrons emitted from the carbon foil regardless of their emission angle will be collected on the detector surface, which guarantees the detection of at least one electron per ion detected assuming 100% detection efficiency for electrons. This feature of the PEM field spectrometer is important for improved sensitivity.

3.2 Cross Electric and Magnetic (CEM) Field Ion Time-of-Flight Spectrometer

A time-of-flight spectrometer was designed based on an earlier proposed design by Bowman et al [76]. An electric field is established between parallel frames at equal potential drops. The energetic ion goes through a thin carbon foil stretched across an aperture on the entrance plate. The passage of the particle through the foil generates the secondary electrons. The ion continues on its straight path, exits the spectrometer and hits the ion detector. The generated electrons are focused on a microchannel plate positioned on the same plane with the carbon foil separated by a certain distance.

3.2.1 Design of the Device

The equations of motion that govern the transport of charged particles in cross electric and magnetic fields are given in Appendix A.2. These equations describe a cycloidal trajectory. The time required to complete one cycle can be found by $y(\tau) = y(0)$, which yields

$$\tau = \frac{2\pi}{\omega} \quad (3.6)$$

where $\omega = e_0 B / m_e$ is the cyclotron frequency.

The magnitude of the electric and magnetic fields is mainly determined by the physical considerations such as the device size, maximum voltage drop that can be maintained and current limitations. For instance, a large voltage drop may result in breakdown and may cause device failure. Likewise, a high magnetic field value requires excessive magnet mass, which may not be possible to accommodate due to lack of space.

The required lateral displacement D to map the electron beam onto the microchannel plate can be calculated by

$$D = z(\tau) - z(0) = \frac{2\pi m_e}{e_0} \frac{E}{B^2} \quad (3.7)$$

Design of the Magnet

The magnetic field can be generated either by a permanent magnet or an electromagnet. The field uniformity is essential in reducing the electron transport time dispersion. Obtaining the field uniformity with permanent magnets requires complicated modeling, which requires field trimmings using Rose shims [115].

A solenoid, as used in the design of PEM field spectrometer, is not appropriate

because of the geometry of the device. Alternatively, a Helmholtz coil can be used to generate the required magnetic field. The Helmholtz coils are commonly used in applications where field uniformity is important.

A Helmholtz pair consists of two identical circular magnetic coils that are placed symmetrically one on each side of the experimental area along a common axis, and separated by a distance equal to the radius of the coil. Each coil carries an equal electrical current in the same direction. A cylindrical region extending between the centers of the two coils and approximately $1/5th$ of the diameter will have a nearly spatially uniform magnetic field. The on-axis field intensity of the Helmholtz pair can be calculated by

$$B(z) = \frac{1}{2}\mu_0 NiR^2 \left\{ \left[R^2 + \left(z + \frac{R}{2} \right)^2 \right]^{\frac{3}{2}} + \left[R^2 + \left(z - \frac{R}{2} \right)^2 \right]^{\frac{3}{2}} \right\} \quad (3.8)$$

where N is the number of turns in each coil, i is the electric current through the coils connected in series, R is the inner radius of the coils, and z is the distance to the center point on the axis. The magnitude of the field in the center is:

$$B(0) = \left(\frac{4}{5} \right)^{\frac{3}{2}} \frac{\mu_0 Ni}{R} \quad (3.9)$$

A Helmholtz coil pair was constructed of AWG #26 copper wire coated with regular enamel. The inner diameter of the coils was chosen to be 125 *mm* to accommodate the CEM spectrometer. The coils do not employ any core material, and each coil consists of 600 windings. With this configuration, the coils generate a nominal magnetic field of $85 \times 10^{-4} T$ at the center of the pair with 1 *A* electrical current. Each coil has a resistance of approximately $R = 30 \Omega$.

Another Helmholtz coil pair was constructed of AWG #23 copper wire wound around aluminum disks. The disks are centered and connected with each other by three aluminum couplings by a distance equal to the radius of the coils. A three-dimensional drawing of the Helmholtz coil pair is shown in Figure 3.5. Experiments with regular enamel coated magnet wire resulted in poor vacuum performance because of the high outgassing rate of the insulator at high temperatures. Polyimide coated magnet wire was purchased from MWS Wire Industries, Westlake Village, CA. Polyimide is a highly stable material in a wide temperature range. Polyimide films like Kapton are extensively used in ultra-high vacuum applications.

The aluminum cores have an inner diameter of 150 *mm*. Each coil has $N = 725$ number of turns. The electrical resistance of each coil was calculated to be approximately

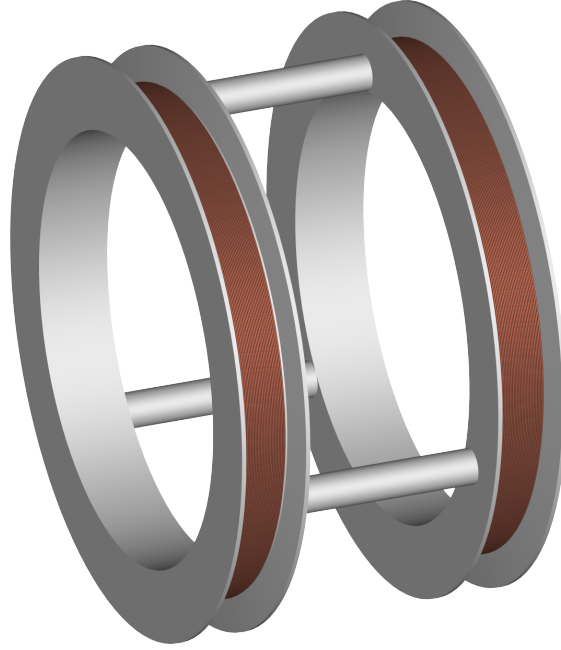


Figure 3.5. Three-dimensional drawing of the Helmholtz coil pair.

28Ω , and measured $R = 27.8 \Omega$. At this impedance, each coil consumes $28 W$ at $1 A$ electrical current, which makes approximately $60 W$ for the coil pair. The on-axis field distribution of the coil pair with these parameters is shown in Figure 3.6. The magnitude of maximum field in the center of the pair is approximately $70 \times 10^{-4} T$ at $1 A$ electrical current through each coil.

Design of the Acceleration Stages

Acceleration stages were made of aluminum frames. The aperture on the entrance plate for the ions has a diameter of $10 mm$, which is aligned with the $10\text{-}mm$ aperture on the exit plate. The number of intermediate stages is determined by the maximum displacement in the transverse direction. The inlet plate has another opening for the microchannel plate assembly to detect the electrons.

An electric field value must be chosen based on the magnet parameters given in the previous section. As the design basis magnetic field, $50 \times 10^{-4} T$ was chosen, which corresponds to approximately $i = 0.7 A$ current through each coil. Another design parameter is the lateral separation between the center of the carbon foil to the center of the electron microchannel plate, which is $D = 50 mm$. Based on the design parameters, the magnitude of the required electric field is calculated to be $E = 35 kV/m$.

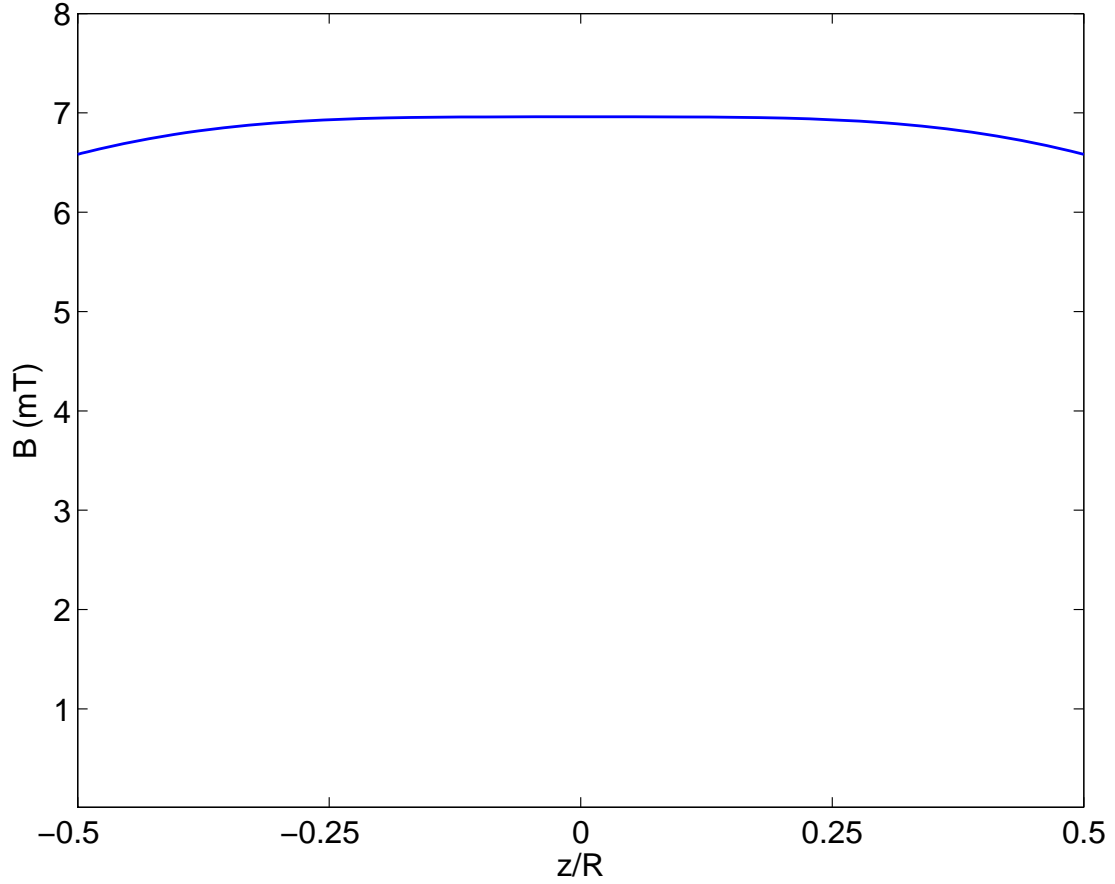


Figure 3.6. On-axis distribution of the magnetic field created by the Helmholtz coil.

The plates were separated from each other by 3.6 mm using precision Nylon 6 stand-offs. The required voltage drop across each acceleration stage to generate the aforementioned electric field value is approximately 125 V for 3.6 mm separation. The time required for one cycle was computed to be $\tau \approx 7.15 \text{ ns}$. The maximum displacement in the transverse direction is calculated approximately to be $y_{\max} = y(\tau/2) \approx 17 \text{ mm}$, which requires at least five stages to allow proper bending of the electron beam. The simulated electron trajectories in x , y and z directions are shown in Figure 3.7.

The electric and magnetic field values can be adjusted as long as the E/B^2 ratio is preserved, which satisfies the lateral displacement equation given by Equation (3.7). For 50 mm lateral displacement, the ratio is calculated as $E/B^2 \approx 1.4 \times 10^9 \text{ Cm/kg}$. For instance, if the magnetic field value is doubled, then the electric field value must be quadrupled to keep the E/B^2 ratio the same.

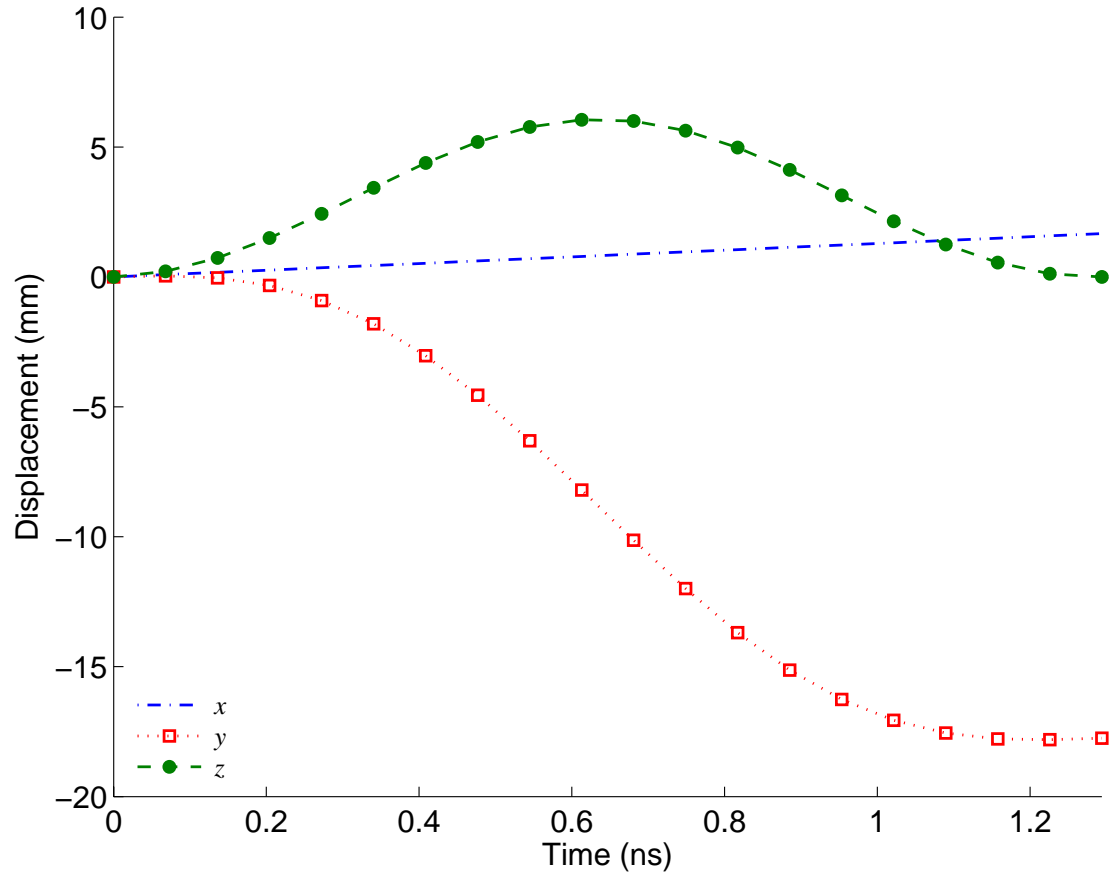


Figure 3.7. The simulated electron trajectories for the CEM field spectrometer in x , y and z directions.

In order to allow adjusting of the electric and magnetic fields without affecting the E/B^2 ratio, eight acceleration stages were used. 125 V voltage drop is needed across each acceleration stage, which corresponds to a total voltage drop of 1000 V to establish the required electric field of $E = 35 \text{ kV/m}$. A three-dimensional drawing of the spectrometer is shown in Figure 3.8.

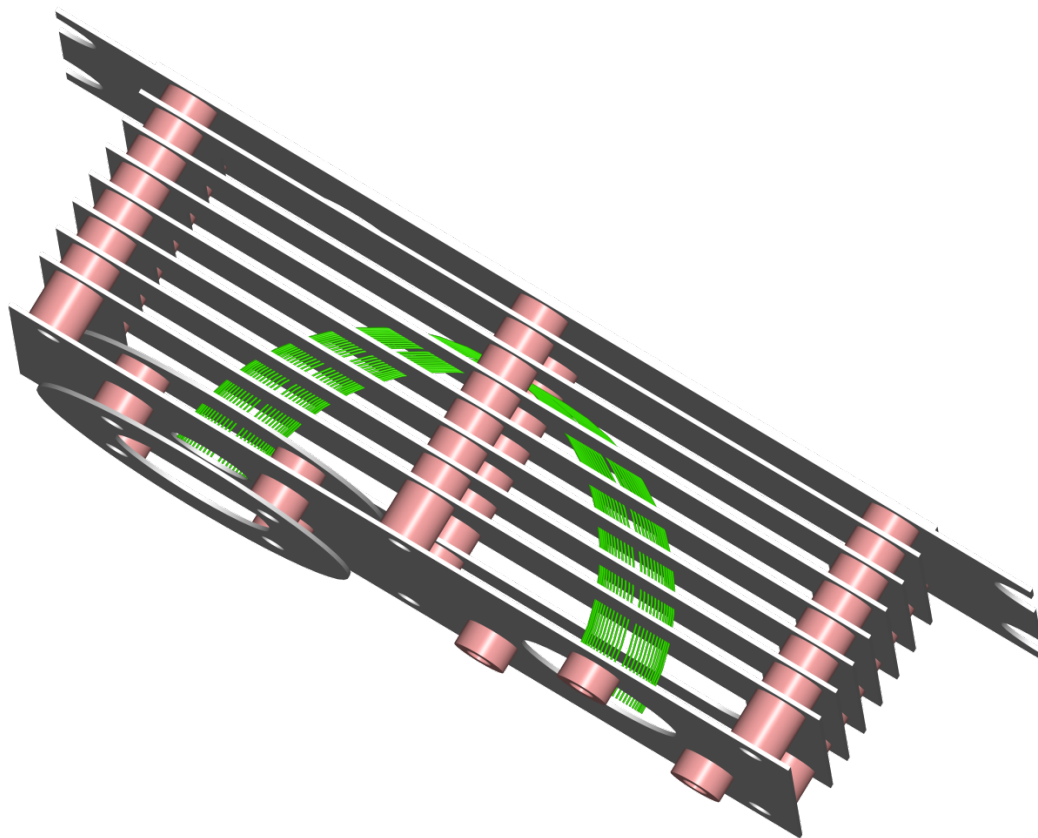


Figure 3.8. Ion time-of-flight spectrometer that employs cross electric and magnetic (CEM) fields.

CHAPTER

4

EXPERIMENTAL

In this chapter, experimental facilities will be briefly described. An overall picture of the experimental setup will be presented for each spectrometer: energy spectrometer, parallel electric/magnetic (PEM) field spectrometer and cross electric/magnetic (CEM) field spectrometer. The design specifications of the two ion time-of-flight spectrometers developed for this study were presented in Chapter [3](#).

4.1 Description of the Experimental Facilities

Neutron depth profiling measurements based on energy spectrometry were performed at the Penn State Radiation Science and Engineering Center (RSEC), Breazeale Nuclear Reactor, University Park, PA. Ion beam measurements with the parallel electric/magnetic (PEM) field spectrometer were performed at IBM T. J. Watson Research Center, Yorktown Heights, NY. Measurements with the cross electric/magnetic field spectrometer were also performed at Penn State RSEC with a ^{210}Po alpha source.

4.1.1 Penn State Radiation Science and Engineering Center, Breazeale Nuclear Reactor

The Radiation Science and Engineering Center (RSEC) at The Pennsylvania State University houses a number of facilities, which includes the Penn State Breazeale Reactor (PSBR), gamma irradiation facilities (in-pool irradiator, dry irradiator and hot cells), and various radiation detection and measurement laboratories. The reactor, which first went critical in 1955, is the nation's longest continuously operating university research reactor. The PSBR is a 1-MW TRIGA Mark III nuclear reactor with moveable core in a 7-m pool with 270,000 l demineralized water. A variety of dry tubes and fixtures are available in or near the core. When the reactor core is moved next to a heavy water tank and the graphite reflector assembly near the beam port locations, a thermal neutron beam becomes available from two of the seven existing beam ports. At steady state operation at 1 MW, the thermal neutron flux is $1 \times 10^{13} \text{ cm}^{-2}\text{s}^{-1}$ at the periphery of the core and $3 \times 10^{13} \text{ cm}^{-2}\text{s}^{-1}$ at the central thimble. The rated power of the reactor in the continuous operation mode is 1 MW. The reactor can be operated at the pulse mode, during which it generates 2000-MW of power and a neutron flux of $6 \times 10^{16} \text{ cm}^{-2}\text{s}^{-1}$ within a period of approximately 10-msec full-width at half maximum (FWHM).

The experiments with the neutrons were performed at the beam port location #4 (BP4). The average thermal neutron flux at the exit of the BP4 is $3 \times 10^7 \text{ cm}^{-2}\text{s}^{-1}$, and the fast neutron flux is $1 \times 10^5 \text{ cm}^{-2}\text{s}^{-1}$. The measured neutron energy spectrum and the theoretical Maxwell-Boltzmann distribution are plotted in Figure 4.1 [116].

The experimental setup for neutron depth profiling measurements consists of a target chamber, the energy or the time of flight spectrometer, and the corresponding measurement electronics. The target chamber is made of aluminum with four beam entrance/exit ports. Two of the ports have thin aluminum windows to allow the entrance of the neutron beam without noticeable attenuation. A turbomolecular pump is mounted horizontally on the bottom section of the chamber, which is backed by a mechanical pump. There are numerous electrical feedthroughs to allow connections to high voltage power supplies and the measurement electronics.

For measurements with neutrons, the vacuum chamber is placed in front of the neutron beam port #4. The beam diameter is 1.5 cm. The beam entrance ports on the target chamber are aligned with the direction of the neutron beam. The sample and the spectrometer are placed inside the chamber. The center point of the sample is aligned with the neutron beam using a laser pointer. A picture of the target chamber in front of the neutron beam port #4 and the measurement electronics is shown in Figure 4.2.

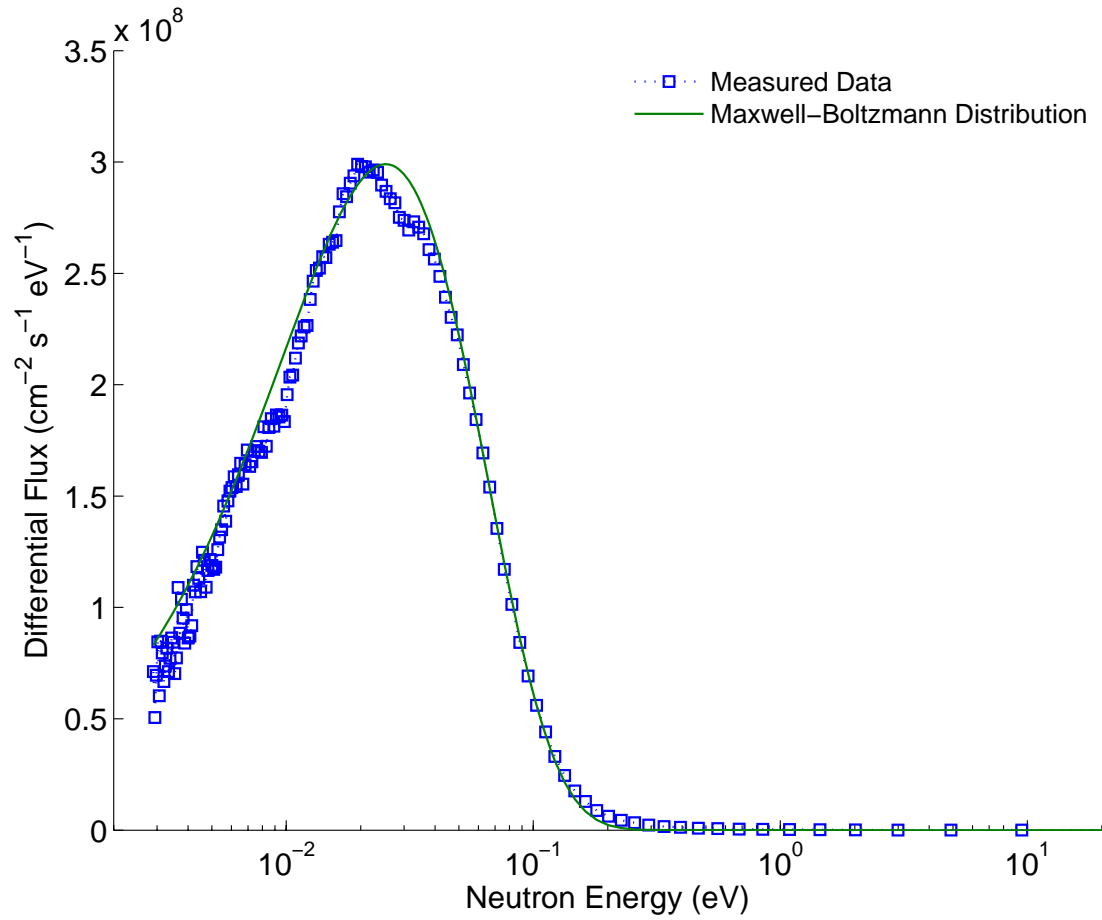


Figure 4.1. Differential neutron flux spectrum at the beam port location #4.



Figure 4.2. The vacuum chamber, beam port BP4 and the measurement electronics in the neutron beam laboratory area.

A simple drawing of the instrumental setup is shown in Figure 4.3. The neutron beam collimator consists of two pieces: The first collimator in the upstream location has 38-*mm* diameter aperture, and the second collimator has 19-*mm* diameter aperture. The vacuum in the target chamber is maintained around 10^{-5} *Pa* during the experiment. When the beam shutter is opened, thermal neutron beam impinges on the sample placed in the target chamber and initiates the prompt (n, p) or (n, α) reactions depending on the isotopes in the sample substrate. A portion of the neutron beam penetrates the sample, sample holder and the back aluminum window, and is stopped by the beam catcher.

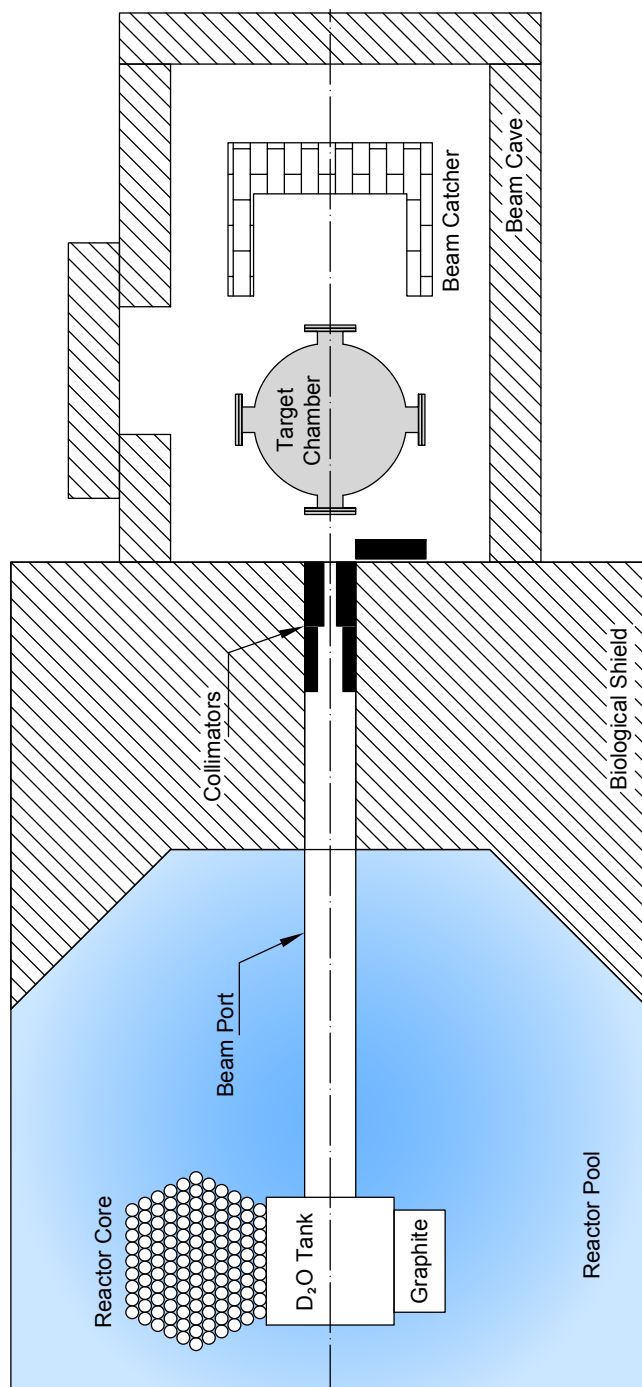


Figure 4.3. Layout of the reactor core, D_2O tank, graphite reflector, concrete wall, target chamber and the beam catcher.

4.1.2 IBM T. J. Watson Research Center, Tandem Linear Accelerator

The parallel electric/magnetic (PEM) field spectrometer was developed partly at IBM T. J. Watson Research Center. The ion beam experiments with the PEM field spectrometer were performed with the linear accelerator at the IBM Tandem Van de Graaff Laboratory. The linear accelerator can produce highly-stable, very narrow-width energy particle beams at high currents, which was quite useful in the spectrometer development. The particle beam current and energy are easily reproducible, hence the accelerator can be used for calibration as well as for the comparison of different operating conditions.

The particle accelerator at the IBM T. J. Watson Research Center, Yorktown Heights, NY is an NEC 3-MV tandem accelerator. The tandem accelerator works on the principle that the negatively charged ion gains energy by attraction to the high positive potential at the geometric center of the pressure vessel. The ion source used for the generation of alpha particles is called alphasource. The alphasource is an RF source, which uses rubidium for charge exchange. The ion emerges from the source at the charge state of -1 . At this charge state, the ion is electrostatically attracted to the positive potential terminal, where it is stripped of some of its electrons by passing through N_2 gas. The ion then becomes positively charged and is accelerated away by the high positive potential.

The ion time-of-flight measurements were performed in the target chamber used for the soft error rate (SER) experiments. The target chamber is made of stainless steel, and ultra-high vacuum (UHV) capable.

The plot of the energy spectra of the alpha beam acquired at different operating conditions is shown in Figure 4.4. The spectra are collected with a surface barrier detector. The detector is located upstream of the beam, and is fixed on a moving arm. The front face of the detector has a tantalum cover disk with a 0.5-mm aperture. Tantalum is a commonly used material in ion beam experiments because of its high Q value for (α, n) reactions.

The particle accelerator provides very high particle flux concentrated in a small area. Since microchannel plates were used for particle detection, the particle rate was reduced to prevent excessive burnout of the emissive coating on the plates.

The particle rate is measured by a number of Faraday cups located upstream. When switched, the cups integrate the charge deposited by the ions. The integrated charge can be read by an electrometer, from which the particle current can be found. The particle current and particle rate are correlated by

$$\varphi = \frac{i}{qe_0} \quad (4.1)$$

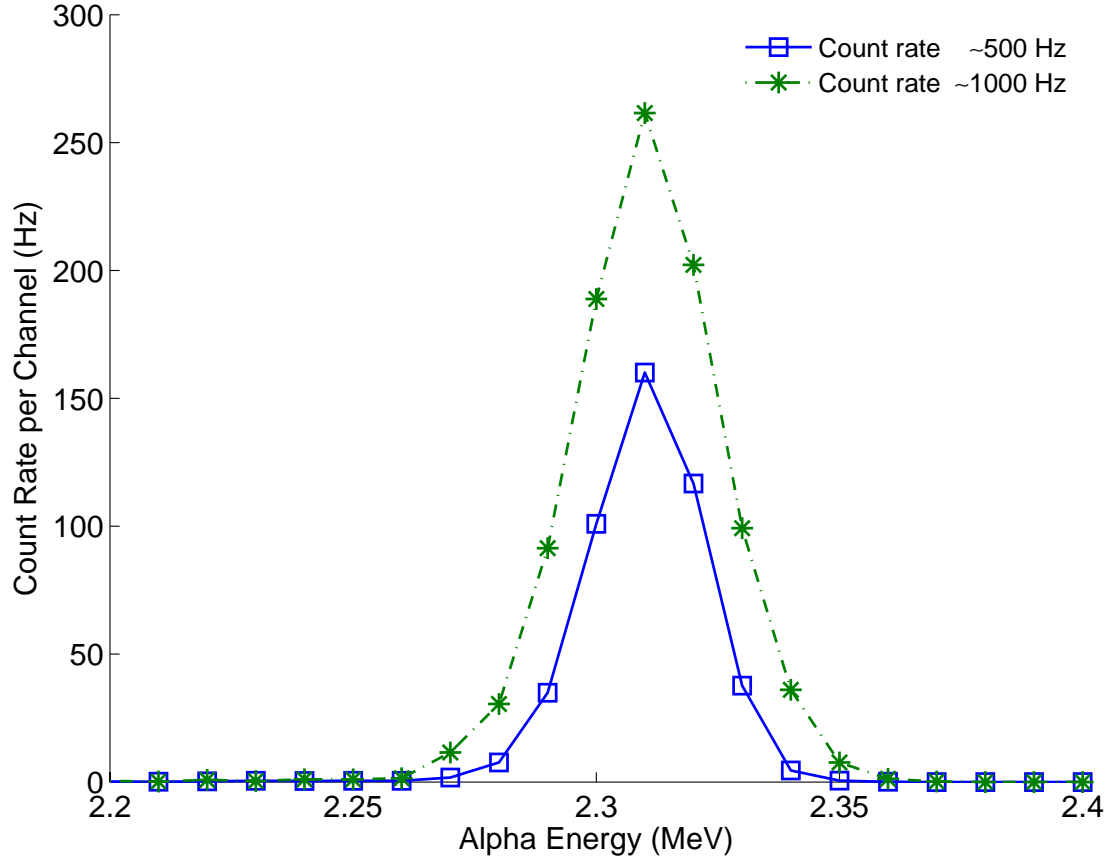


Figure 4.4. Alpha energy spectra obtained with a surface barrier detector measured at IBM T. J. Watson Research Center.

where i is the current measured by the Faraday cup, q is the charge state of the ion, and e_0 is the unit electrical charge.

4.2 Neutron Depth Profiling by Energy Spectrometry

A series of neutron depth profiling measurements were done at the Radiation Science and Engineering Center at Penn State. A brief description of the experimental setup will be given followed by the presentation of the measurements.

4.2.1 Description of the Experimental Setup

The experimental setup for the neutron depth profiling based on energy measurement includes a target chamber, a particle detector and the measurement electronics. The

sample is placed in front of the neutron beam at an angle. A charged particle detector, such as a surface barrier detector (SBD), is placed perpendicular to the surface normal of the sample.

4.2.2 Measurement Electronics

Block diagram representation of the measurement electronics used for the neutron depth profiling by energy spectroscopy is shown in Figure 4.5.

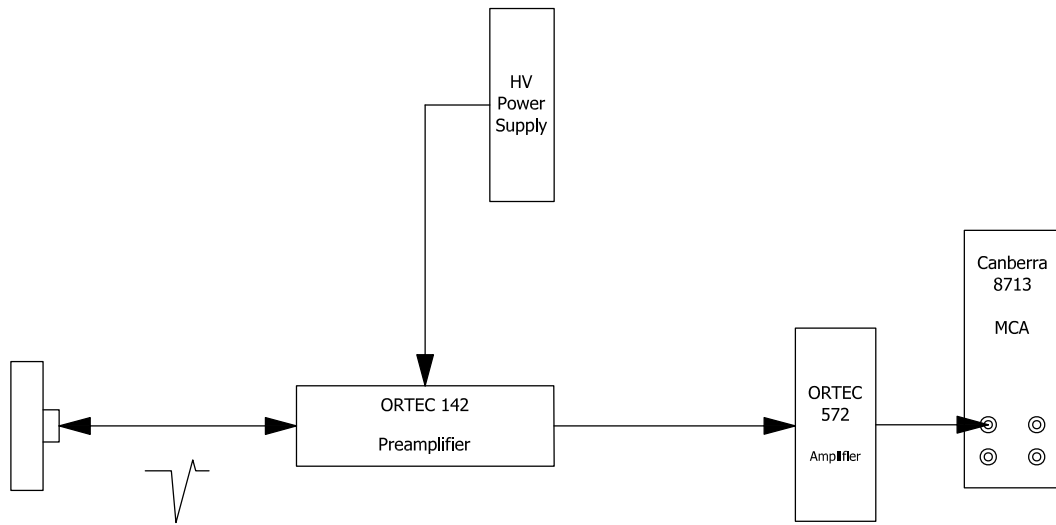


Figure 4.5. Block diagram of the measurement electronics used in neutron depth profiling by energy spectroscopy.

A number of detector types were used for the detection of charged particles, including silicon surface barrier detector (SBD), passivated implanted planar silicon (PIPS) detector, and silicon PIN photodiodes. The best spectral response was obtained with the Hamamatsu S3590-09 PIN photodiode. The S3590 employs a $10 \times 10 \text{ mm}^2$ active area with a depletion layer thickness of 0.3 mm . The specifications of the Hamamatsu S3590-09 PIN photodiode are presented in Table 4.1.

The ORTEC 142A was used as the charge preamplifier. The capacitance value of the PIN photodiode matches the preamplifier accepted capacitance at the input line. The preamplifier introduces $1.60\text{-}3.40 \text{ keV}$ (silicon equivalent) noise marginally to the input signal. The extended performance specifications are provided in Table 4.2.

The ORTEC 572 amplifier is suited for silicon charged particle detectors. It includes

Table 4.1. Performance specifications of the Hamamatsu S3590-09 PIN photodiode as given by the manufacturer

Parameter	Specification
Active Area	$10\text{ mm} \times 10\text{ mm}$
Depletion Thickness	0.3 mm
Maximum Reverse Voltage	100 V
Power Dissipation	100 mW
Operating Temperature	$-20\text{ to }+60\text{ }^{\circ}\text{C}$
Dark Current	$\sim 2 - 6\text{ nA}$

an automatic gated baseline restorer and a built-in pile-up rejector to provide stable performance over a wide dynamic range. The gain is continuously adjustable from 1 to 1500. A detailed listing of the performance specifications is given in Table 4.3.

Canberra Model 8713 ADC is a fixed dead time analog-to-digital converter for high count rate nuclear spectroscopy. The Model 8713 interfaces with a multi-channel analyzer (MCA) through a 34-pin ribbon cable connector. The performance specifications of the 8713 ADC is given in Table 4.4.

Table 4.2. Performance specifications of the ORTEC 142A preamplifier as given by the manufacturer

Parameter	Specification
Maximum Noise (Si equivalent)	1.60 keV at 0 pF ; 3.40 keV at 100 pF
Integral Nonlinearity	$\leq 0.03\%$, $0\text{ to } \pm 7\text{ V}$ at $\infty\text{ }\Omega$ or $\pm 3.5\text{ V}$ at $93\text{ }\Omega$
Temperature Instability	$< \pm 50\text{ ppm}/^{\circ}\text{C}$ from $0\text{ to }50\text{ }^{\circ}\text{C}$
Open Loop Gain	$> 40,000$
Charge Sensitivity	Nominally 45 mV/MeV
Energy Range	$0\text{-}200\text{ MeV}$
Rise Time	$< 100\text{ ns}$ at 100 pF
Decay Time	Nominally $500\text{ }\mu\text{s}$
Detector Bias Voltage	$\pm 1000\text{ V}$ maximum

Table 4.3. Performance specifications of the ORTEC 572 spectroscopy amplifier as given by the manufacturer

Parameter	Specification
Gain Range	Continuously adjustable from 1 to 1500
Pulse Shape	Semi-Gaussian on all ranges
Integral Nonlinearity	For 2- μs shaping time, $< \pm 0.05\%$
Noise	$< 5 \mu V$ for unipolar output with 2- μs shaping time at 100 gain
Temperature Instability	Gain $\leq \pm 0.0075\%/^{\circ}C$, 0 to 50 $^{\circ}C$
Spectrum Broadening	$< 16\%$ FWHM for ^{60}Co 1.33 MeV gamma line at 85% of full scale
Spectrum Shift	$< 0.024\%$ for ^{60}Co 1.33 MeV gamma line at 85% of full scale

Table 4.4. Performance specifications of the Canberra 8713 ADC analog-to-digital converter as given by the manufacturer

Parameter	Specification
Integral Nonlinearity	$< \pm 0.025\%$ of full scale over the top 99.5% of selected range
Differential Nonlinearity	$< \pm 0.0\%$ of range including effects from integral nonlinearity
Gain Drift	$< \pm 0.005\%$ of full scale/ $^{\circ}C$
Zero Drift	$< \pm 0.005\%$ of full scale/ $^{\circ}C$
Long Term Drift	$< \pm 0.005\%$ of full scale/24 hours at a constant temperature
ADC Dead Time	Linear Gate Time + 1.4 μs

4.3 Ion Time-of-Flight Spectrometry

4.3.1 Description of the Experimental Setup

The time-of-flight neutron depth profiling experimental setup used in the measurements includes a start detector -also called time-zero detector, a stop detector, a conductive thin foil for electron generation, electron optical device to separate the electron beam from the ion beam, and the measurement electronics. The assembly of the thin foil, electron optical device and the electron detector is also referred to as the time-zero telescope since it involves having measurements in more than one point.

Electron generation methods were introduced previously in Section 2.5. The main function of the electron transport system is to separate the electrons and the ions. This

can be done electrostatically, magnetically, or through a combination of the two.

The electrons can be detected either by an electron multiplier such as channeltron or microchannel plates. The microchannel plate assemblies are chosen as the electron detectors in this study.

As in the case of the neutron depth profiling by energy measurement, the ion time-of-flight spectrometer is placed inside a target chamber operating under high-vacuum conditions. A better vacuum condition is essential for time-of-flight spectrometers not only to minimize scattering during the ion flight but also to guarantee proper operation of microchannel plates. Microchannel plates are discrete electron multiplier units made of glass channels of a few-micron diameter bundled together in a geometry of 20 to 40-*mm* diameter and 1/2 to 1-*mm* thick. Each microchannel plate operates at around 1-*kV* voltage drop per *mm* thickness. Since the thickness of the device is small, this drop corresponds to a significantly high electric field, which is the driving force for the cascade multiplication along the micro-sized channels. If proper vacuum level is not established in the environment, the output of the microchannel plates becomes extremely noisy from ambient ions in chamber. The chamber pressure must be kept below 1 *mPa* for proper microchannel plate operation, and is recommended to be operated below 10^{-4} *Pa* for better performance.

The start telescope incorporates a secondary electron generating medium in the entrance side of the spectrometer. The medium is expected to cause minimal distortion in the velocity of the ion. The ion then continues on its straight path, exits the start telescope and hits the stop detector.

4.3.2 Measurement Electronics

The block diagram of the measurement electronics is shown in Figure 4.6. The fast time pulses from the microchannel plates are picked by the *time pickoff* circuit, and fed into the Ortec 9327 1-GHz Preamplifier and Timing Discriminator. The microchannel plate time pickoff circuit is shown in Figure 4.7.

The Ortec 9327 is optimized for *mV*-level pulses. The timing discriminator uses a zero-crossing technique that processes pulse widths from 250 *ps* to 5 *ns* to minimize timing jitter and walk as a function of pulse amplitude [117]. The shift in the timing output (walk) as a function of pulse amplitude is typically less than ± 40 *ps* over the top 90% of full scale when employing a 300-*ps* input pulse width. The full listing of performance specifications for the Ortec 9327 timing discriminator is given in Table 4.5.

The dynamic response of the Ortec 9327 unit is shown in Figure 4.8. The AMP INP

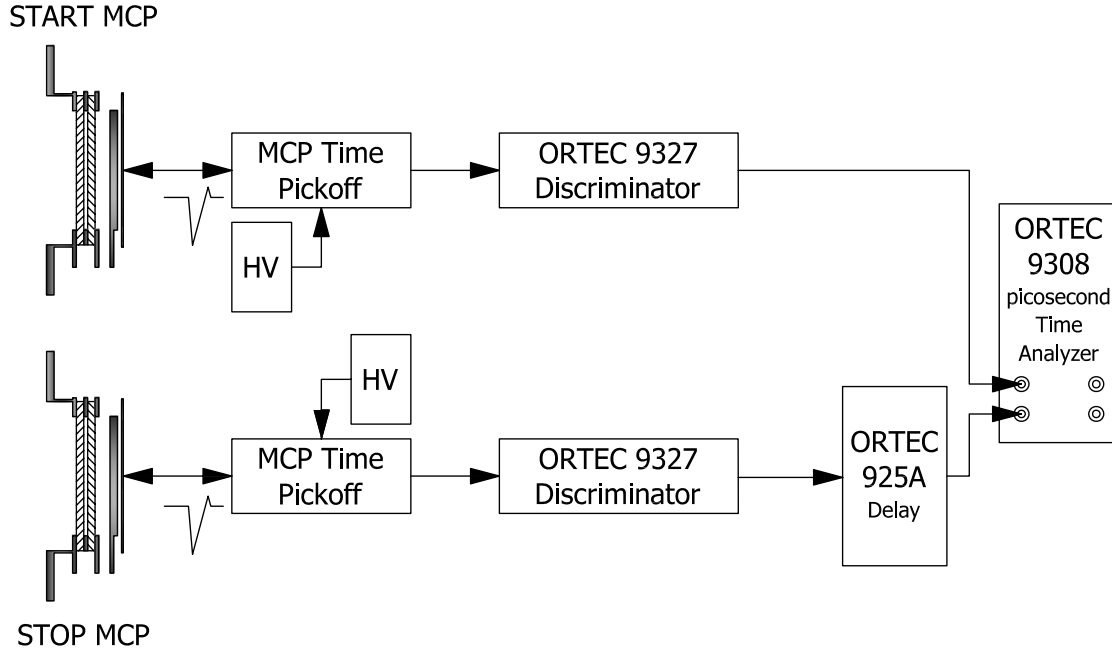


Figure 4.6. Electronics used in the ion time-of-flight spectrometry measurements.

line is the input to the unit generated by Stanford Research Systems DG535 Digital Delay/Pulse Generator. The AMP OUT line is the output of the built-in preamplifier of the Ortec 9327 unit. The NIM OUT line is the 800- mV nominal NIM output pulse that drives the Ortec 9308 picosecond Time Analyzer. The performance specifications of the Ortec 9308 picosecond Time Analyzer are given in Table 4.6.

Table 4.5. Performance specifications of the ORTEC 9327 1-GHz Preamplifier and Timing Discriminator as given by the manufacturer

Parameter	Specification
Input Range	0 to -30 mV full scale or 0 to -150 mV full scale
Equivalent Input Noise	$< 100\text{ }\mu\text{V}$ RMS on the 0 to -30 mV scale
Time Slewing (Walk)	$< \pm 40\text{ ps}$ shift in the timing output
Timing Jitter	$< 20\text{ ps}$ FWHM for a pulse amplitude at 50% of full scale
Pulse-Pair Resolution	$< 10\text{ ns}$ at the fast-negative NIM outputs
Temperature Range	$0 - 50\text{ }^{\circ}\text{C}$
Temperature Sensitivity	$< \pm 10\text{ ps}/^{\circ}\text{C}$ from 0 to $50\text{ }^{\circ}\text{C}$

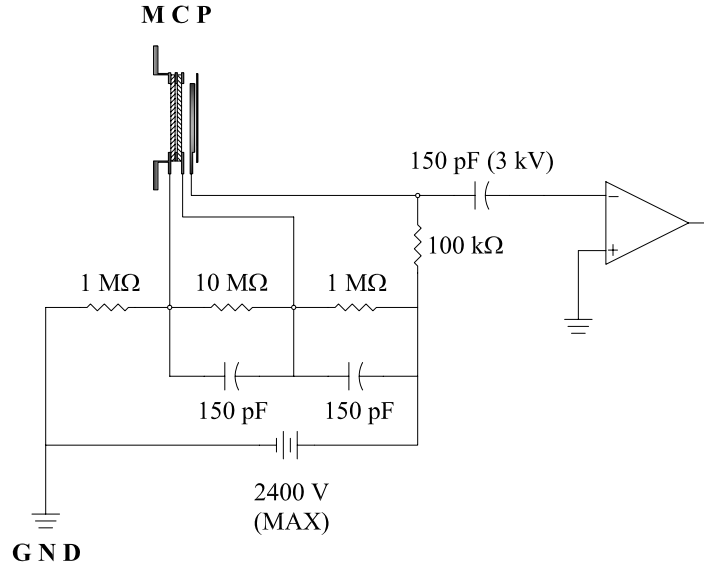


Figure 4.7. Microchannel plate time pick-off circuit.

An overall instrument response function was obtained by applying a wide range of input signals. The signal was generated by Agilent Technologies 81130A 400/660 MHz Pulse/Data Generator. The signal width was varied to from 400 *ps* to 10 *ns*. Also varied was the time delay generated by the Ortec Model 425A Nanosecond Delay. Time delay values of 50, 51 and 60 *ns* were applied and the corresponding spectral shift was measured. It was found that the measured delay was different for the same switch value on the Ortec 425A unit. This deviation was attributed to various drift mechanisms. The effect of such variations will be presented in the subsequent sections.

Table 4.6. Performance specifications of the ORTEC 9308 picosecond Time Analyzer as given by the manufacturer

Parameter	Specification
Pulse-Pair Resolving Time	$< 50 \text{ ns}$
Maximum Event Rates	Maximum burst: 200 <i>MHz</i> ; Average rate: 20 <i>MHz</i>
End-of-Pass Dead Time	$< 1 \mu\text{s}$
Timing Jitter	$\text{FWHM} < 25 \text{ ps} + 1 \text{ ppm}$
Absolute Time Accuracy	within 5 <i>ns</i> + 100 <i>ppm</i>
Differential Nonlinearity	within $\pm 0.2 \text{ ps}$ or $\pm 2\%$ of the bin width
Temperature Range	0 to 50°C

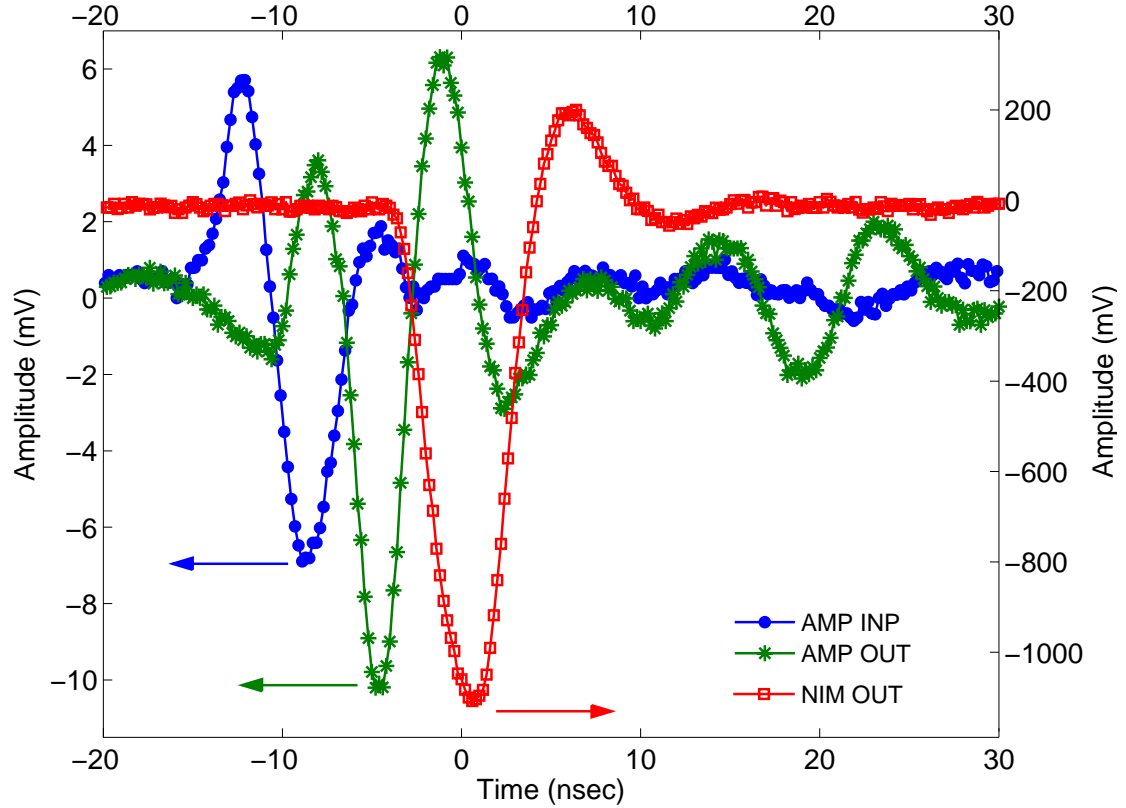


Figure 4.8. The response of the Ortec 9327 1-GHz Preamplifier and Timing Discriminator to 2-*ns* width input pulses (AMP-INP) generated by a precision oscillator.

Effect of Input Signal Width

Input signals with half widths 400, 500 *ps*, 1, 2, 3, 4, 5 and 10 *ns* were sent to the Ortec 9327 timing discriminator unit. The data is plotted in Figure 4.9. The delay value on the Ortec 425A unit was set to 50 *ns*. The pulse frequency was set 1 *MHz*, and each signal was counted for 10 *s*, which totaled to 10^7 counts. Only the signal with 400-*ps* half width exhibited loss of count, and yielded a total of 8366012 counts, which accounts for approximately 17% loss. Although the manufacturer specifications [117] claim that the unit was optimized to operate with input pulses varying between 250 *ps* to 5 *ns*, it was observed that the input signals with half widths below 500 *ps* are not counted effectively.

It is seen that the centroid location of the peaks move as the input signal width varies. The centroid location corresponds to the time offset that results either from the Ortec 425A nanosecond delay, the Ortec 9308 picosecond time analyzer, or both.

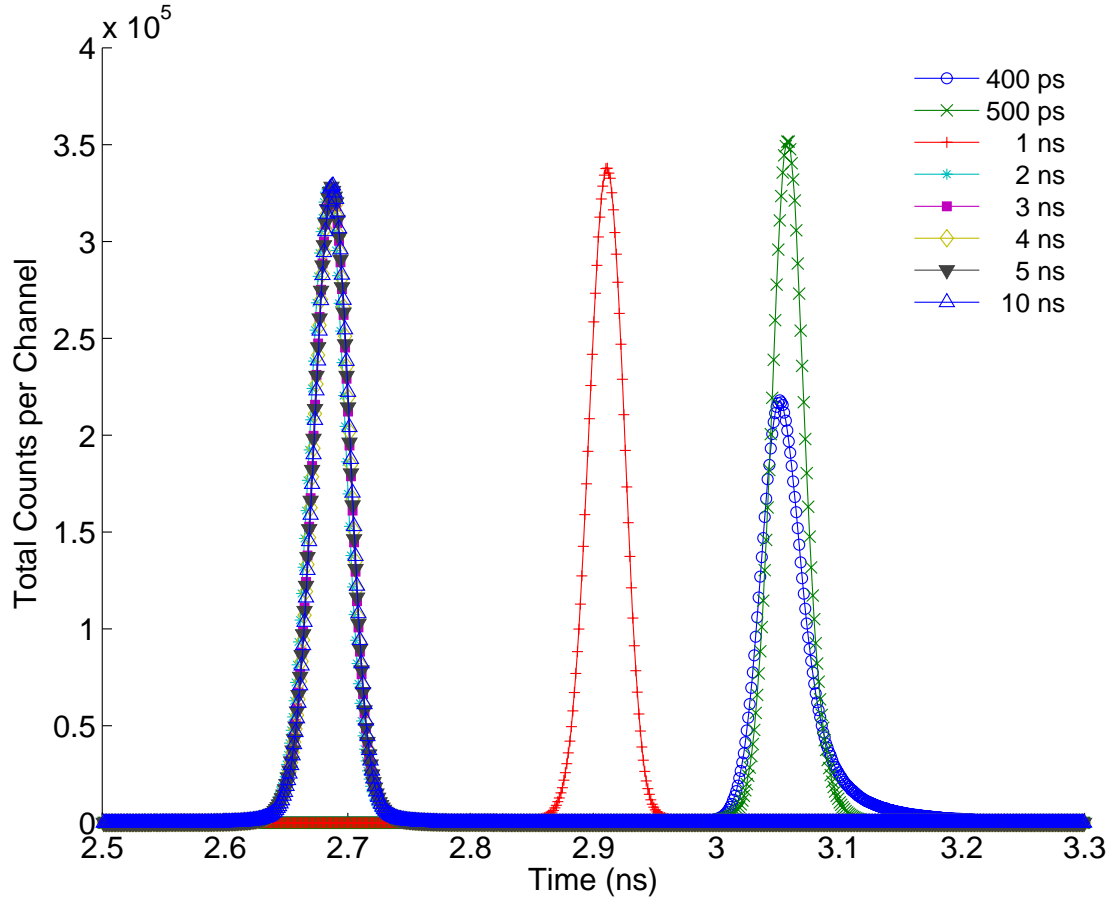


Figure 4.9. Measured uncertainties at various input signal widths.

Also observable in the figure is that the unit best performs for signals with half widths 2 ns and above. There is considerable shift in centroid location for signals with less than 2-ns widths. This specification must be taken into account when designing a fast microchannel plate assembly to take advantage of the full bandwidth of the device.

The variation of the standard deviation of registered spectra is plotted in Figure 4.10. The signal with 400-ps half width yielded the highest standard deviation of 16.53 ps , whereas the input signals with over 2-ns half-width yielded a standard deviation of $\sim 14.5\text{ ps}$.

Time Drift

Multiple spectral measurements were taken for signals with half widths 1 ns and 2 ns with 50-ns delay. The acquired spectra are shown in Figure 4.11. The measurements

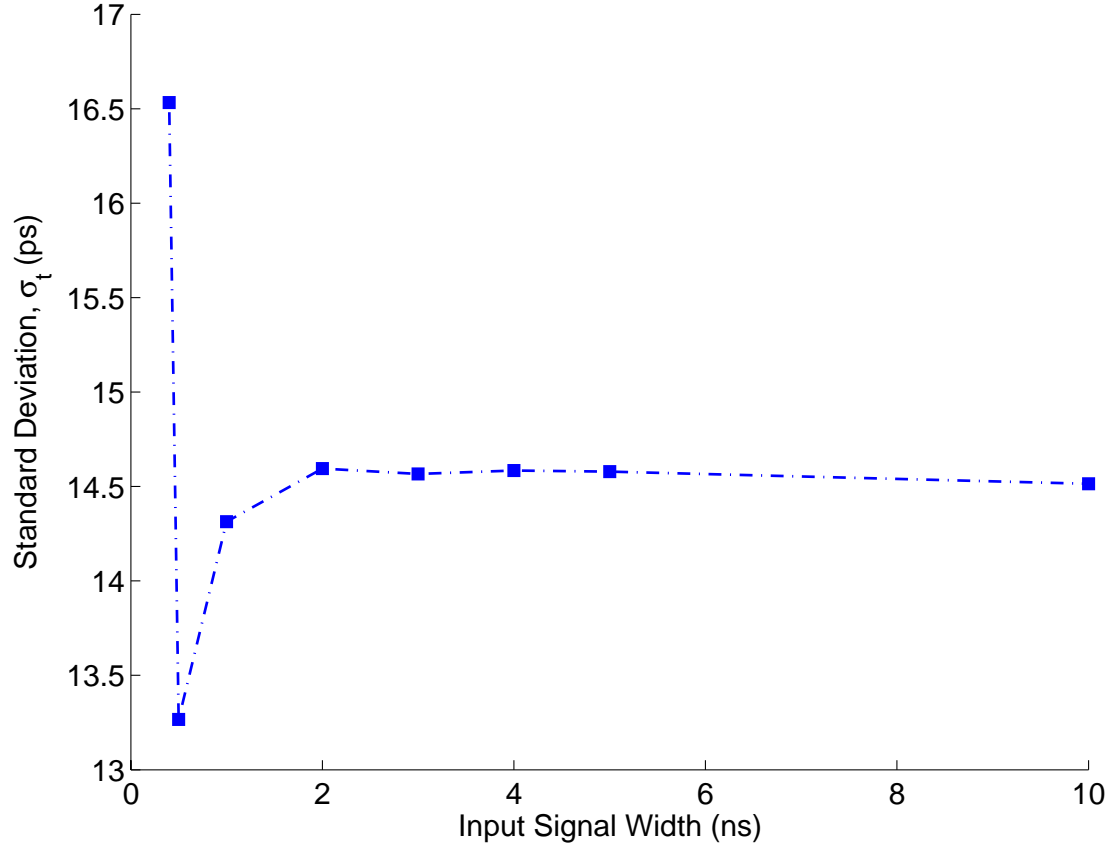


Figure 4.10. Uncertainty variation with respect to input signal width.

were taken immediately after the device was turned on, after 30 minutes, and after 60 minutes. Each peaks had integrated area of 10^7 counts.

The centroid locations are 2.910, 2.897 and 2.878 *ns*, respectively for measurements taken immediately, after 30 minutes, and after 60 minutes. An improvement in standard deviation was observed as the device operated for longer periods: 14.3, 13.9, and 13.0 *ps*, respectively. This indicates that as the device reaches thermal equilibrium, the device performance also improves. Therefore, it is best to allow the measurement electronics to reach a steady state in the ambient for a period of time before the actual measurement is to be taken. It should be noted, however, that this analysis does not designate a discrete component to be responsible for the shift, but rather the whole system.

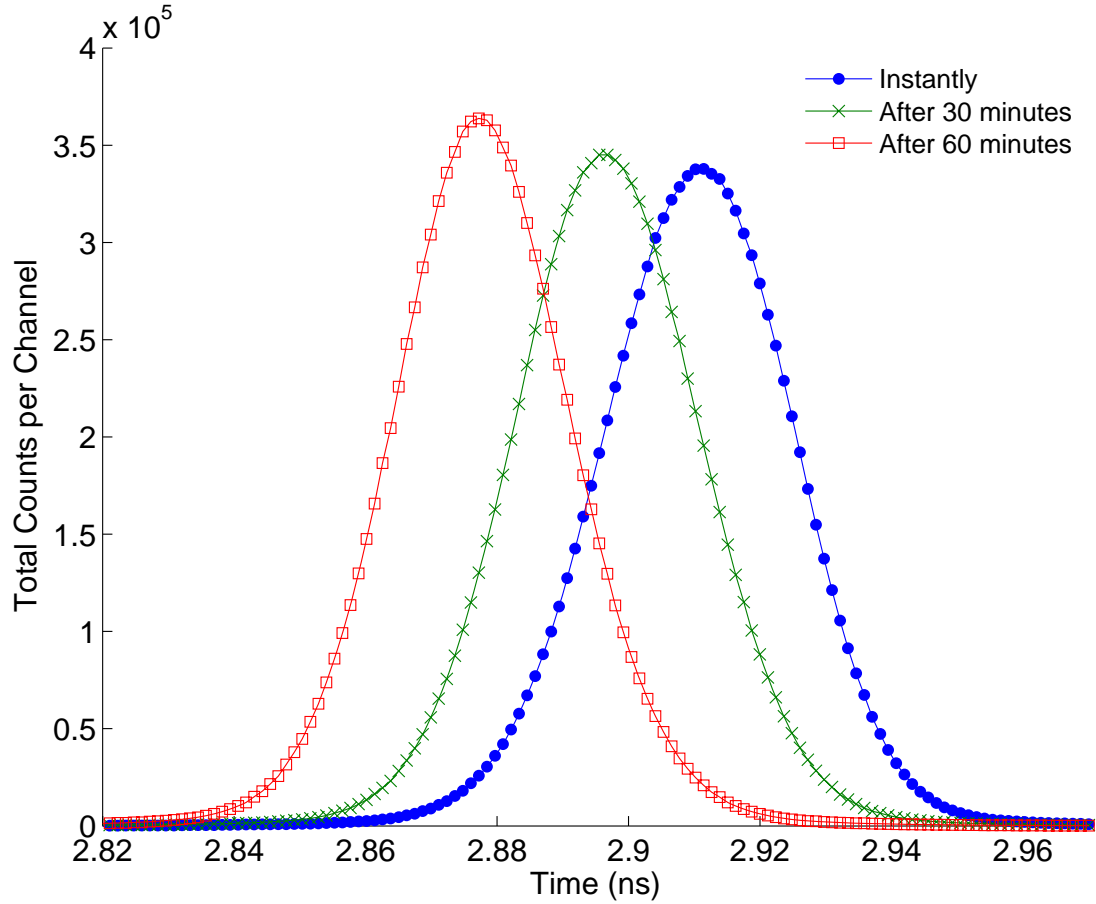


Figure 4.11. The effect of the length of the device operation on 50-*ns* delay for the same input signal.

Effect of Delay

Input signals of equal half widths were delayed by 50, 51, and 60 *ns*. The spectra are shown in Figure 4.12. Although the delay was changed by 1 *ns* and 10 *ns*, respectively, the spectral shift was found to deviate from the corresponding switch values. The centroid locations were calculated as 2.910 *ns*, 3.862 *ns*, and 12.878 *ns*, which correspond to a shift of 0.952 *ns* and 9.957 *ns*, respectively.

Repeated measurements of the delay variation from 50 *ns* to 51 *ns* consistently yielded the same spectral shift of 0.952 *ns*. From the measurements, accuracy in spectral shift was found to be within 1% of the corresponding change in delay value. The manufacturer's specification gives a delay accuracy of ± 100 *ps* or $\pm 1\%$ for each delay section, whichever is larger [117], which are consistent with the measurements.

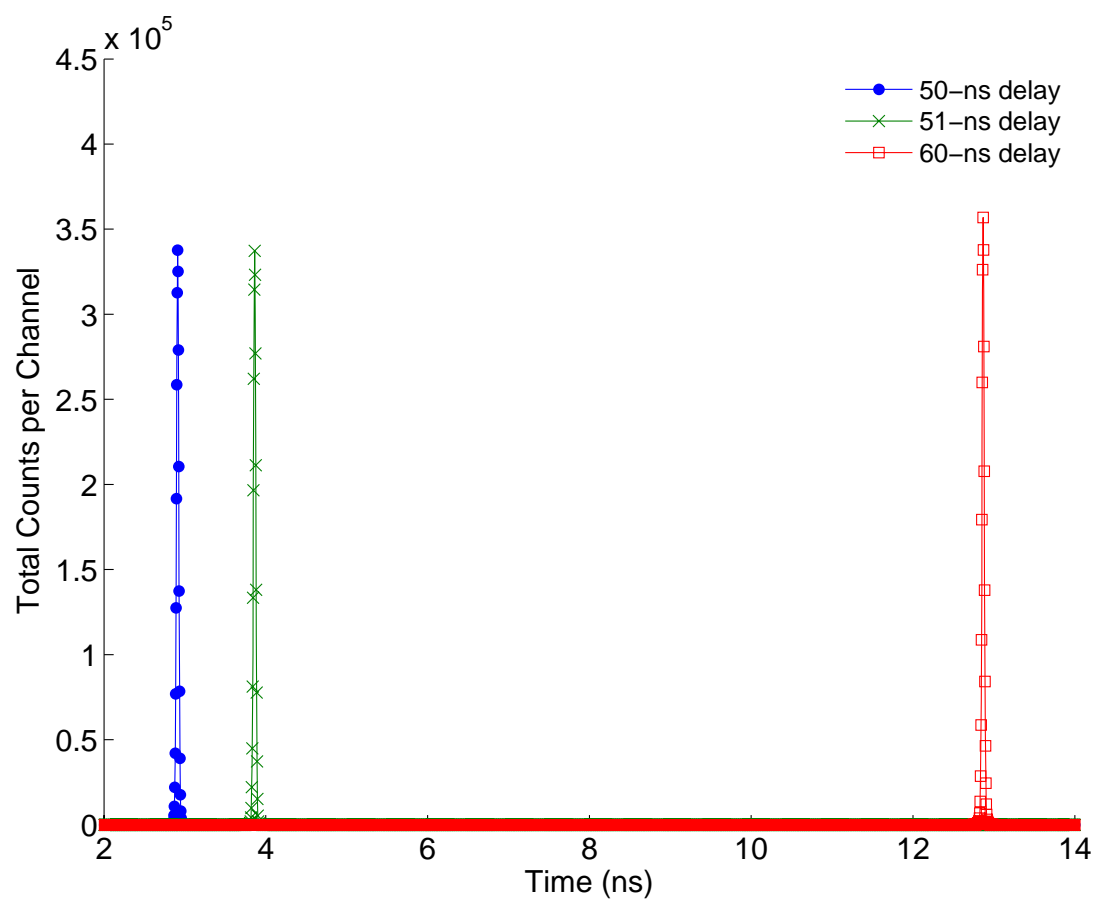


Figure 4.12. Measured time offset at various delay values.

CHAPTER

5

RESULTS AND DISCUSSION

Experimental measurements are presented in the following sections. Section 5.1 presents the measured data of two different samples obtained with neutron depth profiling based on energy spectrometry. Sections 5.2 and 5.3 present the data obtained with the ion time-of-flight spectrometers developed in this study. The experimental data is analyzed in each dedicated section.

5.1 Neutron Depth Profiling based on Energy Measurements

Neutron depth profiling measurements were taken for an Intel SEA2 borophosphosilicate glass (BPSG) calibrated sample, and an AMD 120-keV *B* implanted silicon wafer.

The measurements were made at the Breazeale Nuclear Reactor using the beam port #4. Each measurement was repeated with a silicon surface barrier detector (SBD), PIPS detector, and silicon PIN photodiode. The best spectral response in terms of peak height-to-noise area ratio was obtained with the PIN photodiode. Therefore, the experimental data acquired with the PIN photodiode is presented in this section.

The measured spectra showed significant gamma content at lower energies. The gamma component of the beam at the Penn State Breazeale Reactor BP#4 was known

prior to the experiment. In order to reduce the gamma flux, the collimator was completely covered with a lead plug, which also resulted in significant reduction in neutron flux. A polyethylene slab was placed behind the samples to recover the loss. Polyethylene is a hydrogen-rich medium, which provides a highly scattering environment for neutrons. As a result, a portion of the neutrons are scattered back to the sample and increase the reaction rate in the measured volume. Reaction rate improvements close to 80% were obtained. More details on reaction rate improvement by scattering media can be found in Downing et al [118].

5.1.1 Intel SEA2 Borophosphosilicate Glass Sample

The sample is a borophosphosilicate glass film of known boron dose, i.e. number of atoms per unit area, on silicon substrate. An energy spectrum of the sample was obtained. The data is shown in Figure 5.1. The instrumental resolution was measured to be $\sigma_E = 9.12 \text{ keV}$ using the pulser peak.

The alpha continua starting at 1472.1 keV and 1776.2 keV can be seen well-resolved. However, the two expected lithium continua are indistinguishable from the background radiation and the electronic noise. The gamma component of the beam is seen in the lower-energy side of the spectrum. The background can be subtracted from the raw data by using the leading and trailing edges of the two alpha peaks. Figure 5.2 shows the detail of the first and the second alpha peaks. The ratio of the total counts of the first and the second peaks is calculated to be ~ 14 , which is close to the actual value $94/6 \approx 15.7$ as shown in Equation (2.71). The difference is considered to have resulted from the approximate fitting of the background.

A depth profiling calculation was performed using the first alpha peak. The depth of the reaction site corresponding to each bin in the spectrum was calculated using Equation (2.21). Since the total boron dose of the sample was known, local concentration values were calculated using Equation (2.32). The concentration profile versus substrate depth is shown in Figure 5.3. The layer thickness was calculated as 883.7 nm from the half-width of the continuum.

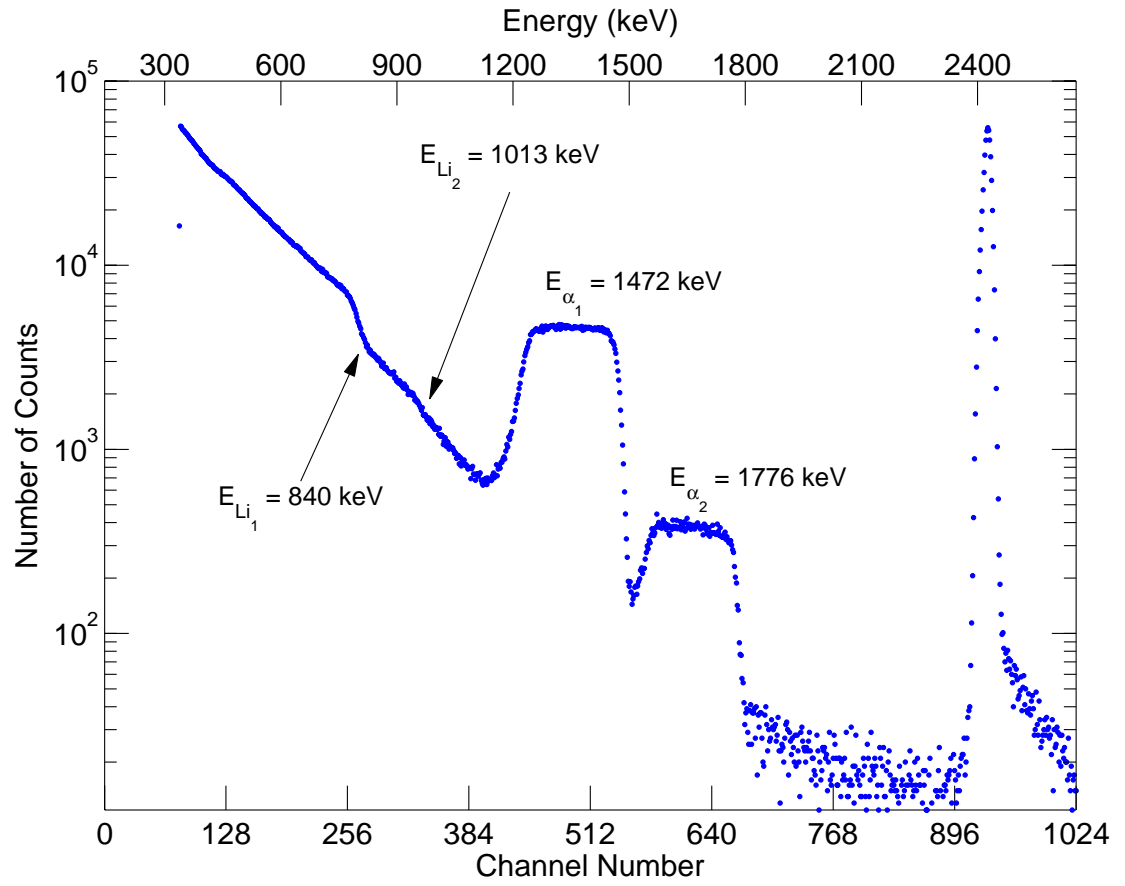


Figure 5.1. Ion energy spectrum of Intel SEA2 borophosphosilicate glass sample obtained with a silicon PIN photodiode.

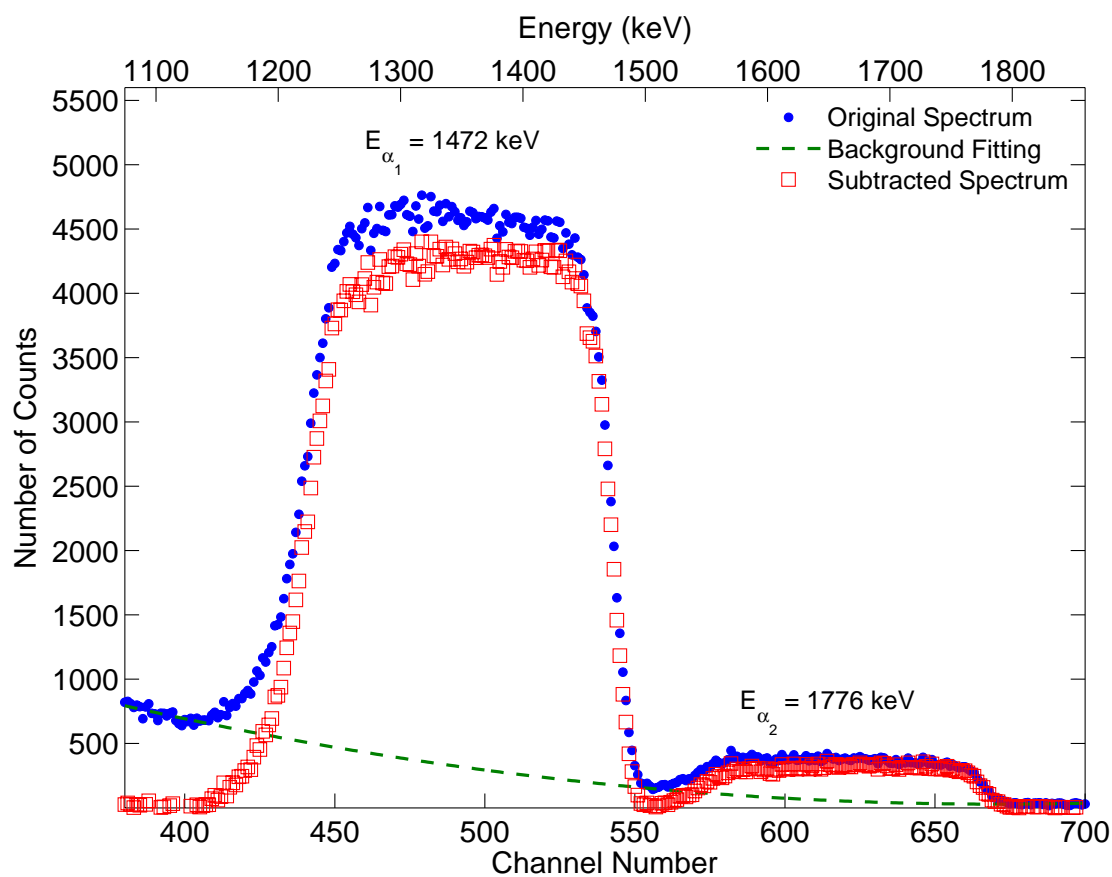


Figure 5.2. Detail from Figure 5.1 showing the two alpha peaks from the $^{10}\text{B}(n, \alpha)^7\text{Li}$ reaction.

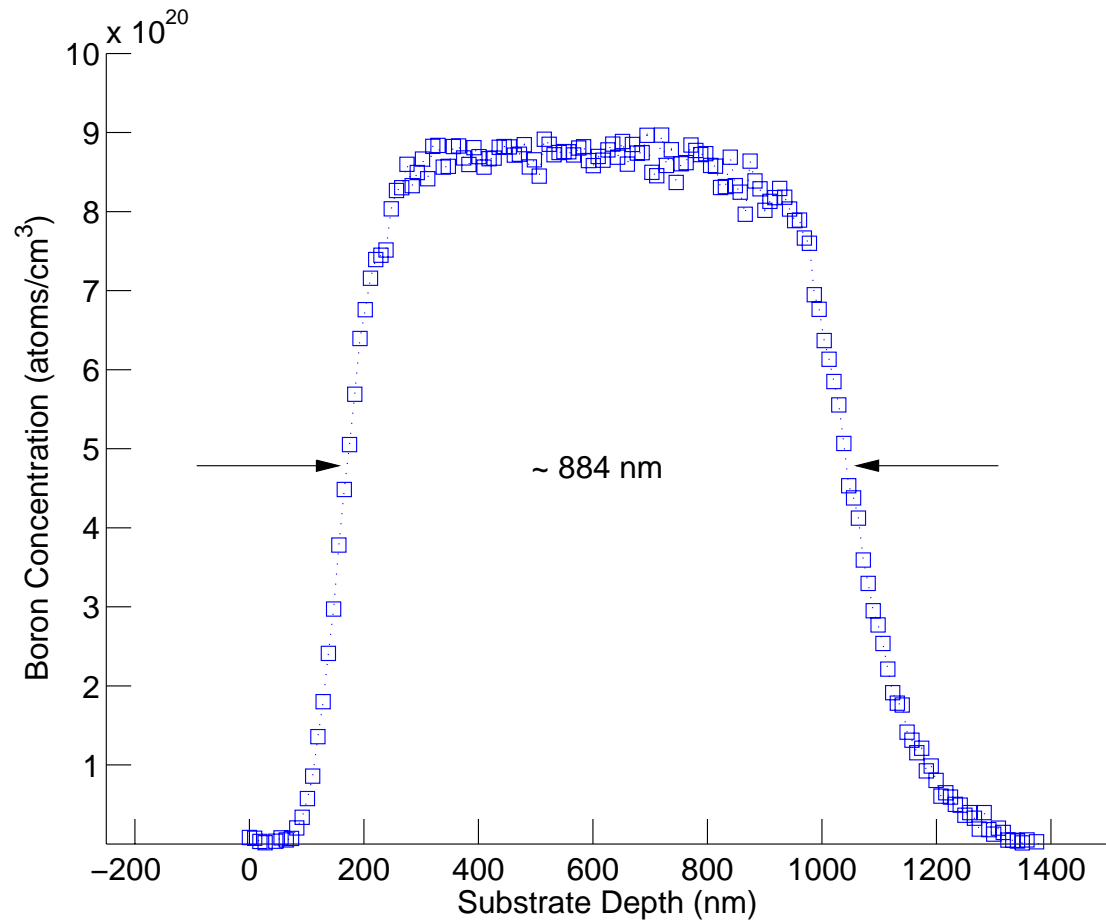


Figure 5.3. Boron concentration profile versus depth in borophosphosilicate glass calculated from the 1471.9-keV alpha spectrum in Figure 5.2.

5.1.2 AMD 120-keV Boron Implanted Silicon Wafer

A particle energy spectrum is obtained with the AMD 120-*keV* boron implanted silicon wafer. The raw data is shown in Figure 5.4. The instrumental resolution was calculated to be $\sigma_E = 14.8 \text{ keV}$ using the pulser peak. Degradation in the instrumental resolution despite similar experimental conditions was attributed to the AC power noise.

The gamma background is quite high in this spectrum, as was the case in the previous measurement. Therefore, the lithium peaks are not distinguishable. The detail of the alpha peaks is shown in Figure 5.5. The ratio of the total counts of the first and the second peaks is calculated to be ~ 17.6 , somewhat higher from what was calculated for the Intel SEA2 borophosphosilicate glass sample.

The boron depth profile was calculated by using the data from the first alpha peak. The calculated profile is shown in Figure 5.6. Also shown in the figure is the TRIM simulation for the 120-*keV* implantation into silicon. The simulated and the measured ranges, i.e. the first moment, of the distributions match within 0.1%. Range straggling of the two distributions, on the other hand, differ drastically. The differences in broadening, i.e. the standard deviations of the distributions, is a result of instrumental noise. Each energy bin corresponding to a discrete depth interval suffers from spreading mechanisms, which results in a broader distribution.

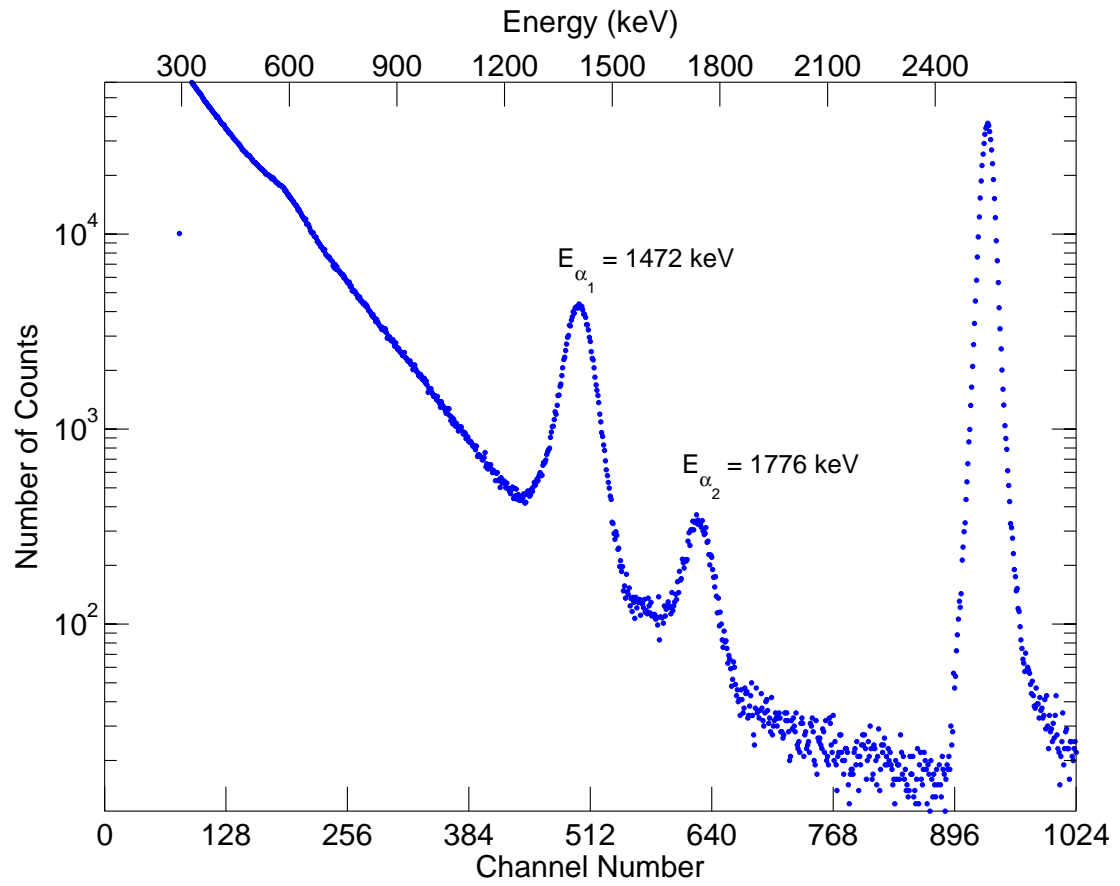


Figure 5.4. Ion energy spectrum from the measurement of AMD 120-keV boron implanted silicon wafer.

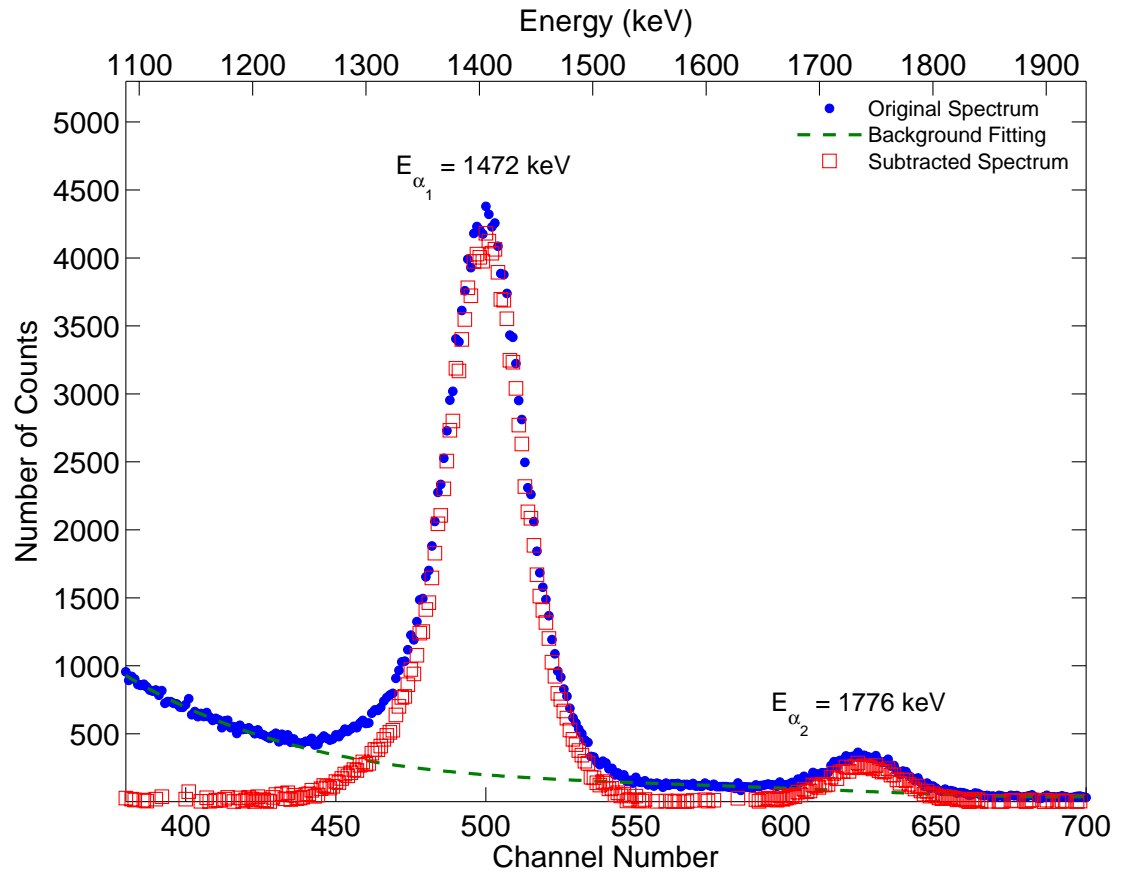


Figure 5.5. Detail from Figure 5.4 showing the alpha peaks from the $^{10}\text{B}(n, \alpha)^7\text{Li}$ reaction.

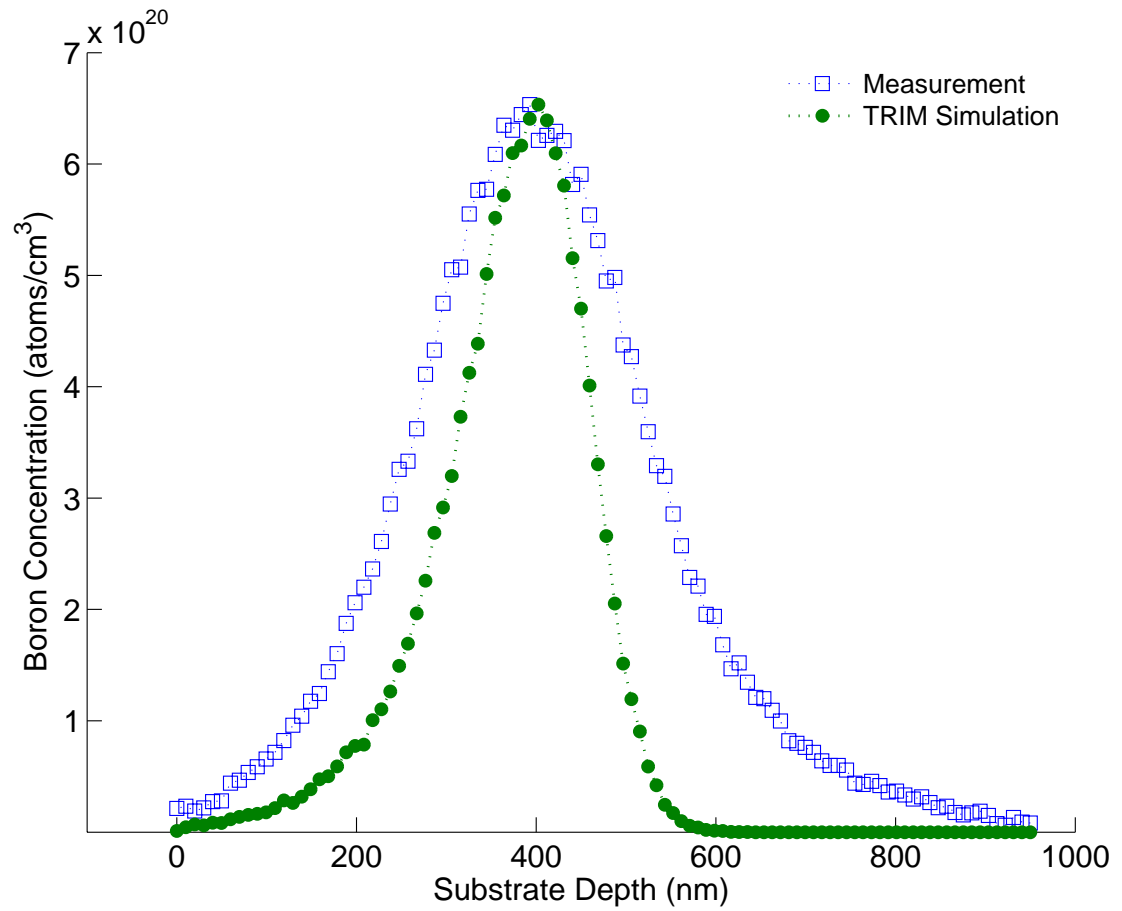


Figure 5.6. Boron concentration versus depth profile in silicon substrate calculated from the 1472-keV peak in Figure 5.5.

5.2 Experiments with the PEM Field Time-of-Flight Spectrometer

Alpha beams of various energies were used to observe the response of the PEM field time-of-flight spectrometer at different field combinations. The alpha flux was reduced by expanding the beam size in order to protect the microchannel plates. The energy spectrum and the count rate of the beam were first measured with a silicon surface barrier detector. Figure 5.7 shows the energy spectrum of the 1.5-MeV alpha beam measured through a 0.5-mm diameter hole in front of the detector. The standard deviation of the peak was calculated to be $\sigma_E = 10.10 \text{ keV}$.

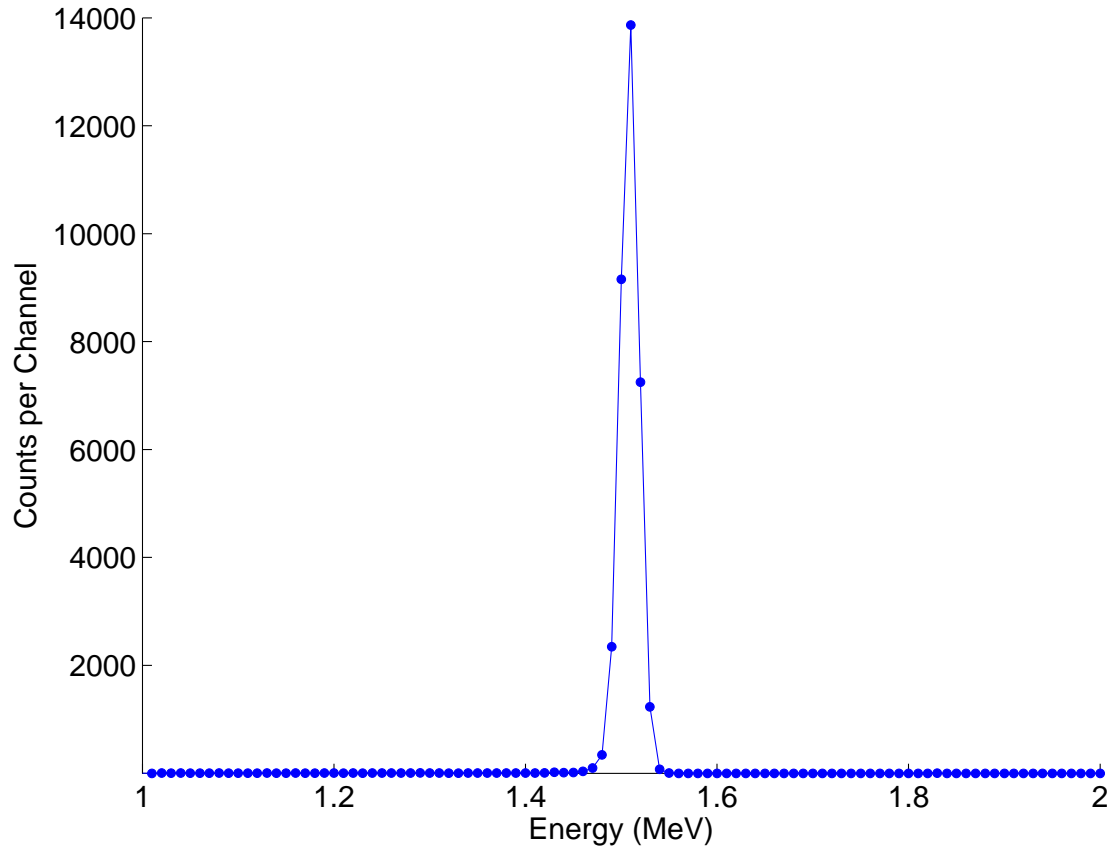


Figure 5.7. Energy spectrum of the alpha beam from the Tandem accelerator measured with a surface barrier detector.

5.2.1 Experimental Measurements

The three-dimensional drawing of the PEM field spectrometer was given in Figure 3.2. Figure 5.8 shows simplified drawing of the spectrometer, ion and electron microchannel plates, the ion beam and the secondary electron trajectories. As seen in the figure, the ion beam goes through an aperture on a tantalum disk and hits the carbon foil inducing secondary electron emission. The secondary electrons are pulled by the uniform electric field towards the electron microchannel plate following a helicoid trajectory due to the presence of the magnetic field.

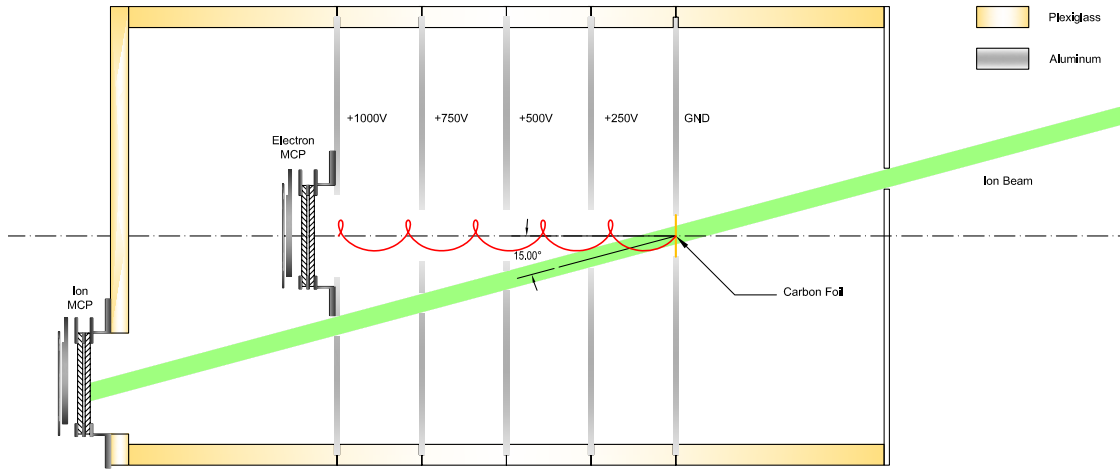


Figure 5.8. A simplified sketch of the PEM field spectrometer.

Once the ion beam penetrates the carbon foil, it loses some of its energy and suffers broadening due predominantly to foil thickness nonuniformity, and partly to straggling and multiple scattering. The amount of energy loss and the spread can be estimated using a Monte Carlo simulation tool such as TRIM (TRansport of Ions in Matter). Figure 5.9 shows the computed energy spectra of alpha beams having penetrated 50-nm and 200-nm thick carbon foils using TRIM. The ions in this simulation impact the foil at 15° angle with a kinetic energy of 1.5 MeV.

It was found that the alpha particles lost approximately 20 *keV* in the 50-nm carbon foil and 80 *keV* in the 200-nm carbon foil. The amount of spread was calculated to be $\sigma_E = 2.12 \text{ keV}$ and $\sigma_E = 4.19 \text{ keV}$ for 50-nm and 202-nm carbon foils, respectively.

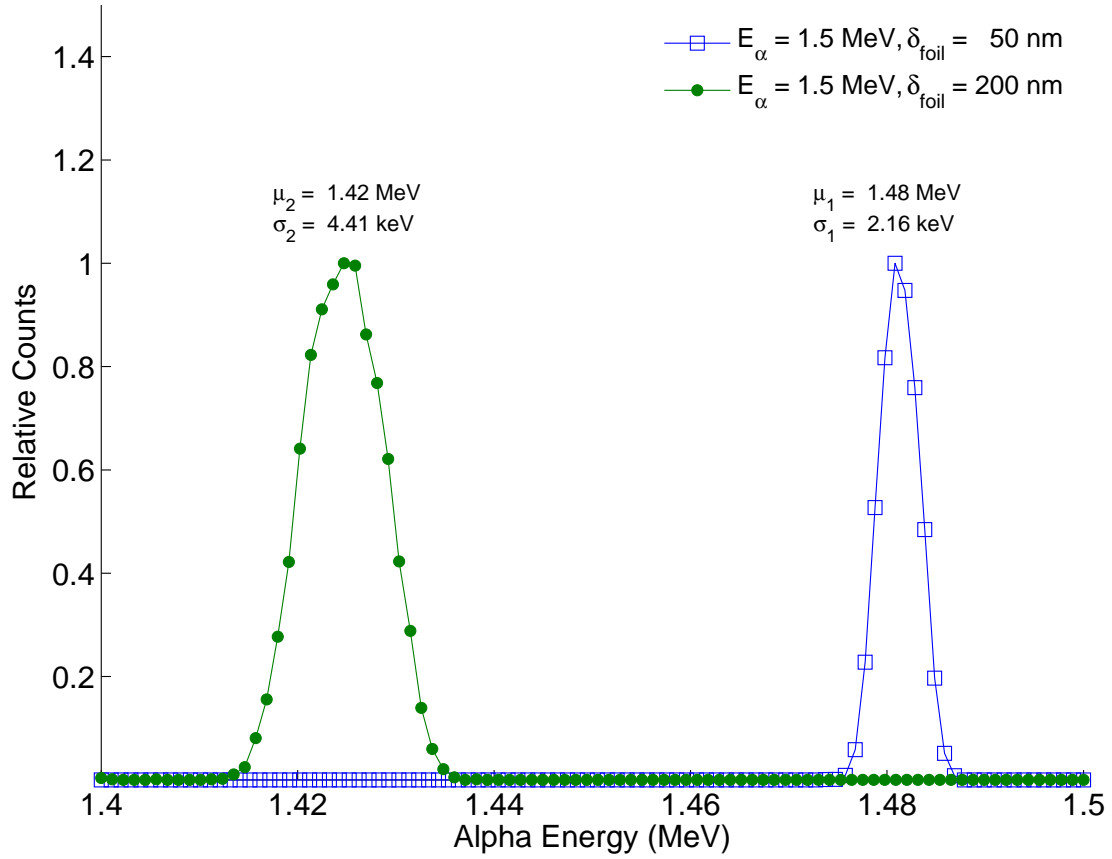


Figure 5.9. Computed energy spectra of alpha particles after penetrating carbon foils of 50 *nm* and 200 *nm*.

Response of the Spectrometer to Beam Energy

Time-of-flight spectra were taken with 1.0, 1.5 and 2.0-*MeV* alpha beams. In these measurements, the electron detector signal was used as the start trigger and the ion detector signal as the stop trigger. The carbon foil used as the secondary electron generator was 200-*nm* thick. The acceleration potential was set to 1000 *V*, which generated an electric field of $E = 10 \text{ kV/m}$. The magnetic field value required to map the electron beam with unity magnification, as explained in Section 3.1, was calculated $B = 35 \times 10^{-4} \text{ T}$, which corresponds to a solenoid current of $i = 0.5 \text{ A}$. The time-of-flight spectra are shown in Figure 5.10. Since the signal from the electron microchannel plate was used as the start trigger, the spectrum shifts left as the ion energy increases. Also observed in Figure 5.10 is that the 1-*MeV* alpha beam suffers more scattering than the other peaks. The scatterings were interpreted as the consequence of imperfections of the apertures

the alpha beam passes before it hits the ion microchannel plate.

The standard deviations of the peaks were calculated as 266.6 *ps*, 253.5 *ps*, and 267.1 *ps*, respectively for 1.0, 1.5 and 2.0-*MeV* alpha beams. The trend of the time resolution of the spectrometer is shown in Figure 5.11.

As expected, the spectral resolution in time is observed to be steady with respect to alpha beam energy. The mean value of the standard deviation is $\bar{\sigma} = 262.40$ *ps*, and fractional deviation is 2.94%.

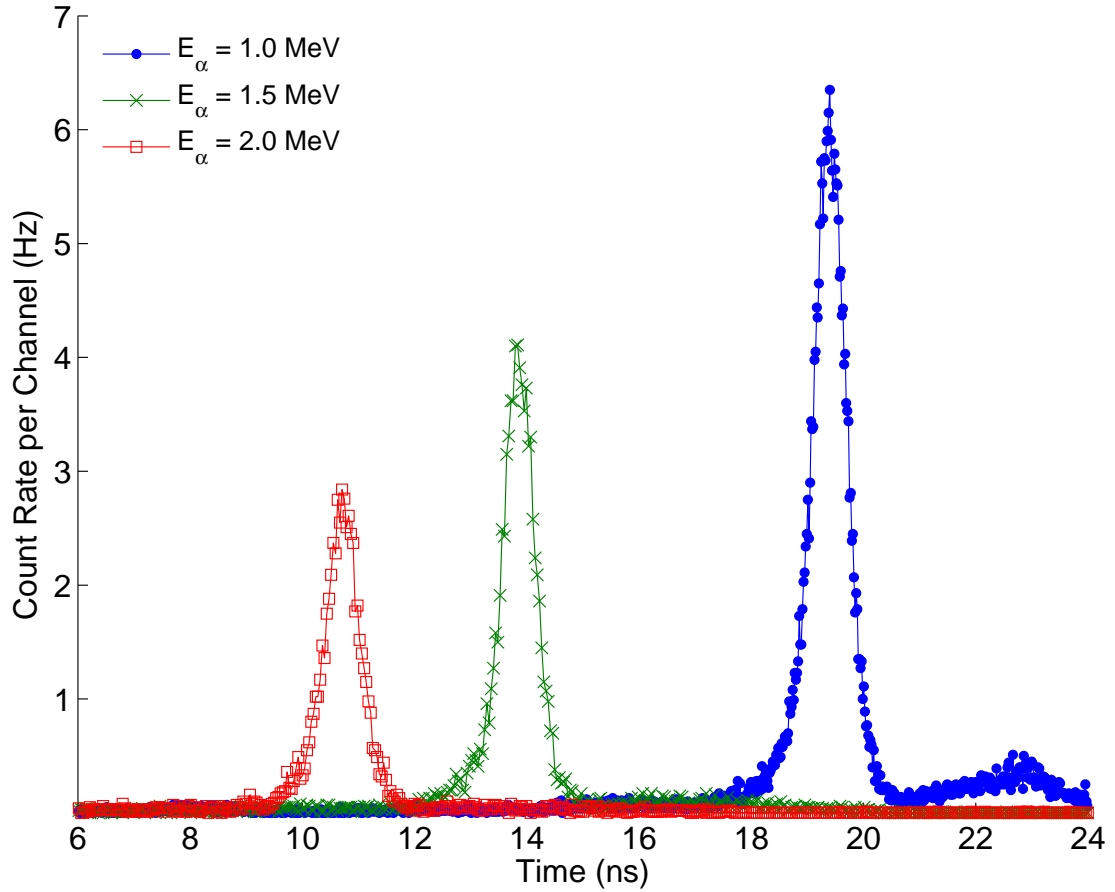


Figure 5.10. Time-of-flight spectra of the alpha beam at various energies.

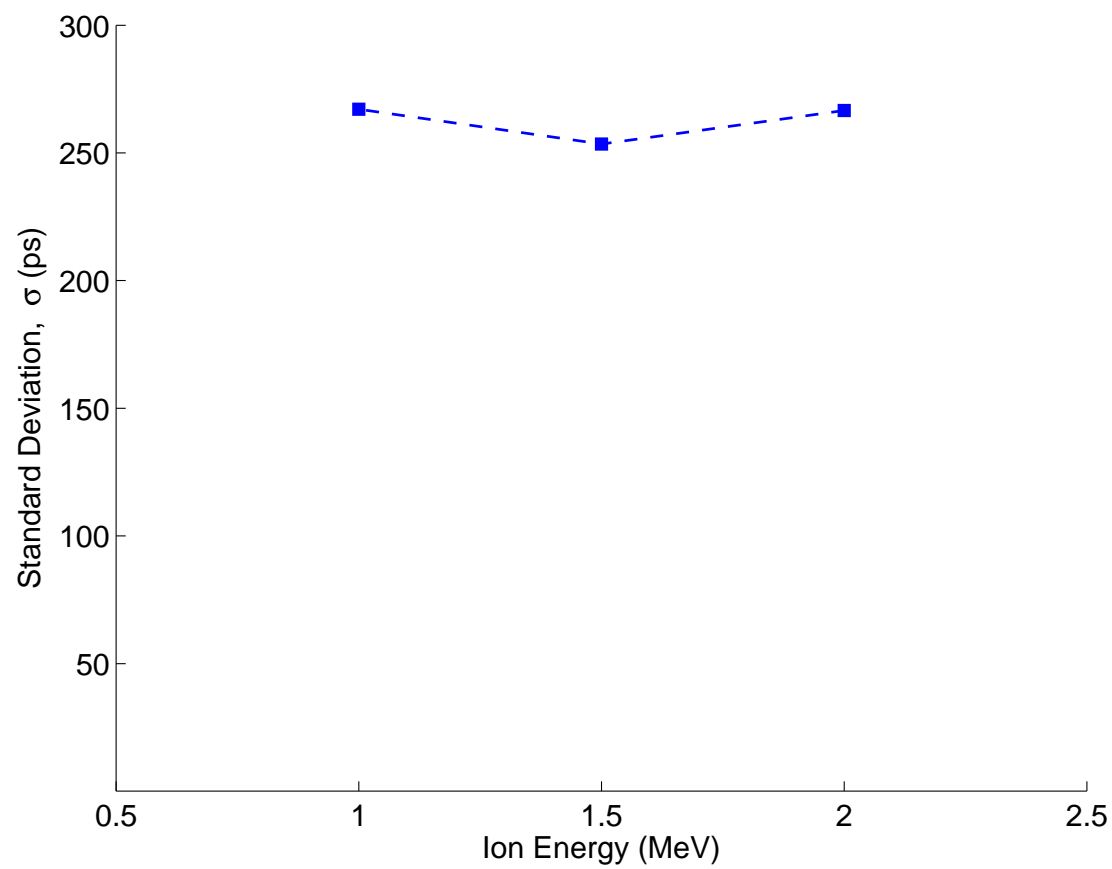


Figure 5.11. Variation of temporal resolution of the spectrometer with respect to beam energy.

Response of the Spectrometer to Electron Acceleration Potential

Measurements were done with 200-*nm* carbon foil and 2.0-*MeV* alpha beam for accelerating voltages of 500, 1000 and 2000 *V*, which correspond to 5-*kV/m*, 10-*kV/m* and 20-*kV/m* electric field, respectively. A time-of-flight spectrum was obtained for each condition with the electron detector signal as the start trigger and the ion detector signal as the stop trigger. The acquired spectra are shown in Figure 5.12.

As the accelerating field increases, the electron flight time drops off. Since the start trigger is the electron signal, the spectrum is expected to shift right. The standard deviations are calculated 431.4 *ps*, 267.1 *ps* and 166.7 *ps* for 500-, 1000- and 2000-*V* acceleration potentials, respectively. This observation shows the importance of electron time-of-flight dispersion in the measurement resolution.

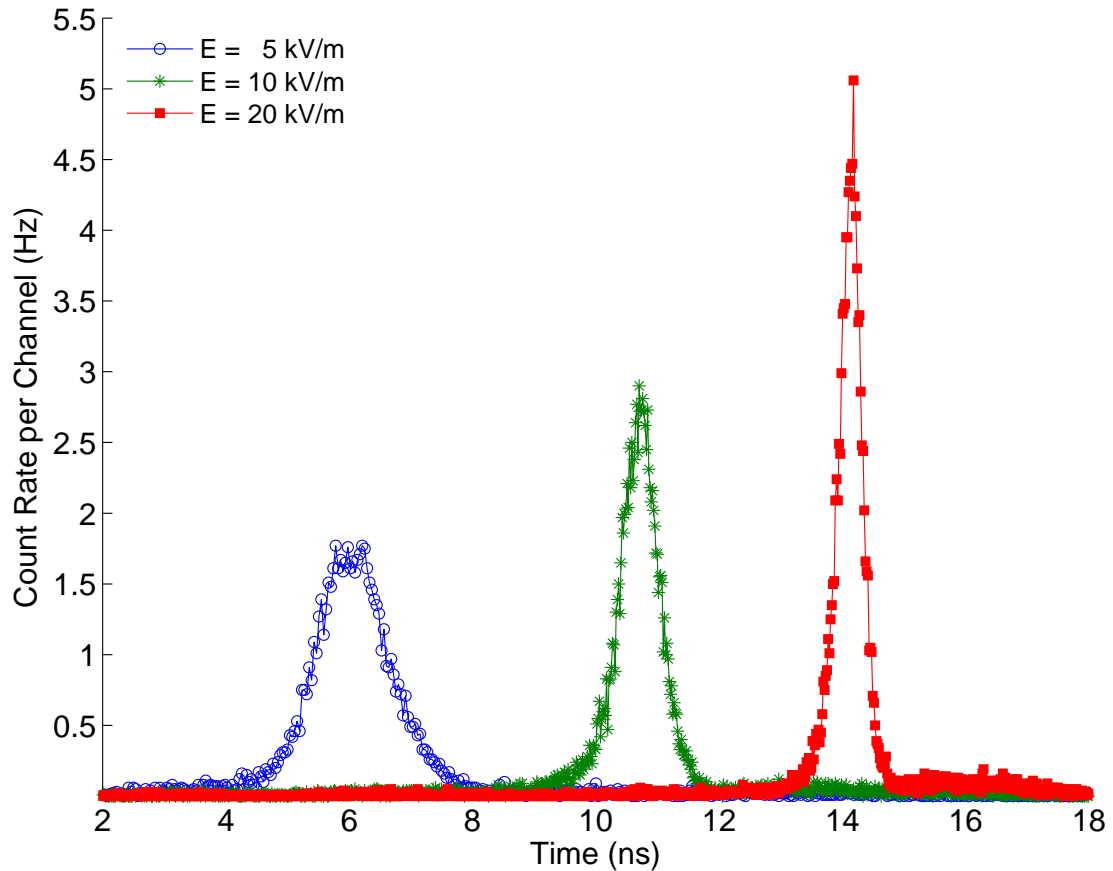


Figure 5.12. Spectral response to variation in electron accelerating electric field.

Another set of measurements was done to pronounce the effect of electron acceleration on peak resolution. This time the alpha beam energy was set to 1.5 MeV and a 50-nm thick carbon foil was used. The acquired spectra are plotted in Figure 5.13. The accelerating potential was varied from 500 V to 5000 V in 500 V increments, which corresponds to an electric field of 5 kV/m through 50 kV/m in 5 kV/m increments.

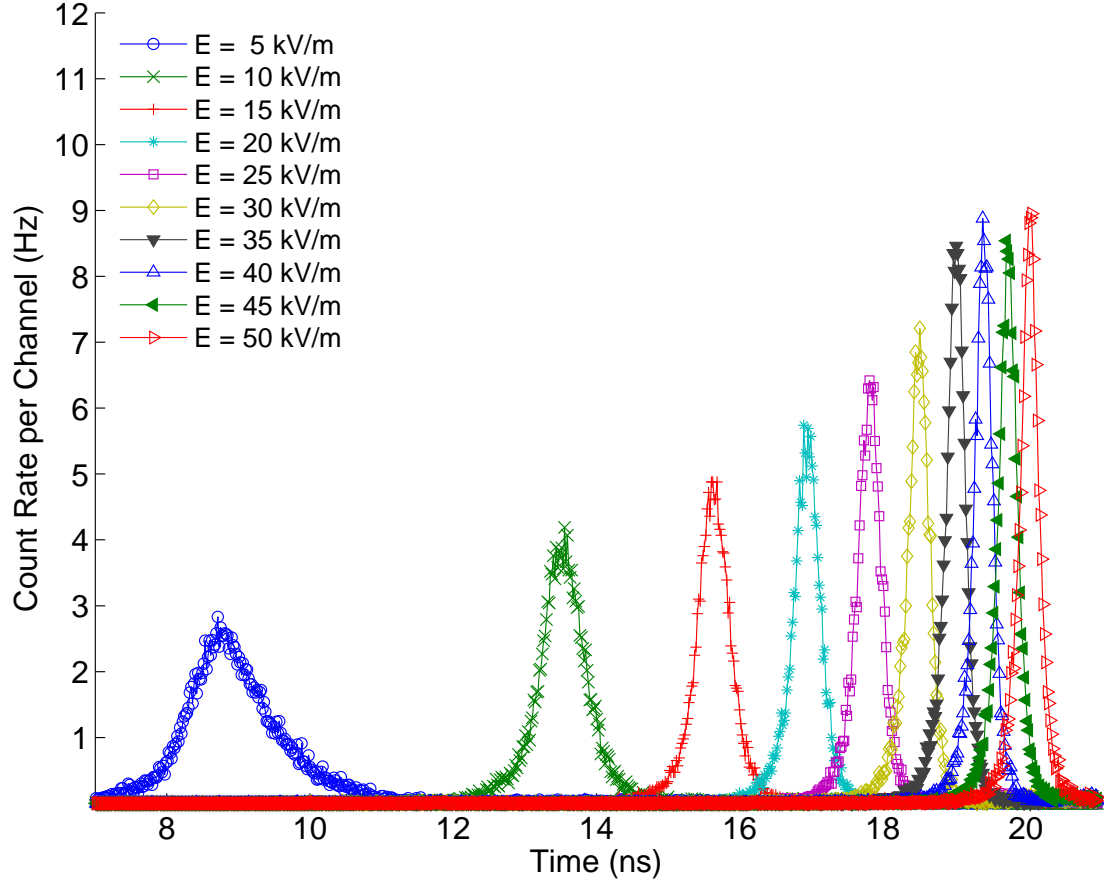


Figure 5.13. Spectral shift and spread variation with respect to electron accelerating potential.

The improvement in peak resolution is noticeable. The standard deviation of distributions start at approximately 420 ps for 500 V and reduces to 110 ps for 5000 V. The variation of the standard deviation is plotted in Figure 5.14. As can be seen in the figure, the spread drops off faster in the beginning, but it starts to level off as the electric field increases further. The limit it reaches, i.e. ~ 100 ps, indicates other broadening mechanisms.

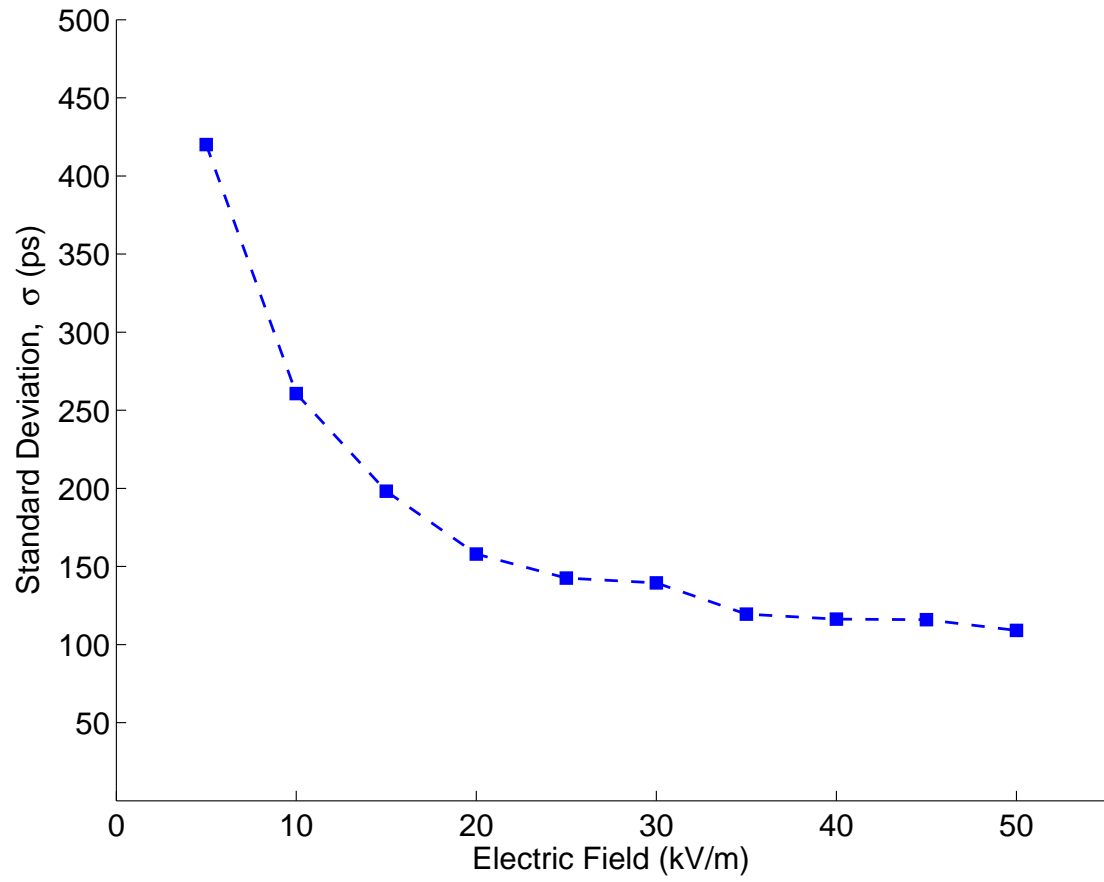


Figure 5.14. Variation of standard deviation with respect to accelerating electric field.

Effect of Carbon Foil Thickness

Measurements were done with 1.5-MeV alpha beam with 1000 V accelerating potential. A time-of-flight spectrum was obtained for carbon foils of $40.4 \mu\text{g}/\text{cm}^2$ and $9.6 \mu\text{g}/\text{cm}^2$, which correspond to $\sim 200 \text{ nm}$ and $\sim 50 \text{ nm}$ nominal thicknesses, respectively. The electron detector signal was used as the start trigger and the ion detector signal as the stop trigger. The acquired spectra are shown in Figure 5.15.

The standard deviations of the distributions are 253.5 ps for 200-nm thick foil, and 223 ps for 50-nm thick foil. The observation confirms that alpha beam suffers less from straggling as it passes through a thinner foil.

Thickness non-uniformity of the carbon foil is a very important component of measurement uncertainty. The manufacturer specifies that the thickness is within $\pm 5\%$ across the foil of its nominal value for arc-evaporated carbon foils.

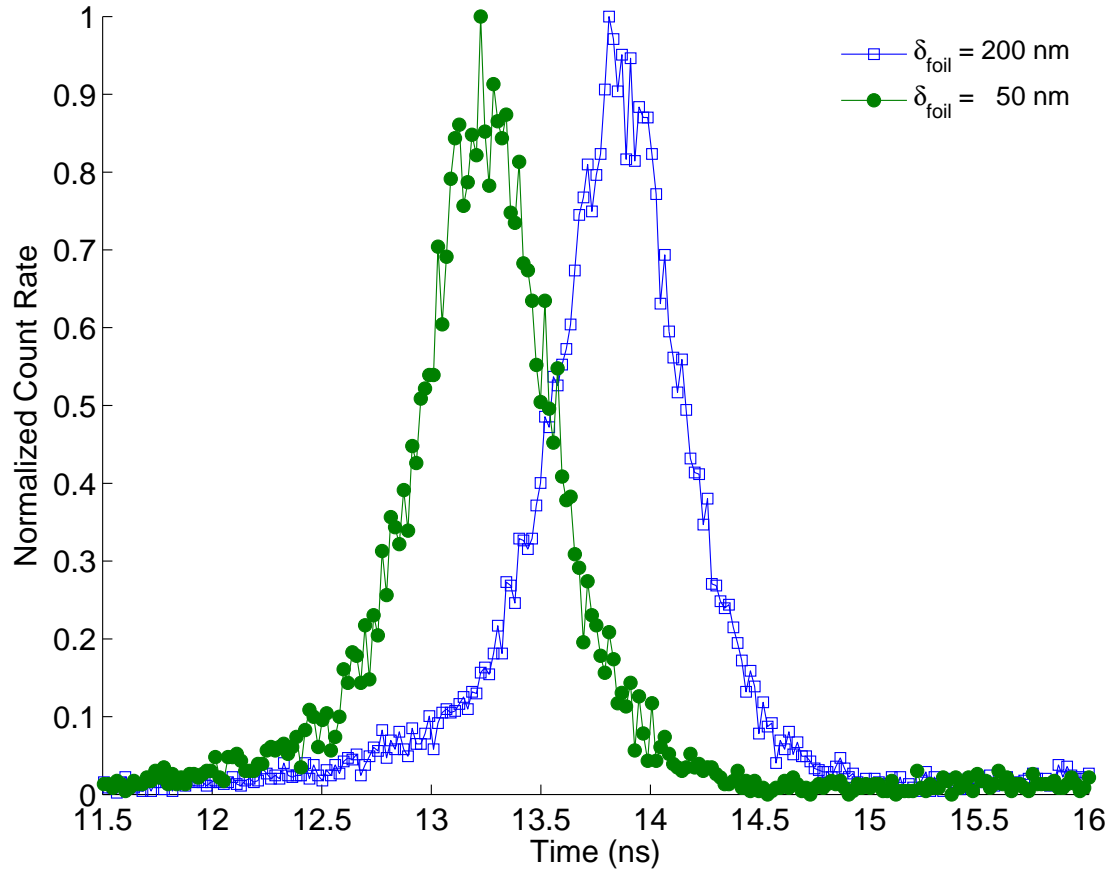


Figure 5.15. Time-of-flight spectra for 1.5-MeV alpha beam obtained with different carbon foil thicknesses. The spectra were normalized with respect to maximum count rate.

5.2.2 Discussions on Experimental Results

The experimental data is analyzed and interpreted in detail. Measurements taken at multiple beam energies and electron acceleration potentials are used to obtain certain physical quantities of the device, such as ion and electron flight path length. The measurement resolution and the detection efficiency of the device are also discussed. Proposed designs to improve the device performance are presented in the Chapter 6.

Calculation of the Ion Flight Path Length

This evaluation intends to accurately determine the ion flight path length using multiple data points obtained with multiple beam energies. The registration time of a particle on the time analyzer can be represented as

$$\begin{aligned}\tau_1 - \tau_{\text{bias}} &= \tau_{\alpha_1} - \tau_{e^-} \\ \tau_2 - \tau_{\text{bias}} &= \tau_{\alpha_2} - \tau_{e^-} \\ \tau_3 - \tau_{\text{bias}} &= \tau_{\alpha_3} - \tau_{e^-}\end{aligned}\tag{5.1}$$

where $\tau_{\text{bias}} = 2.686 \text{ ns}$ from the measurements taken with the precision pulser as described in Section 4.3.2. This system of equations can be represented in matrix form:

$$\begin{pmatrix} \tau_1 - \tau_{\text{bias}} \\ \tau_2 - \tau_{\text{bias}} \\ \tau_3 - \tau_{\text{bias}} \end{pmatrix} = \begin{pmatrix} \sqrt{\frac{m_\alpha}{2E'_{\alpha_1}}} - 1 \\ \sqrt{\frac{m_\alpha}{2E'_{\alpha_2}}} - 1 \\ \sqrt{\frac{m_\alpha}{2E'_{\alpha_3}}} - 1 \end{pmatrix} \begin{pmatrix} L_\alpha \\ \tau_{e^-} \end{pmatrix}\tag{5.2}$$

where the alpha flight times were expressed in energy, and E'_{α_x} represents the mean energy of the alpha particles having penetrated the carbon foil. The system of equations is overdetermined since there are more equations than the number of unknowns. The best solution, which minimizes the error vector $\epsilon = \|Ax - b\|$, can be found by applying the least squares approximation, i.e.

$$\begin{aligned}A^T Ax &= A^T b \\ \Rightarrow x &= (A^T A)^{-1} A^T b\end{aligned}\tag{5.3}$$

By solving Equation (5.3), the vector $x = \begin{pmatrix} L_\alpha \\ \tau_{e^-} \end{pmatrix}$ can be computed. Using the data shown in Figure 5.11, the alpha flight path length and the electron flight times are found to be

$$L_\alpha = 185.4 \text{ mm} \quad (5.4)$$

$$\tau_{e^-} = 11.203 \text{ ns} \quad (5.5)$$

This technique provides a more systematic way to determine the exact flight path length.

Calculation of the Electron Flight Path Length

The same methodology can be used to measure the electron flight path length and flight time more precisely. The data presented in Figure 5.13 offers substantial information to estimate system parameters more precisely. In this series of measurements the alpha energy is fixed at 1.5 MeV , therefore the alpha flight time is invariant. The average electron flight time, on the other hand, varies in accordance with the accelerating potential. The registration time of a particle on the time analyzer can be represented as

$$\begin{aligned} \tau_1 &= \tau_\alpha - \tau_{e_1^-} + \tau_{\text{bias}} \\ &\vdots \\ \tau_i &= \tau_\alpha - \tau_{e_i^-} + \tau_{\text{bias}} \end{aligned} \quad (5.6)$$

τ_α can be calculated using the energy of the beam having passed through the carbon foil, and the computed alpha flight path length, $L_\alpha = 185.4 \text{ mm}$. The carbon foil used in this set of measurements had a nominal thickness of 48 nm . Using this value, the energy of the beam after it passes through the carbon foil E'_α is calculated to be 1.482 MeV . Using these values, the nominal alpha flight time is found

$$\tau_\alpha = L_\alpha \sqrt{\frac{m_\alpha}{2E'_\alpha}} = 21.931 \text{ ns} \quad (5.7)$$

The system of equations in Equation (5.6) can be modified to include the electron flight path length and represented in the linear matrix form as follows:

$$\begin{pmatrix} \tau_\alpha + \tau_{\text{bias}} - \tau_1 \\ \vdots \\ \tau_\alpha + \tau_{\text{bias}} - \tau_i \\ \vdots \\ \tau_\alpha + \tau_{\text{bias}} - \tau_N \end{pmatrix} = \begin{pmatrix} \sqrt{\frac{2m_e E_0}{e_0 V a_1^2} + \frac{2m_e}{e_0 V a_1}} - \frac{m_e}{e_0 V a_1} \sqrt{\frac{2E_0 e_0}{m_e}} \\ \vdots \\ \sqrt{\frac{2m_e E_0}{e_0 V a_i^2} + \frac{2m_e}{e_0 V a_i}} - \frac{m_e}{e_0 V a_i} \sqrt{\frac{2E_0 e_0}{m_e}} \\ \vdots \\ \sqrt{\frac{2m_e E_0}{e_0 V a_N^2} + \frac{2m_e}{e_0 V a_N}} - \frac{m_e}{e_0 V a_N} \sqrt{\frac{2E_0 e_0}{m_e}} \end{pmatrix} \begin{pmatrix} L_e \end{pmatrix} \quad (5.8)$$

where the index i corresponds to the i 'th measurement, and $V_{a_i} = 500i$ V. the least square solution for electron flight path length for Equation (5.8) was calculated to be

$$L_{e^-} = 112.3 \text{ mm}$$

Offset and Delay Correction of the Ion Time-of-Flight Spectrum

Given the time offset of the spectrometer and the electron flight time, the ion time-of-flight spectrum can be corrected, i.e.

$$\tau_\alpha = \tau + \tau_{e^-} - \tau_{\text{bias}} \quad (5.9)$$

where τ_α represents the corrected ion time-of-flight spectrum. Figure 5.16 shows the spectra of corrected ion arrival times for the raw data shown in Figure 5.10, and Figure 5.17 presents two of the corrected alpha arrival time spectra from the raw data presented in Figure 5.13.

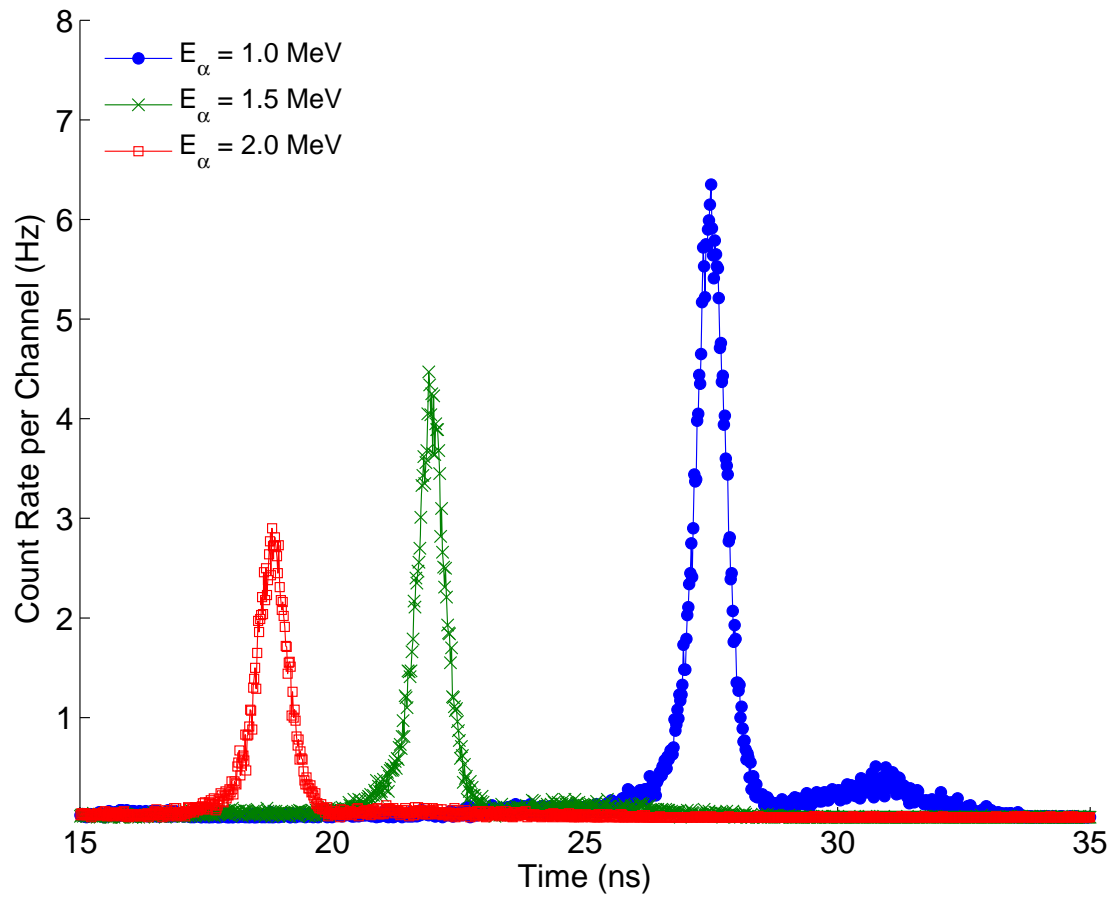


Figure 5.16. Offset and delay corrected ion time-of-flight spectra of the data shown in Figure 5.10.

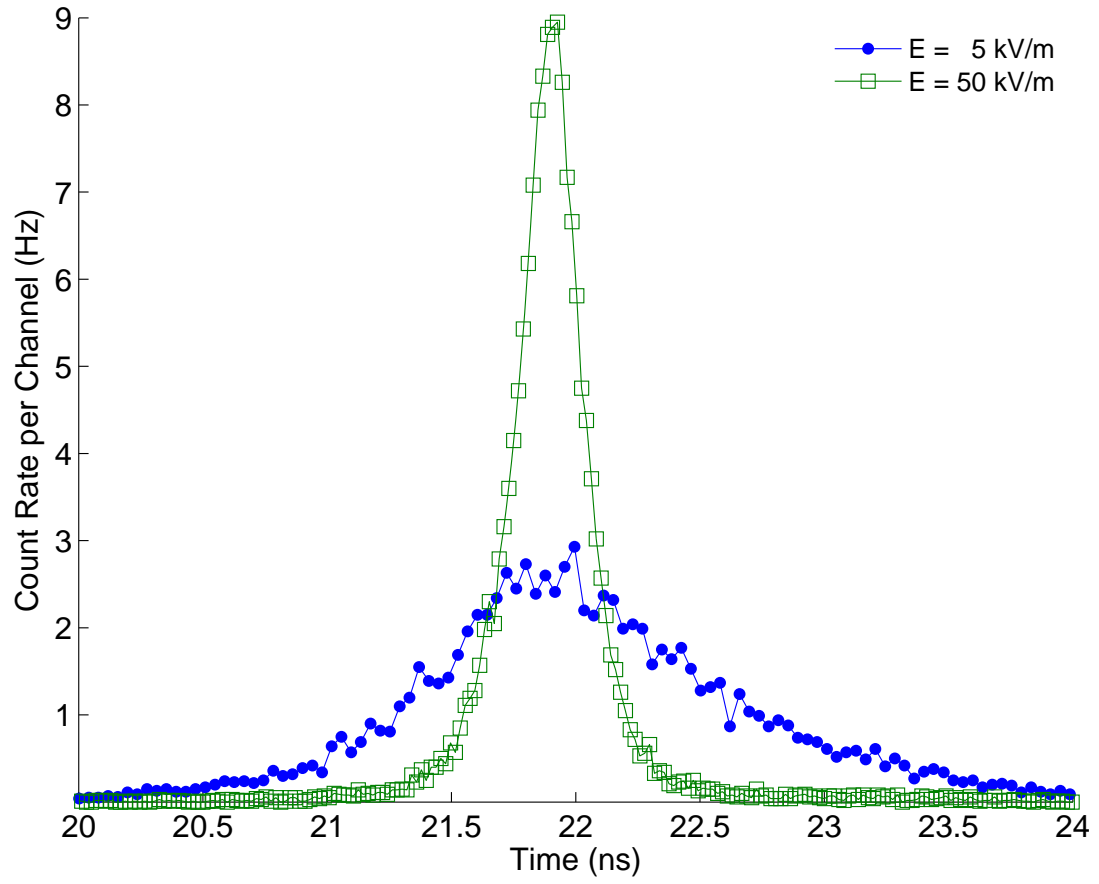


Figure 5.17. Offset and delay corrected spectra for 5-kV/m and 50-kV/m electric fields from the measurements presented in Figure 5.13.

Energy Calibration of the Time-of-Flight Spectrum

The energy spectra can be obtained from the offset and delay corrected time-of-flight spectra. Figure 5.18 shows the energy spectra of the alpha beams at 1.0, 1.5, and 2.0-*MeV* energy.

The centroids of the distributions were calculated 0.954 *MeV*, 1.480 *MeV*, 2.013 *MeV*, whereas the centroids of the distributions obtained by the TRIM simulations were 0.918 *MeV*, 1.427 *MeV*, and 1.936 *MeV*.

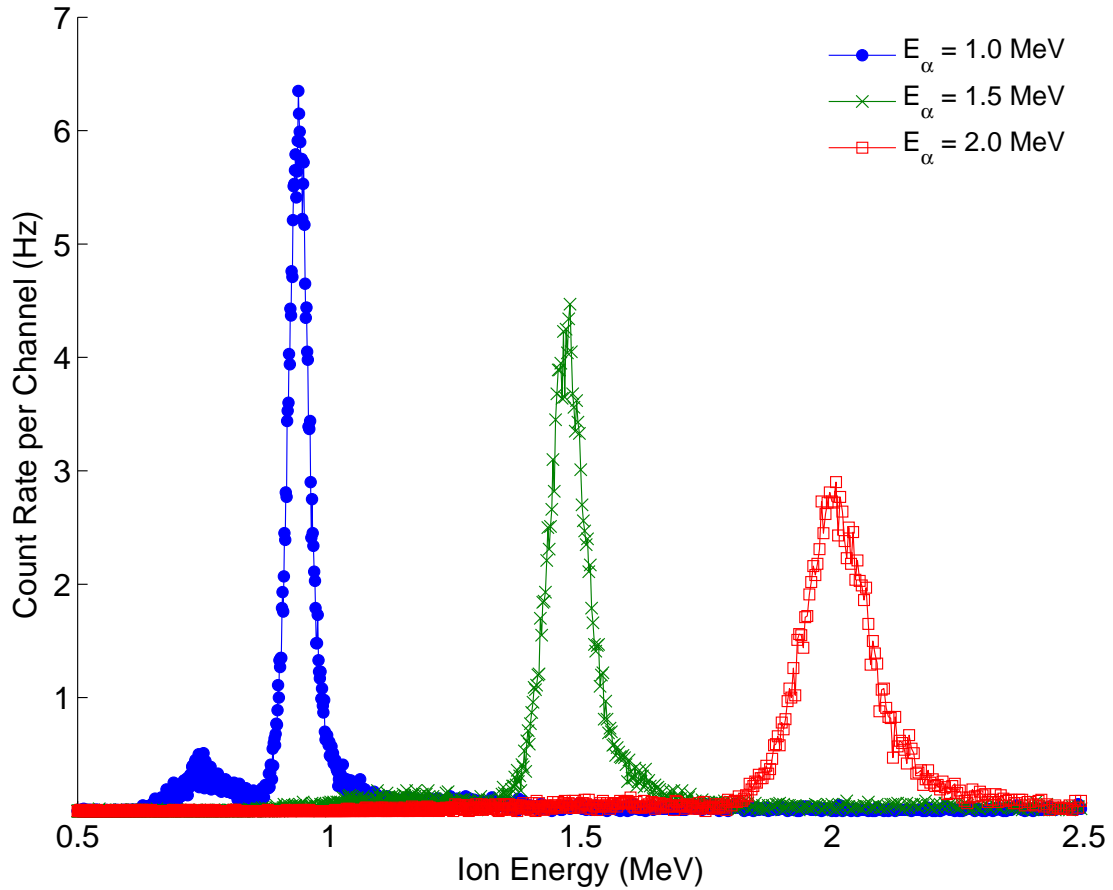


Figure 5.18. Energy spectra obtained from the alpha time-of-flight spectra shown in Figure 5.16.

The standard deviations of the spectra were calculated 18.22 *keV*, 34.07 *keV*, and 57.14 *keV* for 1.0-*MeV*, 1.5-*MeV*, and 2.0-*MeV* alpha beams, respectively. The variation of the standard deviations is presented in Figure 5.19. Although the temporal standard deviations were insensitive to the incident particle energy, as presented in Figure 5.11, the standard deviations in energy vary dramatically. This is an expected behavior

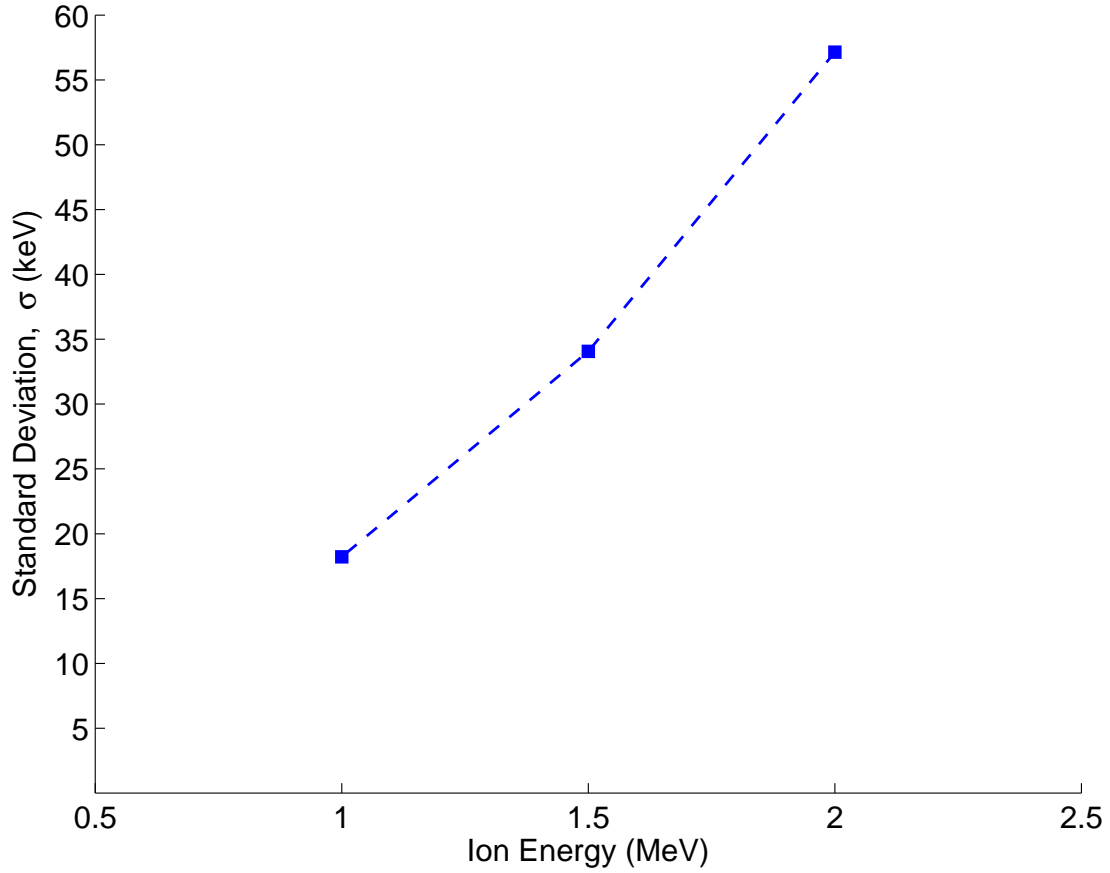


Figure 5.19. Variation of the energy resolution of the spectrometer with respect to beam energy.

due to the variation of the sensitivity of the conversion algorithm from the time spectrum to the energy spectrum, as explained in more detail in Section 2.4.3.

Figure 5.20 shows the energy spectra of 1.5-MeV alpha beams taken at three different acceleration potentials. The spectra were obtained by conversion of the time spectra shown in Figure 5.17. The centroids of the peaks are located at 1.473 MeV and 1.485 MeV for 5-kV/m, and 50-kV/m electric fields corresponding to 500-V and 5000-V acceleration potentials. The standard deviations of the peaks are $\sigma_E = 57.6$ keV and $\sigma_E = 14.82$ keV, respectively. The standard deviation of the spectrum obtained with the surface barrier detector was $\sigma_E = 10.10$ keV.

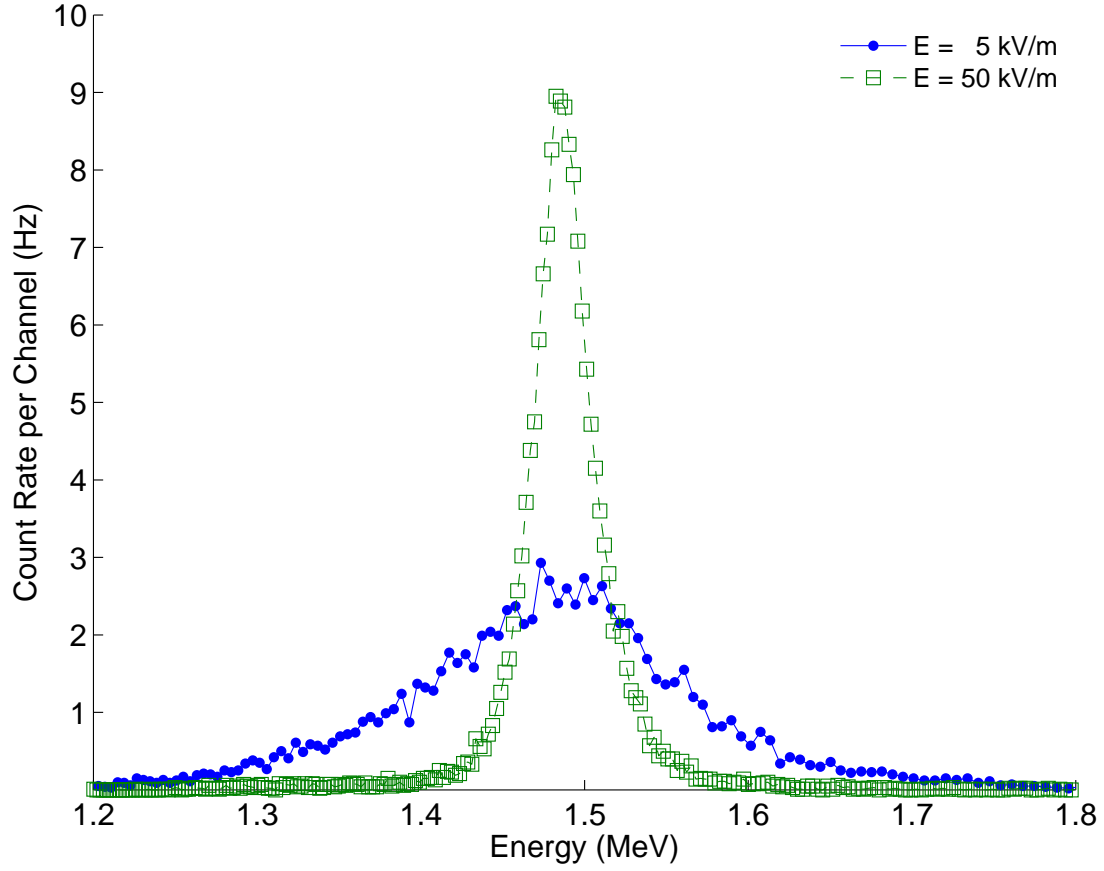


Figure 5.20. Energy spectra obtained from the alpha time-of-flight spectra shown in Figure 5.17.

Resolution of the PEM Field Spectrometer

The resolution of the PEM field spectrometer can be analyzed mathematically by rearranging Equation (A.22) that gives the axial position of the electron:

$$t^2 + \frac{2m_e}{e_0 E} v_{z0} t - \frac{2m_e}{e_0 E} \Delta z = 0 \quad (5.10)$$

The arrival time of the electrons on the microchannel plate can be found by solving Equation (5.10) as

$$t = -\frac{m_e v_{z0}}{e_0 E} \pm \sqrt{\left(\frac{m_e v_{z0}}{e_0 E}\right)^2 + \frac{2m_e \Delta z}{e_0 E}} \quad (5.11)$$

It can be seen that the electron arrival time t is only a function of the axial component of the initial velocity of the electron v_{z0} , and the electric field E for a fixed $\Delta z = L_e$. It

can be shown that the electron arrival time can be approximated as

$$\Delta t \propto \frac{\delta v_{z0}}{E} \quad (5.12)$$

Therefore, as the magnitude of the electric field is increased, the importance of the deviation in initial velocity v_{z0} decreases resulting in lower electron flight time dispersion. This hypothesis was experimentally observed as presented in Figure 5.14. The resolution improvement as measured experimentally by increasing the electric field is shown in Figure 5.21.

In the presence of field nonuniformity, electron flight path length also affects the electron arrival time dispersion. A longer flight path makes the electron beam more vulnerable to stray fields as well as local field variations due to nonuniformities.

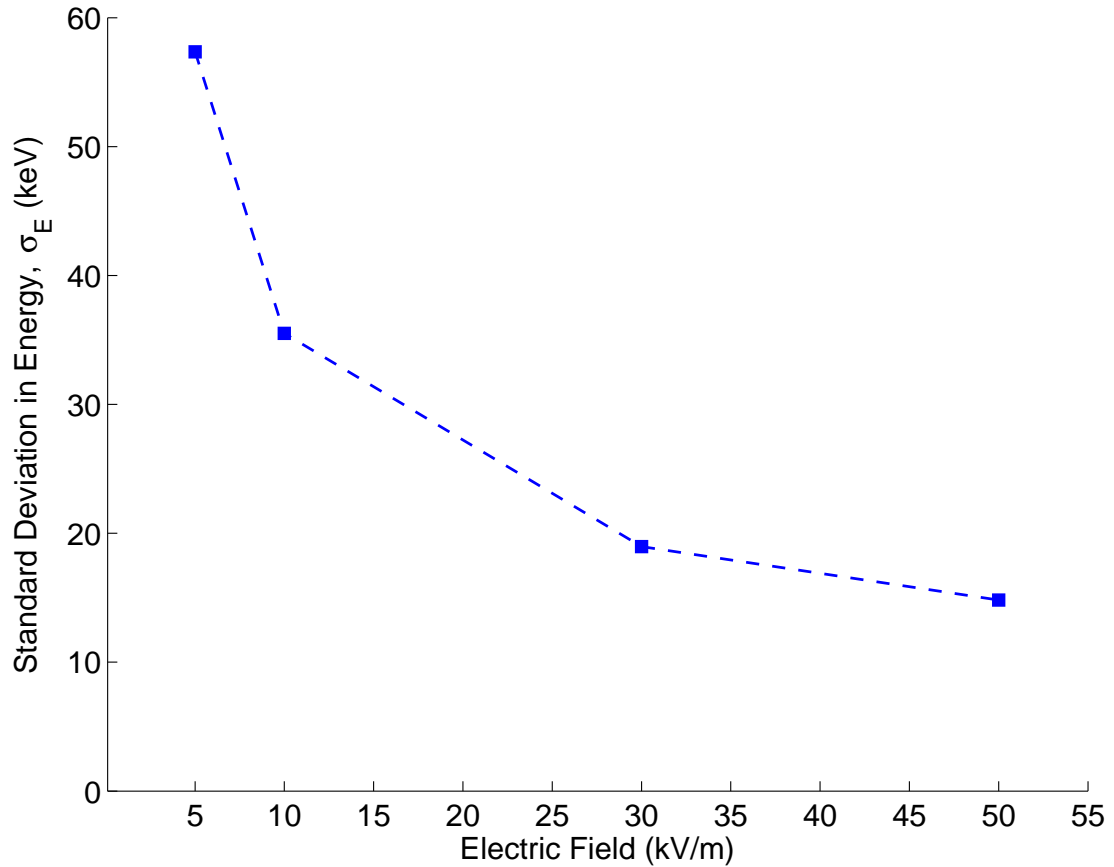


Figure 5.21. Variation of the energy resolution of the PEM spectrometer with respect to accelerating electric field.

Detection Efficiency of the PEM Field Spectrometer

The detection efficiency of the PEM field spectrometer was found by taking the count rate of the ion with the surface barrier detector. The ion beam flux was calculated by the integrated count of the energy spectrum. Figure 5.22 demonstrates the variation of the efficiency of the time-of-flight spectrometer with respect to incident ion energy. Although the ion beam in a particle accelerator is closer to being monodirectional, the detection efficiency is approximately 3.5% for 1-MeV ions, and drops to 1.5% for 2-MeV ions. This kind of dependence is expected because of the fact that (1) More secondary electrons are generated in the carbon foil per alpha particle at lower energies, (2) The detection efficiency of the microchannel plate is higher at lower energies.

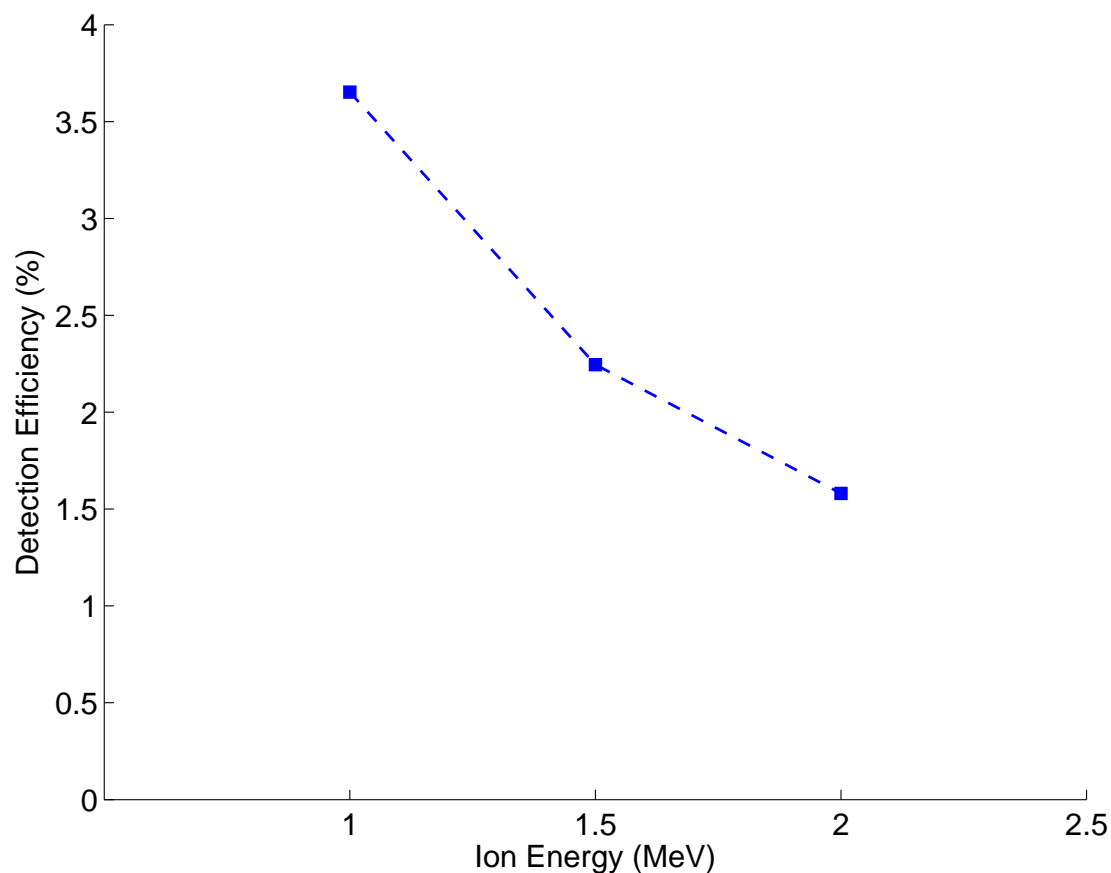


Figure 5.22. Efficiency variation of the PEM field spectrometer with respect to alpha beam energy.

5.3 Experiments with the CEM Field Time-of-Flight Spectrometer

A three-dimensional drawing of the CEM field ion time-of-flight spectrometer was given in Figure 3.8. Figure 5.23 shows a simplified drawing of the spectrometer with the ion and electron trajectories, and the ion and electron microchannel plate detectors. The principle of operation of the device was given previously in Section 3.2.

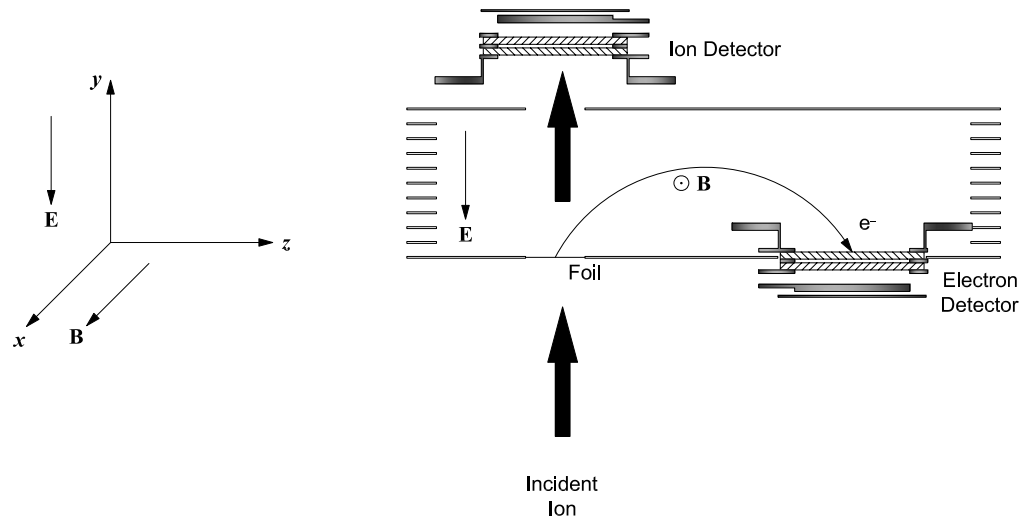


Figure 5.23. Simplified drawing of the CEM field spectrometer showing the ion and secondary electron trajectories and associated detectors.

A ^{210}Po alpha source was used to test the CEM field spectrometer. The source was an industrial ionizer marketed as electrostatic eliminator. ^{210}Po is an alpha emitter with essentially a single decay branch, which makes it an excellent tool for experimentation purposes.

The source contained multiple layers: the first layer is a thick base layer made of silver. This layer is coated with a $3/4\ \mu\text{m}$ gold layer for additional diffusion resistance. The radioactive layer is made of $1/2 - 1\ \mu\text{m}$ silver and polonium mixture. This layer is coated with $1\ \mu\text{m}$ gold, and then $1/4\ \mu\text{m}$ nickel, and finally $1/2\ \mu\text{m}$ gold layers. The objective of multiple-barrier design is to minimize possible contamination.

Since the ^{210}Po source is not a surface deposit and the surface is covered with additional layers, the alpha emission is not expected to be monoenergetic. In order to estimate the energy spectrum of the alpha particles, a TRIM simulation was performed that considers a uniformly-distributed source in the active layer. The expected energy

spectrum of alpha particles as obtained from the simulation is shown in Figure 5.24. The most probable energy was calculated to be $E_* = 4464 \text{ keV}$ as shown in the figure.

The initial activity of the source was $5 \text{ mCi} \pm 10\%$. The half life of ^{210}Po is 138.376 days, which is long enough for the period of an experiment, but will decay to almost 15% of its original activity within one year. At the time of the experiment, the activity of the source was estimated to be $\sim 1 \text{ mCi}$.

The alpha source was masked by an aluminum frame with a 10-mm diameter aperture in the center, and placed 40 mm upstream of the entrance stage of the electric field unit facing the carbon foil. The electric field unit was then positioned in the center of the Helmholtz coil, which was described in Section 3.2.1. The Helmholtz coil in this experiment had 125 mm inner diameter and 600 windings per coil.

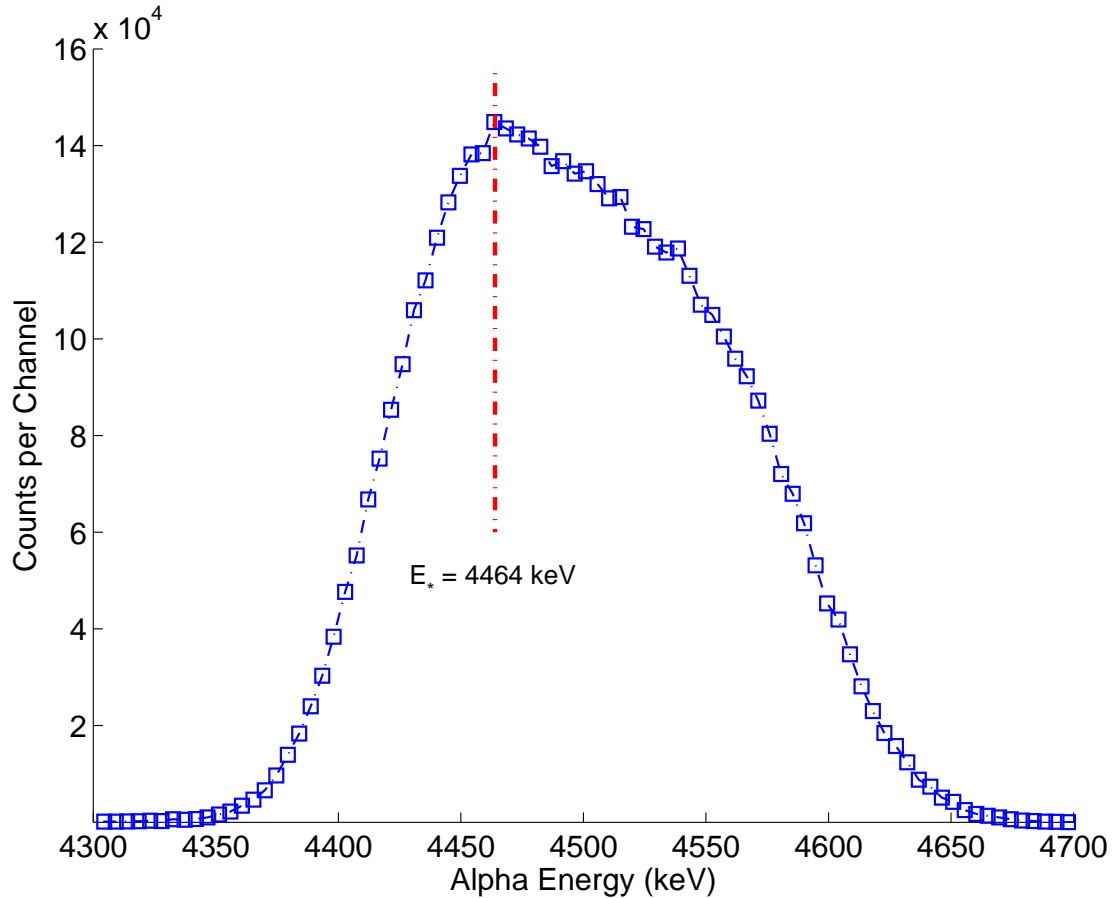


Figure 5.24. Expected alpha energy spectrum of the ^{210}Po alpha source obtained with the TRIM simulation.

As the secondary electron emitter surface, a transmission electron microscope (TEM) grid was used. The TEM grid was 3 mm in overall diameter, and was made of 50%-transmission copper mesh. The grid had carbon foil overlaid on one side. The nominal thickness of the carbon foil was reported to be 50 nm with 1% thickness uniformity. This carbon thickness value is known to be adequate for the generation of sufficient number electrons, and relatively thin enough to minimize straggling through the foil.

5.3.1 Experimental Measurements

Response of the Spectrometer to Electron Acceleration Potential

Time-of-flight spectra were obtained at 6-kV/m and 24-kV/m electric field values, which correspond to 150 V and 600 V acceleration potentials. The magnet current was adjusted to create a magnetic field value that matches the electric field value to transport the ejected electrons onto the electron microchannel plate. In this measurement, the signal from the ion microchannel plate was used as the start trigger, and the electron signal was used as the stop trigger. The stop signal line was delayed by $\tau_{\text{delay}} = 60 \text{ ns}$. The data from the measurements is plotted in Figure 5.25.

The peak centroids were calculated to be at 13.264 ns for 24 kV/m electric field and 18.314 ns for 6 kV/m, from which the spectral shift was found $\Delta\tau_{\text{exp}} = 5.049 \text{ ns}$. Using the definition of cycloid period $\tau = 2\pi m_e / e_0 B$, the expected spectral shift can be calculated as follows:

$$\Delta\tau = \tau_2 - \tau_1 = \frac{2\pi m_e}{e_0} \left(\frac{1}{B_2} - \frac{1}{B_1} \right) = \left(\frac{5}{4} \right)^{\frac{3}{2}} \frac{2\pi m_e r}{e_0 \mu_0 n} \left(\frac{1}{i_2} - \frac{1}{i_1} \right)$$

Using the parameters of the first Helmholtz coil, $r = 62.5 \text{ mm}$, $n = 600$, the expected shift from $i_1 = 0.375 \text{ A}$ to $i_2 = 0.750 \text{ A}$ is

$$\Delta\tau_{\text{theo}} = 4.993 \text{ ns}$$

which is within 1% of the experimental result.

Possible sources of error are the associated reading error on the power supplies, and variations in the magnet current. The manufacturer specifications of the power supplies claim that the display reading is within $\pm 0.1\%$ of the applied voltage. However, the measurements showed that the reading on the display was within $\pm 1\%$ of the applied voltage on top of an offset around 10 V to 14 V. The variation in magnet current is interpreted as a result of increase in resistance due to overheating of the coils in vacuum.

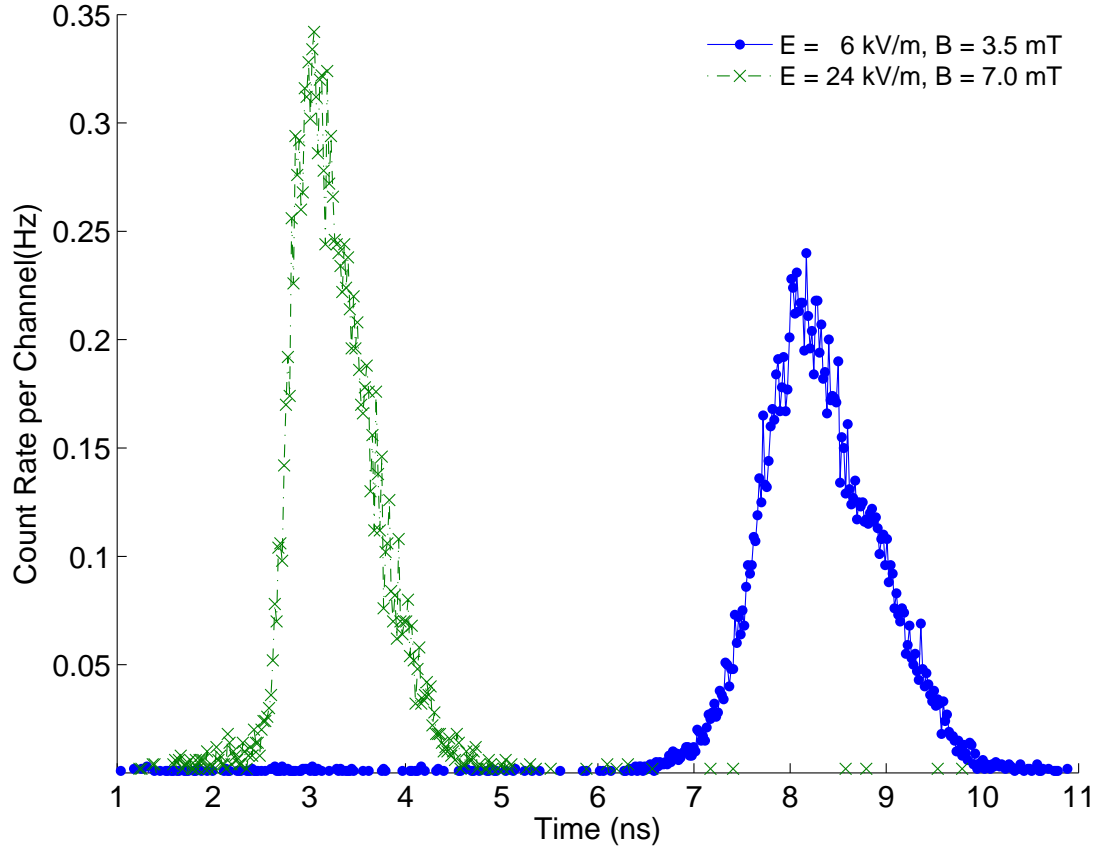


Figure 5.25. Time-of-flight spectra of the ^{210}Po source at different electric and magnetic field values obtained with the CEM field spectrometer.

Although the current supply is expected to maintain the current at a specified value, it was observed that the current drifted over the course of the measurement.

Response of the Spectrometer to Magnetic Field Variation

The electrical current through the magnet coils can be used to control the point where the electron beam falls back onto the same plane it was ejected. At zero magnetic field value, the average bend radius is at infinity. As the magnetic field increases at a constant acceleration potential, the electron beam approaches the microchannel plate from infinity. At the correct ratio of E/B^2 that matches the separation between the electron emitting surface and the electron microchannel plate, the electron beam sweeps across the microchannel plate surface as the magnetic field value is raised. After a certain value, the average bending radius becomes too large, and the beam clears off the

microchannel plate surface. Thus, it is expected that, as the electrical current through the magnet is increased, the count rate should first jump from a background rate to a steady value, then fall sharply to the background value.

Figure 5.26 shows the plot of the variation of the count rate on the electron microchannel plate with respect to the electrical current through the magnet coils. The count rate starts from a low background value and increases as the magnet current is raised. The inset plot in Figure 5.26 shows that the count rate makes a plateau, and then falls gradually. The tail in the main plot was expected to fall more sharply. But it was observed repeatedly that high magnetic field resulted in collection of spurious signals even in the absence of a source. The count rate above the background count rate is attributed to the collection of signals from other sources, such as the Bayard-Alpert gauge, or the ionization gauge, used for vacuum measurement.

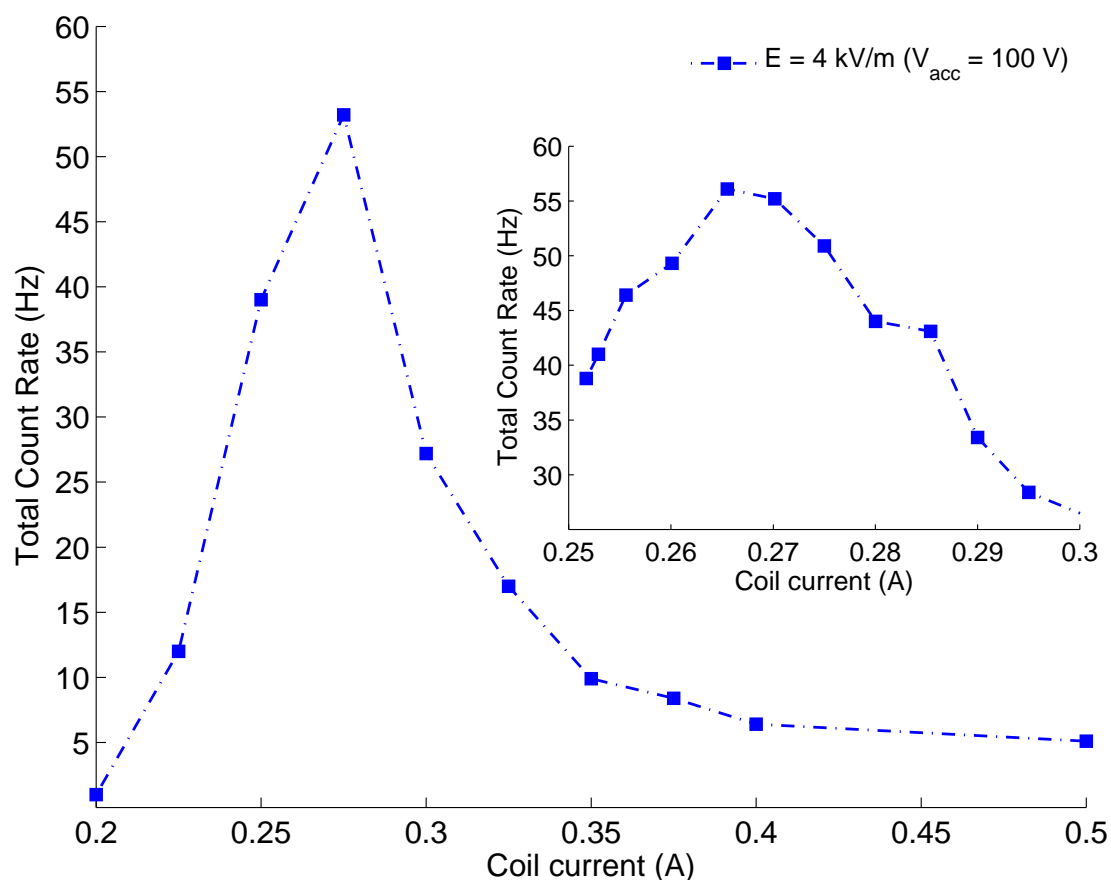


Figure 5.26. Variation of the count rate on the electron microchannel plate with respect to the electrical current through the magnet coils at 4 kV/m electric field.

Another observation was the dependence of the magnet current that maximizes the count rate on the acceleration voltage. Since E/B^2 is a device parameter that is related to the geometry, the electric and magnetic fields must be scaled accordingly to maintain the ratio. Therefore, if the electric field is quadrupled, the magnetic field is expected to double. Figure 5.27 shows the plot for the count rate on the electron microchannel plate with respect to the electrical current through the magnet coils.

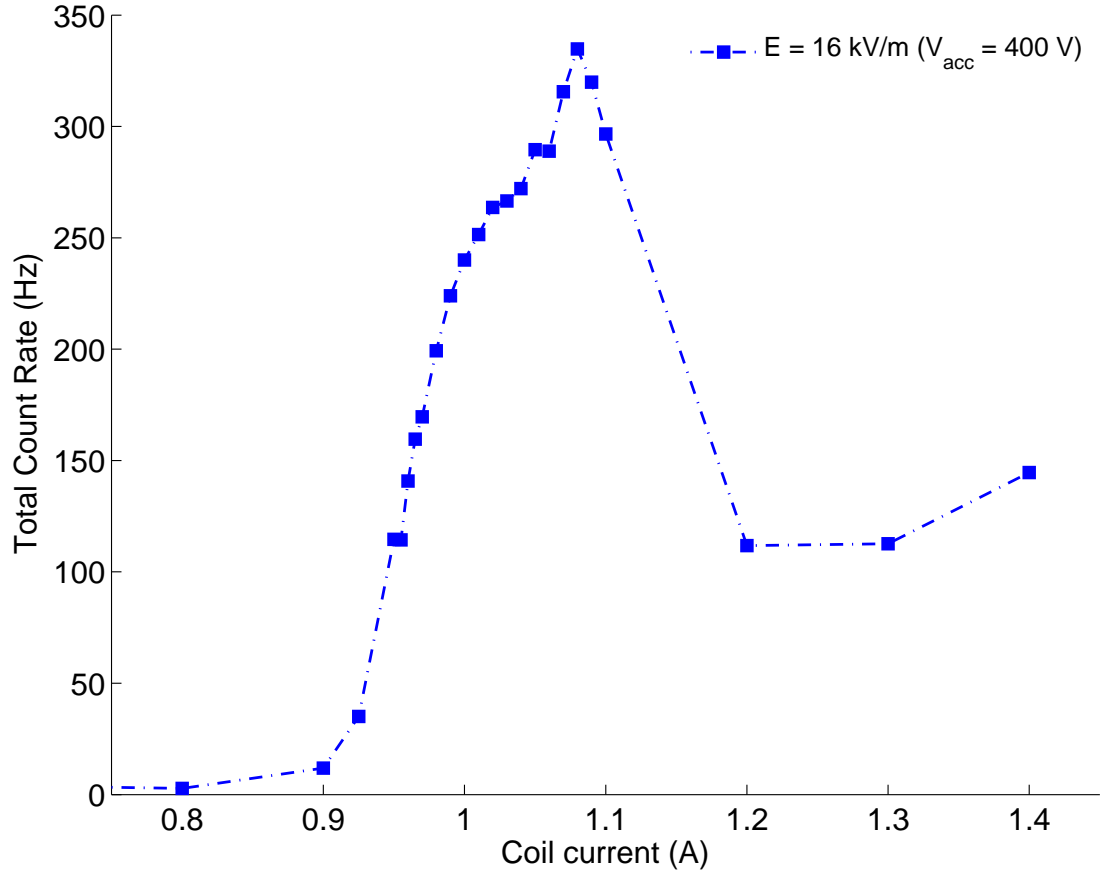


Figure 5.27. Variation of the count rate on the electron microchannel plate with respect to the electrical current through the magnet coils at 16 kV/m electric field.

It was observed that the maximum count rate was achieved with 100-V acceleration potential at $i_{\text{coil}} = 0.265$ A. At 400-V acceleration potential, the magnet current that maximizes the count rate was $i_{\text{coil}} = 1.080$ A, which gives a ratio of 4.08 that scales with the E/B^2 ratio as expected.

Another observation by comparing Figure 5.26 and Figure 5.27 was that the increase in the count rate at 400-V acceleration potential is sharper than the increase at 100-V

acceleration potential. This can be interpreted as an indication that the electron beam is spatially less dispersed at higher electric field values culminating in a more rapid collection of the beam area on the detecting surface.

5.3.2 Discussion on Experimental Results

Below, the interpretation and analysis of the experimental measurements will be presented.

Offset and Delay Correction of the Ion Time-of-Flight Spectrum

Since the signal from the ion detector was used as the start trigger on the Ortec 9308 time analyzer, the raw time-of-flight spectra shown in Figure 5.25 can be expressed as

$$\begin{aligned}\tau_1 &= \tau_{e1} - \tau_\alpha + \tau_{\text{bias}} \\ \tau_2 &= \tau_{e2} - \tau_\alpha + \tau_{\text{bias}}\end{aligned}\tag{5.13}$$

where τ_{e1} and τ_{e2} correspond to nominal electron flight times for acceleration potentials 150 V and 600 V. The offset and delay corrected spectra can be found by

$$\begin{aligned}\tau_\alpha &= \tau_{e1} - \tau_1 + \tau_{\text{bias}} \\ \tau_\alpha &= \tau_{e2} - \tau_2 + \tau_{\text{bias}}\end{aligned}\tag{5.14}$$

Nominal electron flight times can be found by $\tau_{e_i} = 2\pi m_e / e_0 B_i$ using the corresponding magnetic field values. The values are calculated as $\tau_{e1} = 10.630 \text{ ns}$ and $\tau_{e2} = 5.581 \text{ ns}$. Using the measured time offset of the Ortec 9308 time analyzer $\tau_{\text{bias}} = 2.686 \text{ ns}$, offset and time-delay corrected spectra are found. Figure 5.28 shows the corrected spectra. Since the measured source has a nominal thickness of 0.5 to 1.0 μm , the alpha spectra were expected to have a broad distribution. The spectrum obtained with 150-V acceleration potential covers approximately a 4-ns time window with a full-width at tenth maximum (FWTM) of 2.35 ns, and has an integrated count rate of 241.1 cps. The spectrum with 600-V acceleration potential stretches an approximately 2.0-ns time window with a FWTM of 1.29-ns, and has an integrated count rate of 240.5 cps. The count rates are within 0.3%, which is reasonable to consider within the experimental error margins.

The fact that the spectral width narrowed as the electron acceleration potential was increased indicates that the broadening has a significant electron time-of-flight dispersion component. The observation that the count rate is invariant with respect to change in

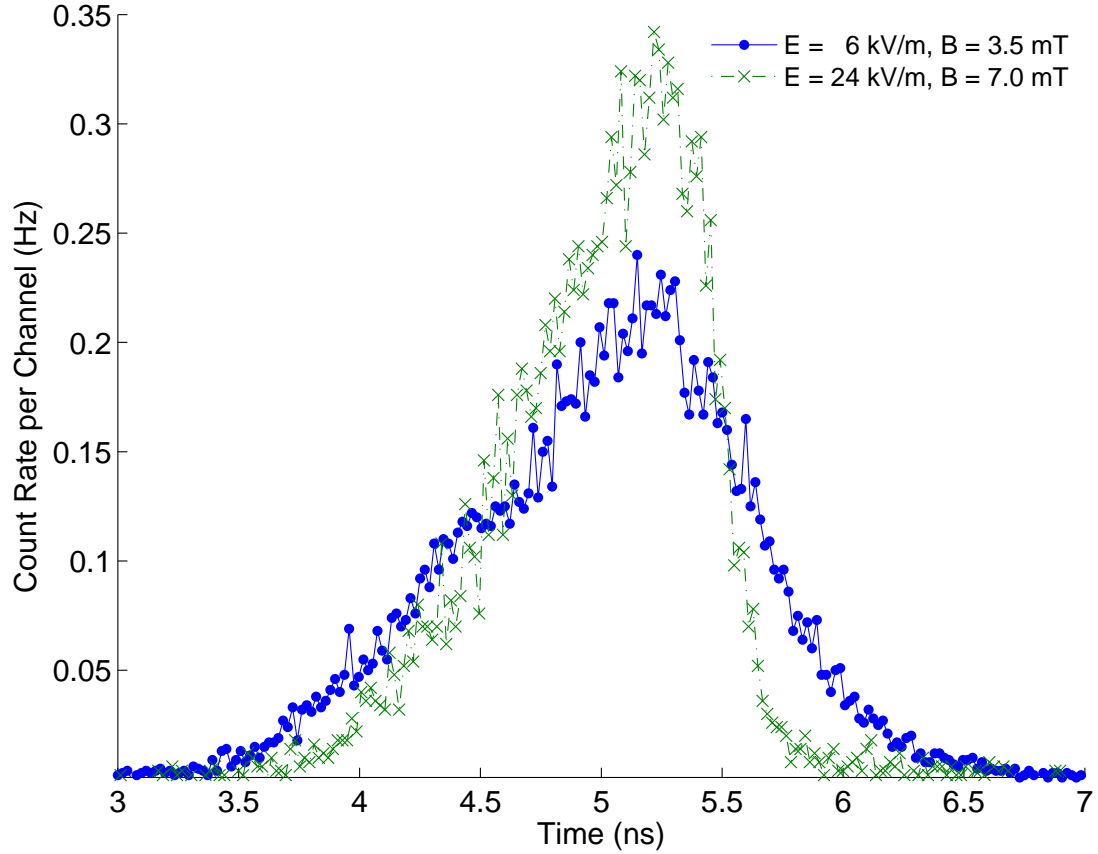


Figure 5.28. Offset and delay corrected ion time-of-flight spectra of the ^{210}Po alpha source obtained with the CEM field spectrometer at different electric and magnetic field values.

acceleration potential also signifies that the broadening is indeed a function of dispersion in electron flight time.

It can be easily discerned that the flight time dispersion is proportional to the total flight time of the electron: the longer it takes the electron to hit the electron microchannel plate, the wider the time-of-flight variation window will become. A quick way to demonstrate the correlation between the electron transport time and the spectral width is to compare the ratios of the processes for the acceleration potentials applied, i.e.

$$\frac{FWHM_1}{\tau_{e1}} \cong 4.52$$

$$\frac{FWHM_2}{\tau_{e2}} \cong 4.33$$

The values are within 5%. It was already expected that the calculated figures would

deviate from each other due to the fact that the distribution has a width resulting from the width of the source. Another reason for deviation is the reading error on the spectrum due to excessive noise.

In order to mitigate this effect if not completely eliminate it, the electron transport time from the surface of the electron emitter to the surface of the microchannel plate must be made as small as possible. The nominal electron transport time for an electron with zero velocity ejected from the origin of the electron emitting surface, i.e. the carbon foil, can be reduced by increasing the magnetic field value as can be seen in the cycloid period equation, $\tau = 2\pi m_e / e_0 B$. As the magnetic field increases, the required electric field also increases. The increase in electric field results in further enhancement in electron collection since a higher field value has a more pronounced effect to correct the course of electrons that are not ejected in the direction of the surface normal.

This hypothesis can be verified by increasing the applied magnetic field. The presented experimental measurements fall short of full demonstration of this effect since the maximum electrical current was reached with the available current supply. Another concern was that the Helmholtz coil could not handle higher current due to the lack of heat removal in the coils. Therefore, a complete data set was not collected.

Energy Calibration of the Time-of-Flight Spectrum

Once the absolute time-of-flight spectra are obtained as presented in the previous section, the spectra can be converted to energy. Since the ion flight path, L_{ion} , is fixed at a nominal value, the energy of the ion corresponding to a certain channel can be found by

$$E_i = \frac{1}{2} m_{\text{ion}} \left(\frac{L_{\text{ion}}}{t_i} \right)^2 \quad (5.15)$$

where the index i denotes the channel number in both the energy and time spectra.

Figure 5.29 shows the energy spectra of the alphas ejected by the ^{210}Po source. The peak locations are found to be 4672 keV for the spectrum acquired with 150-V acceleration, and 4631 keV for the spectrum acquired with 600-V acceleration. From the result of the TRIM simulation calculated with the given geometrical parameters in the experiment, the peak location was expected to be located at 4464 keV. The deviation between the measured and simulated results is within 5%. The major source of the deviation is the uncertainty in the thickness of the source layer. The manufacturer's specification gives a broad range for the thickness of the layer, therefore constituting the highest uncertainty. What is striking is the extreme spread in the energy spectrum.

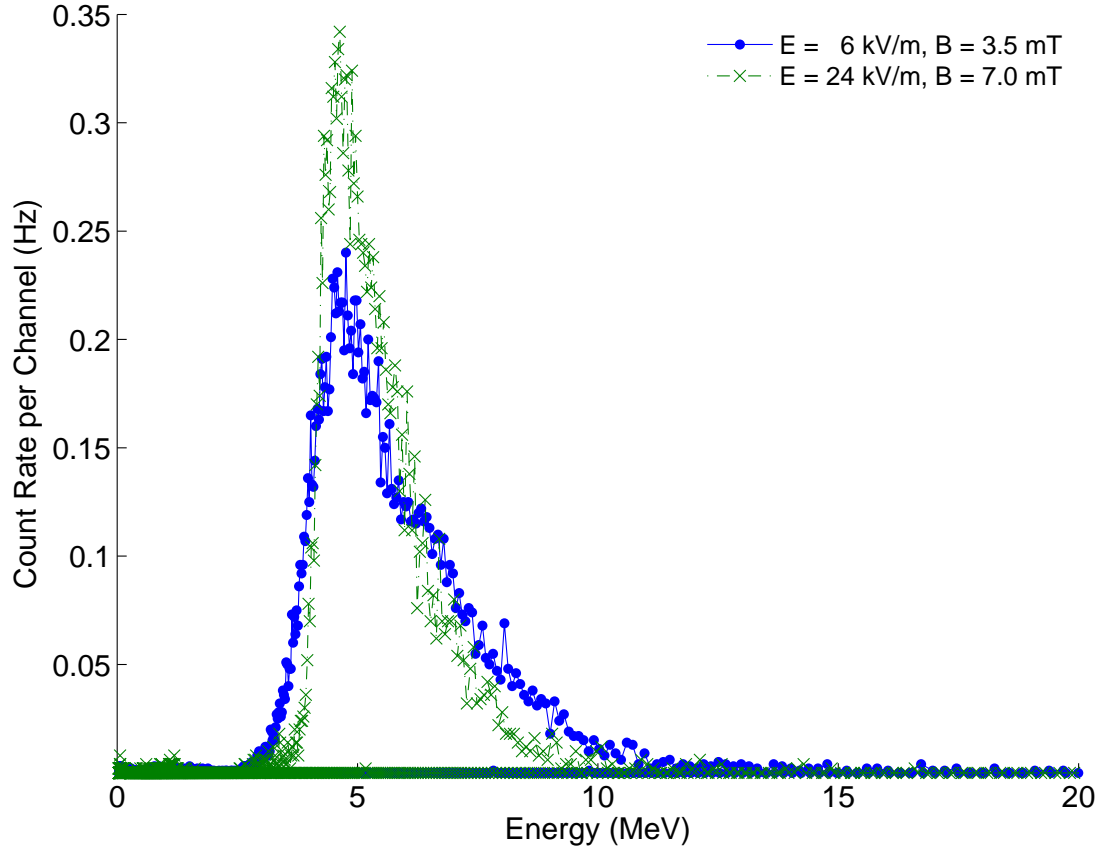


Figure 5.29. Energy spectrum of alpha particles from the ^{210}Po alpha source after calibration.

Since the source is ^{210}Po , which emits 5.3 MeV alpha particles, no particle in excess of this energy would be expected. Furthermore, the TRIM simulation shows that 99.9% of the particles have energies below 4650 keV because the source layer is covered with additional metallic layers, as described previously. The measurements, however, show counts at much higher energies. Although the result seems to be unusual, this was in fact expected due to the spread in electron arrival time. Since the signal from electron microchannel plate was used as the stop trigger, the expression for the ion arrival time is

$$\tau_{\alpha} = \tau_e + \tau_{\text{bias}} - \tau \quad (5.16)$$

Hence, electron arrival times on the electron microchannel plate in excess of the nominal arrival time will result in calculation of shorter alpha arrival times, which will yield an anomalous conversion in the energy spectrum.

The nominal transport times of alpha particles from the surface of the carbon foil

to the surface of the microchannel plate were calculated to be 5.39 *ns* and 5.21 *ns* for the low- and high-extreme of the simulated spectrum shown in Figure 5.24, which gives a full-width of 0.18 *ns*. The width of both distributions is much broader than what is nominally expected from the model, contributing to a more pronounced spread in the energy spectrum because of quadratic dependence of energy on time.

As presented in Section 2.4.3, the sensitivity of the conversion algorithm to the $\delta t \approx 1.2$ *ps* variation around the alpha arrival time of $\tau \sim 5$ *ns* is approximately $\Delta E \approx 2$ *keV*. Considering the FWTM of the spectrum acquired at 600-*V* acceleration potential, which is 1.29*ns*, the unusual spread can be better explained.

Resolution of the CEM Field Spectrometer

The analysis of the resolution of the CEM field spectrometer can be made by resorting to the Equation (A.22). Since the microchannel plate protrudes into the electric field by about $h = 3$ *mm*, the equation can be rearranged as

$$\frac{v_{y0}}{\omega} \sin \omega t - \frac{v_{z0} + E/B}{\omega} (1 - \cos \omega t) - h = 0 \quad (5.17)$$

A simulation of time-of-flight dispersion can be done by sampling the initial velocity of the electron over the theoretical energy and angular distributions, and solving the transcendental equation, Equation (5.17), for each sampled velocities. Figure 5.30 shows a sample simulation of electron flight time dispersion due to initial momentum spread computed at 150-*V* acceleration potential. As seen in the figure, the head of the distribution exhibits a rapid rise. This behavior is observed to have resulted from the secondary electrons emitted close to the axial direction. For such electrons, variations in speed are relatively less consequential than those in angle. The longer tail that extends into longer flight times is found to be the result of the angular cosine distribution of the secondary electron, whereas the relatively sharp rise is a result of the variation in kinetic energy of the secondary electrons that are emitted within a narrow forward cone along the direction of the ion. It is seen that the electrons that are emitted in the opposite direction with respect to the electron microchannel plate have the longest flight time, hence cause the highest spread. The dependence of the electron arrival time dispersion on E/B , as computed by a series of Monte Carlo simulations, is shown in Figure 5.31. The dispersion FWTM falls rapidly at the beginning and continues to drop more gradually at higher E/B values as expected. Also shown in Figure 5.31 is the plot of $(E/B)^{-1}$. On a first-order approach, the flight time fluctuations can be approximated by

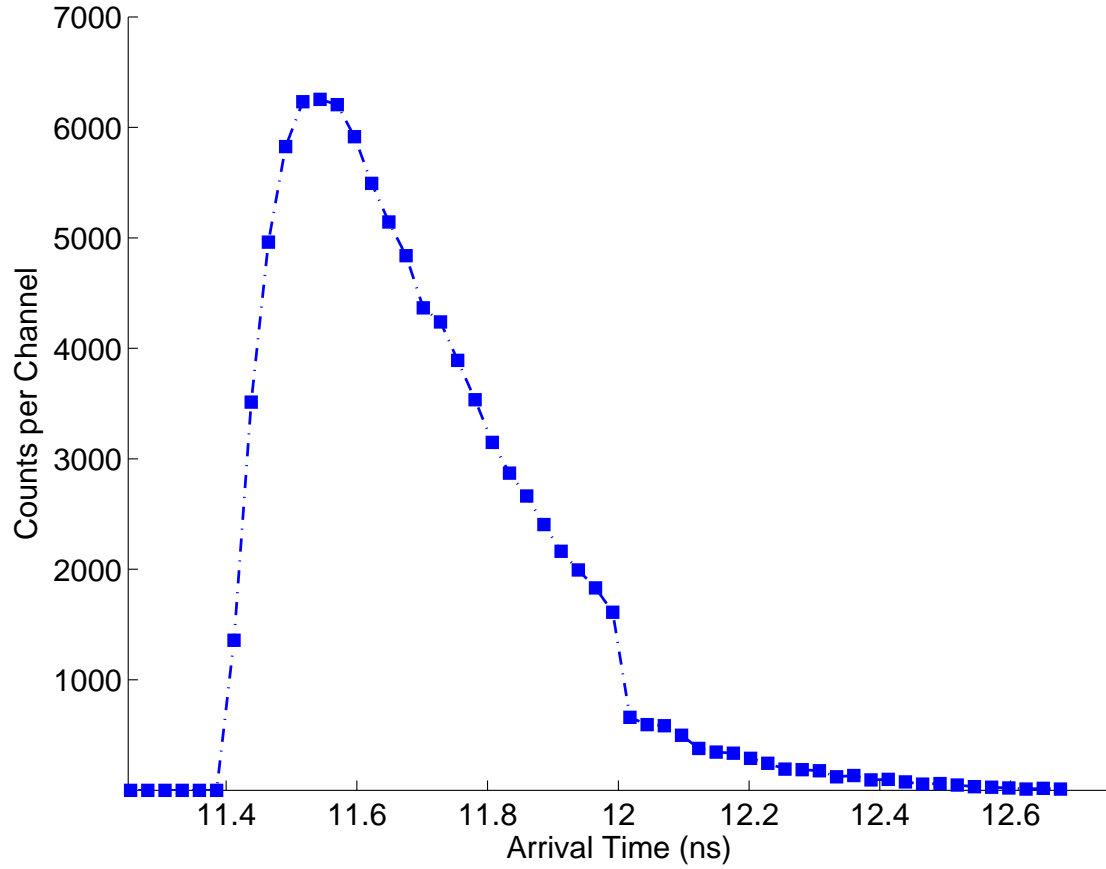


Figure 5.30. Simulate electron flight time dispersion at 150-V acceleration potential due to initial momentum spread.

$$\delta t \propto \frac{1}{\omega} \frac{v(0)}{(E/B)} \quad (5.18)$$

Consider a case where the magnetic field is doubled. In order to preserve the E/B^2 ratio, the electric field must be quadrupled. In this case, E/B ratio doubles, i.e.

$$\frac{E}{B} \mapsto \frac{4E}{2B} = \frac{2E}{B}$$

which, in a first-order approximation, is expected to result in a half-width time dispersion, i.e.

$$\frac{1}{\omega} \frac{v(0)}{(2E/B)} \approx \frac{\delta t}{2}$$

As presented in the previous sections, the full-width at tenth maxima of the distributions

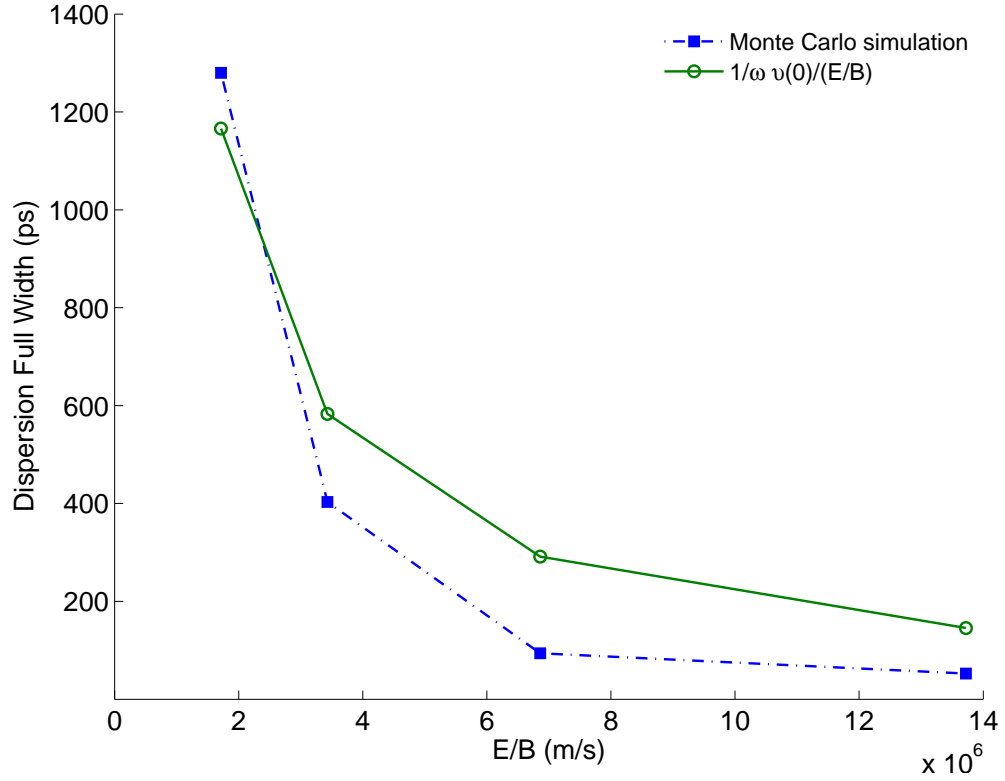


Figure 5.31. Variation of electron flight time dispersion with respect to E/B ratio calculated by the Monte Carlo simulation.

were improved from 2.35 ns to 1.29 ns , the ratio of which gives 1.82, which is close to the expected value from the first-order approximation.

Detection Efficiency of the CEM Field Spectrometer

The geometric efficiency of the time-of-flight telescope was calculated by the Monte Carlo simulation presented in Appendix B.4. The geometric parameters of the spectrometer were given precisely, and a simulation was run with 10^7 particles. The simulation yielded a geometric efficiency of 1.54×10^{-4} . The residual activity of the ^{210}Po source is calculated approximately to be 2 mCi . From these values, the detection efficiency of the CEM field time-of-flight spectrometer was calculated as

$$\varepsilon \approx 3\%$$

As presented in Section 5.2.2, the calculated detection efficiency of the CEM field spectrometer is close to the detection efficiency of the PEM field spectrometer.

CHAPTER

6

SUMMARY AND CONCLUSIONS

6.1 Summary of the Research

Ion time-of-flight spectrometers are investigated for application to neutron depth profiling. Neutron depth profiling has been successfully used since the 1970's to obtain concentration versus depth profile of a number of light elements in almost any substrate. Isotopes that are commonly known to be appropriate for analysis with the technique are listed in Table [2.2](#).

There are two main objectives of this dissertation: (1) to demonstrate the limits of the depth resolution of the neutron depth profiling technique using the conventional methods that rely on energy spectrometry, (2) to show that the ion time-of-flight spectrometers that are widely used in similar applications can be adopted for neutron depth profiling.

In conventional neutron depth profiling, residual energies of the particles that are emitted by the neutron capture reaction are measured with a semiconductor detector. A spectrum of particle energy is obtained from the pulse height analysis. Each individual energy spectrum is a distribution of frequencies related to the depth of the reaction site. A depth distribution can be obtained by a linear transformation of that spectrum. The number of counts for each bin can also be linked to the number of isotopes at the corresponding depth. Two sample spectra are obtained with energy spectrometry at the

Penn State Breazeale Reactor thermal beam port BP4. Experimental data is presented along with ion transport simulations.

Two ion time-of-flight spectrometers have been designed and built. The first design employs parallel electric and magnetic fields created within a solenoid. The solenoid provides magnetic field of uniformity within 9%, and creates a Gaussian surface that delineates the active region of the spectrometer similar to a Faraday cage. A uniform electric field is created by a series of evenly placed plates with static potentials applied through a resistor network.

The ion beam passes through a thin foil made of a conductive material -carbon is the preferred material in this study- that is stretched on an aperture on the first accelerator plane. The thickness of the foil must be kept minimal in order to minimize energy loss straggling as well as scattering in the foil. The passage of the ion causes ejection of electrons from both sides of the foil through a process called *ion-induced secondary electron emission* (IISEE). The ejected electrons are accelerated by the electric field in the axial direction. The magnetic field in the axial direction causes the electrons to move in helical trajectories. The net effect is a helicoid with increasing pitch. The presence of the magnetic field acts as a confining force for the electron beam. By varying the magnetic field, the optical pattern on the source plane, i.e. the carbon foil, can be transferred on the target plane, i.e. the detector, as shrunk or magnified. As the magnetic field increases, the optical image gets smaller, and vice versa.

The field uniformity is essential to minimize flight time dispersions due to initial momentum spread of secondary electrons, and ultimately improve the measurement resolution. The solenoid used in the measurements generates a magnetic field of $70 \times 10^{-4} \text{ T}$ at 1 A electrical current, and provides a field uniformity of 9% within the entire unit. The electric field uniformity is obtained by precise separation of the disks and using well balanced resistors (within 0.1%) in the network. Some field distortion is expected due to variation of geometrical location of aperture for ions on each disk.

Measurements with the PEM field spectrometer were done with a Tandem linear accelerator at IBM T.J. Watson Research Center, Yorktown, NY. Alpha beams of various energy and intensity were used to test the measurement resolution and detection efficiency of the spectrometer. The beam energy is measured with a surface barrier detector placed on a swinging arm upstream in the target chamber. When the arm is raised, the beam hits the entrance window of the spectrometer. Vacuum is maintained inside the chamber at $\sim 10^{-5} \text{ Pa}$ during the experiment to protect the microchannel plates.

Measurements were taken at alpha beam energies of 1.0, 1.5 and 2.0 MeV. The sig-

nal generated by the ion was used as the start trigger, and the signal by the electron as the stop trigger. The stop signal line was delayed by $\tau_{\text{delay}} = 60 \text{ ns}$. Two carbon foils of different thicknesses were used to observe the effect of straggling and multiple scattering in the foil. The axial electric field maintained inside the solenoid is varied from 5 kV/m to 50 kV/m to observe the effect on flight time dispersion. Significant improvement in time resolution is obtained by increasing the electric field: the spectral spreads were measured $\sigma = 420 \text{ ps}$ and $\sigma = 110 \text{ ps}$ at 5 kV/m and 50 kV/m , respectively at 1.5-MeV beam energy with carbon foil of 50 nm nominal thickness. It is found that the measurement resolution is approximately proportional to the square root of the acceleration field keeping all other parameters the same. The energy resolution was calculated to be $\sigma_E = 57.6 \text{ keV}$ at 5 kV/m , and $\sigma_E = 14.82 \text{ keV}$ at 50 kV/m . Measurements at multiple energies allowed for accurate calculation of physical dimensions, which can be used in future calculations.

The detection efficiency of the PEM field spectrometer was calculated based on the beam intensity. The beam intensity prior to entering the spectrometer was measured with a silicon surface barrier detector, from which the efficiency of the spectrometer was calculated as 3.5% for 1-MeV alphas, and 1.5% for 2-MeV alphas.

The second design employs an axial electric field parallel to the ion momentum vector and a cross magnetic field. The electric field is created by a series of equally spaced acceleration stages. Multiple acceleration stages act as field guards providing some degree of protection against stray fields. The potentials on each stage are obtained from a resistor network similar to the PEM field spectrometer. The magnetic field is generated by a Helmholtz coil. The coil pair generated a nominal magnetic field of $85 \times 10^{-4} \text{ T}$ at 1 A electrical current with a field uniformity of 3%.

As in the case of the PEM field spectrometer, ions go through a thin carbon foil stretched on an aperture on the first acceleration plate. A 3-mm diameter TEM grid with 50% transmission was used as the electron generator. The ion continues on its straight path with essentially no significant change in its trajectory. The secondary electrons created by the ion in the carbon foil are accelerated by the electric field, and are turned towards the electron microchannel plate, which is mounted on the same plate as the carbon foil. The net effect on electron is a cycloid trajectory.

Test measurements were made with a ^{210}Po alpha source. The source is uniformly distributed inside a silver matrix of a nominal thickness as per the specifications given by the manufacturer. The source layer was known to be coated with additional gold, nickel and aluminum layers to provide diffusion resistance. Because of the thickness of

the source layer and the presence of additional layers, the alpha energy was expected to have a broad spectrum. It was also known that ^{206}Pb , the recoil from the disintegration, could not be observed due to the fact that the layers are optically thick for the recoil.

Time-of-flight spectra were obtained at 150 V and 600 V acceleration potentials. The magnet current was adjusted to create a magnetic field value that matches the electric field value to transport the ejected electrons onto the electron microchannel plate. In this measurement, the signal generated by the ion was used as the start trigger, and the signal by the electron as the stop trigger.

Peak centroids were calculated to be 13.264 ns for 600 V and 18.314 ns for 150 V. The expected spectral shift from the potential change is $\Delta\tau_{\text{theo}} = 4.993$ ns. The measured spectral shift is $\Delta\tau_{\text{exp}} = 5.049$ ns, which is within 1% of the calculated result. The peak energies are found at 4672 keV for the spectrum acquired with 150-V acceleration, and 4631 keV for 600-V acceleration. The TRIM simulation estimated the peak location to be at 4464 keV. The deviation between the measured and simulated results for peak position is within 5%. The deviation is attributed to the noise content in the measurement as well as the uncertainty in the source layer thickness.

The resolution of the CEM field spectrometer was affected by the initial secondary electron momentum distribution. Since an experimental measurement was not done with an ion beam, the resolution of the spectrometer was demonstrated by simulations. Unlike the PEM field spectrometer, which was quite insensitive to the initial momentum distribution of the secondary electrons, the resolution of the CEM field spectrometer is extremely sensitive to the initial angular distribution of the secondaries. Therefore, even at an identical electric field, the resolution of the CEM field spectrometer suffers more from the electron transport. The full width of the time dispersion was calculated from the Monte Carlo simulation to be ~ 1280 ps at $E/B \approx 1.72 \times 10^6$ m/s, which was obtained at $V_E = 150$ V and $i_B = 0.375$ A. The dispersion full width becomes 52.4 ps at $E/B \approx 1.4 \times 10^7$ m/s that corresponds to $V_E = 9600$ V and $i_B = 3$ A. These electric and magnetic field values maintain the E/B^2 ratio, which is the characteristic parameter of the electron optical device for proper focusing.

In order to achieve the same resolution as the PEM field spectrometer, a higher electric field must be established with the CEM field spectrometer. Since the focal length of the secondary electrons is a function of both the electric and magnetic field in the cross field configuration, the magnetic field needs to be scaled accordingly to properly steer the secondary electron beam onto the microchannel plate detector.

The converted energy spectrum exhibited unusual broadening into the high-energy

values. The observation is a result of the fact that the electron signal was used as the stop trigger. Therefore, spread into longer electron flight times from the nominal value results in the registration of shorter flight times for ions. When converted to an energy spectrum, the ions that are in coincidence with the electrons with long flight times fall are calculated to have higher energy.

The detection efficiency of the CEM field spectrometer was calculated based on the residual activity of the ^{210}Po alpha source and the computed solid angle of the time-of-flight spectrometer. Since the spectrometer employs multiple stages and apertures, an analytical treatment is tedious. The solid angle of the spectrometry system was calculated with a Monte Carlo simulation by tallying a large set of particle history. The detection efficiency of the spectrometer was then found to be $\sim 3\%$.

6.2 Conclusions

It is proven theoretically and demonstrated experimentally that ion time-of-flight spectrometry is a powerful technique that can be used for high-resolution energy measurements provided that certain conditions are met. Improved resolution makes it suitable for application to neutron depth profiling.

The conclusions of this research may be summarized as follows:

1. Ion time-of-flight spectroscopy is a powerful technique to measure the energy of ions with high resolution. Since the response of a time-of-flight spectrometer is not linear in energy, the strength of the technique is more evident for ions with low speed. Therefore, for the (n, p) and (n, α) reactions used in the neutron depth profiling technique, significant measurement resolution improvement can be obtained if the recoil signal is used for depth calculations instead of the p or α signal. This is also the case for the neutron depth profiling measurements made with the conventional methods. However, in the conventional method, the resolution improvement comes only from higher stopping force exerted on the projectile, whereas for time-of-flight spectrometry, the measurement resolution comes from the lower speed of the ion as well as higher stopping force exerted on the particle in the substrate.

For instance, considering $^{14}\text{N}(n, p)^{14}\text{C}$ reaction, using the signal from ^{14}C in the ion time-of-flight spectrometer is expected to improve the measured energy resolution by a factor of ~ 180 compared to using the p signal. In the case of $^{10}\text{B}(n, \alpha)^7\text{Li}$ reaction, however, using the ^7Li signal instead of the α signal improves the measured energy resolution only by a factor of 3. In terms of depth resolution, the gain

is even higher since projectiles with higher atomic numbers have larger stopping force in the material.

Based on this information, it is possible to come up with a figure of merit on advantages of moving to ion time-of-flight spectrometry for neutron depth profiling. The figure of merit can be determined by the projectile mass and energy. The ion flight path that will give the desired depth resolution can be found based on this information. If the detection efficiency is acceptable with the flight path, the use of time-of-flight spectrometry is justified.

2. **Detection Efficiency:** It was observed with the experimental results that one of the major obstacles in adopting ion time-of-flight spectroscopy for neutron depth profiling is the low detection efficiency. The dominant factor that limits the detection efficiency is the low solid angle as seen by the ion detector, which is a consequence of the telescopic configuration. There are proposed methods such as large-area spectrometers to increase the effective solid angle of the start detector.

Microchannel plate efficiency for ions is also an important factor that limits the detection efficiency. As evidenced in the literature [119], there are design modifications that replace the microchannel plate with a fast semiconductor detector, which is 100% efficient for charged particles. If designed carefully, microchannel plates generate very sharp and stable time pulses. The time response of semiconductor detectors is not as fast as of microchannel plates, which will manifest as an uncertainty source to the measurement. The choice of the detector is a tradeoff between the efficiency and resolution. There are, however, commercially available semiconductor detectors that can generate pulses as fast as 200-ps at FWHM.

3. **Source Strength:** Low detection efficiency compared to energy spectrometry requires higher source strength for applicability to neutron depth profiling. In a neutron depth profiling measurement, the source strength can be increased by increasing the neutron flux impinging on the sample, reducing the neutron energy thereby increasing the probability of the capture reaction, or by using a neutron lens to focus the neutron beam to a small spot on the sample. The latter technique can be better applied to cold neutron beam.
4. **Higher Magnetic Field:** The effect of the magnetic field is different in the parallel electric/magnetic (PEM) field spectrometer and the cross electric/magnetic (CEM) field spectrometer. In the PEM field spectrometer, magnetic field value has

no effect on the resolution of the spectrometer as a result of the electron transport time dispersion. In the parallel field configuration, magnetic field acts as a focusing force and confines the electron beam generated in the carbon foil by the ion in a helicoidal trajectory of certain radius. The radius of the helix becomes smaller as the magnetic field increases.

In the CEM field spectrometer, however, there is a direct correlation between the magnetic field and the required electric field, which is a function of the device size. A low electric field results in inadequate electron acceleration, which ultimately causes longer flight times and further dispersion for electrons in the active volume of the device. The electric field must be increased significantly in order to take advantage of the technique. However, the magnetic field must be scaled in accordance with the electric field for proper focusing of the secondary electron beam.

A higher magnetic field for the same magnet size can be achieved in two ways: Either the turn density of the magnet or the magnet current can be increased. The higher turn density can be achieved either by using smaller wire size or employing multiple layers. Either way, the impedance of the magnet becomes larger. The field is proportional to the magnet current, therefore wire current can also be increased to achieve higher field. All these steps increase the power rating of the magnet. As the power consumption increases, the magnet generates more heat, which has to be removed by some fashion in the vacuum to prevent insulation failure. Another way to achieve a higher magnetic field with an electromagnet is by using an iron core. However, the iron core brings additional challenges such as hysteresis.

Permanent magnets have been successfully used in similar applications of ion time-of-flight spectrometry. Although it is challenging to design a volume with a uniformly distributed magnetic field using permanent magnets, the advantages such as no power requirement hence no heat generation, compactness, and field stability for long time periods make them overwhelmingly favorable. There are software packages available that compute the field distribution in a volume from permanent magnet sources as well as field trimming media such as Rose shims [115].

5. **Noise:** Microchannel plate noise was observed to be a very important impediment in achieving an efficient measurement device.

Sharp time pulses generated by microchannel plates are susceptible to reflections at connection boundaries. Sudden impedance change causes a portion of the pulse to be reflected back to the source creating a standing waveform that looks like a

ringing pattern. Therefore, the microchannel plate assembly needs to be designed carefully in compliance with the impedance of the instrumentation, usually $50\ \Omega$. The complete waveguide from the anode of the assembly, cables and connections such as electrical feedthroughs must conform to the impedance matching requirement to minimize the problem. The number of connections must be kept minimal. Gold plated SMA connectors are known to perform well up to $18\ GHz$, and are recommended along the signal line in connections. Double shielded signal cables also help reduce the electronic noise to some extent.

Ringling is an important factor that contributes to spectral broadening with the measurement electronics used in this study, especially so in the stop detector. The Ortec 9308 picosecond time analyzer has multiple stop capability, which means that a single start signal can be accompanied by more than one stop signal. If the main signal has ringing components, each component will be registered by the time analyzer at a corresponding time channel resulting in false coincidences. If the rise time of the pulses generated by the microchannel plate is short and the measured ion has low speed, these false coincidences may fall into the spectral region of interest, and cause broadening and shape distortion.

In order to eliminate this problem, the discriminator level on the Ortec 9327 preamplifier and timing discriminator can be increased. However, if the discriminator level is too high, it will eliminate the legitimate pulses along with the ringing components, further reducing the overall detection efficiency of the spectrometer. The pulse height generated by microchannel plates does not have a fixed value, therefore it is not a trivial task to determine the optimal discriminator level for best performance under the presence of noise and signal reflections.

6.3 Recommendations and Future Work

The source strength, i.e. the (n, p) or (n, α) reaction rate, of a typical neutron depth profiling measurement is relatively low for the geometric configurations used in time-of-flight systems. Considering the fact that the strength of time measurements comes with long ion flight paths, such a configuration drastically reduces the count rate even with the brightest neutron sources and reactions with the highest cross sections.

A time-of-flight spectrometer that will be used in neutron depth profiling must possess two critical qualities: (1) good time, hence energy resolution; (2) high detection efficiency, i.e. large solid angle and detector efficiency. Principally, these qualities are in conflict

with each other. Therefore, it is possible to conclude that an optimal configuration exists for each reaction type and sample implantation dose that satisfies an objective function that maximizes the resolution at the specified efficiency.

A conceptual design that uses parallel electric and magnetic fields is shown in Figure 6.1. As seen in the figure, the active volume of the spectrometer where the electron transport takes place is kept minimal to reduce the electron arrival time dispersion on the electron microchannel plate. It was concluded in Section 5.2.2 that the electron flight time dispersion is proportional to $\delta v_{z0}/E$ where δv_{z0} is the perturbation in the initial velocity of the secondary electrons and E is the electric field. The effect of increasing the electric field was demonstrated experimentally in Section 5.2.1 and shown in Figure 5.13. Keeping the electron flight path shorter increases the electric field at the same acceleration potential. Shortening the flight path also reduces the vulnerability of the electrons to field nonuniformities.

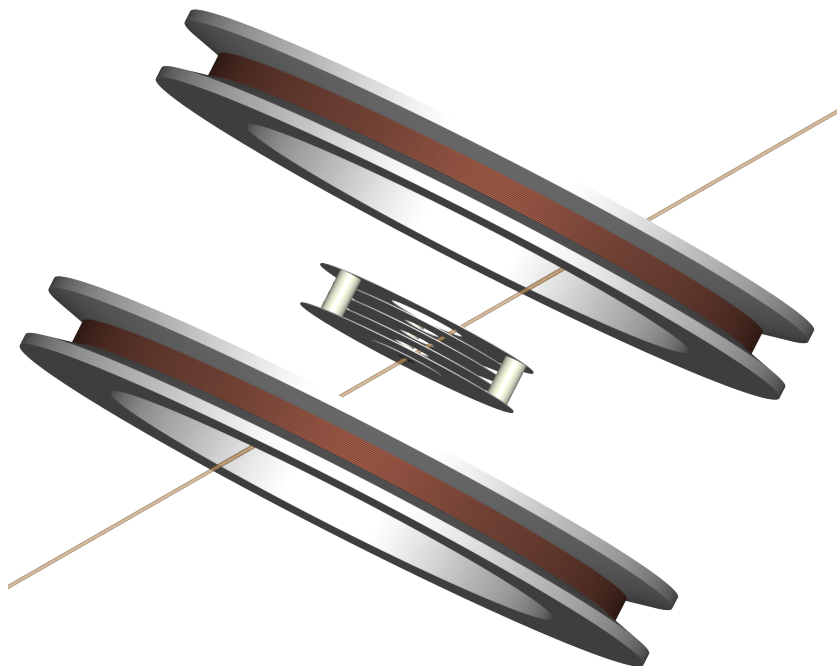


Figure 6.1. Conceptual parallel electric/magnetic (PEM) field spectrometer for improved measurement resolution.

This configuration allows the ion detector to be placed closer to the source to improve the solid angle. This shortens the ion flight path, hence deteriorates the measurement resolution of the time-of-flight system. However, this configuration can be optimal for the profiling of isotopes that yield low-speed massive ions.

Another ion time-of-flight spectrometer design that might be feasible for neutron

depth profiling measurements was proposed by Fang et al [85, 86]. The spectrometer employs a nonuniform electric field produced by three metal plates forming a triangular prism. A cross magnetic field is generated by a Helmholtz coil pair that creates a uniform field in the electron transport region. A three-dimensional drawing of the conceptual spectrometer is shown in Figure 6.2.

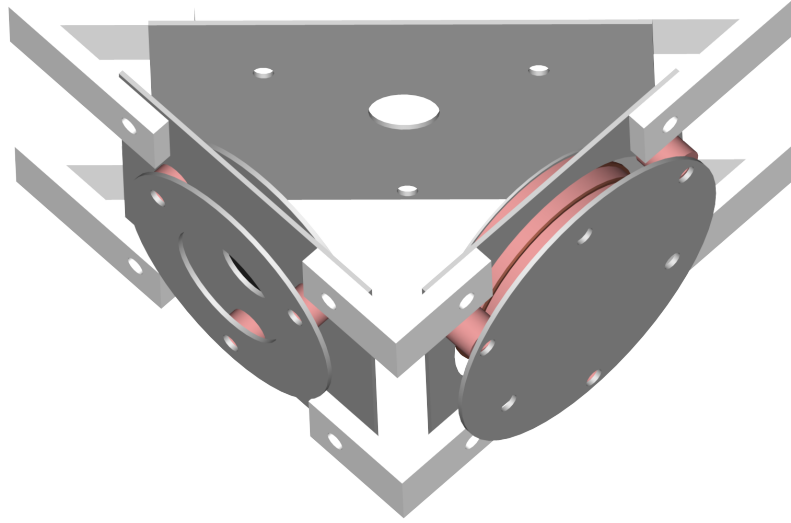


Figure 6.2. Ion time-of-flight spectrometer using a nonuniform electric field in a triangular domain.

The ion beam enters the spectrometer through a thin carbon foil placed on an entrance plate -shown on the left in Figure 6.2. The ion continues on its straight path and leaves the spectrometer through the aperture on the exit plate or the hypotenuse in Figure 6.2. The secondary electrons ejected by the carbon foil are accelerated by the nonuniform electric field and rotated $\pi/2$ by the magnetic field onto the electron microchannel plate detector mounted on the signal plate -shown on the right in Figure 6.2. The nonuniform field creates an environment that selectively accelerates electrons based on their proximity to the electron detector, i.e. the electrons that are ejected from a point on the carbon foil that is closer to the electron detector are accelerated less than those ejected from a farther point on the foil. This nonuniformity reduces the geometric convolution between the source plate and the target plate. However, the nonuniform acceleration results in variable magnetomotive force relative to the speed of the electron, which creates different radii of curvature. However, Fang et al showed that the time

dispersion that results from nonuniform radii of curvature is less than the dispersion due to geometric convolution [85].

6.3.1 Future Designs

There are spectrometer designs that will improve the detection efficiency of the time-of-flight telescope. One technique employs an ion time-of-flight spectrometer for both start and stop detectors. Similar experimental configurations can be found in the literature [83, 84, 87]. The energy loss straggling in multiple foils can be significant for heavier ions. High-uniformity ultrathin carbon foils, i.e. foils under 10 nm, can be used for secondary electron generation to minimize energy loss straggling.

If a focused neutron beam is used, one possibility is to use carbon foils stretched on hemispherical thin grids. The radius of the hemisphere can be adjusted in such a way that the sample is located in the center of the sphere. This virtually eliminates time dispersion of the ion transport time due to geometric convolution between the sample and the detector as presented in Section 2.3.2.

As mentioned in the Conclusions section, fast-rise time large-area semiconductor detectors can be used to gain from the detector efficiency. A rise time of 200 ps is reported for PIPS detectors by the addition of a 200-Å aluminum layer [68]. This results in approximately 2 keV energy resolution for alpha particles at $\sim 5\text{-MeV}$ energy. However, loss of measurement resolution from timing walk and jitter might be smaller than the resolution deterioration due to energy loss straggling, particularly for low-speed particles.

Fast rise time must be matched with a high-bandwidth preamplifier. As stated before, using a 1-GHz preamplifier adds close to 10-ps of timing uncertainty due to integration time associated with the bandwidth of the preamplifier [67]. In order to take advantage of high bandwidth with faster rise time, preamplifier bandwidth must be increased.

BIBLIOGRAPHY

- [1] ZIEGLER, J., B. CROWDER, G. COLE, J. BAGLIN, and B. MASTERS (1972) "Boron atom distributions in ion-implanted silicon by the $n, {}^4_2\text{He}$ nuclear reaction," *Applied Physics Letters*, **21**(1), pp. 16–17.
- [2] BIRSACK, J. P., D. FINK, and S. DATZ (1975) "Channeling, blocking, and range measurements using thermal neutron induced reactions," Plenum Publishing Corporation, New York; Hahn-Meitner Inst., Berlin, United States, pp. 737–747.
- [3] DOWNING, R. G., J. T. MAKI, and R. F. FLEMING "Analytical applications of neutron depth profiling," *Journal of Radioanalytical and Nuclear Chemistry*, **112**(1), pp. 33–46.
- [4] BIRSACK, J. P., D. FINK, R. HENKELMANN, and K. MULLER "The use of neutron induced reactions for light element profiling and lattice localization," *Nuclear Instruments and Methods*, **149**(1-3), pp. 93–97.
- [5] CERVENA, J., V. HNATOWICZ, J. HOFFMANN, Z. KOSINA, J. KVITEK, and P. ONHEISER "The use of the neutron induced reaction for boron profiling in Si," *Nuclear Instruments and Methods*, **188**(1), pp. 185–189.
- [6] ÜNLÜ, K. and B. W. WEHRING (1994) "Neutron depth profiling at the University of Texas," *Nuclear Instruments and Methods in Physics Research A*, **353**, pp. 402–405.
- [7] ÜNLÜ, K. and B. W. WEHRING "Neutron depth profiling applications at The University of Texas research reactor," *Journal of Radioanalytical and Nuclear Chemistry*, **217**(2), pp. 273–278.

- [8] ÇETINER, S., K. ÜNLÜ, and R. DOWNING “Development of time-of-flight neutron depth profiling at Penn State University,” *Journal of Radioanalytical and Nuclear Chemistry*, **271**(2), pp. 275–281.
- [9] EHRSTEIN, J. R., R. G. DOWNING, B. R. STALLARD, D. S. SIMONS, and R. F. FLEMING (1984) *Semiconductor Processing*, chap. Comparison of Depth Profiling ^{10}B in Silicon using Spreading Resistance Profiling, Secondary Ion Mass Spectrometry, and Neutron Depth Profiling, ASTM International, pp. 409–425.
- [10] COX, J. N., R. HSU, P. J. MCGREGOR, and R. G. DOWNING (1987) “NDP and FTIR Studies of Borophosphosilicate CVD Thin Film Glasses,” *Transactions on American Nuclear Society (ANS)*, pp. 207–209, Los Angeles, CA.
- [11] FINK, D. “Helium implantation and thermal annealing behaviour,” *Radiation Effects and Defects in Solids*, **106**(4), pp. 231 – 264.
- [12] JAMIESON, D. N., R. C. BOWMAN, P. M. ADAMS, J. F. KNUDSEN, and R. G. DOWNING *Use of Rutherford backscattering and optical spectroscopy to study boron implantation in cadmium telluride*, Tech. rep.
- [13] DOWNING, R. G., G. P. LAMAZE, J. K. LANGLAND, and S. T. HWANG (1993) “Neutron depth profiling: Overview and description of NIST facilities,” *Journal of Research of the National Institute of Standards and Technology*, **98**, pp. 109–121.
- [14] SCHWEIKERT, E. A. “Advances in nuclear analysis methods,” *The Analyst*, **114**(3), p. 269.
- [15] WELSH, J., W. JAMES, E. SCHWEIKERT, and H. MCWHINNEY “Studies in neutron depth profiling,” *Journal of Radioanalytical and Nuclear Chemistry*, **167**(1), pp. 111–119.
- [16] SCHWEIKERT, E. and J. WELSH “New approaches for neutron depth profiling,” *Journal of Radioanalytical and Nuclear Chemistry*, **180**(2), pp. 255–262.
- [17] WELSH, J. F. (1996) *The Development and Evaluation of Recoil-nucleus Time-of-flight Neutron Depth Profiling*, Ph.D. thesis, Texas A&M University.
- [18] SKŁODOWSKA-CURIE, M. (1900) “Sur la charge électrique des rayons dviabiles du radium,” *Comptes Rendus de l’Acadmie des Sciences*, **130**, p. 76.
- [19] BOHR, N. (1913) “On the decrease of velocity of swiftly moving particles in passing through electrified matter,” *Philosophical Magazine*, **25**, p. 19.
- [20] BOHR, N. (1915) “Decrease of speed of electrified particles in passing through matter,” *Philosophical Magazine*, **30**, p. 581.
- [21] BETHE, H. (1930) “Zur Theorie des Durchgangs schneller Korpuskularstrahlen durch Materie,” *Annalen der Physik*, **397**, pp. 325–400.
- [22] MØLLER, C. (1932) “Zur Theorie des Durchgangs schneller Elektronen durch Materie,” *Annales de Physique*, **5**, p. 531.

- [23] BLOCH, F. (1933) “Bremsvermögen von Atomen mit mehreren Elektronen,” *Zeitschrift für Physik*, **81**, pp. 363–376.
- [24] BLOCH, F. (1933) “Stopping power of matter for swiftly moving charged particles,” *Annales de physique*, **16**, p. 287.
- [25] ZIEGLER, J. F. (1999) “Stopping of energetic light ions in elemental matter,” *Journal of Applied Physics*, **85**, pp. 1249–1272.
- [26] BOHR, N. H. D. (1948) *The penetration of atomic particles through matter*, J. Komm. Hos. E. Munksgaard, Kopenhagen.
- [27] LINDHARD, J. (1954) “On the Properties of a Gas of Charged Particles,” *Kgl. Danske Videnskab. Selskab Mat.-fys. Medd.*, **28**, pp. 1–57.
- [28] LINDHARD, J. and A. WINTHER (1964) *Mat. Fys. Medd. Dan. Vidensk. Selsk.*, **34**, p. 1.
- [29] BONDERUP, E. (1967) *Mat. Fys. Medd. Dan. Vidensk. Selsk.*, **35**.
- [30] SIGMUND, P. (1998) “Stopping power in perspective,” *Nuclear Instruments and Methods in Physics Research B*, **135**, pp. 1–4.
- [31] SIGMUND, P. and J. R. SABIN (2005) “Interplay of Classical and Quantum Mechanics in the Theory of Charged-Particle Stopping,” in *Advances in Quantum Chemistry*, vol. 48, Academic Press, pp. 91–110.
- [32] SIGMUND, P. (2004) *Stopping of Heavy Ions: a Theoretical Approach*, Springer Tracts in Modern Physics, 204, Springer, Berlin.
- [33] ZIEGLER, J. F., B. J. P., and L. U. (1985) *The Stopping and Range of Ions in Solids*, vol. 1, Pergamon Press, New York Oxford Toronto Sydney Frankfurt Tokyo.
- [34] ZIEGLER, J. F. (2004) “SRIM-2003,” *Nuclear Instruments and Methods in Physics Research B*, **219**, pp. 1027–1036.
- [35] BRANDT, W. and M. KITAGAWA (1982) “Effective stopping-power charges of swift ions in condensed matter,” *Phys. Rev. B*, **25**(9), pp. 5631–5637.
- [36] LINDHARD, J., M. SCHARFF, and H. SCHIØTT (1963) “Range concepts and heavy ion ranges. Notes on atomic collisions, II (Low velocity heavy ion ranges and relation to quasi-elastic atomic collisions between ions and atoms),” *Kgl. Danske Vid. Sels. Mat.-Fys. Medd.*, **33**, p. 1.
- [37] ZIEGLER, J. F., “Stopping/Transport and Range of Ions in Matter (SRIM/TRIM),” <http://www.srim.org/>.
- [38] AUDI, G., A. H. WAPSTRA, and C. THIBAULT (2003) “The AME2003 atomic mass evaluation: (II). Tables, graphs and references,” *Nuclear Physics A*, **729**(1), pp. 337–676.

- [39] ROSMAN, K. J. R. and P. D. P. TAYLOR (1998) "Isotopic Compositions of the Elements 1997," *Journal of Physical and Chemical Reference Data*, **27**, pp. 1275–1287.
- [40] TILLEY, D. R., C. M. CHEVES, J. L. GODWIN, G. M. HALE, H. M. HOFMANN, J. H. KELLEY, C. G. SHEU, and H. R. WELLER "Energy levels of light nuclei $A=5, 6, 7$," *Nuclear Physics A*, **708**(1-2), pp. 3–163.
- [41] FIRESTONE, R. B. "Nuclear Data Sheets for $A=22$," *Nuclear Data Sheets*, **106**(1), pp. 1–88.
- [42] BAGLIN, C. M. "Nuclear Data Sheets for $A = 59$," *Nuclear Data Sheets*, **95**(2), pp. 215–386.
- [43] NAKAGAWA, T., S. CHIBA, T. OHSAKI, and M. IGASHIRA (2000) "Maxwellian-Averaged Cross Sections Calculated from JENDL-3.2," *Nippon Genshiryoku Kenkyujo JAERI, Research*.
- [44] SPIELER, H. (2005) *Semiconductor Detector Systems*, Oxford Science Publication, Oxford, New York.
- [45] BOTHE, W. (1921) "Theorie der Zerstreuung der α -Strahlen ber kleine Winkel," *Zeitschrift für Physik A Hadrons and Nuclei*, **4**(2), pp. 300–314.
- [46] MOLIÈRE, G. (1948) "Theorie der Streuung schneller geladener Teilchen. II. Mehrfach-und Vielfachstreuun," *Z. Naturforsch.*, **3a**, pp. 78–79.
- [47] BETHE, H. A. (1953) "Molière's Theory of Multiple Scattering," *Phys. Rev.*, **89**(6), pp. 1256–1266.
- [48] MEYER, L. (1971) "Plural and Multiple Scattering of Low-Energy Heavy Particles in Solids," *Phys. Status Solidi*, **44**, pp. 253–268.
- [49] AMSEL, G., G. BATTISTIG, and A. L'HOIR (2003) "Small angle multiple scattering of fast ions, physics, stochastic theory and numerical calculations," *Nuclear Instruments and Methods in Physics Research B*, **201**, pp. 325–388.
- [50] FINK, D. (1996) *Neutron depth profiling*, HMI, Berlin.
- [51] SPAHN, G. and K. O. GROENEVELD "Angular straggling of heavy and light ions in thin solid foils," *Nuclear Instruments and Methods*, **123**(3), pp. 425–429.
- [52] SIGMUND, P. and K. B. WINTERBON "Small-angle multiple scattering of ions in the screened Coulomb region. I. Angular distributions," *Nucl. Instrum. Methods*.
- [53] BELERY, P., T. DELBAR, and G. GREGOIRE (1981) "Multiple scattering and energy straggling of heavy ions in solid targets," *Nuclear Instruments and Methods*, **179**(1), pp. 1–9.
- [54] GEMMELL, D. S. (1974) "Channeling and related effects in the motion of charged particles through crystals," *Rev. Mod. Phys.*, **46**(1), pp. 129–227.

- [55] FICHTNER, P. F. P., M. BEHAR, C. A. OLIVIERI, R. P. LIVI, J. P. DE SOUZA, F. C. ZAWISLAK, D. FINK, and J. P. BIRSACK “Energy dependence of the Z1-range oscillation effect in silicon,” *Nuclear Instruments and Methods in Physics Research Section B: Beam Interactions with Materials and Atoms*, **15**(1-6), pp. 58–60.
- [56] BIRSACK, J. P. (1987) *Ion Beam Modifications of Insulators*, vol. 1, chap. I, Elsevier Publ. Corp.
- [57] MAKI, J. T., R. F. FLEMING, and D. H. VINCENT (1986) “Deconvolution of neutron depth profiling spectra,” *Nuclear Instruments and Methods in Physics Research B*, **17**, pp. 147–155.
- [58] YAO, W.-M. and ET AL. (2006) “Review of Particle Physics,” *Journal of Physics G Nuclear Physics*, **33**, pp. 1–1232.
- [59] ZHANG, Y. and H. J. WHITLOW (2002) “Response of Si p-i-n diode and Au/n-Si surface barrier detector to heavy ions,” *Nuclear Instruments and Methods in Physics Research B*, **190**, pp. 383–386.
- [60] STEINBAUER, E., G. BORTELS, P. BAUER, J. P. BIRSACK, P. BURGER, and I. AHMAD “A survey of the physical processes which determine the response function of silicon detectors to alpha particles,” *Nuclear Instruments and Methods in Physics Research Section A: Accelerators, Spectrometers, Detectors and Associated Equipment*, **339**(1-2), pp. 102–108.
- [61] INSKEEP, C., E. ELAD, and R. A. SAREEN (1974) “Surface Barrier Structures with Various Metal Electrodes,” *IEEE Transactions on Nuclear Science*, **21**(1), pp. 379–385.
- [62] KANNO, I. (1990) “A model of charge collection in a silicon surface barrier detector,” *Review of Scientific Instruments*, **61**(1), pp. 129–137.
- [63] SIMON, A. and G. KALINKA (2005) “Investigation of charge collection in a silicon PIN photodiode,” *Nuclear Instruments and Methods in Physics Research B*, **231**, pp. 507–512.
- [64] ALKHAZOV, G. D., A. P. KOMAR, and A. A. VOROB’EV “Ionization fluctuations and resolution of ionization chambers and semiconductor detectors,” *Nuclear Instruments and Methods*, **48**(1), pp. 1–12.
- [65] ITO, M., H. KUME, and K. OBA (1984) “Computer analysis of the timing properties in micro channel plate photomultiplier tubes,” *IEEE Transactions on Nuclear Science*, **31**(1), pp. 408–412.
- [66] KUME, H., K. KOYAMA, K. NAKATSUGAWA, S. SUZUKI, and D. FATLOWITZ (1988) “Ultrafast microchannel plate photomultipliers,” *Appl. Opt.*, **27**(6), p. 1170.

- [67] COVA, S., M. GHIONI, and F. ZAPPA (1991) "Optimum amplification of microchannel-plate photomultiplier pulses for picosecond photon timing," *Review of Scientific Instruments*, **62**(11), pp. 2596–2601.
- [68] (2002), "Canberra Passivated Implanted Planar Silicon (PIPS) Detectors," .
- [69] CHU, W.-K. and D. T. WU (1988) "Scattering recoil coincidence spectrometry," *Nuclear Instruments and Methods in Physics Research B*, **35**, pp. 518–521.
- [70] CHU, W.-K. (1989) "Large angle coincidence spectrometry for neutron depth profiling," *Radiation Effects and Defects in Solids*, **108**(1), pp. 125 – 126.
- [71] PARIKH, N. R., E. C. FREY, H. C. HOFSSÄSS, M. L. SWANSON, R. G. DOWNING, T. Z. HOSSAIN, and C. WEI-KAN (1990) "Neutron depth profiling by coincidence spectrometry," *Nuclear Instruments and Methods in Physics Research B*, **45**, pp. 70–74.
- [72] SCHWEIKERT, E. and J. WELSH "An old-new tool for nuclear analysis: Time-of-Flight spectrometry," *Journal of Radioanalytical and Nuclear Chemistry*, **215**(1), pp. 23–30.
- [73] GOULDING, F. S. and B. G. HARVEY (1975) "Identification of Nuclear Particles," *Annual Review of Nuclear and Particle Science*, **25**, pp. 167–240.
- [74] LANG, W. and H. G. CLERC "A fast zero-time detector for time-of-flight measurements with heavy ions," *Nuclear Instruments and Methods*, **126**(4), pp. 535–539.
- [75] ZEBELMAN, A. M., W. G. MEYER, K. HALBACH, A. M. POSKANZER, R. G. SEXTRO, G. GABOR, and D. A. LANDIS "A time-zero detector utilizing isochronous transport of secondary electrons," *Nuclear Instruments and Methods*, **141**(3), pp. 439–447.
- [76] BOWMAN, J. D. and R. H. HEFFNER "A novel zero time detector for heavy ion spectroscopy," *Nuclear Instruments and Methods*, **148**(3), pp. 503–509.
- [77] GLOECKLER, G. and K. C. HSIEH "Time-of-flight technique for particle identification at energies from 2-400 keV/nucleon," *Nuclear Instruments and Methods*, **165**(3), pp. 537–544.
- [78] BUSCH, F., W. PFEFFER, B. KOHLMAYER, D. SCHULL, and F. PUHLHOFFER (1980) "A position-sensitive transmission time detector," *Nuclear Instruments and Methods*, **171**(1), pp. 71–74.
- [79] WILKEN, B. (1984) "Review Article: Identification techniques for nuclear particles in space plasma research and selected experimental results," *Reports of Progress in Physics*, **47**, pp. 767–853.
- [80] NAKAGAWA, T. and W. BOHNE "A compact and gridless channel plate start detector," *Nuclear Instruments and Methods in Physics Research Section A: Accelerators, Spectrometers, Detectors and Associated Equipment*, **271**(3), pp. 523–526.

- [81] KRAUS, R. H., D. J. VIEIRA, H. WOLLNIK, and J. M. WOUTERS “Large-area fast-timing detectors developed for the TOFI spectrometer,” *Nuclear Instruments and Methods in Physics Research Section A: Accelerators, Spectrometers, Detectors and Associated Equipment*, **264**(2-3), pp. 327–332.
- [82] MIZOTA, T., K. YUASA-NAKAGAWA, S. M. LEE, and T. NAKAGAWA “Timing properties of a stop detector for a time-of-flight system,” *Nuclear Instruments and Methods in Physics Research Section A: Accelerators, Spectrometers, Detectors and Associated Equipment*, **305**(1), pp. 125–128.
- [83] ANDREYEV, A. N., V. V. BASHEVOY, D. D. BOGDANOV, V. I. CHEPIGIN, A. P. KABACHENKO, O. N. MALYSHEV, J. ROHAC, S. SARO, A. V. TARANENKO, G. M. TER-AKOPIAN, and A. V. YEREMIN “Large area high-efficiency time-of-flight system for detection of low energy heavy evaporation residues at the electrostatic separator VASSILISSA,” *Nuclear Instruments and Methods in Physics Research Section A: Accelerators, Spectrometers, Detectors and Associated Equipment*, **364**(2), pp. 342–348.
- [84] SARO, S., R. JANIK, S. HOFMANN, H. FOLGER, F. P. HEBERGER, V. NINOV, H. J. SCHOTT, A. P. KABACHENKO, A. G. POPEKO, and A. V. YEREMIN (1996) “Large size foil-microchannel plate timing detectors,” *Nuclear Instruments and Methods in Physics Research Section A: Accelerators, Spectrometers, Detectors and Associated Equipment*, **381**(2-3), pp. 520–526.
- [85] FANG, Z. and D. J. O’CONNOR (1997) “A time detector design for MeV particles using secondary electron emission and microchannel plates,” *Review of Scientific Instruments*, **68**(11), pp. 4027–4034.
- [86] FANG, Z. and D. J. O’CONNOR “Time detector design for MeV particles I - the electric field in a triangular domain,” *Nuclear Instruments and Methods in Physics Research Section A: Accelerators, Spectrometers, Detectors and Associated Equipment*, **413**(1), pp. 83–91.
- [87] KUZNETSOV, A. V., E. J. VAN VELDHUIZEN, L. WESTERBERG, V. G. LYAPIN, K. ALEKLETT, W. LOVELAND, J. BONDORF, B. JAKOBSSON, H. J. WHITLOW, and M. EL BOUANANI “A compact Ultra-High Vacuum (UHV) compatible instrument for time of flight-energy measurements of slow heavy reaction products,” *Nuclear Instruments and Methods in Physics Research Section A: Accelerators, Spectrometers, Detectors and Associated Equipment*, **452**(3), pp. 525–532.
- [88] GLOECKLER, G., J. GEISS, H. BALSIGER, P. BEDINI, J. C. CAIN, J. FISHER, L. A. FISK, A. B. GALVIN, F. GLIEM, and D. C. HAMILTON (1992) “The Solar Wind Ion Composition Spectrometer,” *Astron. Astrophys. Suppl. Ser.*, **92**, pp. 267–289.
- [89] GUBLER, L., P. WURZ, P. BOCHSLER, and E. MOBIUS “High resolution isochronous mass spectrometer for space plasma applications,” *International Journal of Mass Spectrometry and Ion Processes*, **148**(1-2), pp. 77–96.

- [90] RÈME, H. and ET AL. (2001) “First multispacecraft ion measurements in and near the Earth’s magnetosphere with the identical Cluster ion spectrometry (CIS) experiment,” *Annales Geophysicae*, **19**, pp. 1303–1354.
- [91] GLOECKLER, G. and ET AL. (1998) “Investigation of the composition of solar and interstellar matter using solar wind and pickup ion measurements with SWICS and SWIMS on the ACE spacecraft,” *Space Science Reviews*, **86**(1), pp. 497–539.
- [92] DEVOOGHT, J., J.-C. DEHAES, A. DUBUS, M. CAILLER, and J.-P. GANACHAUD (1991) *Particle Induced Electron Emission I*, vol. 122 of *Springer Tracts in Modern Physics*, chap. Theoretical Description of Secondary Electron Emission Induced by Electron or Ion Beams Impinging on Solids, Springer-Verlag, Berlin Heidelberg New York, pp. 67–128.
- [93] KUDO, H. (2001) *Ion-Induced Electron Emission from Crystalline Solids*, vol. 175 of *Springer Tracts in Modern Physics*, Springer-Verlag, Berlin Heidelberg New York.
- [94] VILLARD, M. P. (1899) *J. Phys. Theor. Appl.*, **8**, p. 5.
- [95] AUSTIN, L. and H. STARKE (1902) “Ueber die Reflexion der Kathodenstrahlen und eine damit verbundene neue Erscheinung secundärer Emission,” *Annalen der Physik*, **314**, pp. 271–292.
- [96] THOMSON, J. J. (1904) *Proc. Cambridge Philos. Soc.*, **13**, p. 49.
- [97] RUTHERFORD, E. (1905) *Philos. Mag.*, **10**, p. 193.
- [98] FÜCHTBAUER, C. (1906) *Phys. Z.*, **7**, p. 153.
- [99] RÜCHARDT, E. (1926) *Handbuch der Physik*, vol. 24, chap. 1-2, Springer-Verlag, Berlin, p. 105.
- [100] GEIGER, H. (1926) *Handbuch der Physik*, vol. 24, chap. 1-2, Springer-Verlag, Berlin, p. 171.
- [101] BETHE, A. J., H. A. (1960) *Experimental Nuclear Physics*, chap. 2, 4.1.1, John Wiley, New York, p. 232.
- [102] KAPITZA, P. (1923) *Phil. Mag.*, **45**, p. 989.
- [103] SALOW, H. (1940) “Sekundäre elektronen emission,” *Physik. Z*, **41**, p. 434.
- [104] HASSELKAMP, D. (1992) *Particle induced electron emission II*, vol. 123, chap. 1, Springer-Verlag, Berlin, p. 1.
- [105] STERNGLASS, E. J. (1957) “Theory of Secondary Electron Emission by High-Speed Ions,” *Phys. Rev.*, **108**(1), pp. 1–12.
- [106] HILL, A. G., W. W. BUECHNER, J. S. CLARK, and J. B. FISK (1939) “The Emission of Secondary Electrons Under High Energy Positive Ion Bombardment,” *Phys. Rev.*, **55**(5), pp. 463–470.

- [107] AARSET, B., R. W. CLOUD, and J. G. TRUMP (1954) “Electron Emission from Metals under High-Energy Hydrogen Ion Bombardment,” *Journal of Applied Physics*, **25**(11), pp. 1365–1368.
- [108] PARILIS, E. S. and L. M. KISHINEVSKII (1960) *Sov. Phys.-Solid State*, **3**, p. 885.
- [109] SCHOU, J. (1980) “Transport theory for kinetic emission of secondary electrons from solids,” *Phys. Rev. B*, **22**(5), pp. 2141–2174.
- [110] SCHOU, J. (1988) “Secondary Electron Emission From Solids by Electron and Proton Bombardment,” *Scanning Microsc.*, **2**(2), pp. 607–632.
- [111] CLOUVAS, A., C. POTIRIADIS, H. ROTHARD, D. HOFMANN, R. WÜNSCH, K. O. GROENEVELD, A. KATSANOS, and A. C. XENOULIS (1997) “Role of projectile electrons in secondary electron emission from solid surfaces under fast-ion bombardment,” *Phys. Rev. B*, **55**(18), pp. 12086–12098.
- [112] PAULY, N., A. DUBUS, M. RÖSLER, H. ROTHARD, A. CLOUVAS, and C. POTIRIADIS “Electron emission induced by H^+ and H^0 incident on thin carbon foils: influence of charge changing processes,” *Nuclear Instruments and Methods in Physics Research B*.
- [113] GROVES, T. R. and R. A. KENDALL (1999), “Distributed Direct Write Lithography System using Multiple Variable Shaped Electron Beams,” .
- [114] FERT, C. and P. DURANDEAU (1967) *Focusing of Charged Particles*, vol. 1, chap. Magnetic Electron Lenses, Academic Press, New York and London, pp. 309–352.
- [115] ROSE, M. E. (1938) “Magnetic Field Corrections in the Cyclotron,” *Phys. Rev.*, **53**(9), pp. 715–719.
- [116] NIEDERHAUS, J. H. J. (2003) *A single-disk-chopper time-of-flight spectrometer for thermal neutron beams*, M.Sc. in nuclear engineering, The Pennsylvania State University.
- [117] (2005), “Ortec Modular Pulse-Processing Electronics Catalog,” .
- [118] DOWNING, R. G. and S. CETINER (2006) “Enhanced Reaction Rates in NDP Analysis by Neutron Scattering,” *Transactions of the American Nuclear Society*, **95**, pp. 459–460.
- [119] ARPS, J. H., M. E. MIKLIS, and R. A. WELLER (1994) “Adaptation of particle-telescope technology for medium energy ion beam analysis,” *Review of Scientific Instruments*, **65**(5), pp. 1575–1579.

APPENDIX

A

EQUATIONS OF MOTION FOR ELECTRONS IN FREE SPACE

Following sections present the solutions for the equations of motion for electrons in vacuum for two special cases: static parallel electric and magnetic fields, and static cross electric and magnetic fields.

A.1 Parallel Electric and Magnetic (PEM) Fields

Given static electric field $E_z = -E$ and magnetic field $B_z = B$. The equation of motion of the electron is

$$\frac{d\mathbf{v}_\perp}{dt} = -\frac{e_0}{m_e} (\mathbf{v}_\perp \times \mathbf{B}) \quad (\text{A.1})$$

$$\frac{dv_z}{dt} = \frac{e_0}{m_e} E \quad (\text{A.2})$$

where $\mathbf{v}_\perp = \begin{pmatrix} v_x \\ v_y \end{pmatrix}$ is the velocity component perpendicular to the direction of the magnetic field. The system of equations can be expressed in matrix form as follows:

$$\underbrace{\frac{d}{dt} \begin{pmatrix} v_x \\ v_y \end{pmatrix}}_{\dot{\mathbf{v}}_\perp} = \underbrace{\begin{pmatrix} 0 & -e_0 B/m_e \\ e_0 B/m_e & 0 \end{pmatrix}}_{\mathbf{A}} \underbrace{\begin{pmatrix} v_x \\ v_y \end{pmatrix}}_{\mathbf{v}_\perp} \quad (\text{A.3})$$

$$\frac{d}{dt} v_z = \frac{e_0}{m_e} E \quad (\text{A.4})$$

The solution to the above system of equations is

$$\mathbf{v}_\perp = e^{\mathbf{A}t} \mathbf{v}_{\perp 0} = \begin{pmatrix} \cos \omega t & -\sin \omega t \\ \sin \omega t & \cos \omega t \end{pmatrix} \mathbf{v}_{\perp 0} \quad (\text{A.5})$$

$$v_z(t) = v_{z0} + \frac{e_0}{m_e} Et \quad (\text{A.6})$$

where $\mathbf{v}_{\perp 0} = \begin{pmatrix} v_{x0} \\ v_{y0} \end{pmatrix}$ is the initial velocity perpendicular to the direction of the magnetic field and $\omega = e_0 B/m_e$ is called the *frequency of gyration* or *cyclotron frequency*. The position of the electron can be obtained by integrating the velocity vector:

$$\mathbf{x}(t) - \mathbf{x}(0) = \int_0^t d\xi \mathbf{v}(\xi) \quad (\text{A.7})$$

where $\mathbf{x}(0)$ is the initial position vector. The position vector can be written in open form

$$x(t) = x(0) + \frac{v_{x0}}{\omega} \sin \omega t - \frac{v_{y0}}{\omega} (1 - \cos \omega t) \quad (\text{A.8})$$

$$y(t) = y(0) + \frac{v_{x0}}{\omega} (1 - \cos \omega t) + \frac{v_{y0}}{\omega} \sin \omega t \quad (\text{A.9})$$

$$z(t) = z(0) + v_{z0}t + \frac{1}{2} \frac{e_0}{m_e} Et^2 \quad (\text{A.10})$$

A.2 Cross Electric and Magnetic (CEM) Fields

Given a static electric field $E_y = -E$ and a static magnetic field $B_x = B$. The motion of an electron is governed by the following system of equations:

$$\frac{dv_x}{dt} = 0 \quad (\text{A.11})$$

$$\frac{d\mathbf{v}_\perp}{dt} = -\frac{e_0}{m_e} (\mathbf{v}_\perp \times \mathbf{B} - \mathbf{E}) \quad (\text{A.12})$$

where \mathbf{v}_\perp is the velocity component perpendicular to the direction of the magnetic field.

The first equation yields that v_x is constant since no force acts upon the particle along that direction. The second equation is a non-homogeneous linear first-order differential equation. The general solution of this equation is obtained by the superposition of the homogeneous part and the particular part. The homogeneous part of the solution is found by solving

$$\frac{d\mathbf{v}_\perp}{dt} = -\frac{e_0}{m_e} \mathbf{v}_\perp \times \mathbf{B} \quad (\text{A.13})$$

Using the static field values $E_y = -E$ and $B_x = B$, Equation (A.13) can be represented as

$$\underbrace{\frac{d}{dt} \begin{pmatrix} v_y \\ v_z \end{pmatrix}}_{\dot{\mathbf{v}}_\perp(t)} = \underbrace{\begin{pmatrix} 0 & -e_0 B/m_e \\ e_0 B/m_e & 0 \end{pmatrix}}_{\mathbf{A}} \underbrace{\begin{pmatrix} v_y \\ v_z \end{pmatrix}}_{\mathbf{v}_\perp(t)} \quad (\text{A.14})$$

where $\omega = e_0 B/m_e$ is the frequency of gyration. The solution of this system of equations is

$$\mathbf{v}_\perp(t) = e^{\mathbf{A}t} \mathbf{v}_{\perp 0} = \begin{pmatrix} \cos \omega t & -\sin \omega t \\ \sin \omega t & \cos \omega t \end{pmatrix} \mathbf{v}_{\perp 0} \quad (\text{A.15})$$

where $\mathbf{v}_{\perp 0}$ is the initial velocity vector perpendicular to the direction of the magnetic field. Solution of the non-homogeneous part is the particular solution \mathbf{v}_t :

$$\begin{aligned} \frac{d\mathbf{v}_\perp}{dt} + \frac{e_0}{m_e} \mathbf{v}_\perp \times \mathbf{B} &= \frac{e_0}{m_e} \mathbf{E} \\ \Rightarrow \mathbf{v}_t B^2 - \mathbf{B} (\mathbf{B} \mathbf{v}_t) &= \mathbf{E} \times \mathbf{B} \\ \Rightarrow \mathbf{v}_t &= \frac{1}{B^2} \mathbf{E} \times \mathbf{B} \end{aligned} \quad (\text{A.16})$$

\mathbf{v}_t is commonly referred to as the transverse drift velocity, and is perpendicular to both

E and **B**. By substituting the static field values $E_y = -E$ and $B_x = B$, \mathbf{v}_t reduces to

$$\mathbf{v}_t = \begin{pmatrix} 0 \\ 0 \\ -E/B \end{pmatrix} \quad (\text{A.17})$$

The general solution is

$$v_x(t) = v_{x0} \quad (\text{A.18})$$

$$v_y(t) = v_{y0} \cos \omega t - \left(v_{z0} + \frac{E}{B} \right) \sin \omega t \quad (\text{A.19})$$

$$v_z(t) = v_{y0} \sin \omega t - \left(v_{z0} + \frac{E}{B} \right) \cos \omega t - \frac{E}{B} \quad (\text{A.20})$$

The position of the particle is found by integrating the velocity vector subject to initial conditions $\mathbf{x}(0)$, i.e.

$$\mathbf{x}(t) - \mathbf{x}(0) = \int_0^t d\xi \mathbf{v}(\xi) \quad (\text{A.21})$$

which can be written in open form as

$$x(t) = x_0 + v_{x0}t \quad (\text{A.22})$$

$$y(t) = y_0 + \frac{v_{y0}}{\omega} \sin \omega t - \frac{1}{\omega} \left(v_{z0} + \frac{E}{B} \right) (1 - \cos \omega t) \quad (\text{A.23})$$

$$z(t) = z_0 + \frac{v_{y0}}{\omega} (1 - \cos \omega t) + \frac{1}{\omega} \left(v_{z0} + \frac{E}{B} \right) \sin \omega t - \frac{E}{B}t \quad (\text{A.24})$$

APPENDIX

B

LIBRARY OF COMPUTATIONAL TOOLS

A number of computational tools are presented. These codes were frequently used throughout this research.

B.1 Definitions of Physical Constants

This script initializes the common physical constants and is called by other scripts frequently. The script must be saved with the file name `phys_const.m` for proper execution of other scripts.

```
%  
% Sacit M. Cetiner  
% Department of Mechanical & Nuclear Engineering  
% Penn State University  
%  
  
% Physical constants obtained from NIST database  
  
% (c) 2006  
  
% Fundamental Physical Constants
```

```

c      = 299792458;           % Speed of light in vacuum (m/s)
m_e    = 9.1093826e-31;      % (kg) - electron mass
k      = 1.380650424e-23;    % Boltzmann constant (J/K)
h      = 6.6260693e-34;      % Planck constant
hbar   = h / (2*pi);         %
mu0    = 4*pi*1e-7;          % ~12.566370614e-7 (N/A^2) - Permeability in vacuum
e0     = 1/(mu0*c^2);        % ~8.854187817e-12 (F/m) - Permittivity in vacuum
eV     = 1.60217653e-19;     % (J) - electron volt
keV    = eV * 1e3;           % (J)
MeV    = eV * 1e6;           % (J)
GeV    = eV * 1e9;           % (J)

% Conversion factors
amu_to_kg = 1.660538782e-27; % (kg/u)
N_ava     = 6.02214179e23;    % (1/mol)
amu_to_MeV= 931.494028;      % (MeV/u)

% Commonly used quantities
m_proton  = 1.67262171e-27;    % (kg)
m_neutron = 1.67492728e-27;    % (kg)
m_alpha   = 6.6446565e-27;     % (kg)
m_lithium = 7.0160040 * amu_to_kg; % (kg)
m_carbon  = 12 * amu_to_kg;     % (kg)
m_Po      = 209.9828574 * amu_to_kg; % (kg)
m_Pb      = 205.9744490 * amu_to_kg; % (kg)

```

B.2 Depth Profiling Calculations

The scripts that are provided in this section require that the SRIM package be installed on the computer. The package can be downloaded from <http://www.srim.org> web page.

The following script is called from external scripts to load global variables to perform SRIM/TRIM calculations. The following code must be saved with the file name [LoadSRIMGlobals.m](#) for proper execution of other scripts. The stopping coefficient data file [scoef03.csv](#) must be present in the directory that this code will run. The data file [SCOEF03.DAT](#) can be found under [C:\Program Files\SRIM 2003\Data\](#) if default installation options are chosen for the SRIM package. The file [scoef03.csv](#) can be created by removing the first two columns of [SCOEF03.DAT](#) data file.

```
% Load global data for SRIM calculations

%
% Author: Sacit M. Cetiner
%       Ph.D. Candidate
%       Department of Mechanical & Nuclear Engineering
% (c) 2005
%

% Declare global variables
global ElementSymbol ElementName AtomicNumber MassNumber...
       MAIWeight NaturalWeight Density AtomicDensity...
       FermiVelocity HeatOfSublimation isSRIMGlobalsLoaded

% display('Loading SRIM globals...')

x = importdata('scoef03.csv');
ElementSymbol = x.textdata(:,1);
ElementName   = x.textdata(:,2);
AtomicNumber  = x.data(:,1);
MassNumber    = x.data(:,2);
MAIWeight     = x.data(:,3);
NaturalWeight = x.data(:,4);
Density       = x.data(:,5);      % (g/cm^3)
AtomicDensity = x.data(:,6);      % (atoms/cm^3)
FermiVelocity = x.data(:,7);      % (V_0)
HeatOfSublimation = x.data(:,8);  % (eV)
clear x

isSRIMGlobalsLoaded = true;

H = 1; He = 2; Li = 3; Be = 4; B = 5; C = 6;
N = 7; O = 8; F = 9; Ne = 10; Na = 11; Mg = 12;
```

```

Al = 13; Si = 14; P = 15; S = 16; Cl = 17; Ar = 18;
Fe = 26; Ni = 28; Cu = 29; Ga = 31; Br = 35; Ag = 47;
Au = 79; Pb = 82; Bi = 83; Po = 84; Th = 90; U = 92;
Pu = 94;

```

The following script is a MATLAB function and is the main code that executes the standalone application [SR.Module.exe](#) that is provided in the SRIM package. The code must be saved with the file name [SRIMInterface.m](#) to function.

```

%
% Prepares input for "SR Module.exe" to generate stopping tables
% FORMAT: [ SRIM_OUT Sei Sni Rpi Str_longi Str_lati ] = SRIMInterface(Z1, Z2, Ei)
% SRIM_OUT: [ E(keV) Se Sn Rp(A) Str_long(A) Str_lat(A) ]
%
% Sei:      Interpolated electronic stopping forces (eV/A) -returns vector if Ei is vector
% Sni:      Interpolated nuclear stopping forces vector (eV/A) -returns vector if Ei is vector
% Rpi:      Interpolated projected range vector (A) -returns vector if Ei is vector
% Str_longi: Interpolated longitudinal straggling vector (A) -returns vector if Ei is vector
% Str_lati:  Interpolated lateral straggling vector (A) -returns vector if Ei is vector
% Z1:      Atomic number of the ion
% Z2:      Atomic number of the target material
% Ei:      Energy at which return values are to be calculated (keV) - can be a vector
%
% * All spatial quantities are in Angstrom (A)
%
% Author: Sacit M. Cetiner
%      Ph.D. Candidate
%      Penn State University
%      Department of Mechanical & Nuclear Engineering
% (c) 2005

function [ SRIM_OUT Sei Sni Rpi Str_longi Str_lati ] = SRIMInterface(Z1, Z2, Ei)

outputDir = 'C:\Documents and Settings\User\Desktop'

global ElementSymbol ElementName AtomicNumber MassNumber...
        MAIWeight NaturalWeight Density AtomicDensity...
        FermiVelocity HeatOfSublimation

if (Ei > 1e5)
    sprintf('Excessive energy input! No calculations done...\n')
    return
end

[fid error]= fopen('sr.in', 'w', 'native');

OutputFileName = sprintf('%s in %s.txt', cell2mat(ElementName(Z1)), cell2mat(ElementName(Z2)));
IonData        = sprintf('%d    %0.4f\r\n', Z1, MAIWeight(Z1));
TargetData     = sprintf('0    %0.4f    0\r\n', Density(Z2));

```

```

TargetElements = sprintf('%d "%s" 100 %0.4f\r\n', Z2, cell2mat(ElementName(Z2)), MAIWeight(Z2));
EnergyString    = sprintf('%0.4e    %0.4e\r\n', 1e-3, 1e4);

fprintf(fid, '---Stopping/Range Input Data (Number-format: Period = Decimal Point)\r\n');
fprintf(fid, '---Output File Name\r\n');
fprintf(fid, '"%s"\r\n', OutputFileName);
fprintf(fid, '---Ion(Z), Ion Mass(u)\r\n');
fprintf(fid, IonData);
fprintf(fid, '---Target Data: (Solid=0, Gas=1), Density(g/cm3), Compound Corr.\r\n');
fprintf(fid, TargetData);
fprintf(fid, '---Number of Target Elements\r\n');
fprintf(fid, ' 1\r\n');
fprintf(fid, '---Target Elements: (Z), Target name, Stoich, Target Mass(u)\r\n');
fprintf(fid, TargetElements);
fprintf(fid, '---Output Stopping Units (1-8)\r\n');
%
% 1 -      ev / A
% 2 -      keV / um = eV/nm
% 3 -      MeV / mm
% 4 -      keV / (ug/cm^2)
% 5 -      MeV / (mg/cm^2)
% 6 -      keV / (mg/cm^2)
% 7 -      eV / (10^15 atoms/cm^2)
% 8 -      L.S.S. reduced units
%
fprintf(fid, ' 1\r\n');
fprintf(fid, '---Ion Energy : E-Min(keV), E-Max(keV)\r\n');
fprintf(fid, EnergyString);

out = fclose(fid);

PWD = pwd;

cd(outputDir);

! SRModule_2007

cd(PWD);

% Open the output file for parsing
fid2 = fopen(OutputFileName);

% Skip the first 50 lines
for i = 1:50
    fgetl(fid2);
end

% Read through the input deck
for k = 1:158

```

```

[ a b c d e f g h i j ] = strread(fgetl(fid2), '%f%s%f%f%f%s%f%s%f%s');
bb = cell2mat(b);
if bb(1) == 'e'
    E(k,:) = 1e-3 * a;          % Energy in keV
elseif bb(1) == 'M'
    E(k,:) = 1e3 * a;
else
    E(k,:) = a;
end

Se(k,:) = c;                   % Electronic stopping power
Sn(k,:) = d;                   % Nuclear stopping power

if cell2mat(f) == 'um'
    Rp(k,:) = 1e4 * e;         % Projected range in A
elseif cell2mat(f) == 'mm'
    Rp(k,:) = 1e7 * e;
else
    Rp(k,:) = e;
end

if cell2mat(h) == 'um'
    Str_long(k,:) = 1e4 * g;   % Longitudinal straggling in A
elseif cell2mat(h) == 'mm'
    Str_long(k,:) = 1e7 * g;
else
    Str_long(k,:) = g;
end

if cell2mat(j) == 'um'
    Str_lat(k,:) = 1e4 * i;    % Lateral straggling in A
elseif cell2mat(j) == 'mm'
    Str_lat(k,:) = 1e7 * i;
else
    Str_lat(k,:) = i;
end
end

% We are done with the file; close it!
fclose(fid2);

% Create SRIM output variable
SRIM_OUT = [ E Se Sn Rp Str_long Str_lat ];

% Interpolation
Sei = interp1(E, Se, Ei, 'pchip');
Sni = interp1(E, Sn, Ei, 'pchip');
Rpi = interp1(E, Rp, Ei, 'pchip');
Str_longi = interp1(E, Str_long, Ei, 'pchip');
Str_lati = interp1(E, Str_lat, Ei, 'pchip');

```

A sample depth profiling calculation for a given alpha particle spectrum `E_peak` (keV) in silicon can be performed as follows:

```
% Perform the NDP analysis
LoadSRIMGlobals
Z1 = 2;                                % Atomic number of helium
Z2 = 14;                               % Atomic number of silicon
[ SRIM_OUT Sei Sni Rpi Str_longi Str_lati ] = SRIMInterface(Z1, Z2, E_peak);
dp = ( Rpi(end) - Rpi ) * 1e-1;        % Depth profile (nm)
St = (Sei + Sni);                      % Total stopping power (eV/nm)
```


B.3 Automated TRIM Simulations

This tool gives the simulated energy spectrum of an ion ejected from a depth of a substrate. Initially, the ion is assumed to be monoenergetic. A distribution of energies is obtained due to the ensemble of infinite number of trajectories traced by the projectiles. The parameters given in the script are for a Po^{210} source in a 0.5-micron silver matrix coated with another 1.5-micron gold layer. This script requires that the [SRIM2003](#) package be installed on the computer in its default installation directory.

```
%
% Author: Sacit M. Cetiner
%       Ph.D. Candidate
%       Penn State University
%       Department of Mechanical & Nuclear Engineering
%
%
% (c) 2005
%

clear all

% Go to SRIM directory
cwd = pwd;
srmdir = 'C:\Program Files\SRIM 2003';
srimout = 'C:\Program Files\SRIM 2003\SRIM Outputs';

% Simulation parameters
part_num = 100; % Number of particles to be sent for each layer
lay_start = 1; % Depth where the layer starts (nm)
lay_end = 501; % Depth where the layer ends (nm)
inc = 100; % Layer increments (nm)

cd(srmdir)

% Edit the trimauto file
[fid error]= fopen('trimauto', 'w', 'native');
fprintf(fid, '1\r\n');
fprintf(fid, '\r\n');
fprintf(fid, 'TRIMAUTO allows the running of TRIM in batch mode.\r\n');
fprintf(fid, 'This feature is controlled by the number in line #1 (above).\r\n');
fprintf(fid, ' 0 = Normal TRIM - New Calculation based on TRIM.IN made by setup program.\r\n');
fprintf(fid, ' 1 = Auto TRIM - TRIM based on TRIM.IN. No inputs required.\r\n');
fprintf(fid, ' 2 = RESUME - Resume old TRIM calculation based on files.\r\n');
fprintf(fid, '\r\n');
fprintf(fid, ' Line #2 of this file is the Directory of Resumed data, e.g. A:\\TRIM2\\\r\n');
fprintf(fid, ' If empty, the default is the ''SRIM\SRIM Restore'' directory.\r\n');
fprintf(fid, '\r\n');
fprintf(fid, 'See the file TRIMAUTO.TXT for more details.\r\n');
```

```

fclose(fid);

for layerThickness = lay_start:inc:lay_end
    % Edit the trim input file
    [fid error]= fopen('trim.in', 'w', 'native');

    fprintf(fid, '    ==> SRIM-2003.26 This file controls TRIM Calculations.\r\n');
    fprintf(fid, 'Ion: Z1 ,   M1,   Energy (keV), Angle,Number,Bragg Corr,AutoSave Number.\r\n');
    fprintf(fid, ' 2 4.003 5304   0   %d 0   %d\r\n', part_num, part_num+1);
    fprintf(fid, 'Cascades, Random Number Seed, Reminders\r\n');
    fprintf(fid, '          2              0          0\r\n');
    fprintf(fid, 'Diskfiles: Ranges, Backscatt, Transmit, Sputtered, Recoils\r\n');
    fprintf(fid, '          0          0          2          0          0\r\n');
    fprintf(fid, 'Target material : Number of Elements & Layers\r\n');
    fprintf(fid, '"He (10) into Ag-Po+Thick Au Layer+Thin A" 3 3\r\n');
    fprintf(fid, 'Target Energies (eV): Binding, Surface, Individual Displacement\r\n');
    fprintf(fid, '          3      2.97      25      25      25\r\n');
    fprintf(fid, 'PlotType (0-5); Plot Depths: Xmin, Xmax(Ang.)\r\n');
    fprintf(fid, '          5              0          20000\r\n');
    fprintf(fid, 'Target Elements:      Z   Mass(amu)\r\n');
    fprintf(fid, 'Atom 1 = Ag =          47   107.87\r\n');
    fprintf(fid, 'Atom 2 = Po =          84   210\r\n');
    fprintf(fid, 'Atom 3 = Au =          79   196.97\r\n');
    fprintf(fid, 'Layer   Layer Name /   Width Density   Ag(47) Po(84) Au(79)\r\n');
    fprintf(fid, 'Numb.   Description   (Ang) (g/cm3)   Stoich Stoich Stoich\r\n');
    fprintf(fid, ' 1 "Ag-Po" %d 9.86205 .5 .5 0\r\n', layerThickness);
    fprintf(fid, ' 2 "Thick Au Layer" 10000 19.311   0   0   1\r\n');
    fprintf(fid, ' 3 "Thin Au Layer"  5000 19.311   0   0   1\r\n');
    fprintf(fid, '0 Target layer phases (0=Solid, 1=Gas)\r\n');
    fprintf(fid, '0 0 0 \r\n');
    fprintf(fid, 'Target Compound Corrections (Bragg)\r\n');
    fprintf(fid, ' 1 1 0 \r\n');
    fprintf(fid, 'Target atom displacement energies (eV)\r\n');
    fprintf(fid, '      25      25      25\r\n');
    fprintf(fid, 'Target atom lattice binding energies (eV)\r\n');
    fprintf(fid, '      3      3      3\r\n');
    fprintf(fid, 'Target atom surface binding energies (eV)\r\n');
    fprintf(fid, '      2.97      1.5      3.8\r\n');
    fprintf(fid, 'Stopping Power Version (1=2003, 0=2003)\r\n');
    fprintf(fid, ' 0 \r\n');
    out = fclose(fid);

    display(sprintf('Starting TRIM calculation for the layer at %d nm...', layerThickness))
    ! trim.exe
    display('TRIM calculation for the layer completed successfully...')
    movefile(sprintf('%s\\TRANSMIT.TXT', srimout), sprintf('%s\\TRANSMIT_%dnm.txt', cwd, layerThickness))
end
cd(cwd)

```

B.4 Monte Carlo Simulator for Solid Angle Estimation

This tool provides a straightforward yet a reliable means of estimation of the detection efficiency of a spectrometer. A monolayer of isotropic radioactive emitter is assumed on a circular source surface. The emitted particles pass through three apertures whose center coordinates and diameters can be specified individually. The detector is assumed to be circular as well. The axis of the source, three apertures and the detector need not be concentric.

```
%
% Author: Sacit M. Cetiner
%       Ph.D. Candidate
%       Penn State University
%       Department of Mechanical & Nuclear Engineering
%
% Monte Carlo simulation to estimate the solid angle for complex geometries
%
% (c) 2007
%
clc
clear all
% Load miscellaneous constants
phys_cons;

% Particle mass
m = m_alpha;                % (kg)

% Particles are monoenergetic
E      = 1000*keV;          % (J)
v      = sqrt(2*E/m);       % (m/sec)

history = 1e6;
period  = history/10;

sApp    = 0;                % Number of successful passages
sDet    = 0;                % Number of successful detections
tallyApp = zeros(history/100,1); % History number of the successful passage
tallyDet = zeros(history/100,1); % History number of the successful detection
vDet    = zeros(3, history/100);
normDet  = zeros(history/100,1);

forward = 0;
backward = 0;

%% GEOMETRY
% Source is circular
% Origin is the center of the source;
% and the source is assumed to be a monolayer (surface source)
```

```

Csrc    = [ 0 0 0 ]';          % Coordinates of the source (m)
Dsrc    = 10e-3;              % Source diameter (m)

% First aperture
% Aperture is assumed to be infinitesimally thin
Capp1   = [ 0 0 3e-3 ]';      % Coordinates of the center of aperture (m)
Dapp1   = 10e-3;              % Aperture diameter (m)

% Second aperture
% Aperture is assumed to be infinitesimally thin
Capp2   = [ 0 0 25e-3 ]';     % Coordinates of the center of aperture (m)
Dapp2   = 3e-3;               % Aperture diameter (m)
% Third aperture
% Aperture is assumed to be infinitesimally thin
Capp3   = [ 0 0 55e-3 ]';     % Coordinates of the center of aperture (m)
Dapp3   = 10e-3;              % Aperture diameter (m)

% Detector is circular
Cdet    = [ 0 0 85e-3 ]';     % Coordinates of the center of detector (m)
Ddet    = 14.5e-3;            % Detector diameter (m)

%% SIMULATION
tic
for i    = 1:history
    % Source is homogeneously distributed
    % so each point on the ring has equal probability of emission
    % Generate the emission location in cylindrical coordinates,
    % then convert it to rectangular
    r1    = Dsrc/2 * rand(1); % Distance to center (m)
    theta = 2*pi*rand(1);    % CW angle in radian
    x1    = r1*cos(theta);   % Projection on x (m)
    y1    = r1*sin(theta);   % Projection on y (m)
    Pemit = [ x1 y1 0 ]';    % Position of the emission point (m)

    % Particle emission is isotropic
    % r    = -1 + 2*rand(3,1);
    r      = rand(3,1);       % Only forward emission
    omega  = r/norm(r);       % Unit direction vector

    % Acceptance cone for the first aperture
    d1     = Capp1 - Pemit;   % Emission point-to-aperture center (m)
    d2     = omega * norm(Capp1)/norm(omega(3));
    d21    = d2 - d1;

    % Acceptance cone for the second aperture
    d3     = Capp2 - Pemit;   % Emission point-to-aperture center (m)
    d4     = omega * norm(Capp2)/norm(omega(3));
    d43    = d4 - d3;

```

```

% Acceptance cone for the third aperture
d5      = Capp3 - Pemit; % Emission point-to-aperture center (m)
d6      = omega * norm(Capp3)/norm(omega(3));
d65     = d6 - d5;

% Acceptance cone for the detector
d7      = Cdet - Pemit; % Emission point-to-detector center (m)
d8      = omega * norm(Cdet)/norm(omega(3));
d87     = d8 - d7;

if (norm(d21) < Dapp1/2)
    if (norm(d43) < Dapp2/2)
        if (norm(d65) < Dapp3/2)
            if (norm(d87) < Ddet/2)
                sDet = sDet + 1;
            end
        end
    end
end
end
end
toc

```

APPENDIX

C

BIBLIOGRAPHY ON NEUTRON DEPTH PROFILING

Following is list of articles on neutron depth profiling published after 1983. Downing et al. [\[13\]](#) also provides extensive listing of bibliography for the technique.

1. Downing, R.G., et al., Neutron Depth Profiling at the National Bureau of Standards, *Nuclear Instruments & Methods in Physics Research*, 1983, 218(1-3), pp. 47-51.
2. Downing, R.G., R.F. Fleming, and J.T. Maki, Application of Neutron Depth Profiling to Microelectronics Processing, *Abstracts of Papers of the American Chemical Society*, 1984, 187(APR), p. 39.
3. Vandervorst, W., F.R. Shepherd, and R.G. Downing, High-Resolution SIMS and Neutron Depth Profiling of Boron through Oxide-Silicon Interfaces, *Journal of Vacuum Science & Technology A – Vacuum Surfaces and Films*, 1985, 3(3), pp. 1318-1321.
4. Downing, R.G., J.T. Maki, and R.F. Fleming, Application of Neutron Depth Profiling to Microelectronic Materials Processing, *ACS Symposium Series*, 1986, 295,

pp. 163-180.

5. Maki, J.T., R.F. Fleming, and D.H. Vincent, Deconvolution of Neutron Depth Profiling Spectra, *Nuclear Instruments & Methods in Physics Research Section B – Beam Interactions with Materials and Atoms*, 1986, 17(2), pp. 147-155.
6. Downing, R.G., J.T. Maki, and R.F. Fleming, Analytical Applications of Neutron Depth Profiling, *Journal of Radioanalytical and Nuclear Chemistry*, 1987, 112(1), pp. 33-46.
7. Bowman, R.C., et al., Optical and Structural Characterization of Heavily Boron-Implanted CDTE, *Journal of Crystal Growth*, 1988, 86(1-4), pp. 768-777.
8. Lee, M.C., K. Verghese, and R.P. Gardner, A Model for the Detector Response Function in Neutron Depth Profiling, *Nuclear Instruments & Methods in Physics Research Section B – Beam Interactions with Materials and Atoms*, 1988, 31(4), pp. 567-575.
9. Chu, W.K., Large-Angle Coincidence Spectrometry for Neutron Depth Profiling, *Radiation Effects and Defects in Solids*, 1989, 108(1), pp. 125-126.
10. Wu, A.T., et al., Nitridation-Induced Surface Donor Layer in Silicon, *Applied Physics Letters*, 1989, 55(16), pp. 1665-1667.
11. Downing, R.G., et al., The Measurement of Boron at Silicon-Wafer Surfaces by Neutron Depth Profiling, *Journal of Applied Physics*, 1990, 67(8), pp. 3652-3654.
12. Fink, D., et al., Energy, Fluence and Temperature-Dependence of MeV Nitrogen Implantation Profiles in Steel, *Radiation Effects and Defects in Solids*, 1990, 115(1-3), pp. 121-134.
13. Fink, D. and L. Wang, On The Thermal Annealing Behavior of Boron in Solids, *Radiation Effects and Defects in Solids*, 1990, 114(4), pp. 343-371.
14. Fink, D., et al., 30-keV to 2-MeV Boron Implantation Profiles in Solids. *Radiation Effects and Defects in Solids*, 1990, 115(1-3), pp. 93-112.
15. Parikh, N.R., et al., Neutron Depth Profiling by Coincidence Spectrometry, *Nuclear Instruments & Methods in Physics Research Section B – Beam Interactions with Materials and Atoms*, 1990, 45(1-4), pp. 70-74.

16. Robinson, L., F.F. Dyer, and J.F. Emery, Proposed Neutron-Activation Analysis Facilities in the Advanced-Neutron-Source, *Nuclear Instruments & Methods in Physics Research Section A –Accelerators Spectrometers Detectors and Associated Equipment*, 1990, 299(1-3), pp. 413-415.
17. Unlu, K. and D.H. Vincent, Range Profiles and Thermal Release of He-3 Implanted into Various Nickel-Based Amorphous-Alloys, *Nuclear Instruments & Methods in Physics Research Section A –Accelerators Spectrometers Detectors and Associated Equipment*, 1990, 299(1-3), pp. 606-609.
18. Coakley, K.J., A Cross-Validation Procedure for Stopping the EM Algorithm and Deconvolution of Neutron Depth Profiling Spectra, *IEEE Transactions on Nuclear Science*, 1991, 38(1), pp. 9-15.
19. Bollmann, J., et al., On the Correlation of Implantation Defects and Implanted Species, *Mikrochimica Acta*, 1992, 107(3-6), pp. 179-187.
20. Fink, D., et al., External Oxidation Of Aluminum Lithium Alloys, *Surface & Coatings Technology*, 1992, 51(1-3), pp. 57-64.
21. Kumakhov, M.A. and V.A. Sharov, A Neutron Lens, *Nature*, 1992, 357(6377), pp. 390-391.
22. Lamaze, G.P., et al., The New Cold Neutron Depth Profiling Instrument at NIST, *Journal of Radioanalytical and Nuclear Chemistry*, 1992, 160(2), pp. 315-325.
23. Unlu, K. and D.H. Vincent, He-3 Behavior in Some Nickel-Based Amorphous-Alloys, *Nuclear Science and Engineering*, 1992, 110(4), pp. 386-393.
24. Downing, R.G., et al., Neutron Depth Profiling - Overview and Description Of NIST Facilities, *Journal of Research of the National Institute of Standards and Technology*, 1993, 98(1), pp. 109-126.
25. Goppelt, P., et al., Range Measurement of Boron Isotopes in Silicon from 600 keV TO 2 MeV, *Nuclear Instruments & Methods in Physics Research Section B –Beam Interactions with Materials and Atoms*, 1993, 80-1, pp. 62-64.
26. Havranek, V., et al., Neutron Depth Profiling by Large-Angle Coincidence Spectrometry, *Nuclear Instruments & Methods in Physics Research Section B-Beam Interactions with Materials and Atoms*, 1993, 73(4), pp. 523-530.

27. Lamaze, G.P., et al., Analysis of Boron in CVD Diamond Surfaces using Neutron Depth Profiling, *Applied Surface Science*, 1993, 65-6, pp. 587-592.
28. McWhinney, H.G., et al., Diffusion of Li-6 Isotopes in Lithium Aluminate Ceramics using Neutron Depth Profiling, *Journal of Nuclear Materials*, 1993, 203(1), pp. 43-49.
29. Soni, K.K., et al., Depth Distribution of Lithium in Oxidized Binary Al-Li Alloys Determined by Secondary Ion Mass-Spectrometry and Neutron Depth Profiling, *Corrosion*, 1993, 49(1), pp. 31-41.
30. Svorcik, V., et al., Diffusion into Polypropylene of Chlorides of Alkali-Metals, *European Polymer Journal*, 1993, 29(7), pp. 923-926.
31. Welsh, J.F., et al., Studies in Neutron Depth Profiling, *Journal of Radioanalytical and Nuclear Chemistry*, 1993, 167(1), pp. 111-119.
32. Eleveld, H., et al., Thermal-Desorption of Helium Irradiated Beryllium Studied by THDS, NDP, PA and SEM, *Journal of Nuclear Materials*, 1994, 212, pp. 971-975.
33. Fink, D., et al., Ion Track Doping, *Radiation Effects and Defects in Solids*, 1994, 132(2), pp. 81-90.
34. Hackenberger, L.B., et al., Effect of Stoichiometry on the Phases Present in Boron-Nitride Thin-Films, *Journal of Vacuum Science & Technology A - Vacuum Surfaces and Films*, 1994, 12(4), pp. 1569-1575.
35. James, W.D., J.B. Shapiro, and E.A. Schweikert, Nuclear Analytical Facilities at Texas A&M University, *Journal of Radioanalytical and Nuclear Chemistry*, 1994, 180(2), pp. 309-312.
36. Lamaze, G.P., et al., Analysis of Cubic Boron-Nitride Thin-Films by Neutron Depth Profiling, *Diamond and Related Materials*, 1994, 3(4-6), pp. 728-731.
37. Rossi, F., et al., Physical-Properties of Nitrogenated Amorphous-Carbon Films Produced by Ion-Beam-Assisted Deposition, *Thin Solid Films*, 1994, 253(1-2), pp. 85-89.
38. Schweikert, E.A. and J.F. Welsh, New Approaches For Neutron Depth Profiling, *Journal of Radioanalytical and Nuclear Chemistry*, 1994, 180(2), pp. 255-262.

39. Unlu, K. and B.W. Wehring, Neutron Depth Profiling at the University of Texas, *Nuclear Instruments & Methods in Physics Research Section A –Accelerators Spectrometers Detectors and Associated Equipment*, 1994, 353(1-3), pp. 402-405.
40. Vobecky, M., History of Development and Applications of Nuclear Analytical Methods in the Czech-Republic, *Biological Trace Element Research*, 1994, 43-5, pp. 1-6.
41. Wehring, B.W., J.Y. Kim, and K. Unlu, Neutron Focusing System for the Texas Cold Neutron Source, *Nuclear Instruments & Methods in Physics Research Section A –Accelerators Spectrometers Detectors and Associated Equipment*, 1994, 353(1-3), pp. 137-140.
42. Coakley, K.J., et al., Modeling Detector Response for Neutron Depth Profiling, *Nuclear Instruments & Methods in Physics Research Section A –Accelerators Spectrometers Detectors and Associated Equipment*, 1995, 366(1), pp. 137-144.
43. Downing, R.G. and G.P. Lamaze, Near-Surface Profiling of Semiconductor Materials using Neutron Depth Profiling, *Semiconductor Science and Technology*, 1995, 10(11), pp. 1423-1431.
44. Fink, D., et al., Doping of Nuclear Tracks With Fullerene Solution, *Radiation Measurements*, 1995, 25(1-4), pp. 85-88.
45. Fink, D., et al., Depth Profiles of Fullerene in Ion-Irradiated Polyimide, *Nuclear Instruments & Methods in Physics Research Section B –Beam Interactions with Materials and Atoms*, 1995, 100(1), pp. 69-79.
46. Fink, D., et al., Three-dimensional implantation distribution of lithium implanted into pyrographite, as revealed by solid state tomography in combination with neutron depth profiling, *Nuclear Instruments & Methods in Physics Research Section B –Beam Interactions with Materials and Atoms*, 1995, 103(4), pp. 423-428.
47. Hnatowicz, V., et al., Doping of ion implanted polyethylene with metallocarborane, *Nuclear Instruments & Methods in Physics Research Section B –Beam Interactions with Materials and Atoms*, 1995, 105(1-4), pp. 241-244.
48. Ronning, C., et al., Conduction Processes in Boron-Doped and Nitrogen-Doped Diamond-Like Carbon-Films Prepared by Mass-Separated Ion-Beam Deposition, *Diamond and Related Materials*, 1995, 4(5-6), pp. 666-672.

49. Fink, D., et al., On the redistribution of Li-6(+) ions implanted into polypropylene foils, *Applied Physics a-Materials Science & Processing*, 1996, 62(4), pp. 359-367.
50. Fink, D., et al., Bonding of dopants to irradiated polymers, *Nuclear Instruments & Methods in Physics Research Section B –Beam Interactions with Materials and Atoms*, 1996, 116(1-4), pp. 434-439.
51. Fink, D., et al., Doping of 20 MeV fullerene ion tracks in polyimide, *Nuclear Instruments & Methods in Physics Research Section B –Beam Interactions with Materials and Atoms*, 1996, 119(4), pp. 591-595.
52. Mackey, E.A., et al., Use of neutron beams for chemical analysis at NIST, *Journal of Radioanalytical and Nuclear Chemistry*, 1996, 203(2), pp. 413-427.
53. Prask, H.J., Materials characterization with cold neutrons, *Nondestructive Characterization of Materials VII*, Pts 1 and 2, 1996, 210-, pp. 711-718.
54. ChenMayer, H.H., et al., A polycapillary bending and focusing lens for neutrons, *Review of Scientific Instruments*, 1997, 68(10), pp. 3744-3750.
55. ChenMayer, H.H., et al., Capillary neutron optics for prompt-gamma activation analysis, *Journal of Radioanalytical and Nuclear Chemistry*, 1997, 215(1), pp. 141-145.
56. Hnatowicz, V., et al., Doping of ion irradiated polyethyleneterephthalate from water solution of LiCl, *Physica Status Solidi A –Applied Research*, 1997, 159(2), pp. 327-333.
57. Kolarova, P., et al., Relation between optical properties and lithium concentration in lithium niobate waveguiding layers, *Chemicke Listy*, 1997, 91(9), pp. 784-785.
58. Unlu, K. and B.W. Wehring, Neutron depth profiling applications at The University of Texas research reactor, *Journal of Radioanalytical and Nuclear Chemistry*, 1997, 217(2), pp. 273-278.
59. Vacik, J., et al., High-fluence boron implantation into polymers, *Radiation Effects and Defects in Solids*, 1997, 143(2), pp. 139-156.
60. Fink, D., et al., On the uptake of aqueous tracer solutions by pristine and ion-irradiated PEEK, *Nuclear Instruments & Methods in Physics Research Section B –Beam Interactions with Materials and Atoms*, 1998, 134(1), pp. 61-72.

61. Kolarova, P., et al., Neutron depth profiling study of lithium niobate optical waveguides, *Nuclear Instruments & Methods in Physics Research Section B –Beam Interactions with Materials and Atoms*, 1998, 141(1-4), pp. 498-500.
62. McGuire, S.C. and J.D. Sulcer, Nickel aluminide thin film fabrication via ion beam sputtering of compound targets, *Surface & Coatings Technology*, 1998, 100(1-3), pp. 362-365.
63. Perina, V., et al., RBS measurement of depth profiles of erbium incorporated into lithium niobate for optical amplifier applications, *Nuclear Instruments & Methods in Physics Research Section B –Beam Interactions with Materials and Atoms*, 1998, 139(1-4), pp. 208-212.
64. Svorcik, V., et al., Doping of ion irradiated poly(aryl ether ether ketone) from water solution of LiCl, *Polymer Degradation and Stability*, 1998, 62(3), pp. 535-540.
65. Turcicova, H., et al., Plasma processing of LiNbO₃ in a hydrogen/oxygen radio-frequency discharge, *Journal of Physics D –Applied Physics*, 1998, 31(9), pp. 1052-1059.
66. Turcicova, H., et al., LiNbO₃ exposed to radio-frequency plasma, *Nuclear Instruments & Methods in Physics Research Section B –Beam Interactions with Materials and Atoms*, 1998, 141(1-4), pp. 494-497.
67. Vacik, J., et al., Pulse-shape discrimination in neutron depth profiling technique, *Nuclear Instruments & Methods in Physics Research Section B–Beam Interactions with Materials and Atoms*, 1998, 142(3), pp. 397-401.
68. Vacik, J., et al., Damage profile examination on ion irradiated peek by Li-6 doping and neutron depth profiling technique, *Nuclear Instruments & Methods in Physics Research Section B –Beam Interactions with Materials and Atoms*, 1998, 141(1-4), pp. 216-222.
69. Vacik, J., et al., Prompt nuclear analytical techniques for material research in accelerator driven transmutation technologies, Prospects and quantitative analyses, *Nuclear Instruments & Methods in Physics Research Section B –Beam Interactions with Materials and Atoms*, 1998, 139(1-4), pp. 264-267.
70. Fink, D., et al., On the redistribution of 20-keV lithium in CuInSe₂, *Solar Energy Materials and Solar Cells*, 1999, 59(3), pp. 217-231.

71. Fink, D., et al., New ways of polymeric ion track characterization, *Nuclear Instruments & Methods in Physics Research Section B-Beam Interactions with Materials and Atoms*, 1999, 156(1-4), pp. 170-176.
72. Fink, D., et al., Tomographic study of the three-dimensional distribution of a high-fluence implant in a polymer, *Applied Physics a-Materials Science & Processing*, 1999, 68(4), pp. 429-434.
73. Ghosh, S., et al., On the penetration of aqueous solutions into pristine and radiation damaged polyimide, *Radiation Physics and Chemistry*, 1999, 55(3), pp. 271-284.
74. Krings, L.H.M., et al., Lithium depth profiling in thin electrochromic WO₃ films, *Journal of Vacuum Science & Technology A*, 1999, 17(1), pp. 198-205.
75. Lamaze, G.P., et al., In situ measurement of lithium movement in thin film electrochromic coatings using cold neutron depth profiling, *Surface and Interface Analysis*, 1999, 27(7), pp. 644-647.
76. Mildner, D.F.R. and H.H. Chen-Mayer, Neutron absorption measurements using converging beams - increased reaction rate, *Nuclear Instruments & Methods in Physics Research Section A -Accelerators Spectrometers Detectors and Associated Equipment*, 1999, 422(1-3), pp. 21-25.
77. Schut, H., et al., Annealing behaviour of defects in helium implanted MgO, *Nuclear Instruments & Methods in Physics Research Section B-Beam Interactions with Materials and Atoms*, 1999, 147(1-4), pp. 212-215.
78. Svorcik, V., et al., Li⁺ grafting of ion irradiated polyethylene, *Nuclear Instruments & Methods in Physics Research Section B -Beam Interactions with Materials and Atoms*, 1999, 149(3), pp. 331-335.
79. Unlu, K., M. Saglam, and B.W. Wehring, Helium-3 and boron-10 concentration and depth measurements in alloys and semiconductors using NDP, *Nuclear Instruments & Methods in Physics Research Section A -Accelerators Spectrometers Detectors and Associated Equipment*, 1999, 422(1-3), pp. 885-890.
80. Vacik, J., et al., Pulse-shape discrimination in neutron depth profiling radioanalytical methods: Part II, *Czechoslovak Journal of Physics*, 1999, 49, pp. 417-422.

81. Vacik, J., et al., Molten fluoride salts incorporation into pristine and ion-modified carbon allotropes and metallic foils, *Czechoslovak Journal of Physics*, 1999, 49, pp. 997-1002.
82. Vacik, J., et al., High fluence boron implantation into polyimide, *Nuclear Instruments & Methods in Physics Research Section B-Beam Interactions with Materials and Atoms*, 1999, 148(1-4), pp. 1126-1130.
83. van Veen, A., et al., The formation of microvoids in MgO by helium ion implantation and thermal annealing, *Nuclear Instruments & Methods in Physics Research Section B-Beam Interactions with Materials and Atoms*, 1999, 148(1-4), pp. 768-772.
84. Busker, G., et al., Predicted vacancy cluster structures in MgO and their interaction with helium, *Nuclear Instruments & Methods in Physics Research Section B-Beam Interactions with Materials and Atoms*, 2000, 171(4), pp. 528-536.
85. Fink, D. and M. Muller, Capillarie penetration of etchant solution into swift heavy ion-irradiated silicone rubber, *Nuclear Instruments & Methods in Physics Research Section B-Beam Interactions with Materials and Atoms*, 2000, 170(1-2), pp. 134-144.
86. Fink, D., et al., Redistribution of boron in silicon after Ne⁺ postirradiation and thermal annealing, *Radiation Effects and Defects in Solids*, 2000, 152(1), pp. 67-86.
87. Godey, S., et al., Helium desorption from cavities induced by high energy He-3 and He-4 implantation in silicon, *Materials Science and Engineering B-Solid State Materials for Advanced Technology*, 2000, 73(1-3), pp. 54-59.
88. Kooi, B.J., et al., Rectangular nanovoids in helium-implanted and thermally annealed MgO(100), *Applied Physics Letters*, 2000, 76(9), pp. 1110-1112.
89. Lamaze, G.P. and H.H. Chen-Mayer, Elemental analysis of thin films by neutron depth profiling, *Abstracts of Papers of the American Chemical Society*, 2000, 220, pp. U20-U20.
90. Lamaze, G.P., et al., Analysis of lithium transport in electrochromic multilayer films by neutron depth profiling, *Surface and Interface Analysis*, 2000, 29(9), pp. 638-642.

91. Levenson, M.S. and K.J. Coakley, Adaptive use of prior information in inverse problems, an application to neutron depth profiling, *Measurement Science & Technology*, 2000, 11(3), pp. 278-284.
92. Neeft, E.A.C., et al., Helium irradiation effects in single crystals of MgAl_2O_4 , *Nuclear Instruments & Methods in Physics Research Section B – Beam Interactions with Materials and Atoms*, 2000, 166, pp. 238-243.
93. Sharov, V.A., et al., Cold neutron microprobe for materials analysis using tapered capillary optics, *Review of Scientific Instruments*, 2000, 71(9), pp. 3247-3253.
94. Turcicova, H., et al., Sheet resistance of LiNbO_3 wafers processed in radio-frequency plasma of hydrogen, *Czechoslovak Journal of Physics*, 2000, 50, pp. 461-465.
95. Turcicova, H., et al., Li depth profile anomaly after radio-frequency hydrogen plasma processing of single crystal LiNbO_3 , *Ferroelectrics*, 2000, 239(1-4), pp. 1183-1190.
96. Turcicova, H., et al., Surface analysis of LiNbO_3 single crystals modified by radiofrequency hydrogen plasma, *Surface and Interface Analysis*, 2000, 29(4), pp. 260-264.
97. Vacik, J., et al., Annealing behaviour of boron atoms implanted into polyethyleneterephthalate, *Nuclear Instruments & Methods in Physics Research Section B-Beam Interactions with Materials and Atoms*, 2000, 166, pp. 637-640.
98. Neeft, E.A.C., et al., Annealing effects of helium implanted single crystals and polycrystalline magnesium aluminate spinel, *Progress in Nuclear Energy*, 2001, 38(3-4), pp. 287-290.
99. Spirkova-Hradilova, J., et al., The possibility of tailoring the $n(e)$ vs $c(\text{Li})$ relationship in lithium niobate optical waveguides, *Optical Materials*, 2001, 15(4), pp. 269-278.
100. Vacik, J., et al., Energy loss and energy straggling of light ions in fullerite, *Fullerene Science and Technology*, 2001, 9(2), pp. 197-209.
101. van Huis, M.A., et al., Lithium ion implantation effects in MgO (100), *Positron Annihilation - ICPA-12*, 2001, 363-3, pp. 448-450.

102. Cervena, J., et al., Decoration of radiation damages in polyimide implanted with rare gas ions, *Surface & Coatings Technology*, 2002, 158, pp. 391-394.
103. Cervena, J., et al., Coloring of radiation damages in ion-implanted poly(aryl ether ether ketone), LiCl uptake and thermal desorption, *Journal of Applied Polymer Science*, 2002, 83(13), pp. 2780-2784.
104. Coakley, K.J., et al., Calibration of a stopping power model for silicon based on analysis of neutron depth profiling and secondary ion mass spectrometry measurements, *Nuclear Instruments & Methods in Physics Research Section B –Beam Interactions with Materials and Atoms*, 2002, 192(4), pp. 349-359.
105. Damen, P.M.G., et al., Helium damage and helium effusion in fully stabilised zirconia, *Nuclear Instruments & Methods in Physics Research Section B-Beam Interactions with Materials and Atoms*, 2002, 191, pp. 571-576.
106. Fink, D., et al., Aqueous marker penetration into ion irradiated polyimide, *Nuclear Instruments & Methods in Physics Research Section B –Beam Interactions with Materials and Atoms*, 2002, 191, pp. 662-668.
107. Grisolia, J., et al., Growth mechanism of cavities in MeV helium implanted silicon, *Journal of Applied Physics*, 2002, 91(11), pp. 9027-9030.
108. Nekvindova, P., et al., Annealed proton exchanged optical waveguides in lithium niobate, differences between the X- and Z-cuts, *Optical Materials*, 2002, 19(2), pp. 245-253.
109. van Veen, A., et al., Nanocavity formation processes in MgO(100) by light ion (D, He, Li) and heavy ion (Kr, Cu, Au) implantation, *Nuclear Instruments & Methods in Physics Research Section B –Beam Interactions with Materials and Atoms*, 2002, 191, pp. 610-615.
110. Chen-Mayer, H.H., et al., Two aspects of thin film analysis, boron profile and scattering length density profile, *Nuclear Instruments & Methods in Physics Research Section a-Accelerators Spectrometers Detectors and Associated Equipment*, 2003, 505(1-2), pp. 531-535.
111. Coakley, K.J., et al., Modeling detector response for neutron depth profiling, *Nuclear Instruments & Methods in Physics Research Section a-Accelerators Spectrometers Detectors and Associated Equipment*, 2003, 515(3), pp. 892-893.

112. Damen, P.M.G., et al., Thermal annealing behaviour and defect evolution of helium in fully stabilised zirconia, *Journal of Nuclear Materials*, 2003, 319, pp. 65-73.
113. Lamaze, G.P., et al., Cold neutron depth profiling of lithium-ion battery materials, *Journal of Power Sources*, 2003, 119, pp. 680-685.
114. Nekvindova, P., et al., Features of APE waveguides in different Er , LiNbO₃ and (Er+Yb), LiNbO₃ cuts, electrooptical coefficient $r(33)$, *Optical Materials*, 2003, 24(3), pp. 527-535.
115. Salavcova, L., et al., Lithium migration based fabrication of few-modes planar glass waveguides, *Solid State Chemistry V*, 2003, 90-91, pp. 577-582.
116. Soares, M.R.F., et al., B-10(+)-ion implantation into photoresist, *Applied Physics A –Materials Science & Processing*, 2003, 77(7), pp. 891-898.
117. Lamaze, G.P., H.H. Chen-Mayer, and K.K. Soni, Analyses of thin films and surfaces by cold neutron depth profiling, *Applied Surface Science*, 2004, 238(1-4), pp. 108-112.
118. Otano-Rivera, W., et al., Effect of Al additions and AlN interlayers on the stabilization of cBN sputtered thin films, *Diamond and Related Materials*, 2004, 13(9), pp. 1690-1696.
119. Shultis, J.K., Computation and inversion of ion spectra for neutron depth profiling of curved surfaces, *Nuclear Instruments & Methods in Physics Research Section A –Accelerators Spectrometers Detectors and Associated Equipment*, 2004, 526(3), pp. 359-375.
120. Soares, M.R.F., et al., Li-6(+) ion implantation into polystyrene, *Nuclear Instruments & Methods in Physics Research Section B –Beam Interactions with Materials and Atoms*, 2004, 218, pp. 300-307.
121. van Huis, M.A., et al., Formation, growth and dissociation of He bubbles in Al₂O₃, *Nuclear Instruments & Methods in Physics Research Section B –Beam Interactions with Materials and Atoms*, 2004, 216, pp. 149-155.
122. Gilliam, S.B., et al., Helium retention and surface blistering characteristics of tungsten with regard to first wall conditions in an inertial fusion energy reactor, *Nuclear Instruments & Methods in Physics Research Section B –Beam Interactions with Materials and Atoms*, 2005, 241(1-4), pp. 491-495.

123. Gilliam, S.B., et al., Retention and surface blistering of helium irradiated tungsten as a first wall material, *Journal of Nuclear Materials*, 2005, 347(3), pp. 289-297.
124. Vacik, J., et al., Diffusion of Li-6 in tantalum and tungsten studied by the neutron depth profiling technique, *Diffusion in Materials*, DIMAT 2004, Pt 1 and 2, 2005, 237-240, pp. 485-490.
125. Fink, D., et al., 100 keV $^{10}\text{B}^{+}$ implantation into poly-(di-n-hexyl silane), (PDHSi), *Applied Physics A –Materials Science & Processing*, 2006, 84(1-2), pp. 131-137.
126. Mackova, A., et al., RBS, PIXE and NDP study of erbium incorporation into glass surface for photonics applications, *Nuclear Instruments & Methods in Physics Research Section B –Beam Interactions with Materials and Atoms*, 2006. 249, pp. 856-858.
127. Majeed, R., et al., Dielectric constant and surface morphology of the elemental diffused polyimide, *Journal of Physics D-Applied Physics*, 2006, 39(22), pp. 4855-4859.
128. Vacik, J., et al., Diffusion of Li-6 in tungsten and tantalum, *Acta Physica Slovaca*, 2006, 56(2), pp. 99-102.
129. Vacik, J., et al., Diffusion of Li-6 in Ta and W, *Nuclear Instruments & Methods in Physics Research Section B –Beam Interactions with Materials and Atoms*, 2006, 249, pp. 865-868.
130. Cetiner, S.M. and K. Unlu, Depth profiling of boron in ultra-shallow junction devices using time-of-flight neutron depth profiling (TOF-NDP), *Nuclear Instruments & Methods in Physics Research Section A –Accelerators Spectrometers Detectors and Associated Equipment*, 2007, 579(1), pp. 148-152.
131. Cetiner, S.M., K. Unlu, and R.G. Downing, Development of time-of-flight neutron depth profiling at Penn State University, *Journal of Radioanalytical and Nuclear Chemistry*, 2007, 271, pp. 275-281.
132. Salavcova, L., et al., Localised doping of Li-silicate glasses by Er^{3+} ion exchange to fabricate thin optical layers, *Optical Materials*, 2007, 29(7), pp. 753-759.
133. Salavcova, L., et al., Study of anomalous behaviour of LiTaO_3 during the annealed proton exchange process of optical waveguide's formation - comparison with LiNbO_3 , *Optical Materials*, 2007, 29(7), pp. 913-918.

134. Simons, D.S., et al., Development of certified reference materials of ion-implanted dopants in silicon for calibration of secondary ion mass spectrometers, *Journal of Vacuum Science & Technology B*, 2007, 25(4), pp. 1365-1375.
135. Vacik, J., et al., Study of damaged depth profiles of ion-irradiated PEEK, *Surface & Coatings Technology*, 2007, 201(19-20), pp. 8370-8372.

Vita

Mustafa Sacit Çetiner

Mustafa Sacit Çetiner was born to Gülser and Abdullah Çetiner in Izmir, Turkey. He attended Izmir Atatürk Lisesi for high school education. He graduated from Hacettepe University, Nuclear Energy Engineering Department with a B.Sc. degree with distinction. He joined the Ph.D. program in Nuclear Engineering at the Pennsylvania State University, where he concurrently obtained an M.Sc. degree in Electrical Engineering. He is a member of the American Nuclear Society (ANS) and the American Society of Mechanical Engineers (ASME).

He is married to Nesrin Özgan Çetiner. He and his beloved wife have now one child, Sarp Tarık Çetiner. They currently reside in the United States.